polymers

MDPI

Article

Structure of Cellulose Isolated from Rapeseed Stalks

Bogdan-Marian Tofanica [1], Emanuela Callone [2], Elena Ungureanu [1,*], Ovidiu C. Ungureanu [3,*] and Valentin I. Popa [4]

[1] "Ion Ionescu de la Brad" Iasi University of Life Sciences, 3 Mihail Sadoveanu Alley, 700490 Iasi, Romania; bogdan.tofanica@iuls.ro
[2] "Klaus Müller" Magnetic Resonance Laboratory, Department of Industrial Engineering, University of Trento, Via Sommarive 9, 38123 Trento, Italy; emanuela.callone@unitn.it
[3] Faculty of Medicine, "Vasile Goldis" Western University of Arad, 94 the Boulevard of the Revolution, 310025 Arad, Romania
[4] "Gheorghe Asachi" Technical University of Iasi, 73 Prof. dr. docent Dimitrie Mangeron Alley, 700050 Iasi, Romania; vipopa@tuiasi.ro
* Correspondence: elena.ungureanu@iuls.ro (E.U.); ungureanu.ovidiu@uvvg.ro (O.C.U.)

Abstract: Solid state Cross-Polarization/Magic-Angle-Spinning ^{13}C CP/MAS Nuclear Magnetic Resonance (NMR) spectra were obtained for cellulose and α-cellulose isolated from rapeseed stalks. This study provides the first characterization of the rapeseed stalk cellulose, revealing that native cellulose occurs as cellulose I allomorph, while α-cellulose exhibits distinct crystalline structures similar to those found in cellulose II. Additionally, Fourier Transform Infrared (FTIR) spectroscopy, Scanning Electron Microscopy (SEM), and Energy-Dispersive X-ray Microanalysis (EDX) were employed to further investigate and unveil the structural properties of cellulose extracted from rapeseed stalks. These complementary techniques offered a more comprehensive understanding of the cellulose morphology, crystallinity, and chemical composition, providing valuable insights into the potential utilization of rapeseed stalks as a renewable biomass resource for various industrial applications.

Keywords: rapeseed stalks; cellulose; α-cellulose; CP/MAS ^{13}C NMR; FTIR

Academic Editor: Ľuboš Krišťák

Received: 25 March 2025
Revised: 7 April 2025
Accepted: 7 April 2025
Published: 11 April 2025

Citation: Tofanica, B.-M.; Callone, E.; Ungureanu, E.; Ungureanu, O.C.; Popa, V.I. Structure of Cellulose Isolated from Rapeseed Stalks. *Polymers* **2025**, *17*, 1032. https://doi.org/10.3390/polym17081032

1. Introduction

Cellulose [1], the Earth's most abundant biopolymer, exhibits a remarkable versatility, underpinning its presence and fundamental role in both natural and manufactured environments. As the primary structural component of plant cell walls, cellulose serves a broad range of applications, from traditional construction materials to advanced biomaterials [2]. Its inherent fibrous nature, evident in materials like cotton and wood pulp, provides the tensile strength essential for textiles, pulp, and paper products. As a macromolecular entity, cellulose can be further processed—dissolving pulp, for instance, acts as precursor for regenerated fibers and cellulose derivatives, expanding its utility in advanced materials [3]. Moreover, the emerging field of cellulosic biofuels highlights the potential of this macromolecule as a renewable energy source.

Recognizing the importance of resource conservation, the well-established practice of recycling cellulose-based materials, especially paper and wood products, highlights its role in supporting circular economy principles [4]. Consequently, ongoing research into optimizing cellulose extraction, modification, and recycling processes, including the exploration and utilization of novel cellulose sources, remains crucial for addressing global sustainability challenges and fostering innovation in material development [3–5].

While the traditional cellulose sources, particularly wood pulp, have historically dominated industrial applications since the Industrial Revolution, growing awareness of environmental sustainability has driven significant interest in alternative feedstocks. Notably, before widespread industrialization, annual plants were the primary raw material for cellulose production [6]. Concurrently, the increasing generation of agricultural waste necessitates the development of effective utilization strategies [7].

The conversion of agricultural residues, such as crop stalks and husks, into valuable cellulose-based resources is driven by several critical factors. First, the sheer volume of these residues generated annually poses a significant waste management challenge. Second, the rising demand for sustainable materials calls for a transition away from reliance on conventional, often forest-derived, cellulose sources. Third, these residues represent an abundant and renewable feedstock, making their utilization a key element in fostering a circular bioeconomy. This approach directly addresses the challenging need for development of environmentally responsible industrial practices.

Building on the recognition of agricultural residues as valuable resources, *Brassica napus* L. (rapeseed) emerges as a particularly compelling case. This crop is primarily cultivated for its high-quality oil and protein cake. While the seed is the most valuable harvested component, the stalks are typically used in crop rotation to both enhance soil humus content and facilitate the incorporation, immobilization and transformation of available nitrogen and sulfur into stable organic forms in nutrient-poor soils [8].

Rapeseed stalks, an abundant agricultural byproduct, occur in large quantities at low costs. They contain significant amounts of polysaccharides and lignin, key raw materials for a variety of integrated biorefinery concepts in the emerging bioindustry as well as conventional industrial processes. In rapeseed stalks, holocellulose content ranges between 70–75%, with α-cellulose accounting for 38–42%, lignin for 17–21% and ash for 2–5% [9–14]. This compositional profile highlights the potential of rapeseed stalks as a valuable source of raw materials, warranting further investigation into their structural characteristics and potential application in sustainable production.

Given their significant chemical composition and sustainable resource potential, this study aims to isolate and comprehensively characterize cellulose derived from rapeseed stalks. Specifically, Nuclear Magnetic Resonance (NMR) and Fourier-Transform Infrared (FTIR) spectroscopy will be employed to determine the chemical composition and structural attributes of the extracted cellulose. Additionally, the study will encompass an analysis of extractives and inorganic constituents within the rapeseed stalks, thereby providing a holistic understanding of this raw material composition. Scanning Electron Microscopy (SEM) will be used to visualize the morphological features of the isolated cellulose, offering insights into its structural organization.

The elucidation of the native cellulose structure within rapeseed stalks has critical implications for understanding the transformation pathways of these lignocellulosic biomass feedstocks. This knowledge is essential for assessing cellulose behavior both as a fiber constituent and a macromolecule in various materials [15–17], as well as for advancing the use of alternative raw materials and biorefinery strategies to produce bio-based products, including materials, fibers, chemicals, and energy [18].

2. Materials and Methods

The methods commonly used to study wood and nonwood chemical compositions [10,19,20], based on standardized procedure and generally approved methods from the literature, were used for determination, isolation and purification of chemical components in rapeseed stalks (TAPPI methods, ISO standards) [21]. Figure 1 shows the scheme of the experimental procedure.

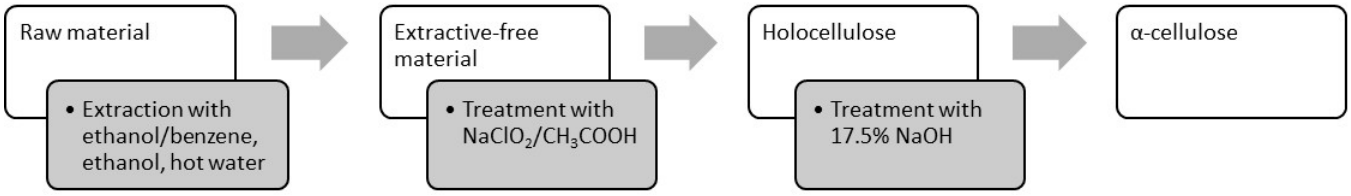

Figure 1. Method for determination of chemical components in rapeseed stalks.

Rapeseed stalks, free of leaves and dust, were harvested after seed collection from Vaslui County, Romania. The harvested stalks were air-dried and subsequently stored under laboratory conditions. Prior to testing, the stalks were manually segmented into 3–5 cm lengths. Moisture content determination was conducted in accordance with Technical Association of the Pulp and Paper Industry (TAPPI) standard T258 om-06—Basic Density and Moisture Content of Pulpwood, employing oven drying at 105 ± 3 °C.

For chemical compositional analysis, the stalks were ground and sieved to achieve a uniform particle size, passing through a 0.40 mm screen, as per TAPPI standard T257 cm-02—Sampling and Preparing Wood for Analysis.

The raw material underwent sequential extraction: initially, with an ethanol–benzene mixture (1:2) for 8 h under reflux, followed by ethanol extraction for 4 h under reflux, and finally with boiling distilled water for 1 h, adhering to TAPPI standards T204 cm-07—Solvent Extractives of Wood and Pulp and TAPPI T264 cm-07—Preparation of Wood for Chemical Analysis. The resulting extractives were concentrated using a rotary evaporator, and the solvent was removed, yielding the extractable fraction in solid form. Extractive-free material samples were utilized for the determination of holocellulose content and α-cellulose content within the raw material by a mild delignification step with an acidified solution of sodium chlorite to remove the lignin [22,23], and then with strong hydroxide solutions of NaOH (TAPPI Standard T 203 cm-09—Alpha-, Beta-, and Gamma-Cellulose in Pulp) to obtain undegraded high-molecular-weight cellulose, the "classical" α-cellulose [24,25]. All analytical results are reported on an oven-dry weight basis.

Following the extraction and purification processes, three distinct materials were obtained: extractive-free samples, holocellulose, and α-cellulose. These materials were subjected to analysis to determine their principal chemical composition using NMR and FTIR spectroscopy.

Solid-State ^{13}C CP/MAS NMR was used in the sample preparation for structural analysis of extractive-free, holocellulose and α-cellulose [26,27]. Solid-state NMR experiments were carried out on a Bruker Avance 400 WB spectrometer (Bruker Biospin, Billerica, MA, USA), operating at 100.613 MHz for ^{13}C. Samples were packed in 4 mm diameter zirconia rotors. Experimental conditions: ^{13}C ramp CP-MAS: 2.7 μs for 90° pulse, 5 s for recycle delay, 2 ms of contact time, and 10 kHz of rotating speed. Tetramethylsilane—$Si(CH_3)_4$ (TMS) was used as a primary shift scale reference for ^{13}C analyses.

FTIR spectroscopy was performed using a Bruker Vertex 70 spectrometer (Bruker Optics, Billerica, MA, USA) on potassium bromide (KBr) pellets with a 2 cm^{-1} resolution. The concentration of the samples was a constant of 2 mg/200 mg of KBr [28]. Spectral data were analyzed using Spectragryph—Optical Spectroscopy Software. Version 1.2.16.1 (2025), an optical spectroscopy software Spectragryph [29]. Scanning electron microscope (SEM) images were obtained with JSM 5500 Jeol (Jeol LTD, Tokyo, Japan) together with energy-dispersive X-ray spectroscopy (EDX) spectra [30,31].

3. Results and Discussions

The chemical composition of rapeseed stalks is characterized by a high holocellulose content, reaching 72.1%, which accounts for about three-quarters of the raw material's

weight. The stems contain approximately 40% α-cellulose and 32% hemicelluloses, along with significant amounts of soluble substances (extractable in cold water, warm water, and 1% NaOH solution) [11]. The chemical composition of rapeseed stems is similar to that of cereal straw, exhibiting a high ash content and pentosans, which are typical for annual plants [7]. Additionally, rapeseed stalks contain a considerable amount of extractable substances, ranging from 5 to 10%, including waxes, fats, and resins, which are soluble in organic solvents such as ethanol–benzene and ethanol.

Cellulose is the primary constituent of plant tissues, accounting for approximately half of the dry matter in biomass and serving as the fundamental framework of the vegetable kingdom [24]. From Figure 2, it can be seen that cellulose is a homopolymer of β-D-glucopyranose units arranged in a $^4C_1$ chain conformation, linked together by glycosidic bonds [32], with glucose as the repeating unit [33]. In cellulose, carbon atoms 2, 3 and 6 bear free hydroxyl groups that are available for chemical reactions [34]. However, every carbon is bonded to at least one oxygen, except for C-1, which is connected with two oxygen atoms.

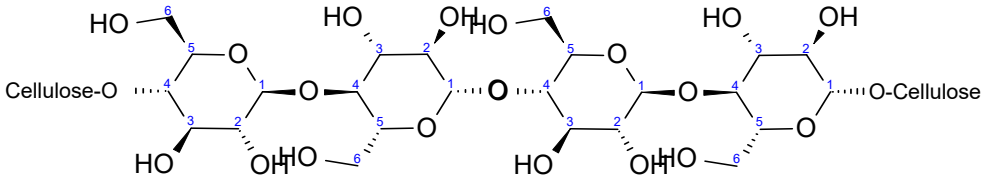

Figure 2. Schematic representation of cellulose I (native cellulose) structure.

Figure 3 shows the ^{13}C CP/MAS NMR spectra of the representative samples. The resonances in the range 50–110 ppm refer to the carbons bonded to oxygen in the cellulose structure. Both chemical shift and line shape help the discrimination of the carbons signals in the anhydroglucose unit; therefore, the description of cellulose polymorphs can be predicted. Broad resonances in the 180–120 ppm range belong to the residual lignin fraction.

Assignment of the spectra was made with the aid of previous works by Atalla and Vander Hart and [35–37] is given in Table 1 and Figure 4.

Table 1. Assignment of chemical shifts in the NMR spectrum of rapeseed stalks.

Functional Group	Extractive-Free	Holocellulose	α-Cellulose
Alkyl (0–50 ppm)	20.34 (methyl in H)	20.92 (methyl in H)	n.d.
Methoxyl (50–60 ppm)	55.41 (methoxyl in L)	n.d.	n.d.
O-alkyl (60–110 ppm)	62.05 (C6 in C) 64.33 (C6 in C) 71.86 (C2, C3, C5 in C) 73.85 (C2, C3, C5 in C) 83.61 (C4 amorphous C) 88.50 (C4 crystalline C) 104.66 (C1 in C)	62.95 (C6 in C) 64.40 (C6 in C) 72.01 (C2, C3, C5 in C) 74.62 (C2, C3, C5 in C) 82.54 (C4 amorphous C) 88.39 (C4 crystalline C) 104.64 (C1 in C)	62.18 (C6 in C) - - 74.47 (C2, C3, C5 in C) 84.25 (C4 amorphous C) 87.29 (C4 crystalline C) 104.81 (C1 in C)
Aromatic (110–145 ppm)	134.66 (aromatic in L)	n.d.	n.d.
Phenolic (145–160 ppm)	151.98 (phenolic in L)	n.d.	n.d.
Carbonyl (160–200 ppm)	(173.5) (carbonyl in H)	(174.48) (carbonyl in H)	n.d.

Abbreviation: C—cellulose, H—hemicellulose, L—lignin, n.d.—not detected.

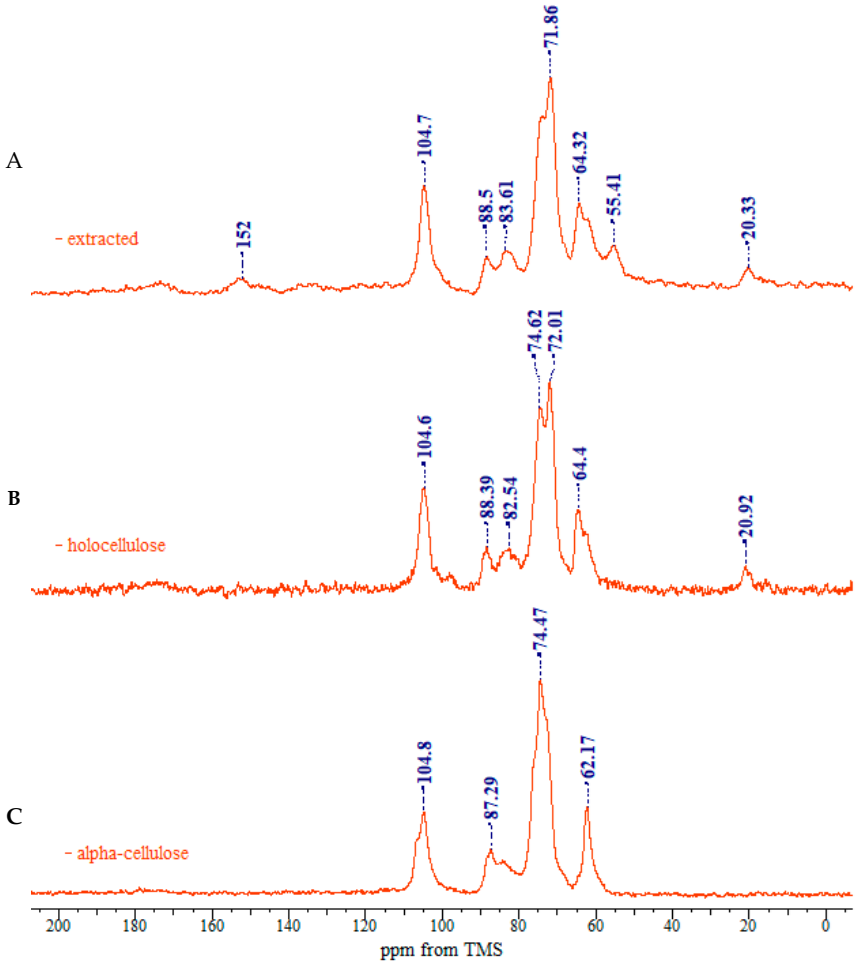

Figure 3. CP/MAS ^{13}C NMR spectra of rapeseed stalks: (**A**) extractive-free, (**B**), holocellulose, and (**C**) α-cellulose.

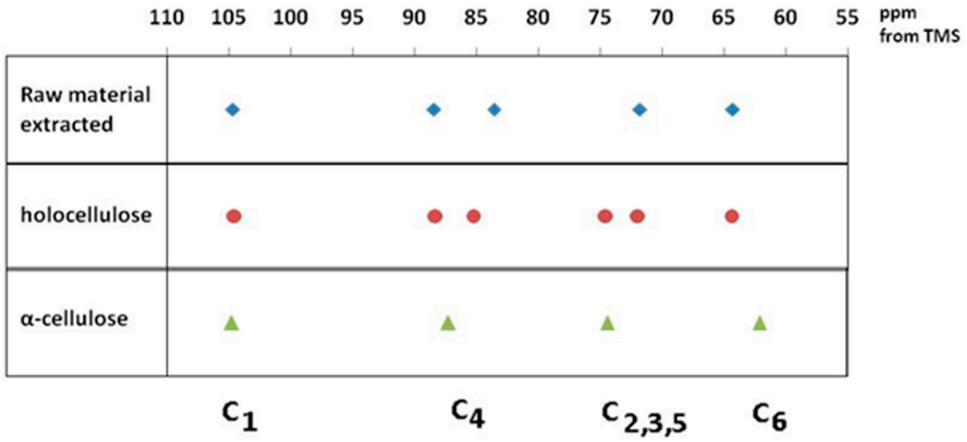

Figure 4. Main peak assignment of cellulose samples.

In the upfield region of the spectrum, resonances between 60 and 70 ppm are assigned to C-6 of the primary alcohol group. The composite peak between 70 and 81 ppm is attributed to the ring carbons C-2, C-3, and C-5, excluding those involved in the glycosidic linkage. The region between 81 and 93 ppm is associated with C-4, both crystalline and amorphous, while the range between 102 and 108 ppm is associated with the anomeric carbon C-1. The ^{13}C NMR spectra of rapeseed stalk extractive-free and holocellulose samples, as shown in Figure 3A,B are quite similar, indicating that the cellulose structure remained relatively unaffected by the treatment for the lignin removal.

Native cellulose is metastable, and it is classified as cellulose I. It features a parallel chain-packing arrangement consisting of two distinct crystalline forms, Iα and Iβ, with their proportion varying depending on the cellulose source. The cellulose I structure exhibits a complex and disordered hydrogen-bonding network. Two distinct intra-molecular hydrogen bonds are present (one between the O3-H and adjacent ring O5′, and another between the O2-H and the neighboring glucose unit O6′). Additionally, one intermolecular hydrogen bond between O6-H and O3′ is observed [38]. Between the molecular layers, van der Walls forces [39] and potential weak hydrogen bonds [40,41] contribute to the structural cohesion.

As shown in Figure 3C, the ^{13}C NMR spectrum of the α-cellulose sample is typical of cellulose II, as evidenced by the splitting of the ring carbon C-1 signal [42]. The region between 70 and 81 ppm, corresponding to C-2, C-3 and C-5, differs from that of the extractive-free and holocellulose samples. These variations may be linked to changes in hydrogen-bonding patterns, which allow the cellulose chain to adopt a new molecular conformation. The crystalline structure of cellulose II features an antiparallel chain-packing arrangement with a complex network of hydrogen bonds within and between molecular layers [43]. This extensive hydrogen bonding confers greater stability on cellulose II, compared to cellulose I.

The occurrence of the C-6 resonance as a singlet at 62 ppm indicates a conformational shift [44], specifically from the *tg*-rotamer, characteristic of the glucose unit in cellulose I, to a *gt* conformation for the hydroxymethyl group in cellulose II, as illustrated in Figure 5 [39,40].

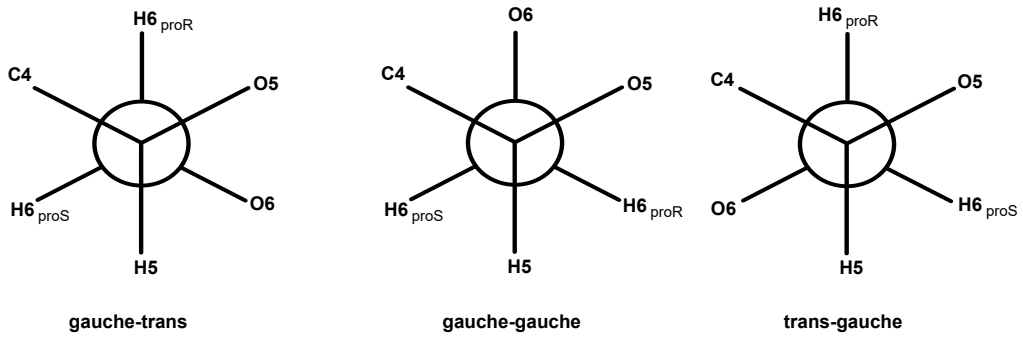

Figure 5. Rotational positions of the hydroxymethyl group: gauche-trans (gt), gauche-gauche (gg) and trans-gauche (tg).

The α-cellulose, isolated after treatment with 17.5% NaOH, followed by washing and neutralization, differs from native cellulose, not only in lattice dimensions but also in its degree of crystallinity [45].

The transition from cellulose I to cellulose II polymorphs is further identified by an increase in the relative intensity of the C-6 signal at 62 ppm, which is associated with the amorphous regions of cellulose, and a corresponding decrease in the signal at 64 ppm, associated with the crystalline regions of cellulose I. Moreover, the C-4 resonances belonging to the crystalline region decrease in intensity, while the C-4 related to the amorphous region expands into a broader resonance [46].

The polysaccharides that make up the cell wall of rapeseed stalks primarily consist of hexoses (D-glucose, D-mannose, D-galactose, and L-galactose), pentoses (D-xylose and L-arabinose), 6-deoxy-hexoses (L-rhamnose and L-fucose), and hexuronic acids (D-galacturonic acid and D-glucuronic acid) [47]. Hemicelluloses represent a significant group of plant-derived polysaccharides, ranking second in abundance after cellulose. The monomeric units of hemicelluloses associated with cellulose in the plant cell wall include hexoses, pentoses, and uronic acids, the latter resulting from the oxidation of hexoses.

Rapeseed contains common terrestrial plant polysaccharides that fulfill both structural and physiological functions. The hexose content in whole rapeseed stems ranges from 8.8% to 10.5% (determined by difference). The pentosan yield from whole stems was 23.4%, reaching up to 33.7% in the pith tissue.

The analysis of the IR spectra (Figure 6) reveals distinct absorption bands corresponding to the functional groups of carbohydrates: a broad OH stretching band at 3354 cm^{-1}, indicative of strong hydrogen bonding, and CH, CH_2 stretching vibrations at 2906 cm^{-1}. The presence of lignin in the residue is confirmed by absorption bands at 1732 cm^{-1} (carbonyl groups) and at 1632 and 1506 cm^{-1}, which are characteristic of aromatic structures. The spectral region between 1200 and 1500 cm^{-1} contains multiple overlapping absorption bands associated with CH, CH_2, C=O, and OH functional groups, common to various chemical components. The stretching vibrations of C–O, C–O–C, and C–C bonds within pyranose rings are identified at 1061 and 897 cm^{-1}.

From the analysis of the IR spectra (Figure 6 and Table 2) for the α-cellulose fraction, the most notable observations include the appearance of absorption maxima corresponding to carboxyl groups at 1230 and 1270 cm^{-1}, as well as the disappearance of ether bonds between hemicelluloses and cellulose at 1111 cm^{-1}.

Extractable substances in wood represent the only non-macromolecular components, although they are often associated with polymeric compounds. These substances are present in plant materials in relatively small proportions and can be separated through physical extraction processes. They can be extracted using organic solvents as well as under the action of hot water.

Understanding the content of extractable substances holds significant practical importance, particularly in cellulose manufacturing, as these compounds increase chemical consumption during pulping, inhibit the cooking process, and negatively impact the properties of the obtained cellulose (e.g., color and brightness). A high content of extractable substances leads to reduced cellulose yield in sulfate and natron-AQ pulping processes.

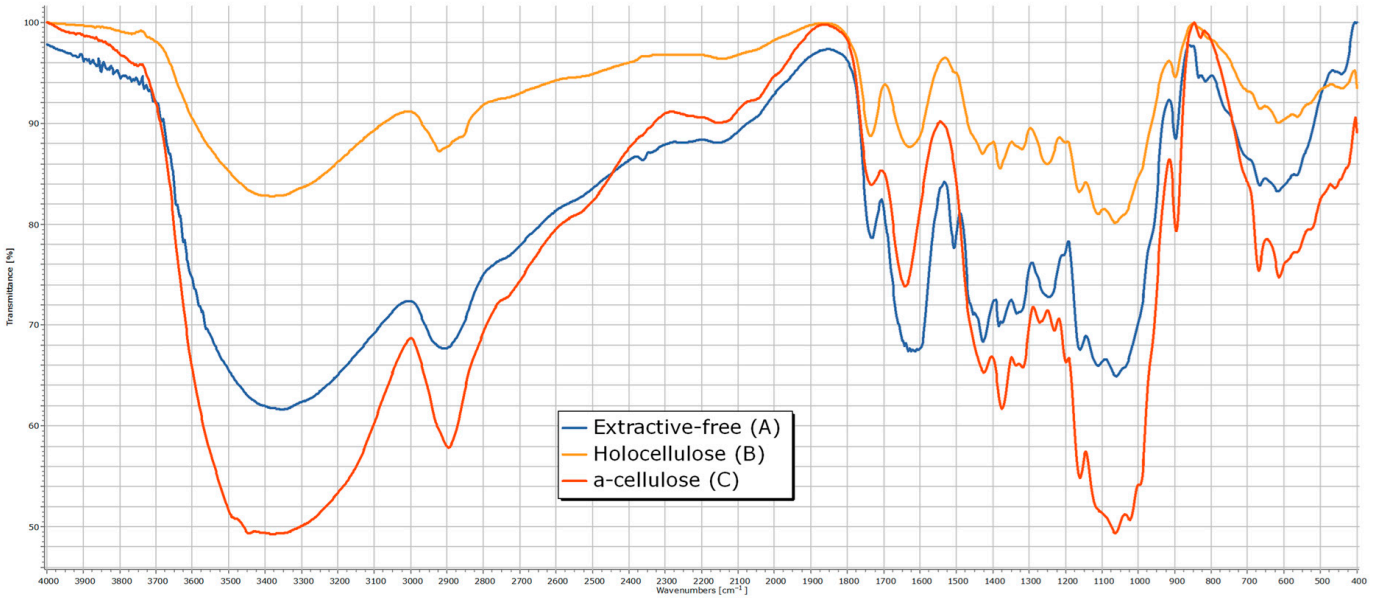

Figure 6. The IR spectrum of rapeseed stalks—extractive-free (A), holocellulose (B) and α-cellulose (C).

Benzene, ethanol, and their mixtures exhibit maximum extraction capacity and facilitate the removal of waxes, fats, phytosterols, low-molecular-weight carbohydrates, salts, and other compounds.

The infrared (IR) spectrum analysis of the extract obtained with an ethanol–benzene mixture can be divided into four characteristic regions (Figure 7), containing absorption bands indicative of specific structural elements:

- Wavelength region 3700–3200 cm^{-1}—The presence of absorption bands in this region suggests the existence of hydroxyl (-OH) groups characteristic of alcohols (νOH = 3418 cm^{-1}). The broad appearance of the absorption band indicates hydrogen bonding. Confirmation of the alcohol structure is supported by an additional intense absorption band corresponding to the C-O stretching vibration located in the fingerprint region (νC-O = 1092 cm^{-1}).
- Wavelength region 3200–2700 cm^{-1}—Absorption bands in this region correspond to the stretching vibrations of C-H bonds in alkanes (νCH = 2922 and 2853 cm^{-1}), including asymmetric and symmetric stretching vibrations of methylene (-CH_2-) groups present in alkanes, such as R(CH_2)$_4$-C, R(CH_2)$_4$-OR, and R-CH_2-R. The presence of these functional groups is further confirmed by absorption bands corresponding to alkane C-H stretching vibrations, particularly in the νCH = 1377 cm^{-1} region of the IR spectrum.
- Wavelength region 1900–1400 cm^{-1}—This region exhibits intense absorptions primarily attributed to the stretching vibration of the heterogeneous C=O bond (νC=O = 1734 cm^{-1}), which is characteristic of functional groups such as aldehydes, ketones, carboxylic acids, and esters. Additionally, this region contains bands indicative of C=C double bonds (νC=C = 1647 cm^{-1}), which may appear less intense but are highly useful in structural assignments for alkenes and aromatic compounds. The absorption band at 1508 cm^{-1} is characteristic of benzene ring vibrations.
- Wavelength region 1400–400 cm^{-1} (fingerprint region)—This region contains numerous absorption bands that characterize the overall molecular structure, including skeletal vibrations such as deformation, combination, and harmonic vibrations that cannot be assigned to normal vibrational modes. This region is particularly useful for compound identification by comparison with reference IR spectra. Notable absorptions include those associated with C-H stretching vibrations in alkanes, alkenes, and aromatic hydrocarbons (νCH = 1377 cm^{-1}), as well as C-O stretching vibrations in alcohols, ethers, esters, and carboxylic acids (νC-O = 1263 cm^{-1}). Additionally, C-H deformation vibrations (both in-plane and out-of-plane) in alkanes, alkenes, and aromatic hydrocarbons appear at δC-H = 725 and 650 cm^{-1}, respectively. The presence of C-O-C bonds is confirmed by asymmetric (νC-O-C = 1092 cm^{-1}) and symmetric (νC-O-C = 806 cm^{-1}) stretching vibrations, which are characteristic of pyranose derivatives.

The extraction of plant material represented by rapeseed stems using ethanol shows both similarities and differences when compared to the extraction with a mixture of ethanol–benzene. The absorption bands in the wavelength regions 3200–2700 cm^{-1} and 3200–2700 cm^{-1} are similar, with both extracts removing alcohol derivatives (with vibration maxima at 3416 and 1080 cm^{-1}) and alkanes (2922, 2851, and 1385 cm^{-1}) from the plant material. The spectral maxima observed in the characteristic spectrum include a peak at 1603 cm^{-1} (due to bending vibrations of C=O groups in ketones such as C-(C=O)-C=C-OH), a peak at 1267 cm^{-1} (due to bending vibrations of C-O-C groups found in ethers), and a peak at 1049 cm^{-1} (due to bending vibrations of C-O groups typical for alcohols and esters).

The examination of the IR spectrum of the hot water extract can be divided into four representative regions, which contain characteristic absorption bands determined by the presence of structural elements:

- Wavelength region 3700–3200 cm^{-1}: The presence of absorption bands in this region suggests the presence of OH groups, indicating the structure of an alcohol (νOH = 3420 cm^{-1}). The broad nature of the absorption indicates hydrogen bonding. To confirm the alcohol structure, an additional absorption band due to the stretching vibration of the C-O bond in the fingerprint region (νC-O = 1103 and 1011 cm^{-1}) is identified.
- Wavelength region 3200–2700 cm^{-1}: The absorption bands in this region are attributed to the stretching vibrations of C-H bonds in alkanes (νCH = 2936 cm^{-1} and a shoulder at 2830 cm^{-1}), as well as asymmetric and symmetric stretching vibrations specific to methylene groups in alkanes: $R(CH_2)_4$-C, $R(CH_2)_4$-OR, and R-CH_2-R. To confirm the presence of these functional groups in the molecule, additional absorption bands due to the stretching vibration of C-H bonds in alkanes located at the characteristic νCH = 1398 cm^{-1} region of the IR spectrum should be identified.
- Wavelength region 1900–1400 cm^{-1}: In this region, the spectral maxima characteristic of bending vibrations of C=O groups in ketones of the type C-(C=O)-C=C-OH (δC=O = 1616 cm^{-1}) appear, as well as an absorption band at 1506 cm^{-1}, which is typical for the benzene ring nucleus.
- Wavelength region 1400–400 cm^{-1} (fingerprint region): This region contains numerous intense absorption bands, but their structural significance is minor.

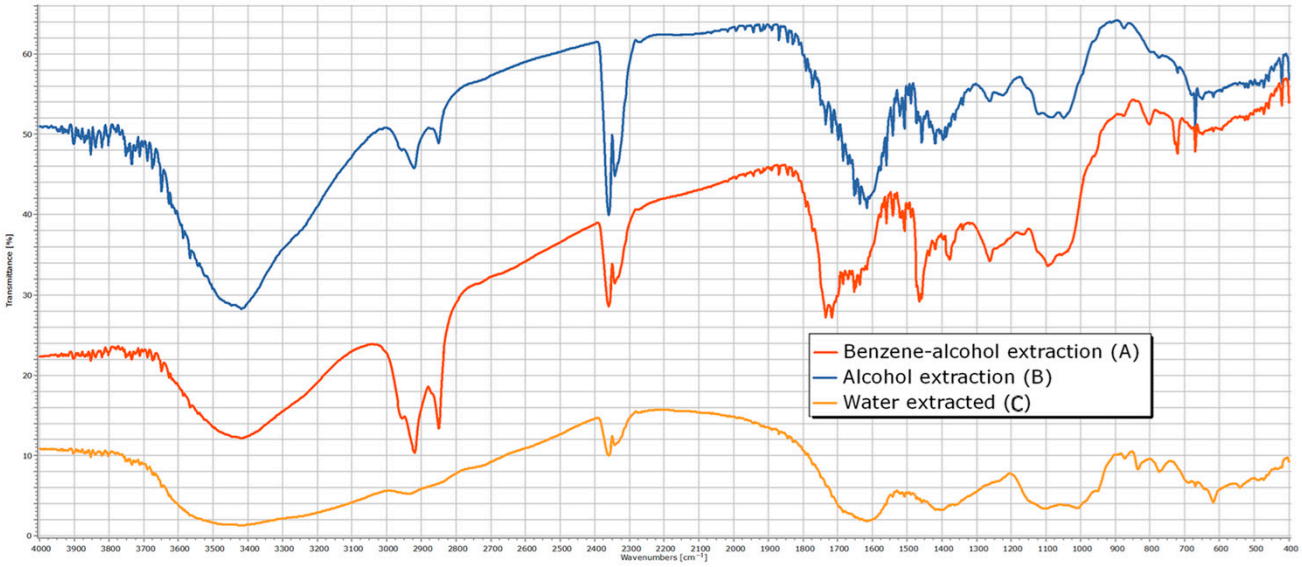

Figure 7. The IR spectrum of extractives from rapeseed stalks—benzene–alcohol extraction (A); alcohol extraction (B); water-extracted (C).

The SEM images provide valuable insight into the microstructural characteristics of rapeseed stalks, which are crucial for understanding their mechanical properties, processing potential, and applications in bio-based materials. For SEM images of rapeseed stalks in the tangential section at 100× and 500× magnifications (Figure 8a,b), it can be observed as follows:

- At 100× magnification: The overall cellular structure of the rapeseed stalk becomes visible, showing distinct fibrous regions along with the parenchyma tissue in the core. The fibers appear elongated and well organized, contributing to the mechanical strength of the stalk. The parenchyma cells, which are more loosely arranged, can be identified in the central region, serving as a storage and transport tissue.
- At 500× magnification: The finer details of the fibrous network are more pronounced. The individual fibers appear more distinct, with their elongated structure and thick

cell walls visible. The parenchyma cells, with their thinner walls and more irregular shapes, can be seen forming a matrix around the fibers. The contrast between these two tissue types highlights the hierarchical structure of cells in the rapeseed stalk, with the fibers providing rigidity and the parenchyma contributing to flexibility and metabolic functions.

Table 2. Main absorption bands in the IR spectrum of rapeseed stalks.

Absorption Bands (cm^{-1})	Vibration Type *	Intensity **	Chemical Bond ***	Functional Group	Extractive-Free	Holocellulose	α-Cellulose
3650–3000	ν (O-H)	s	H-OH; $R-CH_2-OH$; $(R)_2CH-OH$; $(R)_3C-OH$ Ar-OH	Water, alcohols	3354	3381	3381
3300; 3100–3000 3000–2800	ν (C-H)	s; m; s	≡C-H; =C-H; -C-H	-	2906	2920	2897
1820–1680	ν (C=O)	vs	R-HC=O; R-CO-OH C=C-CO-O-R Ph-CO-O-R	Aldehydes, carboxylic acids, esters, phenolic esters	1732	1736	1732
1900–1500	ν (C=C)	0-w	-HC=CH-	Alkenes	1632	1630	1641
1525–1470	ν (C=C), aromatics	m-s	Ar-R	Phenols: m-disubstituted, p-disubstituted, 1,3,4-substituted, 1,3,4,5-substituted	1506	-	-
1440–1395	δ (O-H)	w	-CO-OH	Carboxylic acids	1427	1429	1425
1450–1330	δ (O-H)	s-m	-R-OH	Alcohols	1383	1379	1375
1400–1300 1350–1320	δ (C=O) δ (O-H)	s	R-CO-OH R-O-H	Carboxylic acids, alcohols	1335	1321	1319
1300–1100	ν (C-O-C)	s	R-OC-O-C	Esters	1244	1252	-
1320–1211	ν (C-O)	s	-C-OC-OH	Carboxylic acids	-	-	1271, 1230
1300–1100	ν (C-O-C)	s	R-OC-O-C	Esters	1161	1163	1161
1150–1060 1125–1090	ν (C-O-C) ν (C-O)	m-s	$-H_2C-O-CH_2-$ R_2HC-OH	Ethers, alcohols	1111	1111	-
1100–1000	ν (C-O)	s	-C-OH	Alcohols	1061	1063	1063

* ν—valence vibrations, δ—elongation vibrations; ** Intensity: s—strong, m—medium, w—weak, 0—very weak; *** R—organic radical, Ar—aromatic nucleus = benzene.

In the SEM micrographs of a rapeseed stalk core at 100× and 500× magnification (Figure 8c,d), the cross-sectional structure reveals specific anatomical features characteristic of lignocellulosic plant materials:

- At 100× magnification, the overall cellular organization is visible, highlighting the differentiation between the outer protective layers and the inner core. The parenchyma in the central region appears as a porous, loosely packed structure, with thin-walled cells forming an interconnected network. This tissue plays a key role in storage and transport, and its open structure suggests a high potential for moisture retention and enzymatic accessibility.
- At 500× magnification, finer details of the parenchyma become more apparent, showing individual cell walls and the varying sizes of lumen spaces. The parenchyma cells appear somewhat collapsed or deformed in certain areas, likely due to the drying process, but their overall arrangement remains discernible.

The contrast between the outer region and the core of the stalks highlights the heterogeneity of the composition, which influences its mechanical properties and potential applications in bio-based materials.

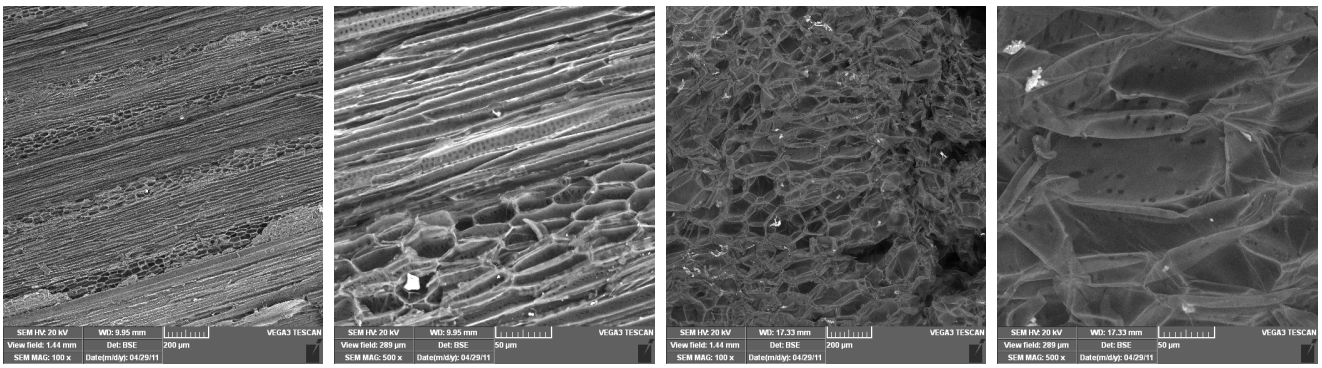

(**a**) (**b**) (**c**) (**d**)

Figure 8. Scanning electron microscopy of rapeseed stalks at different magnifications. (**a**) Tangential section 100×; (**b**) tangential section 500×; (**c**) cross section 100×; (**d**) cross section 500×.

The mineral composition of rapeseed stalks, totaling approximately 6%, was analyzed using EDX (Figure 9), revealing a combination of soluble salts predominantly consisting of carbonates, sulfates, chlorides, and oxalates, along with an insoluble fraction made up of silicates, phosphates, calcium oxide, magnesium oxide, ferric oxide, manganese oxides, and other compounds. Elemental analysis of the rapeseed stalk samples (Figure 9) indicates that calcium (Ca) is the most abundant metal, with trace amounts of sodium (Na), magnesium (Mg), aluminum (Al), silicon (Si), potassium (K), manganese (Mn), iron (Fe), and copper (Cu) also detected.

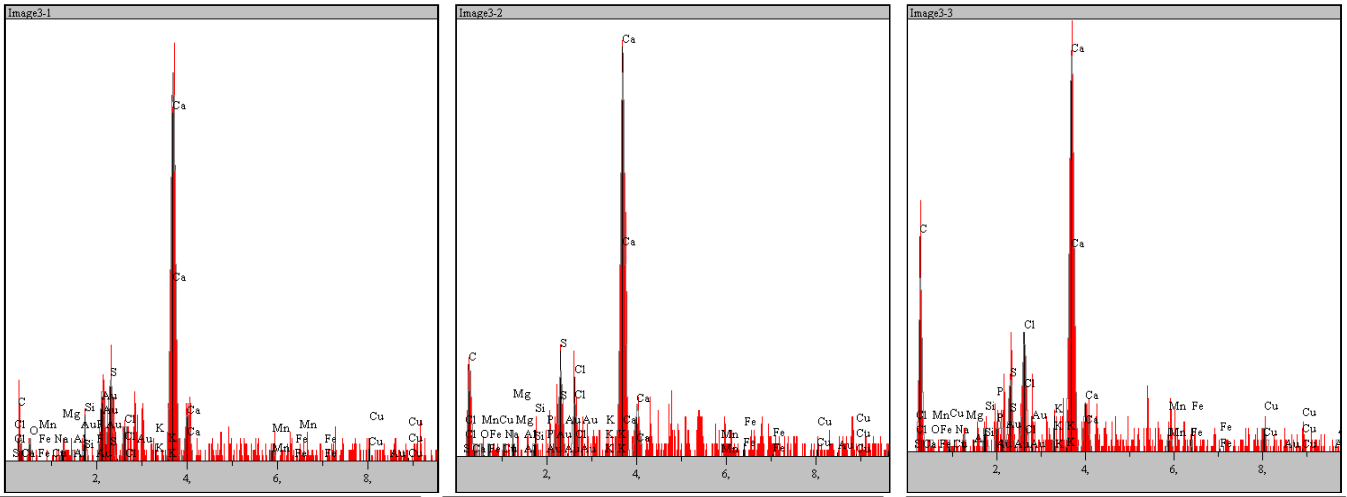

Element	Line	Intensity (c/s)	Error 2-sig	Atomic Wt %	Conc. %	Units
C	Ka	2.01	0.517	64.135	32.965	wt.%
N	Ka	0.17	0.151	12.238	7.335	wt.%
O	Ka	0.23	0.173	4.039	2.765	wt.%
Na	Ka	0.33	0.210	0.583	0.573	wt.%
Mg	Ka	0.39	0.229	0.477	0.497	wt.%
Al	Ka	0.02	0.057	0.023	0.027	wt.%
Si	Ka	0.48	0.253	0.399	0.479	wt.%
P	Ka	0.17	0.149	0.124	0.164	wt.%
S	Ka	2.39	0.565	1.996	2.739	wt.%
Cl	Ka	1.55	0.454	1.190	1.806	wt.%
K	Ka	0.20	0.162	0.148	0.248	wt.%
Ca	Ka	12.38	1.285	10.022	17.189	wt.%
Mn	Ka	0.16	0.148	0.170	0.399	wt.%
Fe	Ka	0.27	0.191	0.309	0.739	wt.%
Cu	Ka	0.30	0.201	0.503	1.368	wt.%
Au	La	1.27	0.412	3.643	30.706	wt.%
Total				100.00	100.00	wt.%

(**A**)

Element	Line	Intensity (c/s)	Error 2-sig	Atomic Wt %	Conc. %	Units
C	Ka	0.00	0.000	0.000	0.000	wt.%
N	Ka	0.00	0.000	0.000	0.000	wt.%
O	Ka	0.48	0.254	32.976	14.001	wt.%
Na	Ka	0.15	0.139	1.090	0.665	wt.%
Mg	Ka	0.46	0.248	2.309	1.489	wt.%
Al	Ka	0.20	0.164	0.775	0.555	wt.%
Si	Ka	0.63	0.289	2.009	1.497	wt.%
P	Ka	0.00	0.000	0.000	0.000	wt.%
S	Ka	2.66	0.595	7.607	6.473	wt.%
Cl	Ka	1.20	0.400	3.237	3.045	wt.%
K	Ka	0.27	0.191	0.683	0.708	wt.%
Ca	Ka	14.44	1.388	40.321	42.885	wt.%
Mn	Ka	0.59	0.279	2.183	3.183	wt.%
Fe	Ka	0.15	0.142	0.611	0.906	wt.%
Cu	Ka	0.37	0.222	2.207	3.722	wt.%
Au	La	0.39	0.229	3.992	20.869	wt.%
Total				100.00	100.00	wt.%

(**B**)

Element	Line	Intensity (c/s)	Error 2-sig	Atomic Wt %	Conc. %	Units
C	Ka	4.44	0.769	83.596	58.187	wt.%
N	Ka	0.00	0.000	0.000	0.000	wt.%
O	Ka	0.24	0.179	3.114	2.888	wt.%
Na	Ka	0.22	0.170	0.236	0.314	wt.%
Mg	Ka	0.48	0.252	0.351	0.494	wt.%
Al	Ka	0.13	0.132	0.075	0.117	wt.%
Si	Ka	0.64	0.291	0.318	0.518	wt.%
P	Ka	0.86	0.339	0.387	0.695	wt.%
S	Ka	2.29	0.552	1.011	1.879	wt.%
Cl	Ka	3.69	0.702	1.552	3.188	wt.%
K	Ka	0.54	0.269	0.225	0.510	wt.%
Ca	Ka	14.36	1.384	6.462	15.009	wt.%
Mn	Ka	0.72	0.309	0.447	1.423	wt.%
Fe	Ka	0.41	0.233	0.280	0.906	wt.%
Cu	Ka	1.03	0.370	1.079	3.972	wt.%
Au	La	0.47	0.251	0.867	9.900	wt.%
Total				100.00	100.00	wt.%

(**C**)

Figure 9. EDX spectra of rapeseed stalks: (**A**) extractive-free, (**B**), holocellulose, and (**C**) α-cellulose.

4. Conclusions

The structural characteristics of rapeseed cellulose are of critical importance for the future utilization of rapeseed stalks as a valuable cellulose source for the production of various chemicals and materials. The main transformation detectable in the crystalline structure following treatment of holocellulose with 17.5% NaOH is the conversion of the crystal lattice from cellulose I to cellulose II. In addition, a decrease in the crystalline region of the C-4 and C-6 visible from the NMR spectra is observed, along with a reduction in degree of crystallinity and conformational change in the hydroxymethyl groups at the C-6 position.

Infrared spectroscopy provided key insights into the structural features of rapeseed stalks, identifying functional groups associated with carbohydrates, lignin, and other extractable substances. Notable spectral features include a broad OH stretching band, characteristic C-H stretching vibrations, and the presence of lignin-related aromatic structures. The IR spectra also facilitated the differentiation of the chemical components within the extractives, offering insights into the molecular composition of the extractable substances, which affect the processing and quality of cellulose extracted from the rapeseed stalks.

The study also highlighted the presence of extractable substances, such as alcohols, alkanes, and waxes, in rapeseed stalks. These extractives can significantly impact the cellulose production process, particularly in pulping, by increasing chemical consumption, inhibiting the cooking process, and reducing both quality and yield of cellulose. Therefore, understanding and managing these substances is crucial for optimizing cellulose extraction from rapeseed stalks.

Scanning Electron Microscopy (SEM) images provided valuable insights into the microstructure of rapeseed stalks, revealing a well-organized fibrous network and the structural arrangement of parenchyma tissue. The fibers were found to be highly organized, contributing to the mechanical strength of the stalk, while the parenchyma tissue played a key role in flexibility and metabolic functions. The distinct structure between the outer protective layers and the inner core highlighted the rapeseed stalk potential for various bio-based applications.

The mineral composition of rapeseed stalks, accounting for approximately 6% of their weight, includes both soluble and insoluble salts, with calcium being the most abundant element. Other trace elements, such as magnesium, sodium, and iron, further contribute to the complex mineral profile of rapeseed stalks. This mineral composition may influence both the chemical properties and the suitability of rapeseed stalks for various industrial applications.

Overall, this study suggests that rapeseed stalks, with their high cellulose and hemicellulose content, along with their unique structural and mineral composition, hold significant promise as a renewable resource for bio-based materials. However, the presence of extractives and minerals must be carefully considered during processing to optimize material yield and quality, particularly in the context of cellulose production.

Author Contributions: Conceptualization, B.-M.T. and E.C.; methodology, B.-M.T. and E.C.; validation, B.-M.T., E.C., E.U., O.C.U. and V.I.P.; formal analysis, B.-M.T. and E.C.; investigation, B.-M.T., E.C., E.U., O.C.U. and V.I.P.; resources, B.-M.T., E.C., E.U., O.C.U. and V.I.P.; writing—original draft preparation, B.-M.T., E.C., E.U., O.C.U. and V.I.P.; writing—review and editing, B.-M.T., E.C., E.U., O.C.U. and V.I.P.; visualization, B.-M.T., E.C., E.U., O.C.U. and V.I.P.; supervision, V.I.P. All authors have read and agreed to the published version of the manuscript.

Funding: This research received no external funding.

Institutional Review Board Statement: Not applicable.

Data Availability Statement: All the research data obtained during the study are presented in this article, providing a comprehensive analysis of the structural, chemical, and mineral characteristics of rapeseed stalks and their potential applications.

Acknowledgments: This paper is dedicated to the memory of Klaus Müller. His wisdom, passion, and dedication were instrumental in sparking our short yet fruitful collaboration. His absence left a void in the hearts of those privileged to have known him, as he embodied the qualities of a distinguished scientist, an inspiring educator, a supportive mentor, a cherished friend, and a remarkable person.

Conflicts of Interest: The authors declare no conflicts of interest.

References

1. Klemm, D.; Heublein, B.; Fink, H.; Bohn, A. Cellulose: Fascinating biopolymer and sustainable raw material. *Angew. Chem. Int. Ed.* **2005**, *44*, 3358–3393. [CrossRef] [PubMed]
2. Puitel, A.C.; Marin, N.; Petrea, P.; Gavrilescu, D. Lignocellulosic agricultural residues—A virgin fibre supply solution for paper-based packaging. *Cellul. Chem. Technol.* **2015**, *49*, 633–639.
3. Lamoudan, H.; Abenghal, L.; Belosinschi, D.; Brouillette, F.; Dolez, P.; Panneton, R.; Fonrouge, C. Sustainable Transformation of Cellulose-Containing Textile Waste into Multifunctional Panels with Tailored FR-Lignocellulosic Fibres. *Polymers* **2024**, *16*, 3242. [CrossRef] [PubMed]
4. Tofanica, B.M.; Ungureanu, E.; Ungureanu, O.C.; Fortuna, M.E.; Volf, I.; Popa, V.I. Circular Economy Solutions: Exploring Agricultural Residues. Bulletin of the Polytechnic Institute of Iaşi. *Chem. Chem. Eng. Sect.* **2024**, *70*, 33–48. [CrossRef]
5. Belosinschi, D.; Tofanica, B. A new bio-material with 3D lightweight network for energy and advanced applications. *Cellulose* **2018**, *25*, 897–902. [CrossRef]
6. Alén, R. Manufacturing Cellulosic Fibres for Making Paper: A Historical Per-spective. In *Technological Trans-Formation in the Global Pulp and Paper Industry 1800–2018*; Särkkä, T., Gutiérrez-Poch, M., Kuhlberg, M., Eds.; World Forests; Springer: Cham, Switzerland, 2018; Volume 23. [CrossRef]
7. Gavrilescu, D.; Tofanica, B.M.; Puitel, A.C. Environmental Friendly Pulping and Bleaching of Rapeseed Stalk Fibers. *Environ. Eng. Manag. J.* **2012**, *11*, 681–686. [CrossRef]
8. Tofanica, B.M. Rapeseed—A Valuable Renewable Bioresource. *Cellul. Chem. Technol.* **2019**, *53*, 837–849. [CrossRef]
9. Housseinpour, R.; Latibari, A.J.; Farnood, R.; Fatehi, P.; Sepiddehdam, S.J. Fiber morphology and chemical composition of rapeseed (*Brassica napus*) stems. *IAWA J.* **2010**, *31*, 457–464. [CrossRef]
10. Tofanica, B.M.; Cappelletto, E.; Gavrilescu, D.; Mueller, K. Properties of Rapeseed (*Brassica napus*) Stalks Fibers. *J. Nat. Fibers* **2011**, *8*, 241–262. [CrossRef]
11. Kiaei, M.; Mahdavi, S.; Kialashaki, A.; Nemati, M.; Samariha, A.; Saghaf, A. Chemical Composition and Morphological Properties of Canola Plant and Its Potential Application in Pulp and Paper Industry. *Cellul. Chem. Technol.* **2014**, *48*, 105.
12. Aguado, R.; Moral, A.; Mutjé, P.; Tijero, A. Rapeseed stalks for papermaking: Studies on pulping, refining and dewatering. *Cellul. Chem. Technol.* **2015**, *49*, 833.
13. Moral, A.; Aguado, R.; Tijero, A.; Tarrés, Q.; Delgado-Aguilar, M.; Mutjé, P. High-Yield Pulp from *Brassica napus* to Manufacture Packaging Paper. *BioResources* **2017**, *12*, 2792–2804. [CrossRef]
14. Potůček, F.; Milichovský, M. Rapeseed straw as a possible source of non-wood fibre materials. *Cellul. Chem. Technol.* **2011**, *45*, 23. Available online: https://www.cellulosechemtechnol.ro/ (accessed on 15 January 2025).
15. Ungureanu, E.; Samuil, C.; Ţopa, D.C.; Ungureanu, O.C.; Tofanica, B.-M.; Fortună, M.E.; Brezuleanu, C.O. Adsorption of Ni(II) from Aqueous Media on Biodegradable Natural Polymers—Sarkanda Grass Lignin. *Crystals* **2024**, *14*, 381. [CrossRef]
16. Mikhailidi, A.; Volf, I.; Belosinschi, D.; Tofanica, B.; Ungureanu, E. Cellulose-Based Metallogels—Part 2: Physico-Chemical Properties and Biological Stability. *Gels* **2023**, *9*, 633. [CrossRef]
17. Simionescu, C.I.; Rusan, V.; Popa, V.I. Options Concerning Phytomass Valorification. *Cellul. Chem. Technol.* **1987**, *21*, 3–16.
18. French, A.D.; Johnson, G.P. *Cellulose: Molecular and Structural Biology*; Brown, R.M., Saxena, I.M., Eds.; Springer: Berlin/Heidelberg, Germany, 2007; p. 257.
19. Baeza, J.; Freer, J. Chemical characterization of wood and its components. In *Wood and Cellulosic Chemistry*; Hon, D.N.-S., Shiraishi, N., Eds.; Marcel Dekker: New York, NY, USA, 2000; pp. 275–384.
20. Ona, T.; Sonoda, T.; Shibata, M.; Fukazawa, K. Small-scale method to determine the content of wood components from multiple eucalypt samples. *Tappi J.* **1995**, *78*, 121–126.
21. Technical Association of the Pulp and Paper Industry. *TAPPI Test Methods*; TAPPI Press: Norcross, USA, GA, 1992.
22. Wise, L.E.; Murphy, M.; D'Addieco, A.A. Chlorite holocellulose, its fractionation and bearing on summative wood analysis and on studies on hemicellulose. *Pap. Trade J.* **1946**, *122*, 35–43.
23. Jayme, G. Preparation of holocellulose and cellulose with sodium chlorite. *Cellul. Chem.* **1942**, *20*, 43–49.

24. French, A.D. Glucose, not cellobiose, is the repeating unit of cellulose and why that is important. *Cellulose* **2017**, *24*, 4605–4609. [CrossRef]
25. Gruber, E. Analytical Characterization of Pulps. In *Handbook of Pulp*; Sixta, H., Ed.; Wiley-VCH: Weinheim, Germany, 2006; pp. 1211–1290.
26. Callone, E.; Carturan, G.; Ischia, M.; Sicurelli, A. Size stabilization of nanoparticles by polysaccharides: Effectiveness in the wet and curing steps. *J. Mater. Res./Pratt's Guide Ventur. Cap. Sources* **2007**, *22*, 3344–3354. [CrossRef]
27. Sinnott, M.L. *Carbohydrate Chemistry and Biochemistry*; The Royal Society of Chemistry: London, UK, 2007; pp. 168–170.
28. Rotaru, R.; Fortună, M.E.; Ungureanu, E.; Brezuleanu, C.O. Effects of Ultrasonication in Water and Isopropyl Alcohol on High-Crystalline Cellulose: A Fourier Transform Infrared Spectrometry and X-ray Diffraction Investigation. *Polymers* **2024**, *16*, 2363. [CrossRef] [PubMed]
29. Menges, F. Spectragryph—Optical Spectroscopy Software. Version 1.2.16.1. 2025. Available online: http://www.effemm2.de/spectragryph/ (accessed on 15 January 2025).
30. Ungureanu, E.; Fortună, M.E.; Țopa, D.C.; Lobiuc, A.; Ungureanu, O.C.; Jităreanu, D.C. Design of Functional Polymer Systems to Optimize the Filler Retention in Obtaining Cellulosic Substrates with Improved Properties. *Materials* **2023**, *16*, 1904. [CrossRef] [PubMed]
31. Ungureanu, E.; Fortună, M.E.; Țopa, D.C.; Brezuleanu, C.O.; Ungureanu, V.I.; Chiruță, C.; Rotaru, R.; Tofanica, B.M.; Popa, V.I.; Jităreanu, D.C. Comparison Adsorption of Cd (II) onto Lignin and Polysaccharide-Based Polymers. *Polymers* **2023**, *15*, 3794. [CrossRef]
32. Heinze, T.; Liebert, T.; Koschella, A. *Esterification of Polysaccharides*; Springer: Berlin/Heidelberg, Germany, 2006; p. 6.
33. Klemm, D.; Schmauder, H.-P.; Heinze, T. *Biopolymers—Volume 6: Polysaccharides II*; Vandamme, E.J., de Baets, S., Steinbuchel, A., Eds.; Wiley-Vch.: Hoboken, NJ, USA, 2002; p. 280.
34. O'Sullivan, A.C. Cellulose: The structure slowly unravels. *Cellulose* **1997**, *4*, 173–207. [CrossRef]
35. Atalla, R.; VanderHart, D. The role of solid state NMR spectroscopy in studies of the nature of native celluloses. *Solid State Nucl. Magn. Reson.* **1999**, *15*, 1–19. [CrossRef]
36. Santoni, I.; Callone, E.; Sandak, A.; Sandak, J.; Dirè, S. Solid state NMR and IR characterization of wood polymer structure in relation to tree provenance. *Carbohydr. Polym.* **2014**, *117*, 710–721. [CrossRef]
37. Callone, E.; Fletcher, J.M.; Carturan, G.; Raj, R. A low-cost method for pro-ducing high-performance nanocomposite thin-films made from silica and CNTs on cellulose substrates. *J. Mater. Sci.* **2008**, *43*, 4862–4869. [CrossRef]
38. Nishiyama, Y.; Langan, P.; Chanzy, H. Crystal Structure and Hydrogen-Bonding System in Cellulose Iβ from Synchrotron X-ray and Neutron Fiber Diffraction. *J. Am. Chem. Soc.* **2002**, *124*, 9074–9082. [CrossRef]
39. Nishiyama, Y.; Sugiyama, J.; Chanzy, H.; Langan, P. Crystal Structure and Hydrogen Bonding System in Cellulose Iα from Synchrotron X-ray and Neutron Fiber Diffraction. *J. Am. Chem. Soc.* **2003**, *125*, 14300–14306. [CrossRef]
40. Zugenmaier, P. *Crystalline Cellulose and Derivatives: Characterization and Structures*; Springer: Berlin/Heidelberg, Germany, 2008; pp. 129–138.
41. Klemm, D.; Philipp, B.; Heinze, T.; Heinze, U.; Wagenknecht, W. *Comprehensive Cellulose Chemistry, Volume 1: Fundamentals and Analytical Methods*; Wiley-Vch.: Hoboken, NJ, USA, 1998; p. 14.
42. Hesse, S.; Jäger, C. Determination of the 13C chemical shift anisotropies of cellulose I and cellulose II. *Cellulose* **2005**, *12*, 5–14. [CrossRef]
43. Zugenmaier, P. Conformation and packing of various crystalline cellulose fibers. *Prog. Polym. Sci.* **2001**, *26*, 1341–1417. [CrossRef]
44. Langan, P.; Nishiyama, Y.; Chanzy, H. X-ray structure of mercerized cellulose II at 1 å resolution. *Biomacromolecules* **2001**, *2*, 410–416. [CrossRef] [PubMed]
45. Sixta, H. (Ed.) Pulp Purification. In *Handbook of Pulp*; Wiley-Vch.: Hoboken, NJ, USA, 2006; pp. 933–966.
46. Raymond, S.; Kvick, A.; Chanzy, H. The structure of Cellulose II: A revisit. *Macromolecules* **1995**, *28*, 8422–8425. [CrossRef]
47. O'Neill, M.A.; York, W.S. The composition and structure of plant primary cell walls. In *Annual Plant Reviews*; The Plant Cell Wall; Rose, J.K.C., Ed.; Blackwell Publishing Ltd.: Oxford, UK, 2003; Volume 8, ISBN 978-1-841-27328-0.

applied sciences

MDPI

Article

In Situ and Partial In Situ Synthesis of Cellulose Magnetite/Maghemite Composites

Razvan Rotaru [1], Maria Emiliana Fortună [1,*], Elena Ungureanu [2,*], Ovidiu Ungureanu [3], Andrei Dascalu [1] and Valeria Harabagiu [1]

[1] "Petru Poni" Institute of Macromolecular Chemistry, Department of Inorganic Polymers, 41A Gr. Ghica Voda Alley, 700487 Iasi, Romania; rotaru.razvan@icmpp.ro (R.R.); idascalu@icmpp.ro (A.D.); hvaleria@icmpp.ro (V.H.)
[2] Department of Exact Sciences, "Ion Ionescu de la Brad" Iasi University of Life Sciences, 3 Mihail Sadoveanu Alley, 700490 Iasi, Romania
[3] Department of Biology and Life Sciences, "Vasile Goldis" Western University of Arad, 94 the Boulevard of the Revolution, 310025 Arad, Romania; ovidiu.c.ungureanu@gmail.com
* Correspondence: fortuna.maria@icmpp.ro (M.E.F.); elena.ungureanu@iuls.ro (E.U.)

Abstract: The current study aims to prepare ferromagnetic iron oxides (magnetite and/or maghemite) using the coprecipitation method of an iron salt in a basic environment stimulated by ultrasound, with cellulose added at the start of the synthesis and after 15 min in order to perform an in situ and partial in situ synthesis. The structures, morphology, and properties of composites are analyzed by IR, XRD, SEM, TEM, TGA, DSC, and magnetic measurements. The cumulative effect of the ultrasonic waves is observed by a reduction in the degree of crystallinity of the native cellulose compared to the composites (from 73.2 to 36.4, respectively 38.3). The vibrating sample magnetic measurement shows a single hysteresis curve characteristic of ferromagnetic materials with superparamagnetic properties.

Keywords: cellulose; composites; maghemite; magnetite; magnetic properties; ultrasonication

Academic Editor: Andrei Sarbu

Received: 25 November 2024
Revised: 2 January 2025
Accepted: 3 January 2025
Published: 7 January 2025

Citation: Rotaru, R.; Fortună, M.E.; Ungureanu, E.; Ungureanu, O.; Dascalu, A.; Harabagiu, V. In Situ and Partial In Situ Synthesis of Cellulose Magnetite/Maghemite Composites. *Appl. Sci.* **2025**, *15*, 492. https://doi.org/10.3390/app15020492

1. Introduction

Cellulose is a natural polysaccharide that is in high demand in many industries. It is present in almost every sphere of human life, starting from the paper and packaging sector, textile industries, agriculture and food production, chemical and oil industries, wastewater treatment, biomedicine, cosmetics and healthcare, and electronic devices. The utilization of cellulose-based products offers a variety of environmental and economic benefits. Considered an abundant organic polymer in nature, cellulose has also been studied and applied as a precursor for functional composite materials [1]. Several scientific studies show that cellulose can form composites with various materials due to good mechanical properties, a large surface area, and biodegradable and renewable properties [2]. Besides these, cellulose contains powerful intra- and inter-molecular hydrogen bonds owing to plenty of hydroxyl groups, which may be an important factor in anchoring iron oxides [3].

Iron oxides, whether monodispersed or polydispersed, have attracted increasing attention due to their excellent biocompatibility, low toxicity, and magnetic properties. They have considerable potential for use in the biomedical industry, especially in recent years due to increasing the frequency of some types of diseases [4] (magnetic resonance imaging, targeted drug delivery, cell separation, and hyperthermia treatment), the electrical industry (electric motors and power transformers), magnetic recording, information storage media, and environmental processes (treatment of wastewater) [5,6].

The main oxides of iron are hematite (α-Fe_2O_3), maghemite (γ-Fe_2O_3), magnetite (Fe_3O_4), ferrite (Fe_2O_4), wüstite (Fe_1-xO), and the oxide hydroxides (goethite: α-FeOOH, lepidocrocite: γ-FeOOH, akaganéite: β-FeOOH) [6]. Hematite, maghemite, magnetite, and ferrite are interesting for their high magnetization (saturation magnetization is higher than 60 emu/g), and goethite, lepidocrocite, and akaganéite for their superparamagnetic properties, as well as for the existence of hydroxyl groups that can create chemical bonds with other compounds [7,8].

Cellulose–iron oxide composites have been studied in the last few years to be of interest as transparent films for magnetic and/or optical applications, magnetic resonance imaging (antibacterial or contrasting materials), recyclable catalysts, magnetically retrievable oil adsorbents, or magnetic aerogels [8]. Composites are obtained by incorporating magnetic particles into the cellulose matrix or by performing in situ synthesis (iron oxides are generated in the presence of cellulose or cellulose is prepared in the presence of magnetic particles) [8–10]. Due to the distinct synthesis conditions of the two precursors, cellulose, and magnetic iron oxides, in situ synthesis is less commonly used. However, a few examples have been described in the literature. Khalil et al. obtained superparamagnetic papers from cellulose fiber suspension with 5–13 wt% ferrite nanoparticles, iron oxides, and mixed oxides (oxides of iron with cobalt and/or nickel) by using a one-cycle in situ synthesis [11]. Magnetic particles are prepared in the presence of suspensions of suitable natural cellulose fibers via careful oxidation of ferrous hydroxide precipitated with sodium hydroxide from the ferrous ions. The saturation magnetization has values between 10 and 15 emu/g (smaller for nickel ferrite and higher for cobalt ferrite). Liu and his colleagues prepared magnetic nanocomposite cellulose/maghemite film by using an in situ synthesis of plate-like Fe_2O_3 nanoparticles in the cellulose matrix [12]. In their study, the cellulose was dissolved directly into sodium hydroxide/urea aqueous solution pre-cooled to −12 °C, and the resulting solution was centrifuged at 8000 rpm for 20 min at 15 °C for degasification and then cast on a glass plate and immersed into 5 wt% H_2SO_4 solutions for 5 min to coagulate and regenerate. Then, the obtained wet films were immersed in an aqueous ferric chloride ($FeCl_2$ or $FeCl_3$) solution with different concentrations for 1 day and then treated with an aqueous sodium hydroxide solution (4 M) for 20 min, followed by rinsing with deionized water several times. The composite films were fixed on a poly(methyl methacrylate) plate and dried at ambient temperature. The saturation magnetization obtained has values between 0.5 and 2.5 emu/g. In other work, Low et al. presented a rapid sonochemical in situ co-precipitation approach in order to prepare magnetite/cellulose nanocomposites [13]. Differing from the conventional method, this proposed in situ co-precipitation reaction was performed under atmospheric conditions without azote purging to yield the nanocomposite. The obtained magnetic composites show a high saturation magnetization, between 20 and 35 emu/g. In another study, Luo and collaborators [14] obtained cellulose microspheres by using the sol/gel transition method from cellulose drops in a sodium hydroxide (7 wt%)/urea (12 wt%) aqueous solution precooled to −12 °C. Magnetic magnetite/cellulose microspheres were produced by in situ synthesis of Fe_3O_4 nanoparticles into the cellulose pores, which were used as the solid template microreactor. The saturation magnetization presents values between 4 and 8 emu/g. In another original study, Dimitrov et al. describe a new synthesis method for producing cellulose–ferrite micro- and nano-composites using a mixture of Fe^{+2}/Fe^{+3} [15].

Another issue of interest is the superparamagnetic phenomenon (SP), which represents the state of a single magnetic domain-sized grain when the thermal energy is enough to overcome barriers to a reversal of magnetization. These barriers are proportional to grain volume and can arise from shape anisotropy, magnetoelastic anisotropy, or magnetocrystalline anisotropy. When the energy barriers are large with respect to thermal energy, the

magnetization process is stopped with the consequence that the probability of spontaneous reversal magnetization decreases drastically. If the barriers are low, thermal excitations can result in the reversal of the magnetization in a very short time, and the grain is in a SP state. For a specific temperature, the volume at which a particle goes from being in an unblocked state to a blocked state is known as the blocking volume. For this specific volume, we can block the grain by lowering the temperature below the blocking temperature (the temperature at which the reversal magnetization begins) [7,16]. Depending on the material, this type of magnetism occurs in small ferrimagnetic or ferromagnetic particles and implies sizes from a few nanometers to a couple of tenths of nanometers [17,18]. These nanoparticles are single-domain particles, so the total magnetic moment can be regarded as one giant magnetic moment, composed of all the individual magnetic moments of the atoms that form the nanoparticle [19]. The size factor is not the only element that can provide a state of SP. The surface effects [20,21] and the crystallinity affect the magnetic properties and the SP phenomena [22,23]. The main interest of the study of these materials is represented by biomedical applications [24].

This work presents a classic co-precipitation method modified by using ultrasound to obtain a ferromagnetic cellulosic composite in situ and partially in situ. Thus, cellulose/magnetite/maghemite composites with varying proportions (73.4/8.1/18.5% for total in situ and 74.6/12.5/12.9% for partial in situ) and different magnetizations were obtained. We are especially interested in whether the presence of cellulose still allows a complete transformation of iron sulfate into magnetite and/or maghemite and if ultrasonication in a basic medium involves the physical and/or chemical transformation of the cellulose.

2. Materials and Methods

2.1. Materials

Sigmacell cellulose (type 20, 20 μm, Sigma Aldrich, Oakville, ON, Canada) Sigma–Aldrich, iron sulfate heptahydrate ($FeSO_4 \cdot 7H_2O$: Sigma-Aldrich, 99% purity, Sigma Aldrich, Hamburg, Germany), kalium hydroxid pellets (Chemapol, 99% purity, Chemapol, Prague, Czech Republic), ethyl alcohol (Chimreactiv, Chemapol, Prague, Czech Republic), and Milli-Q ultrapure distilled water (our laboratory) were used without further purification.

2.2. Preparation of Cellulose/Magnetite Composites

Cellulose/magnetite/maghemite (CM) composites were prepared through a multistep procedure as follows. First, a potassium hydroxide solution with a mass of eight molars was prepared. Then, the iron sulfate, together with the potassium hydroxide solution, is added to a Schott–Duran Berzelius glass (100 mL in volume) with 40 mL of water used as an ultrasound bath. According to other previous works [5,6,8], 40 mL of water were chosen as the ideal quantity for the technical specifications of the ultrasound generator used. (The ultrasonic probe should be immersed in a liquid medium for at least 40% of its length, and the distance between it and the glass walls should be as small as possible). According to Table 1, cellulose is added at the start of the 30-min synthesis or in the middle of the synthesis (in the 15th minute), in the case of partially in situ synthesis. From a quantitative point of view, each synthesis involved the use of 2 g of iron sulfate, 2 g of cellulose, and 8 mL of potassium hydroxide solution (eight molars). Ultrasonication is performed for 30 min, with the wave amplitude adjusted to 40% from the generator's maximum power (electrical power of 750 W converted into ultrasonic at a frequency of 20 kHz). After 30 min of ultrasonication, the samples were then centrifuged, washed with Milli-Q water first, and then washed with ethyl alcohol (to remove sulfate ions), centrifuged again, and dried in a vacuum oven at 40 °C for 24 h. The final samples are fine brown powders.

Table 1. Samples and the terms of the synthesis.

Sample	Total Time of Ultra-sonication [min]	Cellulose Addition Time [min]	Sonication Time After Cellulose Addition [min]	Total Energy Dissipated [kJ]	Final Temperature [°C]
CM_0	30	t: 0	30	64.5	71
CM_{15}	30	t: 15	15	53.3	87

A simplified description of the syntheses is shown below in Schemes 1 and 2.

$FeSO_4 + 2KOH + C_6H_{10}O_5$

30 min ↓ ultrasonication

$2\,(\gamma\text{-}Fe_2O_3) + Fe_3O_4 + C_6H_{10}O_5 + K_2SO_4 + H_2O$

ethyl alcohol, milli Q ↓ centrifugation

$2\,(\gamma\text{-}Fe_2O_3) + Fe_3O_4 + C_6H_{10}O_5$

Scheme 1. In situ synthesis.

$FeSO_4 + 2KOH$

15 min ↓ ultrasonication

$Fe(OH)_2 + K_2SO_4 + H_2O$

15 min ↓ $+ C_6H_{10}O_5$, ultrasonication

$2\,(\gamma\text{-}Fe_2O_3) + 2Fe_3O_4 + C_6H_{10}O_5 + K_2SO_4 + H_2O$

ethyl alcohol, milli Q ↓ centrifugation

$2\,(\gamma\text{-}Fe_2O_3) + 2Fe_3O_4 + C_6H_{10}O_5$

Scheme 2. Partial in situ synthesis.

2.3. Equipment and Methods

The ultrasonication experiments were performed with an ultrasonic generator, Sonics Vibracell, at 750 W nominal electric power and 20 kHz ultrasound frequency, provided with a display providing the energy delivered to the end of the probe and a sensor for temperature. The samples were dried in a Trade Raypa vacuum oven at 40 °C. The resulting powder was centrifuged in an Eba 21 Hettich Zentrifugen centrifuge at 4000 revolutions per minute.

The structures of the precursors and the composites were investigated by FTIR spectroscopy on potassium bromide pellets by using a Bruker Vertex 70 spectrometer (2 cm^{-1} resolution) and by X-ray diffraction (XRD) performed on a Rigaku Miniflex 600 diffractometer using CuKα emission in the angular range of 2–90° (2θ). The scanning step was 0.01°, and the recording rate was 2° per minute.

The crystallinity index (Cr.I.) of cellulose was determined using the peak height method with the equation [8]:

$$\text{Cr.I.} = \frac{I_{002} - I_{am}}{I_{002}} \times 100 \quad (1)$$

where I_{200} is the intensity of the peak at the diffraction angle 2θ of 22.7 °C (corresponding to the Miller plane (200) and is also called the crystalline peak) and I_{am} is the intensity of the peak at 18 °C (corresponding to the Miller plane (110) and is called the amorphous peak).

The weight fraction [%] between cellulose and iron oxides (maghemite and magnetite) was determined using whole powder pattern fitting (WPPF—a program used in X-ray diffraction performed with the Rigaku Miniflex 600 diffractometer, which allows the quantitative measurement of the crystalline phases of the analyzed powder, in our case, cellulose, magnetite, and maghemite in percentages) and Rietveld analysis.

In order to determine the empirical crystallinity index, or lateral order index (LOI), by using FTIR spectroscopy, the following equation was used [7]:

$$LOI = I_{1433}/I_{897} \quad (2)$$

where I_{1435} and I_{899} are the intensity of the absorbance peaks, at 1435 and 899 cm^{-1} wavenumbers. Total crystallinity index (TCI) was determined with Equation (3):

$$TCI = I_{1371}/I_{2899} \quad (3)$$

where I_{1371} and I_{2899} are the intensity of the absorbance peaks at 1371 and 2899 cm^{-1} wavenumbers.

The hydrogen bond intensity (HBI) was established with the following ratio:

$$HBI = I_{3346}/I_{1321} \quad (4)$$

Some of the characteristic spectral bands are quite sensitive to the crystalline structure in cellulose materials. Thus, the bands located at 1435 and 1371 cm^{-1}, and the one at 899 cm^{-1}, correspond to crystalline and amorphous domains, respectively. I_{1435}/I_{899} and I_{1371}/I_{2899} ratios (I is the intensity of the absorbance peak $\approx 1 -$ intensity of the transmittance peak) were used to calculate the empirical crystalline index or lateral order index (LOI) and the total crystalline index (TCI), respectively. TCI is proportional to the crystallinity degree of cellulose, and LOI is correlated with the overall degree of order in the cellulose. The ratio of two other infrared bands, I_{3346}/I_{1321}, is known as the hydrogen bond intensity (HBI) closely related to the crystal system and the degree of intermolecular regularity, considering the chain mobility and bond distance, as well as the amount of bound water [7,8].

The magnetic measurements (magnetization curves) were performed on a Lake Shore 8600 vibrating sample magnetometer (3.2 T for applied magnetic field at room temperature).

The surface morphologies were visualized by scanning electron microscopy (SEM) on an ESEM Quanta 200 electronic deflection microscope. The settled voltage electron acceleration rate to gather the SEM images was 5 kV.

Transmission electron microscopy (TEM) analysis for CM_0 and CM_{15} composites was conducted with a Hitachi High-Tech HT7700 instrument, operated in high-resolution mode at 100 kV accelerating voltage. Samples were prepared by drop casting from the diluted dispersions of nanoparticles in ethanol on 300 meshes of holey carbon-coated copper grids (Ted Pella) and vacuum-dried.

Thermal degradation was performed using a thermobalance model STA 449F1 Jupiter (Netzsch, Germany) for simultaneous thermal analysis TG-DTA. The thermogravimetric analyzer was calibrated on temperature and sensitivity using the melting points of some standard metals (Hg, In, Sn, Bi, Zn, and Al) from −38.5 °C to 600 °C. Sample masses ranging from 7 to 10 mg were heated from 25 °C to 600 °C with a 10 °C/min heating rate. The helium (99.999% purity) as an inert gas with a flow rate of 50 mL/min and a protective

purge for thermobalance of 20 mL/min was used. The samples were heated in open Al_2O_3 crucible, and Al_2O_3 was used as reference material. Data collection was conducted with Proteus® software, version 8.17.

3. Results

3.1. Structural Characterization

3.1.1. FTIR Analysis

The structure of the pristine cellulose and composites was first assessed by infrared spectroscopy. Infrared spectra of pristine cellulose (C) and CM_0 and CM_{15} composite samples are shown in Figure 1.

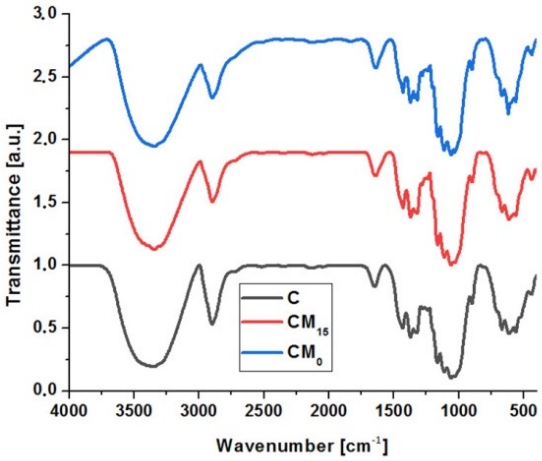

Figure 1. Infrared spectra for cellulose (C) and ferromagnetic composites (CM_0 and CM_{15}).

For pristine cellulose, peaks are observed at 3346 and 3385 cm^{-1} (OH stretching vibration), 2899 cm^{-1} (CH symmetrical stretching), 1647 cm^{-1} (OH bending of absorbed water), 1433 cm^{-1} (HCH in-plane bending vibration and/or CH_2 scissoring motion and/or CH_2 symmetric bending at C6), 1371 cm^{-1} (CH in-plane bending), 1317 cm^{-1} (CH_2 rocking vibration at C6), 1163, 1111 cm^{-1} (COC stretching), 1059 cm^{-1} (CC stretching), 1030 cm^{-1} (CO at C6), 897 cm^{-1} (COC stretching at β-(1→4)-glycoside linkages), 667, and 613 cm^{-1} (δ COH out-of-plane bending) [8,25–27]. Some peaks in ferromagnetic samples are practically unchanged, while ultrasonic irradiation also causes certain variations. The Fe-O stretching band of the magnetite located at 560 cm^{-1} and maghemite at 580 cm^{-1} in the spectrum of CM_0 and CM_{15} composites is superposed on cellulose absorptions in the 400–700 cm^{-1} region [5,7,8].

Table 2 shows the results of the TCI, LOI, and HBI calculated using Equations (1)–(3). The TCI is proportional to the crystallinity degree of cellulose, while the LOI is about the overall degree of order in cellulose and the hydrogen bond intensity. Considering the chain mobility and bond distance, the amount of bound water HBI refers to the crystal system and the degree of intermolecular regularity.

Table 2. Lateral order index (LOI), total crystallinity index (TCI), and hydrogen bond intensity (HBI) for pristine cellulose C and sonicated composites.

Sample	LOI	TCI	HBI
C	1.95	1.33	2.16
CM_0	1.12	1.08	2.52
CM_{15}	1.16	1.14	2.27

From Table 2, a decrease can be observed for the composites in the crystallinity parameters, as well as an increase in the intensity of the hydrogen bond. Low values of crystallinity parameters (LOI and TCI) indicate degradation of cellulose in the presence of iron oxides in the crystalline region due to ultrasonication. The HBI index increases slightly, indicating the potential presence of new hydrogen bonds.

3.1.2. X-Ray Diffraction Analysis

X-ray diffraction (XRD) analysis was used to accomplish a deeper structural characterization of the studied cellulose and ferromagnetic composites. Diffractograms for native cellulose and sonicated composites are depicted in Figure 2.

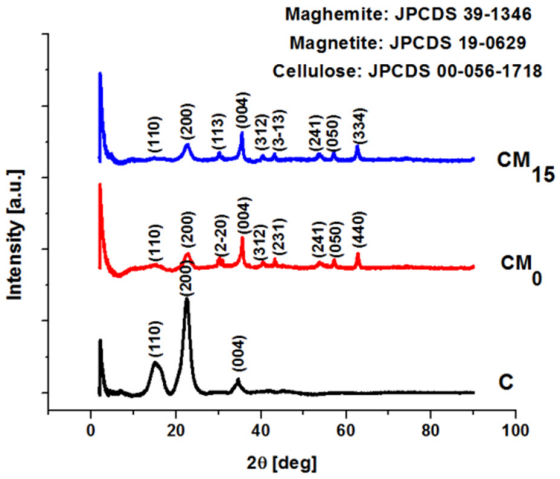

Figure 2. XRD patterns for pristine cellulose (C) and ferromagnetic composites (CM_0 and CM_{15}).

The quantitative and qualitative data: lattice parameters (a, b, c [Å], α, β, γ [°]), lattice volume (V), WPPF weight fraction [%], interplanar distance d [Å], Miller planes hkl, and crystallinity index CrI are provided in Tables 3–6.

Table 3. Lattice parameters for CM_0 composite.

Phase	WPPF [%]	a [Å]	b [Å]	c [Å]	α [°]	β [°]	γ [°]	V [Å ^{3}]
Cellulose	73.4	7.9	8.2	10.4	90	95	95.1	679.5
Magnetite	8.1	8.1	6.8	6	90	92	90	633.2
Maghemite	18.5	8.3	8.3	25.1	90	90	90	1764.1

Table 4. Lattice parameters for CM_{15} composite.

Phase	WPPF [%]	a [Å]	b [Å]	c [Å]	α [°]	β [°]	γ [°]	V [Å ^{3}]
Cellulose	74.6	7.8	8	10.5	90	90	95.4	662.6
Magnetite	12.5	5.9	5.9	16.7	90	90.2	90	587.8
Maghemite	12.9	8.4	8.4	24.9	90	90	90	1791.8

The microcrystalline cellulose diffractogram presents a typical cellulosic pattern for cellulose I with five crystalline planes at about 14.8°, 16.2°, 20.3°, 22.4°, and 34.3° corresponding to (1–10), (110), (102), (200), and (004) crystallographic planes [8]. The peaks from 2θ of 14.8, 22.4, and 34.3 degrees are prominent and can be easily observed in the cellulose spectrum. During the ultrasonication, the cellulose undergoes small changes in terms of the interplanar distances. Thus, for the crystallographic plane (1–10), d decreases from 5.96 Å to 5.89 Å (CM_0) and 5.87 Å (CM_{15}), respectively; for (110), from 5.45 Å to 5.39 Å and 5.34 Å; for (102), we see a very small increase from 4.35 Å to 4.36 Å and 4.37 Å; for (200), a

small decrease from 3.96 Å to 3.94 Å and 3.92 Å; and for plane (004), from 2.6 Å to 2.62 Å and 2.19 Å. All these movements are attributed to the ultrasonication process and do not fundamentally change the structure of the cellulose.

Table 5. XRD data, interplanar distance d [Å], and Miller planes hkl for C, CM_0, and CM_{15}.

C	2θ [Deg]	d [Å]	(hkl)
	14.8	5.96	(1–10)
	16.2	5.45	(110)
	20.3	4.35	(102)
	22.4	3.96	(200)
	34.3	2.6	(004)
CM_0	15.01	5.89	(1–10)-C
	16.41	5.39	(110)-C
	20.3	4.36	(102)-C
	22.53	3.94	(200)-C
	30.29	2.94	(2–20)-γ-Fe_2O_3
	34.14	2.62	(004)-C
	40.81	2.20	(312)-Fe_3O_4
	43.30	2.08	(231)-γ-Fe_2O_3
	53.66	1.70	(241)-γ-Fe_2O_3
	57.26	1.60	(050)-γ-Fe_2O_3
	63.01	1.47	(440)-Fe_3O_4
	73.78	1.28	(6–20)-γ-Fe_2O_3
CM_{15}	15.05	5.87	(1–10)-C
	16.57	5.34	(110)-C
	20.27	4.37	(102)-C
	22.62	3.92	(200)-C
	30.41	2.93	(113)-γ-Fe_2O_3
	33.97	2.63	(004)-C
	41.01	2.19	(312)-Fe_3O_4
	43.71	2.06	(3–13)-γ-Fe_2O_3
	54.24	1.68	(241)-Fe_3O_4
	57.82	1.59	(050)-Fe_3O_4
	62.91	1.47	(334)-γ-Fe_2O_3
	74.00	1.27	(6–20)-γ-Fe_2O_3

Table 6. Crystallinity index (CrI) for cellulose fibers in C, CM_0, and CM_{15}.

Sample	**Cr.I. %**
C	73.22
CM_0	36.47
CM_{15}	38.32

It is evident from the WPPF weight fraction study that magnetite and maghemite are components of both cellulosic composites. With the exception of temperature, the coprecipitation synthesis of magnetite and maghemite is the same. For magnetite, temperatures above 90 degrees are required for the complete conversion of the iron salt. Maghemite can be synthesized at temperatures below 80 degrees. It also contains iron oxyhydroxides such as goethite, lepidocrocite, or akaganeite but at room temperature (20–25 °C) [5,8]. In contrast to partial in situ synthesis (CM_{15}), where the temperature ultimately reaches 87 °C, in total, during situ synthesis (CM_0), part of the energy of the ultrasonic waves is also absorbed by the cellulose, resulting in a maximum reaction medium temperature of 71 °C. Maghemite and magnetite are present in approximately equal amounts (12.5% and 12.9%) in the CM_{15} composite. Another direct effect of this ultrasonic synthesis method is found

in the degradation of the crystalline structure of the cellulose. The crystallinity index CrI dropped from 73% to 36% and 38%, respectively, for the two composites. This phenomenon was in agreement with other studies [9]. In accordance with the data obtained by X-ray diffraction, we propose the following reaction schemes for the two syntheses.

From Schemes 3 and 4, the fragmentation of the cellulose chains can be observed, which leads to a decrease in crystallinity, but also to a change in hydrogen bonds.

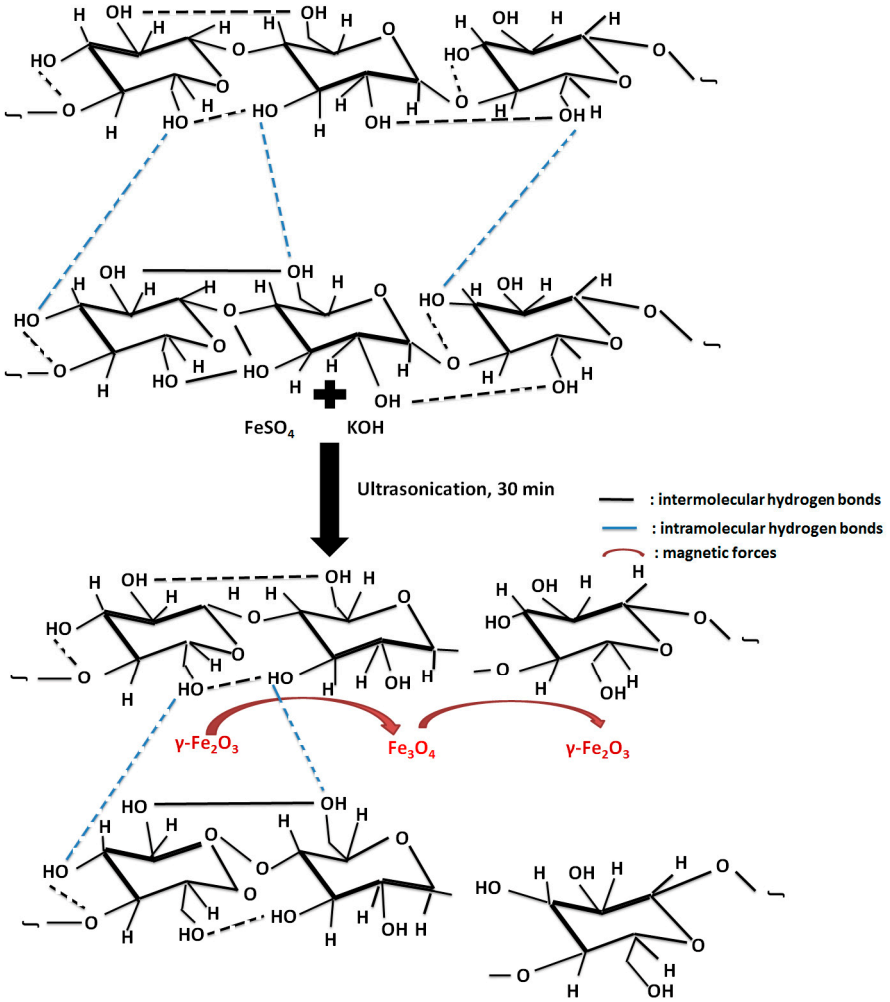

Scheme 3. In situ synthesis.

3.1.3. Morphology/Dimensional Characterization

SEM was used to identify the supramolecular structures and composition of the resulting composites, CM_0 and CM_{15}, and compare them to those of pure cellulose (C). The SEM images of the components and composites are shown in Figure 3. The SEM micrograph of the pristine cellulose sample clearly shows well-separated fibrils of about 20–35 μm in length and diameters of around 15 μm.

Agglomerations of roughly spherical particles (magnetite and maghemite) distributed relatively evenly on the cellulose fibers are readily visible with regard to the composites. As the SEM images of magnetite and maghemite particles are not conclusive, the CM_0 and CM_{15} composites were analyzed by TEM (on a smaller scale) (Figure 4).

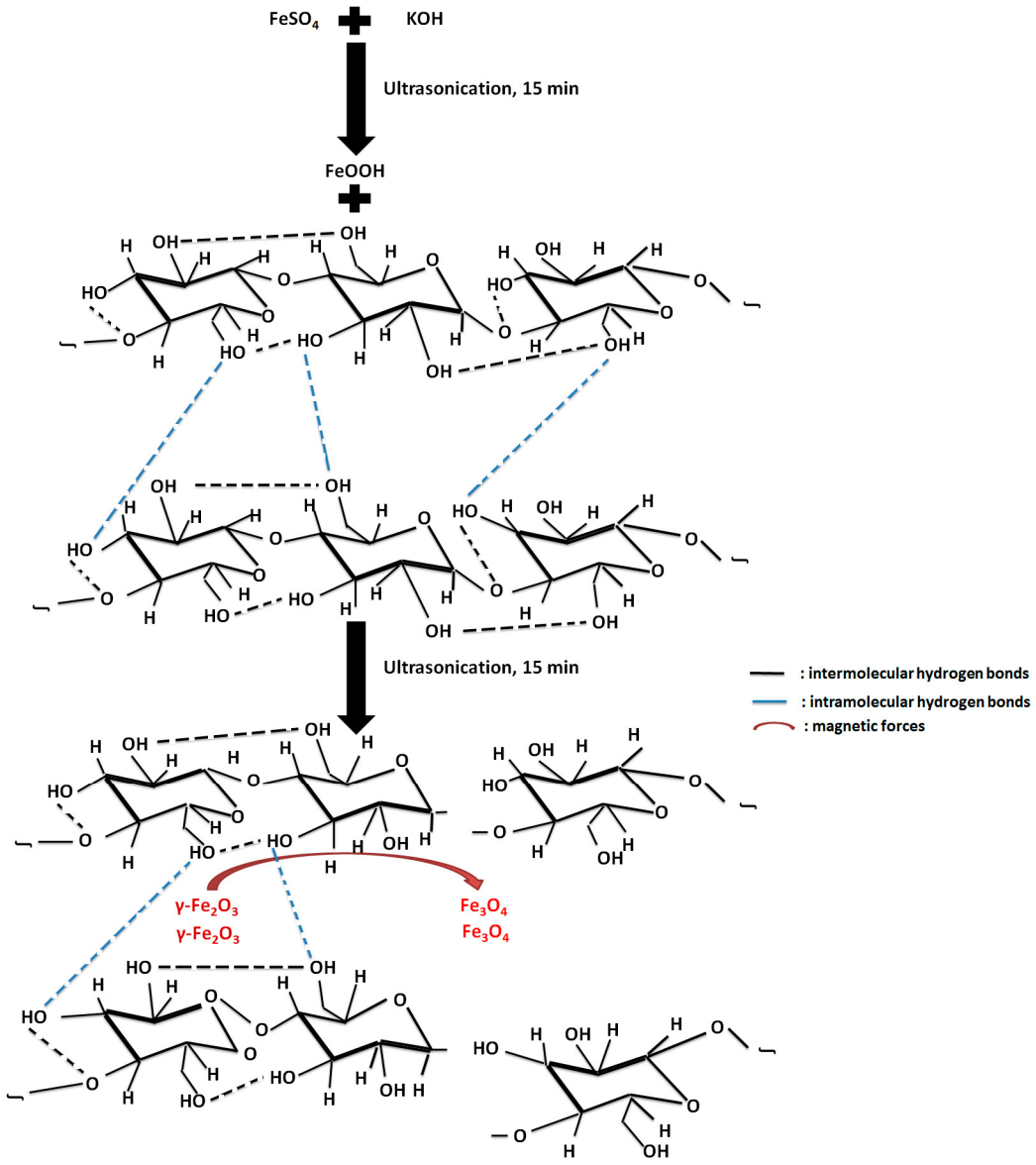

Scheme 4. Partial in situ synthesis.

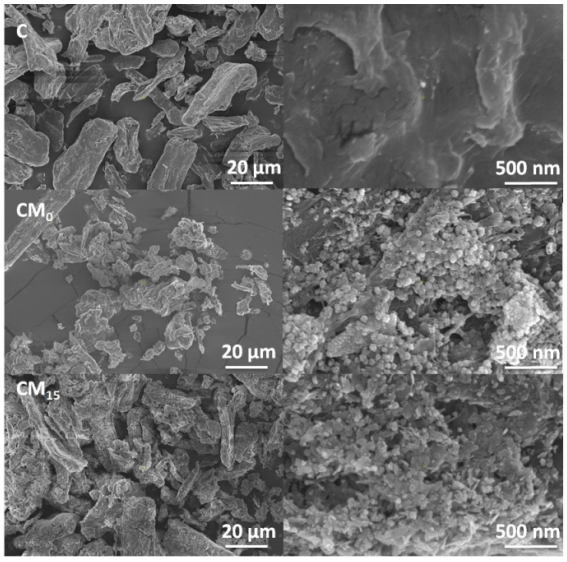

Figure 3. SEM micrographs for cellulose and ferromagnetic composites.

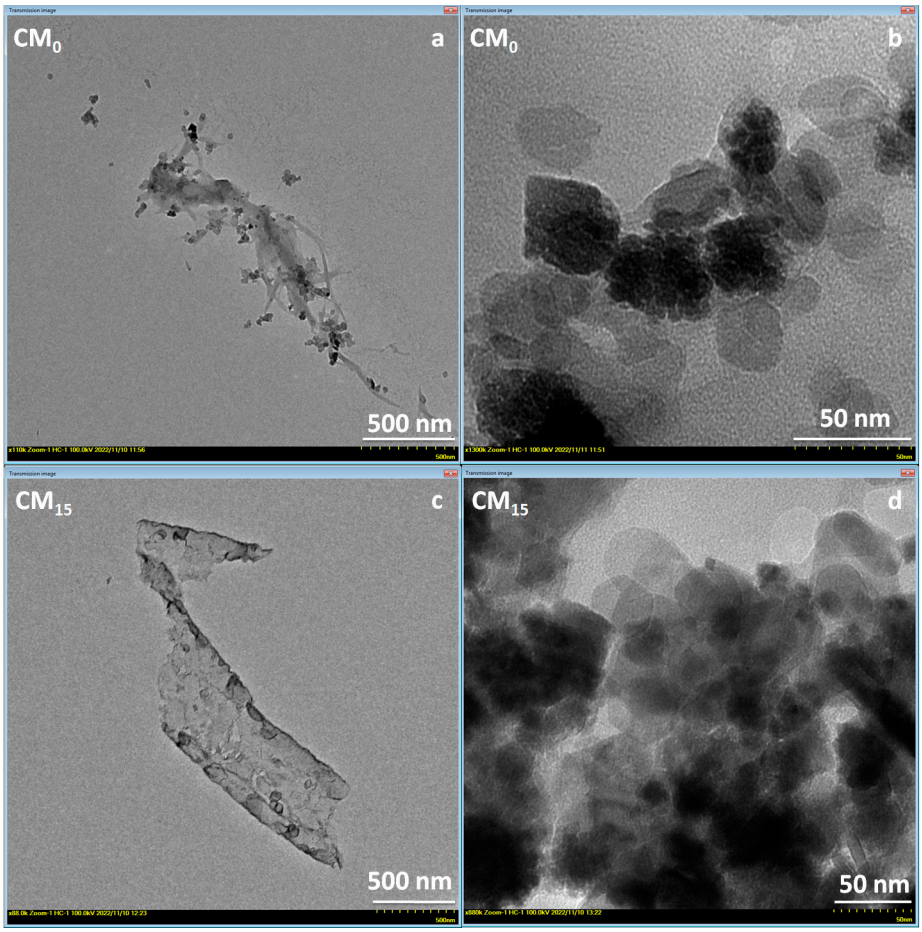

Figure 4. TEM images for ferromagnetic composites CM_0 and CM_{15}.

Through ultrasonication, the cellulose fiber undergoes fragmentation and reduces its size from 20 microns to around 1–2 microns (Figure 4a,c). Furthermore, a process of lateral fragmentation in the form of strips is also observed for the 30 min ultrasonicated composite (CM_0) (Figure 4a). The particles of magnetite and maghemite are 20–30 nanometers in size (Figure 4b,d).

3.1.4. Thermal Analysis Study

Thermal degradation (TG) of the precursors and magnetic composites (Figure 5a) was achieved in the inert gas atmosphere (He) with a flow of 40 mL/min, a heating rate of 10 °C/min, and a temperature range of 30 to 680 °C. DTG and DTA curves for C, CM_0, and CM_{15} are shown in Figure 5b,c. Table 7 displays the weight loss and important thermal characteristics derived from thermal degradation.

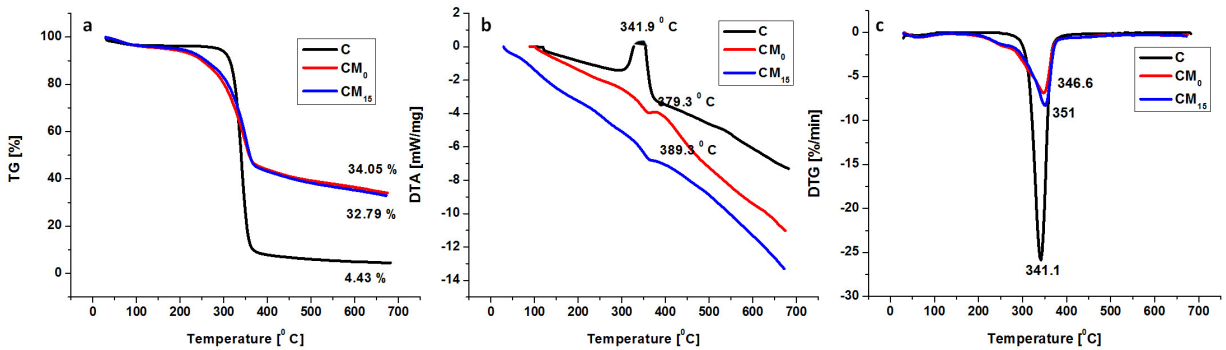

Figure 5. TG, DTA, and DTG curves for C, CM_0, and CM_{15}.

According to TG for cellulose (C), the degradation stage occurs in one stage that runs through an endothermic process with a maximum of 341.9 °C and results in a significant weight loss of 95.57% (weight). Higher temperatures of the maximum (379.3 °C for CM_0 and 389.3 °C for CM_{15}) are registered for the thermal degradation of the two ferromagnetic composites, indicating a chemical bond (via hydrogen bonds) between cellulose and the magnetite/maghemite phenomenon observed in other ferromagnetic cellulosic composites produced by ultrasonication [8]. In the case of composites, we observe a weight loss of 65.95% (CM_0) and 67.21% (CM_{15}). The magnetite, maghemite, and carbon from cellulose are represented by the residues of 34.05% (CM_0) and 32.79% (CM_{15}), and ferromagnetic oxides are stable at temperatures of 700 degrees. According to the XRD analysis, we can appreciate the amount of magnetite/maghemite in the composites to be around a quarter of the total mass.

Table 7. Thermo-gravimetric data.

Sample	Degradation Stage	T_{onset} °C	T_{peak} DTG, °C	W wt%	T_{10} °C	T_{20} °C	T_{peak} DTA, °C
C	I residue	312	341.1	95.57 4.43	314	325	341.9
CM_0	I residue	40.4 210.6 255 258.5	346.6	65.95 34.05	259	309	379.3
CM_{15}	I residue	40.7 56.4 207 262 265.1	351	67.21 32.79	254	309	389.3

Where T_{onset}—the temperature at which the thermal decomposition begins; T_{peak}—the temperature at which the degradation rate is maximum; W—weight loss; T_{10} and T_{20}—the temperatures corresponding to 10% and 20% respectively, weight loss.

3.1.5. Magnetic Properties Study

The magnetic properties of the composites (CM_0, CM_{15}) were monitored by measuring the hysteresis loops (magnetization curves) at room temperature (Figure 6).

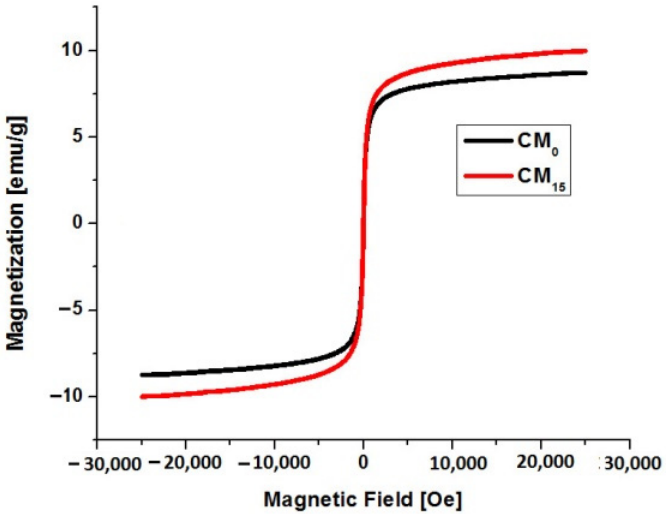

Figure 6. Magnetization curves for ferromagnetic composite CM_0 and CM_{15}.

The total in situ composite CM_0's saturation magnetization is 8.7 emu/g. Moreover, 9.9 emu/g for the partial in situ composite CM_{15} was obtained. The magnetization of the two composites differs because magnetite generally has a higher saturation magnetization than maghemite [7], with CM_{15} containing a higher proportion of magnetite. The magnetization curve and the demagnetization curve are the same, and the hysteresis cycle of the two composites describes a single curve. This indicates that superparamagnetism (SP) is present in CM_0 and CM_{15} [28,29]. The difference is provided by the quantitative ratio between magnetite and maghemite. Magnetite usually has a higher saturation magnetization than maghemite [7]. It makes sense that the magnetization would be higher in the case of CM_{15}, which contains more magnetite than the CM_0 composite.

4. Conclusions

Two ferromagnetic cellulosic composites were obtained through a modified coprecipitation method (using ultrasound), representing an in situ and partially in situ synthesis. The method allows obtaining magnetite and maghemite in a one-pot synthesis, with the quantities of the two iron oxides being variable according to the temperature of the reaction medium (higher for partially in situ synthesis). The saturation magnetization is higher in the partially in situ synthesis compared to the totally in situ one (9.9 emu/g and 8.7 emu/g). Both composites show the phenomenon of superparamagnetism, which makes them interesting for biomedical applications. The presence of cellulose at the beginning or middle of the synthesis of iron oxides seems to have the role of regulating the quantitative ratio between maghemite and magnetite, but also of the appearance of the phenomenon of superparamagnetism. As future perspectives, it is desired to observe the ratio between maghemite and magnetite when introducing cellulose at different reaction times (for example, 5, 10, 20, and 25 min) in order to observe the role of cellulose and establish a stoichiometric relationship.

Author Contributions: Conceptualization, R.R., M.E.F. and V.H.; methodology, E.U., O.U. and M.E.F.; software, R.R., O.U. and A.D.; validation, R.R. and V.H.; formal analysis, E.U., A.D. and O.U.; investigation, R.R., A.D. and M.E.F.; resources, E.U. and O.U.; data curation, V.H. and E.U.; writing—original draft, R.R. and M.E.F.; writing—review and editing, R.R. and V.H.; visualization R.R., E.U. and M.E.F.; supervision, V.H. and M.E.F. All authors have read and agreed to the published version of the manuscript.

Funding: This research received no external funding.

Institutional Review Board Statement: Not applicable for studies not involving humans or animals.

Informed Consent Statement: Not applicable.

Data Availability Statement: The raw data supporting the conclusions of this article will be made available by the authors on request.

Conflicts of Interest: The authors declare no conflicts of interest.

References

1. Zhang, Y.; Li, Q.J.; Lin, Y.; Huang, Z.; Lu, Y.; Sun, G.; Yang, M.; Huang, A.; Hu, H. A green and efficient technology for the degradation of cellulosic materials: Structure changes and enhanced enzymatic hydrolysis of natural cellulose pretreated by synergistic interaction of mechanical activation and metal salt. *Bioresour. Technol.* **2015**, *177*, 176–181. [CrossRef]
2. Arantes, A.C.C.; Almeida, C.D.G.; Dauzacker, L.C.L.; Bianchi, M.L.; Wood, D.F.; Williams, T.G.; Orts, W.J.; Tonoli, G.H.D. Renewable hybrid nanocatalyst from magnetite and cellulose fortreatment of textile effluents. *Carbohydr. Polym.* **2017**, *163*, 101–107. [CrossRef] [PubMed]
3. Jiao, Y.; Wan, C.; Bao, W.; Gao, H.; Liang, D.; Li, J. Facile hydrothermal synthesis of Fe_3O_4 cellulose aerogel nanocomposite and its application in Fenton-like degradation of Rhodamine B. *Carbohydr. Polym.* **2018**, *189*, 371–378. [CrossRef] [PubMed]

4. Mosii, P.; Jari, I.; Ursu, A.M.; Naum, A.G. The relationship between job strain and ischemic heart disease mediated by endothelial dysfunction markers and imaging. *Medicina* **2024**, *60*, 1048. [CrossRef] [PubMed]
5. Rotaru, R.; Samoila, P.; Lupu, N.; Grigoras, M.; Harabagiu, V. Ferromagmetic Materials Obtained Trought Ultrasonication. Maghemite/Goetthite nanocomposites. *Rev. Roum. Chim.* **2017**, *62*, 131–138.
6. Rotaru, R.; Fortuna, M.E.; Cojocaru, C.; Samoila, P.; Pricop, L.; Harabagiu, V. Viscose-Maghemite/Goethite Polymeric Composite Absorbent For Oil Spill Cleanup. *Environ. Eng. Manag. J.* **2019**, *18*, 1193–1200.
7. Cornell, R.M.; Schwertmann, U. *The Iron Oxides*; Wiley-VCH, Verlag GmbH & Co KGaA: Weinheim, Germany, 2003; pp. 14–20, ISBN 3-527-30274-3.
8. Rotaru, R.; Savin, M.; Tudorachi, N.; Peptu, C.; Samoila, P.; Sacarescu, L.; Harabagiu, V. Ferromagnetic iron oxides-cellulose prepared by ultrasonication. *Polym. Chem.* **2018**, *9*, 860–868. [CrossRef]
9. Torgbo, S.; Sukyai, P. Fabrication of microporous bacterial cellulose embedded with magnetite and hydroxyapatite nanocomposite scaffold for bone tissue engineering. *Mater. Chem. Phys.* **2019**, *237*, 121868. [CrossRef]
10. Carrazana-García, J.A.; Lopez-Quintela, M.A.; Rivas-Rey, J. Characterization of ferrites particles synthesized in presence of cellulose fibers. *Colloids Surf. A Physicochem. Eng. Asp.* **1997**, *121*, 61–66. [CrossRef]
11. Khalil, M.S.; Hassan, M.L.; Ali, A.F. One Cycle in-situ Processing of Nanoparticle-loaded Superparamagnetic Cellulose Fibers. *Egypt. J. Chem.* **2012**, *55*, 355–366.
12. Liu, S.; Zhou, J.; Zhang, L. In situ synthesis of plate-like Fe_2O_3 nanoparticles in porous cellulose films with obvious magnetic anisotropy. *Cellulose* **2011**, *18*, 663–673. [CrossRef]
13. Low, L.E.; Tey, B.T.; Ong, B.H.; Tang, S.Y. A facile and rapid sonochemical synthesis of monodispersed Fe_3O_4 cellulose nanocrystal nanocomposites without inert gas protection. *Asia-Pac. J. Chem. Eng.* **2018**, *13*, e2209. [CrossRef]
14. Luo, X.; Liu, S.; Zhou, J.; Zhang, L. In situ synthesis of Fe_3O_4/cellulose microspheres with magnetic-induced protein delivery. *J. Mater. Chem.* **2009**, *19*, 3538–3545. [CrossRef]
15. Dimitrov, K.V.; Herzog, M.; Nenkova, S. Fe_3O_4 Modification of Microcrystalline Cellulose for Composite Materials. *Am. J. Chem.* **2013**, *3*, 140–147.
16. Bowles, J.; Jackson, M.; Chen, A. Peter Solheid, Interpretation of low temperature data part 1: Superparamagnetism and paramagnetism. *IRM Q.* **2009**, *19*, 1–12.
17. Pankhurst, Q.A.; Connolly, J.; Jones, S.K.; Dobson, J. Applications of magnetic nanoparticles in biomedicine. *J. Phys. D Appl. Phys.* **2003**, *36*, R167. [CrossRef]
18. Papaefthymiou, G.C. Nanoparticle Magnetism. *Nano Today* **2009**, *4*, 438–447. [CrossRef]
19. Chen, A.P. Exploring the magnetic behavior of partially-oxidized single-domaine magnetite bellow the Verwey transition. *IRM Q.* **2009**, *19*, 507.
20. Batlle, X.; Labarta, A. Finite-Size Effects in Fine Particles: Magnetic and Transport Properties. *J. Phys. D Appl. Phys.* **2002**, *35*, 15–42.
21. Sorensen, C.M. *Nanoscale Materials in Chemistry*; Klabunde, K.J., Ed.; Wiley: New York, NY, USA, 2001.
22. Feltin, N.; Pileni, M.P. New Technique for Synthesizing Iron Ferrite Magnetic Nanosized Particles. *Langmuir* **1997**, *13*, 3927–3933. [CrossRef]
23. Murad, E.; Bowen, L.H.; Long, G.J.; Quin, T.G. The influence of crystallinity on magnetic ordering in natural ferrihydrites. *Clay Miner.* **1988**, *23*, 161–173. [CrossRef]
24. Xiao, Y.; Du, J. Superparamagnetic nanoparticles for biomedical applications. *J. Mater. Chem. B* **2020**, *8*, 354–367. [CrossRef]
25. Spiridon, I.; Teaca, C.A.; Bodirlau, R. Structural Changes Evidenced By FTIR Spectroscopy In Cellulosic Materials After Pre-Treatment with Ionic Liquid And Enzymatic Hydrolysis. *BioResources* **2010**, *6*, 400–413. [CrossRef]
26. Ciolacu, D.; Kovac, J.; Kokol, V. The effect of the cellulose-binding domain from Clostridium cellulovorans on the supramolecular structure of cellulose fibers. *Carbohydr. Res.* **2010**, *345*, 621–630. [CrossRef]
27. Oh, S.Y.; Yoo, D.I.; Shin, Y.; Kim, H.C.; Kim, H.Y.; Chung, Y.S.; Park, W.H.; Youk, J.H. Crystalline structure analysis of cellulose treated with sodium hydroxide and carbon dioxide by means of X-ray diffraction and FTIR spectroscopy. *Carbohydr. Res.* **2005**, *340*, 2376–2391. [CrossRef] [PubMed]
28. Ahmadzadeh, M.; Romero, C.; McCloy, J. Magnetic analysis of commercial hematite, magnetite, and their mixtures. *AIP Adv.* **2018**, *80*, 056807. [CrossRef]
29. Alborzi, Z.; Hassanzadeh, A.; Golzan, M.M. Superparamagnetic Behavior of the Magnetic Hysteresis Loop in the Fe_2O_3@Pt Core-Shell Nanoparticles. *Int. J. Nanosci. Nanotechnol.* **2012**, *8*, 93–98.

polymers

MDPI

Article

Effects of Ultrasonication in Water and Isopropyl Alcohol on High-Crystalline Cellulose: A Fourier Transform Infrared Spectrometry and X-ray Diffraction Investigation

Răzvan Rotaru [1], Maria E. Fortună [1,*], Elena Ungureanu [2,*] and Carmen O. Brezuleanu [2]

[1] "Petru Poni" Institute of Macromolecular Chemistry, Department of Inorganic Polymers, 41A Grigore Ghica Voda Alley, 700487 Iasi, Romania; rotaru.razvan@icmpp.ro
[2] "Ion Ionescu de la Brad" Iasi University of Life Sciences, 3 Mihail Sadoveanu Alley, 700490 Iasi, Romania; olgutabrezuleanu@iuls.ro
* Correspondence: fortuna.maria@icmpp.ro (M.E.F.); elena.ungureanu@iuls.ro (E.U.)

Abstract: This paper investigates the effects of ultrasonication on cellulose microparticles in different conditions. FTIR (Fourier transformed infrared spectrometry) and XRD (X-ray diffraction) analyses were used to compare the changes in the cellulose microstructure caused by the following various ultrasonic treatment conditions: time, amplitude of generated ultrasound waves, output power converted into ultrasound, the liquid medium (water and isopropyl alcohol) used for ultrasonication, and the shape of the vessel used for sonication. The cumulative results lead to an increase in the crystalline region directly proportional to the condition of sonication. Also, the total crystallinity index varied from 1.39 (pristine cellulose) to 1.94 for sonication in alcohol to 0.56 for sonication in water. The crystallinity index varied from 67% (cellulose) to 77% for the sample with 15 min of sonication in isopropyl alcohol and 50.4% for the sample with 15 min of sonication in water.

Keywords: alcohol; cellulose; ultrasonication; water

Citation: Rotaru, R.; Fortună, M.E.; Ungureanu, E.; Brezuleanu, C.O. Effects of Ultrasonication in Water and Isopropyl Alcohol on High-Crystalline Cellulose: A Fourier Transform Infrared Spectrometry and X-ray Diffraction Investigation. *Polymers* **2024**, *16*, 2363. https://doi.org/10.3390/polym16162363

Academic Editor: Guantian Li

Received: 19 July 2024
Revised: 18 August 2024
Accepted: 19 August 2024
Published: 21 August 2024

1. Introduction

Due to its abundance and renewable nature, cellulose is perhaps the most significant biopolymer on earth and has been a part of human life since the dawn of time (such as paper woven from cotton). Over the last 150 years, there have been many uses for cellulose, its derivatives, and its composites, including the manufacturing of food and paper [1,2], bio- and pharmaceutical materials, magneto-optical and recyclable catalyst applications, the electrotechnical industry, etc. [3,4]. In its natural form, this polymer is made by a linear chain of anhydroglucose molecules united by a β-1, 4-glycosidic bond [5]. Due to the hydrogen bonds and van der Waals forces holding these chains together, cellulose is insoluble in most common solvents [6]. In order to extract cellulose from biomass, obtain composites or derivatives, or modify structure and morphology, cellulose is treated in different ways. The nanoparticles of crystalline cellulose are obtained from the acid hydrolysis of cellulose fibers [7]. Ionic liquid (1-butyl-3-methylimidazolium chloride, 1-ethyl-3-methylimidazolium tetrachloroaluminate) is used as a pretreatment for cellulosic materials [6,8], and as a result, there appears to be variation in the crystallinity index. A new method for generating cellulose composites is presented using the ultrasonic technique. W. Chen used hard ultrasonication (20–25 kHz ultrasound frequency, 1000 watts of output power, and 30 min of sonic treatment) to obtain cellulose nanofibers from plant cellulose fibers with a noticeably increased crystallinity (in the case of wood used as a source of cellulose, there was an increase from 56% in raw materials to 71–73.2% on ultrasonic-treated cellulose) [9]. X.F. Li and his colleagues [10] created spherical nano-crystal cellulose from cellulose I and II using a novel technique that involved acid hydrolysis and ultrasonication (20 kHz, 400 W output power, and more than 8 h of ultrasound irradiation). The time of the ultrasonic treatment was correlated with the shape and degree of the scatter of particles.

Using high-intensity ultrasonication (20 kHz, 1500 W, and varying times: 5, 10, and 15 min), rod-shaped nanocrystalline cellulose was formed from microcrystalline cellulose. In this case, the time of ultrasonication directly affected the length of rod-shaped cellulose [11]. A.N. Frone and collaborators managed to prepare cellulose nanofibers from microcrystalline cellulose and then obtained composites with nanofibers and poly (vinyl alcohol) via the ultrasonication technique (20 kHz, 500 W, 10–20 min) [12]. Using a chemical procedure and high-intensity ultrasonication (20–25 kHz frequency, 400–1200 W output power, and 30 min of ultrasonication), W. Chen and associates extracted cellulose nanofibers from poplar trees [13]. They found that the diameter distributions of the nanofibers, which have a crystallinity of roughly 69%, depend on the output power (0.4–1.2 kW) of the ultrasonic treatment. S. Parveen and associates developed cellulose-reinforced cementation composites by homogeneously dispersing microcrystalline cellulose using ultrasonication energy (45 kHz frequency and 80 W power) [14]. Ultrasonication was carried out for different time periods, such as 15, 30, 45, and 60 min, in order to investigate the influence of the time of ultrasonication on dispersion quality. In another study, Girard et al., used the ultrasonication modeling methodology to investigate the ultrasonic (20 kHz frequency) dispersion of cellulose nanocrystals. They used the solution of a coupled problem between the Navier–Stokes equations and a steady-state variant of the wave equation [15]. Using numerical modeling, several key parameters were identified to obtain a well-dispersed CNC suspension, such as the beaker geometry, the probe position, and, more specifically, depth and centering. A.M. Barbosa and associates obtained cellulose nanocrystal membranes as excipients for drug delivery systems from flax fibers via acid hydrolysis assisted by sonochemistry [16]. These nanocrystals of cellulose exhibited a high crystallinity, and the ultrasonic process was conducted at a frequency of 37 kHz for different periods of time: 30, 45, and 60 min. Wong et al. studied the effect of prolonged ultrasonication on the molecular weight and crystallinity index of cellulose (bacterial and plant cellulose) [17]. They found a reduction in molecular mass and crystallinity index. The ultrasound process (37 kHz frequency and 150 W powers) was conducted in a cuprammonium hydroxide solution for 5, 10, 15, 30, 60, and 90 min. In general, it can be said that the synthesis, dispersion, or homogenization of cellulose by ultrasound in certain media can cause a change in crystallinity, shape, or hydrogen bonds. Thus, the reactivity of cellulose can be modified, and this can matter a lot, especially in medical applications [18]. In a previous investigation, we discovered that ultrasonic treatment in water causes cellulose with fiber lengths of 20 microns, whether in composite or alone, to lose part of its crystallinity [4,19]. In a recent investigation (unpublished), we discovered that high-crystalline cellulose with fiber lengths of 1 micron ultrasonicated in different types of alcohol (pristine or in composites with different inorganic particles) presents an increase in crystallinity. The purpose of this investigation is to conduct research on the behavior of micronized cellulose under ultrasonic waves in water and alcohol.

2. Materials and Methods

2.1. Materials

Microcrystalline cellulose (C, Avicel, Wilmington, Delaware, U.S.CAS 9004-34-6, grade PH-101) was used with density = 1.5 g/cm^3 (20 °C), bulk density = 70–400 kg/m^3, isopropyl alcohol (IPA, Sigma-Aldrich, Burlington, MA, USA) with Mw = 60.1 g/mol, and a purity of 99.5%. Milli-Q ultrapure-distilled water (H_2O, our laboratory) was used without further purification.

Ultrasonic irradiation of cellulose

Each 2 g sample of pristine cellulose (C) was ultrasonicated in 70 mL of liquid (isopropyl alcohol or water) in a 100 mL beaker under various conditions (time: 5, 10, and 15 min of ultrasonication, amplitude of ultrasonic wave: half (50%) or the whole (100%), liquid medium for ultrasonication: isopropyl alcohol or water; and vessel for ultrasonic process: cylindrical Berzelius or spherical-round-bottomed flask) as shown in Table 1.

Following decantation (24 h at room temperature), the samples were dried in a vacuum oven at 50 °C overnight. Each sample was collected as a fine white powder.

Table 1. Sample notations and the conditions of ultrasonic irradiation.

Sample	Time [min]	Amplitude [%]	Liquid	Vessel
C	-	-	-	-
C_5	5	50	C_3H_7OH	Berzelius
C_{10}	10	50	C_3H_7OH	Berzelius
C_{15}	15	50	C_3H_7OH	Berzelius
C_{2x5}	5	100	C_3H_7OH	Berzelius
C_F	5	50	C_3H_7OH	Round-bottomed flask
C_{5H2O}	5	50	H_2O	Berzelius
C_{10H2O}	10	50	H_2O	Berzelius
C_{15H2O}	15	50	H_2O	Berzelius

2.2. Methods

The ultrasonication experiments were performed using a Sonic Vibracell ultrasonic generator with a nominal electric power of 750 W and an ultrasound frequency of 20 kHz, provided with a display giving the energy delivered to the end of the probe and a temperature sensor. The samples were dried in a Trade-Raypa vacuum oven at 50 °C.

FTIR spectroscopy was performed using a Bruker Vertex 70 spectrometer on potassium bromide (KBr) pellets with a 2 cm^{-1} resolution. The concentration of the samples was a constant of 2 mg/200 mg of KBr.

To calculate the empirical crystallinity index, or lateral order index (LOI), the following equation was used:

$$LOI = I_{1435}/I_{899} \quad (1)$$

where I is the intensity of the absorbance peak, and the wavenumbers are 1435 and 899 cm^{-1}, respectively.

The total crystallinity index (TCI) was determined using Equation (2):

$$TCI = I_{1366}/I_{2914} \quad (2)$$

The hydrogen bond intensity (HBI) was established with the following ratio:

$$HBI = I_{3339}/I_{1323} \quad (3)$$

The energy of the hydrogen bonds (noted E_H) for several OH stretching bands was calculated using Formula (4):

$$E_H = \frac{1}{k} \cdot \frac{\nu o - \nu}{\nu} \quad (4)$$

where k = 1.68 × 10^{-2} $kcal^{-1}$, ν_0 is the standard frequency corresponding to free OH groups (3600 cm^{-1}), and ν is the frequency of the bonded OH groups [20,21].

Pimentel and Sederholm [22] proposed Equation (5), which yields the hydrogen bond distances, R, as follows:

$$\Delta(\nu) = 4430(2.84 - R) \quad (5)$$

where $\Delta(\nu) = \nu_0 - \nu$, ν_0 is the monomeric OH stretching frequency, which is taken to be 3600 cm^{-1}, and ν is the stretching frequency observed in the infrared spectrum of the sample (deconvolution spectra).

X-ray diffraction (XRD) on a Bruker Advance D8 X-ray diffractometer (λ: 1.5405 Å, with the wavelength of Cu-Kα radiation, 2θ, ranging from 4 to 60°).

The values of the crystallinity index (C_rI) of cellulose and sonic-treated samples were obtained with the Segal method according to Equation (6) [23]:

$$C_rI = 100 \cdot \frac{I002 - Iam}{I002}\% \quad (6)$$

where I_{002} represents the maximum intensity of the 002 lattice diffraction with a peak corresponding to a 2θ angle around 22–24°, and I_{am} is the intensity of diffraction of the non-crystalline (amorphous) material, which is taken at a 2θ angle of about 18°.

The average size of the crystallites, measured in the directions orthogonal to the (101), (10$\bar{1}$), and (002) planes, is calculated using the Scherrer Formula (7):

$$D = \frac{K \cdot \lambda}{\beta \cdot \cos\theta} \quad (7)$$

where D is the average crystallite size, K is the Scherrer constant (0.89), λ is the wavelength of the incident X-ray (Kα1 = 1.5406 Å, Kα2, 1.5443 Å. and Kβ, 1.3923 Å), β represents the full width at half maximum of the reflection in the radial direction (diffraction band), and θ is the angle corresponding to the crystalline peak (Bragg angle) [21,24]. We filtered out the Kβ radiation, leaving a weighted average of 1.5418 Å with a Ni filter. Lattice parameters and lattice volume were calculated with the decomposition method using Origin software, 8 Pro.

3. Results and Discussion

3.1. The Chemical Structure of the Irradiated Samples Established by FTIR Analysis

Infrared spectroscopy was used to examine the structure of both pure cellulose and ultrasonic-irradiated samples. Figure 1 presents the infrared spectra for pristine cellulose (C) and ultrasonic-irradiated samples (C_5, C_{10}, C_{15}, C_{2x5}, C_F, C_{5H2O}, C_{10H2O}, and C_{15H2O}).

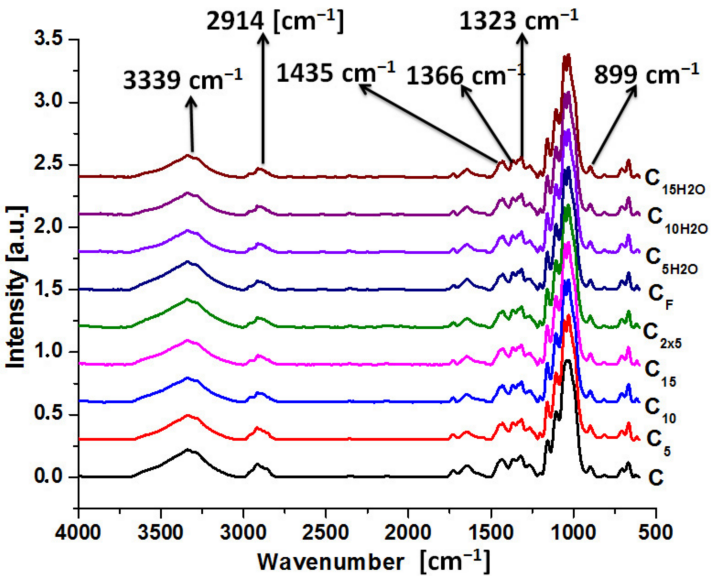

Figure 1. Infrared spectra for pristine cellulose and ultrasonicated samples.

The type of vibration and wave number are given in Table 2. For sonicated samples, some peaks were practically unmodified, but there were also noticeable changes.

Except for the hydroxyl groups, the largest displacements of the wave number were found at ν_{CH} vibrations (2914 cm^{-1} for pristine cellulose) from 48 to 65 cm^{-1}. The smallest displacements were observed for ν_{CO}- and δ_{CH2}-type vibrations (1055, 1030, and 899 cm^{-1}) from 4 to 8 cm^{-1}.

Table 2. Wavelength (W) shifts in ultrasound samples ($\Delta W = W_C - W_{ultrasonicated\ sample}$).

W_C [cm^{-1}]	Type of Vibration	$W_{samples}$ [cm^{-1}]	Sample	ΔW [cm^{-1}]
3339	hydroxyl groups	3336	C_5	3
		3341	C_F, C_{5H2O}	−2
		3352	C_{10H2O}	−13
		3435	C_{15H2O}	−96
2914	ν_{CH}	2918	C_5	−4
		2916	C_{10}	−2
		2962	C_{10}	−48
		2897	C_{10}	17
		2962	C_{15}	−48
		2851	C_{15}	63
		2916	C_{2x5}	−2
		2955	C_{2x5}	−41
		2899	C_{2x5}	15
		2962	C_F	−48
		2901	C_F	−13
		2962	C_{5H2O}	−48
		2897	C_{5H2O}	17
		2849	C_{5H2O}	65
		2903	C_{10H2O}	11
		2959	C_{15H2O}	−45
		2905	C_{15H2O}	9
1435	δ_{CH2}	1429	C_5, C_{10}, C_{15}, C_{2x5}, C_{5H2O}	6
		1427	C_F	8
		1433	C_{10H2O}	2
		1437	C_{15H2O}	−2
1366	δ_{CH}, ν_{COO}	1367	C_5, C_{10}, C_{15}, C_{2x5}, C_F, C_{5H2O}	−1
		1371	C_{10H2O}	−5
		1375	C_{15H2O}	−9
1323	CH_2	1315	C_5, C_{10}, C_{15}, C_{2x5}, C_F, C_{5H2O}	8
		1319	C_{10H2O}, C_{15H2O}	4
1157	ν_{CO}, δ_{OH}	1159	C_5, C_{10}, C_{15}, C_{2x5}, C_F, C_{5H2O}, C_{10H2O}, C_{15H2O}	
1055, 1030	ν_{CO}	1059, 1032	C_{10H2O}	−4, −2
		1059, 1038	C_{15H2O}	−4, −8
899	δ_{CH2}	895	C_{10H2O}, C_{15H2O}	4

Some of the characteristic spectral bands were quite sensitive to the crystalline structure in cellulose materials. Thus, the bands located at 2914, 1435, 1366 cm^{-1}, and 899 cm^{-1} corresponded to crystalline and amorphous domains, respectively [4]. So, TCI, LOI, and HBI were calculated with Formulas (1)–(3), and the results of these parameters are shown in Table 3. Taking into account chain mobility, bond distance, and the amount of bounded water, the TCI is proportional to the crystallinity of cellulose, the LOI is the overall degree of order in cellulose, and the hydrogen bond intensity HBI refers to the crystal system and the degree of intermolecular regularity.

Table 3. Lateral order index (LOI), total crystallinity index (TCI), and hydrogen bond intensity (HBI) of pristine cellulose and sonicated samples.

Sample	LOI	TCI	HBI
C	1.68	1.39	1.29
C_5	1.22	1.45	1.19
C_{10}	1.45	1.72	1.40
C_{15}	1.50	1.89	1.39
C_{2x5}	1.46	1.75	1.37
C_F	1.64	1.93	1.36
C_{5H2O}	1.48	1.94	1.23
C_{10H2O}	2.05	0.76	2.12
C_{15H2O}	1.29	0.56	2.92

For ultrasonication in isopropyl alcohol, the lateral order index (LOI) suffers a small decrease, indicating that ultrasonic irradiation directly affects the overall degree of order in cellulose, but the total crystallinity index (TCI) is increased, and so the crystallinity degree of cellulose is bigger. The ultrasonication time is directly proportional to this crystallinity increase (TCI for 5 min is 1.45, 10 min is −1.72, and 15 min is −1.89).

The intensity of ultrasonic irradiation is directly proportional to the amplitude of the vibration of the sonic source. Therefore, an increment in the amplitude leads to an increase in the intensity of vibration and an increase in the sonochemical effects (for the main microcavitation effect, bubble formation is observed, followed by their growth and, finally, implosion, which can cause temperatures of approximately 5000 °C in gas phases or more than 2000 °C in liquid phases and pressures higher than 500 atmospheres). Bubble collapse during cavitation serves as a very effective means of concentrating the power energy of the sound: the compression of gas always generates heat. When the compression of bubbles occurs during cavitation, heating is much more rapid than usual thermal transport, creating a short-lived localized hot spot. Ultrasonic irradiation is different from traditional energy sources (e.q., heat, light, or ionizing radiation) in duration, pressure, and energy per molecule. The immense local temperatures and pressures, together with the extraordinary heating and cooling rates generated by cavitation bubble collapse, mean that ultrasound provides a very unique mechanism for generating high-energy chemistry [25]. By doubling the amplitude of the wave (100%) for 5 min, TCI is almost equivalent to 10 min of ultrasonication at a 50% amplitude (TCI C_{2x5} = 1.75~TCI C_{10} = 1.72 compared with TCI C_5 = 1.45). The shapes of the vessels also affect the TCI index (TCI-C_F = 1.93 compared with TCI-C_5 = 1.45). It is already known that a round-bottomed flask minimizes the "dead zone" for ultrasound wave action better than a Berzelius beaker [26].

Isopropyl alcohol is commonly employed in ultrasonic synthesis for the deagglomeration of powders [27]. Water, like ultrasonication liquid medium, has a different effect than alcohol (TCI-C_5H_2O = 1.94, the highest value) [28].

However, when the ultrasound time is increased to 10 and 15 min, the TCI index significantly decreases to 0.76 for C_{10H2O} and 0.56 for C_{15H2O} [4]. Another aspect is represented by hydrogen bonding. This is considered to be responsible for various properties of cellulose. Thus, the closer or more distant the cellulose chains are, the larger or smaller the interactions between them, resulting in more and stronger hydrogen bonds or, conversely, weaker connections.

The broadband in the FTIR spectra between 3000 and 3700 cm^{-1} corresponds to the hydroxyl stretching vibration and offers information about hydrogen bonding (intra and intermolecular).

The assignments of intramolecular hydrogen bonds are shown for O(2)H-O(6) in the cellulose crystalline structure at 3410–3460 cm^{-1}, for intramolecular O(3)H-O(5) at 3340–3375 cm^{-1} and for the intermolecular hydrogen bonding of O(6)H-O(3) in the region 3230–3310 cm^{-1} [14,27]. Since the absorbance peaks of pristine celluloses and sonicated samples in this range (3000–3700 cm^{-1}) were overlapped, the resolution of the spectra was

improved by their deconvoluted graphics from background scattering using a Gaussian function curve—multiple peak fit analysis using Origin 8.5 Pro software. The energy of hydrogen bonds and hydrogen bond distances for pristine cellulose and sonicated samples are presented in Table 4, and the deconvoluted spectra in 3000–3700 cm^{-1} regions are presented in Figures 2–4.

Table 4. Energy bonds and hydrogen bond distances.

Sample	Type of Hydrogen Bond	E_H [kJ]	R [Å]
C	intermolecular O(6)H-O(3)	E_{3305}: 23.43	R_{3305}: 2.773
	intramolecular O(3)H-O(5)	E_{3363}: 18.49	R_{3363}: 2.786
C_5	intermolecular O(6)H-O(3)	E_{3278}: 25.78	R_{3278}: 2.767
	intramolecular O(3)H-O(5)	E_{3344}: 20.09	R_{3344}: 2.782
C_{10}	intermolecular O(6)H-O(3)	E_{3278}: 25.78	R_{3278}: 2.767
	intermolecular O(6)H-O(3)	E_{3286}: 25.08	R_{3286}: 2.769
	intramolecular O(3)H-O(5)	E_{3344}: 20.09	R_{3344}: 2.782
C_{15}	intermolecular O(6)H-O(3)	E_{3251}: 28.17	R_{3251}: 2.761
	intermolecular O(6)H-O(3)	E_{3286}: 25.08	R_{3286}: 2.769
C_{2x5}	intermolecular O(6)H-O(3)	E_{3234}: 29.70	R_{3234}: 2.757
	intermolecular O(6)H-O(3)	E_{3276}: 25.96	R_{3276}: 2.766
C_F	intermolecular O(6)H-O(3)	E_{3269}: 26.57	R_{3269}: 2.765
	intermolecular O(6)H-O(3)	E_{3280}: 25.60	R_{3280}: 2.767
	intramolecular O(3)H-O(5)	E_{3342}: 20.26	R_{3342}: 2.781
C_{5H2O}	intermolecular O(6)H-O(3)	E_{3285}: 25.17	R_{3285}: 2.768
	intermolecular O(6)H-O(3)	E_{3289}: 24.82	R_{3289}: 2.769
	intramolecular O(2)H-O(6)	E_{3454}: 11.09	R_{3454}: 2.807
C_{10H2O}	intermolecular O(6)H-O(3)	E_{3267}: 26.75	R_{3267}: 2.764
	intramolecular O(2)H-O(6)	E_{3459}: 10.70	R_{3459}: 2.808
C_{15H2O}	intermolecular O(6)H-O(3)	E_{3278}: 25.78	R_{3278}: 2.798
	intramolecular O(3)H-O(5)	E_{3341}: 20.34	R_{3341}: 2.781
	intramolecular O(3)H-O(5)	E_{3361}: 18.66	R_{3361}: 2.786

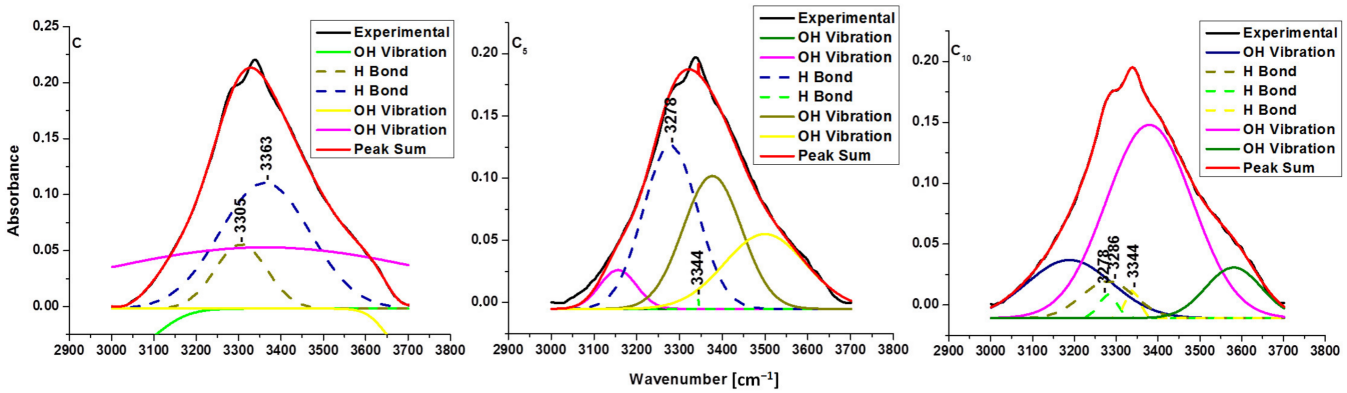

Figure 2. Deconvoluted FTIR spectra (range 300–3700 cm^{-1}) for C, C_5, and C_{10} samples.

In black, the experimental curve obtained from the infrared spectrometer is shown, and in red, the theoretical curve obtained from the sum of all deconvoluted curves is shown. Ideally, black and red curves need to overlap. The small differences represented hydroxyl groups from the atmosphere (moisture) or small errors from the infrared sensor.

It is observed that the intermolecular hydrogen bond O(6)H-O(3) changes energy (an increase with sonication) and distances (a decrease with sonication). Ultrasonication reduces hydrogen bond distances in pure cellulose for 5, 10 min, and for 15 min, indicating a minor decline in the linear chain of anhydroglucose molecules. The high energy and the small distances were obtained for C_{2x5} when the amplitude of ultrasound was double. Table 4 shows how the shape of the reaction vessel (flask/Berzelius) and the ultrasonication time had a direct influence on the energy of hydrogen bonding.

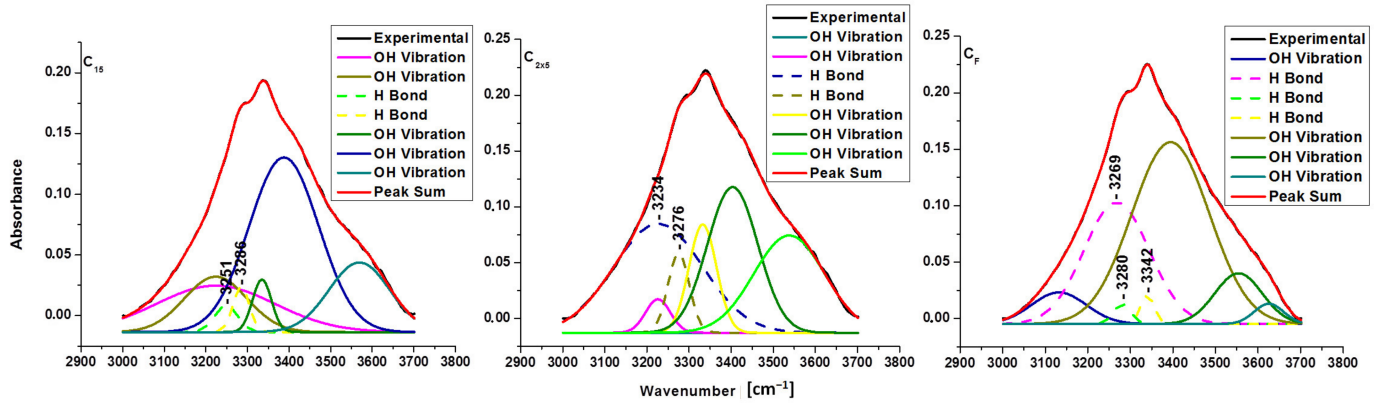

Figure 3. Deconvoluted FTIR spectra for C_{15}, C_{2x5}, and C_F samples.

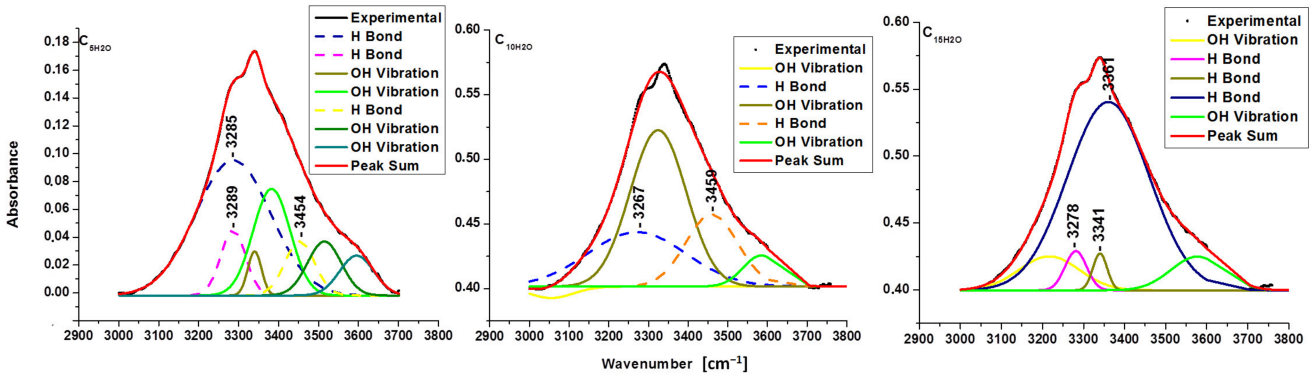

Figure 4. Deconvoluted FTIR spectra for C_{5H2O}, C_{10H2O}, and C_{15H2O} samples ultrasonicated in water.

The reduced distances for the intermolecular hydrogen bond O(6)H-O(3) in sonic-irradiated samples increased crystallization by facilitating the ordering of the linear chain of glucose residue.

3.2. Crystalline Structure of the Ultrasonicated Sample: X-ray Diffraction Analysis

X-ray diffraction (XRD) analysis was used to accomplish a deeper structural characterization (in order to measure the crystallinity, apparent crystallinity, and size of the crystallites) of the studied cellulose and sonicated samples. Figure 5 depicts the diffractograms for native cellulose and sonicated materials, while Table 5 provides quantitative and qualitative data (space group, crystal system, lattice parameters, lattice volume, and crystallite size).

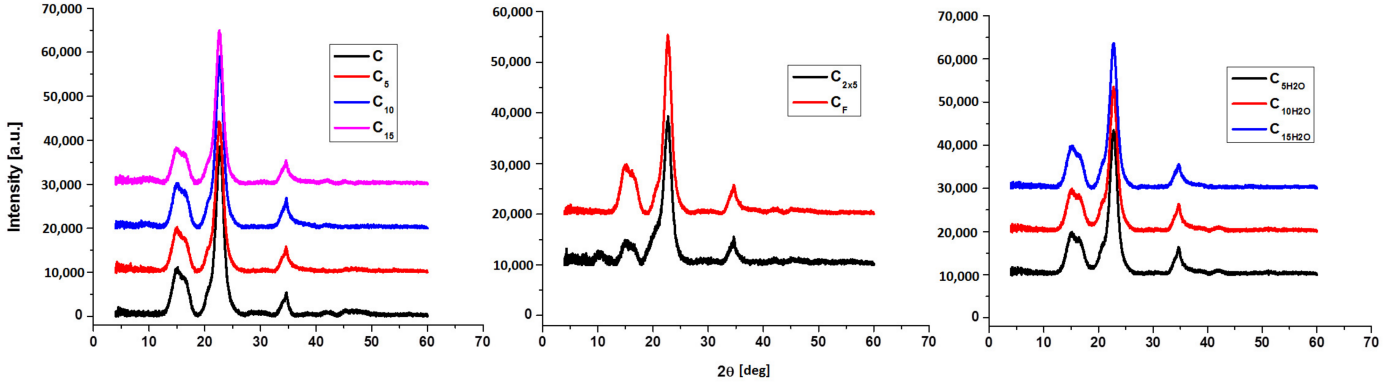

Figure 5. XRD pattern for pristine cellulose powder and ultrasonicated samples.

Table 5. Quantitative and qualitative data.

Sample	JCPDS Card No	Space Group	Crystal System	Lattice Parameters [Å]			Lattice Volume [Å]	Crystallite Size [Å]
				a	b	c		
C	4114994	4:P1121	Monoclinic (C-unique)	7.82	8.03	10.35	647.9	41
C_5	4114383	1:P1	Triclinic	10.45	6.56	6.03	331.6	49
C_{10}	4114383	1:P1	Triclinic	10.43	6.46	5.93	332.2	46
C_{15}	4114383	1:P1	Triclinic	10.26	6.49	5.85	324.6	56
C_{2x5}	4114383	1:P1	Triclinic	10.40	6.61	5.91	317.4	27
C_F	4114383	1:P1	Triclinic	10.32	6.53	5.97	342.1	63
C_{5H2O}	4114994	4:P1121	Monoclinic (C-unique)	8.02	8.37	10.40	695.3	39
C_{10H2O}	4114994	4:P1121	Monoclinic (C-unique)	7.96	8.25	10.38	680.6	54
C_{15H2O}	4114994	4:P1121	Monoclinic (C-unique)	7.98	8.15	10.43	676.3	36

The X-ray diffractograms of pristine celluloses and sonicated samples show the characteristic shapes of the cellulose I crystalline structure corresponding to crystallographic (1–10), (110), and (200) planes at Bragg angles of 14.71°, 16.63°, and 22.55°, respectively. Figure 6 shows that ultrasonication in isopropyl alcohol changes the space group (from P1121 to 1: P1) and the crystalline structure (from monoclinic to triclinic), whereas ultrasonication in water does not change these parameters.

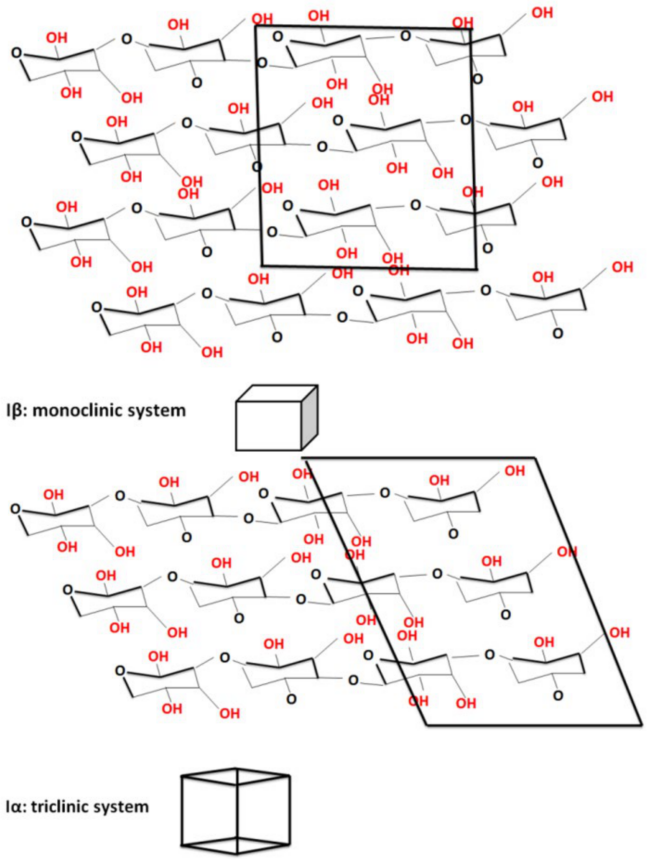

Figure 6. Monoclinic and triclinic cellulose system.

Alcohol-treated samples saw a significant decrease in lattice volume (from 647 to 331–342 Å), while Milli-Q Watter treatment resulted in a modest increase to 676–695 Å.

In order to correctly calculate the values of the crystallinity index (CrI), the resulting diffraction patterns were deconvoluted from background scattering using a Gaussian function curve-fitting analysis.

Deconvoluted diffractograms for native cellulose and sonicated samples are depicted in Figures 7–9, and data for the crystallinity index are given in Table 6.

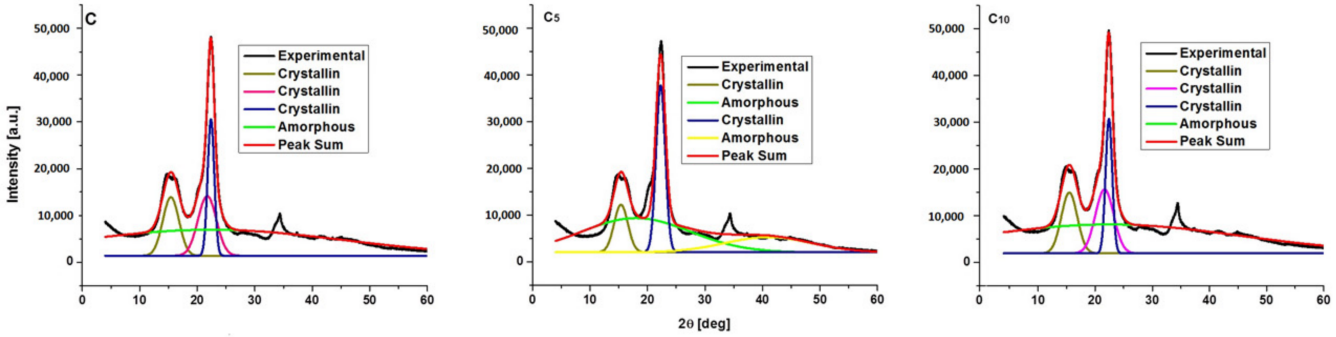

Figure 7. Deconvoluted X-ray diffractograms for C, C_5, and C_{10}.

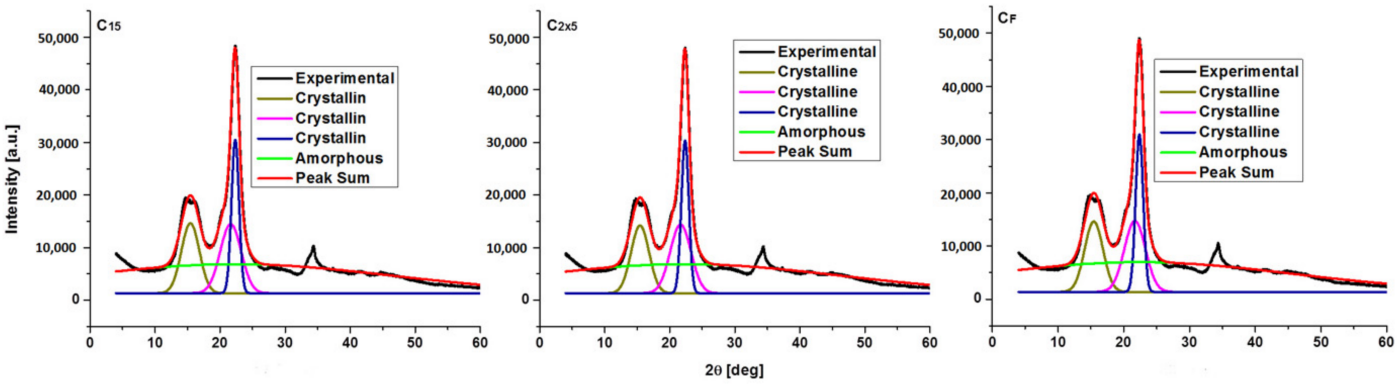

Figure 8. Deconvoluted X-ray diffractograms for C_{15}, C_{2x5}, and C_F.

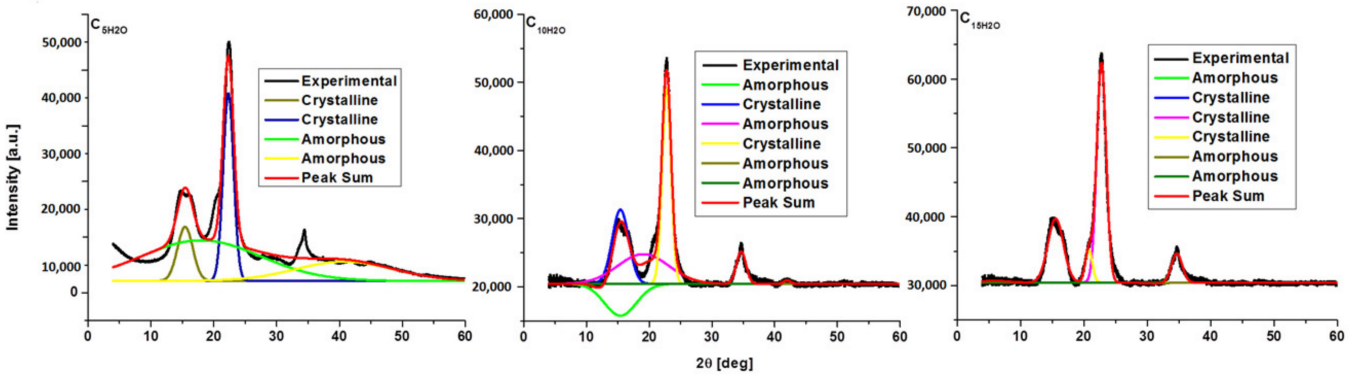

Figure 9. Deconvoluted X-ray diffractograms for C_{5H2O}, C_{10H2O}, and C_{15H2O}.

Before deconvolution, the X-ray diffraction pattern exhibits a big peak at 2θ, 14.8° (secondary peak), and a noticeable peak (major peak) at 2θ, 22.6° [29,30]. There are changes after deconvolution, and these are not limited to peak intensity.

For C, C_{10}, C_{15}, C_{2x5}, CF, and $C_{15H2O,}$ three sharp peaks indicate three crystalline regions with three types of crystallites, with 2θ angles of 15.3°, 21.5°, and 22.6° corresponding to the (10), (020), and (200) planes. C_5, C_{5H2O}, and C_{10H2O} samples show two crystalline peaks only at 15.3° and 22.6° (planes (10) and (200)). The ultrasonication of cellulose in alcohol causes an increase in the crystallinity index, from 67 to 74–77%, and a decrease in the lattice volume, while the ultrasonication procedure in Milli-Q water causes a decrease in the crystallinity index (from 67 to 50–66%) and a slight increase in lattice volume.

Table 6. Crystallinity index for cellulose and sonicated samples.

Samples	C_rI [%]
C	67.6
C_5	74.2
C_{10}	74.6
C_{15}	77.8
C_{2x5}	77.4
C_F	77.6
C_{5H2O}	66.9
C_{10H2O}	51.6
C_{15H2O}	50.4

The crystalline region is affected, probably through the realignment of the cellulose microfibers. According to data from the literature [4], for long fibers (20 µm), fragmentation appears, which leads to a decrease in crystallinity. For short fibers (1–2 µm), this realignment could lead to an increase in crystallinity. This increase in crystallinity is in accord with the Z.Z. Chowdury study (ultrasonication and acid treatment provide nanocrystalline cellulose with lengths of 0.9–0.1 µm and an 88.3 crystallinity index) [3,9]. For comparison, Table 7 gives some results with an increase or decrease in the crystallinity index compared with the lengths of cellulose fibers.

Table 7. Crystallinity index of ultrasonicated cellulose in different conditions.

Sample	Lenghts of Fiber [µm]	Treatment	Time of Treatment [min]	CI [%] before Treatment	CI [%] after Treatment	References
cellulose nano-crystals	0.105	ultrasound assisted acid hydrolysis	35	55.3–63.8-72.4	88.3	[3]
cellulose microfibers	1	ultrasonication in isopropyl alchool	5–15	67.6	72.9–77.6	[this work]
cellulose microfibers	1	ultrasonication in Milli-Q water	5–15	67.6	50–4–66.9	[this work]
cellulose microfibers	20	ultrasonication in Milli-Q water	15	42.5	42.4	[4]
cellulose microfibers with anorganic nanoparticle	20	ultrasonication in Milli-Q water	15	42.5	9.6	[4]
cellulose microfibers	20	ultrasonication in sodium hydroxide solution (1–10%)	240	77	73.8	[29]
cellulose microfibers	50	ultrasonication in sodium hydroxide solution	240	79.8	68.2	[29]
cellulose microfibers	100	ultrasonication in sodium hydroxide solution	240	78.8	67.7	[29]
cellulose microfibers	180	ultrasonication in sodium hydroxide solution	240	76.5	71.7	[29]
cellulose microfibers	180	ultrasonication in sodium hydroxide solution	120	76.5	71.65	[29]

4. Conclusions

In this study, microscopic particles of cellulose were subjected to ultrasonication in isopropyl alcohol and Milli-Q water. It was discovered that when ultrasonic irradiation was performed in alcohol, the crystallinity region suffered an increase proportionally with the conditions of the sonic treatment (time, amplitude of the generated ultrasound wave, and the shape of the vessel used for sonication), while when it was made in water, there was degradation in the crystalline region. This mechanism is different in water and alcohol because these two liquids have different properties (specific density, specific weight), and thus, the ultrasonic waves propagate differently.

Author Contributions: Conceptualization, R.R. and M.E.F.; methodology, E.U. and M.E.F.; software, R.R. and C.O.B.; validation, R.R., M.E.F. and C.O.B.; formal analysis, E.U. and R.R.; investigation, R.R., E.U. and M.E.F.; resources, E.U. and C.O.B.; data curation, M.E.F. and E.U.; writing—original draft preparation, R.R. and M.E.F.; writing—review and editing, R.R., E.U. and C.O.B.; visualization R.R. and M.E.F.; supervision, E.U. and M.E.F. All authors have read and agreed to the published version of the manuscript.

Funding: This research received no external funding.

Institutional Review Board Statement: Not applicable.

Data Availability Statement: Data are contained within the article.

Conflicts of Interest: The authors declare no conflicts of interest.

References

1. Ungureanu, E.; Fortună, M.E.; Țopa, D.C.; Lobiuc, A.; Ungureanu, O.C.; Jităreanu, D.C. Design of the functional polymer systems to optimize the filler retention in obtaining cellulosic substrates with improved properties. *Materials* **2023**, *16*, 1904. [CrossRef]
2. Li, Y.; Guan, X.; Chaffey, P.K.; Ruan, Y.; Ma, B.; Shang, S.; Himmel, M.E.; Beckham, G.T.; Longand, H.; Tan, Z. Carbohydrate-binding module *O*-mannosylation alters binding selectivity to cellulose and lignin. *Chem. Sci.* **2020**, *11*, 9262–9271. [CrossRef] [PubMed]
3. Chowdury, Z.Z.; Hamid, S.B.A. Preparation and Characteriazation of Nanocrystalline Cellulose using ultrasonication combined with a microwave-assisted pretreatment process. *Bioresources* **2016**, *11*, 3397–3415.
4. Rotaru, R.; Savin, M.; Tudorachi, N.; Peptu, C.; Samoila, P.; Sacarescu, L.; Harabagiu, V. Ferromagnetic iron oxide–cellulose nanocomposites prepared by ultrasonication. *Polym. Chem.* **2018**, *9*, 860–868.
5. Li, Y.; Wang, J.; Liu, X.; Zhang, S. Towards a molecular understanding of cellulose dissolution in ionic liquids: Anion/cation effect, synergistic mechanism and physicochemical aspects. *Chem. Sci.* **2018**, *9*, 4027–4043. [CrossRef]
6. Spiridon, I.; Teaca, C.A.; Bodirlau, R. Structural changes evidenced by FTIR Spectroscopy in cellulosic materials after pre-treatment with ionic liquid and enzimatic hydrolysis. *Bioresources* **2010**, *6*, 400–413. [CrossRef]
7. Peng, B.L.; Dhar, N.; Liu, H.L.; Tam, K.C. Chemistry and applications of nanocrystalline cellulose and its derivatives: A nanotechnology perspective. *J. Chem. Eng.* **2011**, *9999*, 1–16. [CrossRef]
8. de Oliveira, H.F.N.; Farès, C.; Rinaldi, R. Beyond a solvent: The roles of 1-butyl-3-methylimidazolium chloride in the acid-catalysis for cellulose depolymerization. *Chem. Sci.* **2015**, *6*, 5215–5224. [CrossRef]
9. Chen, W.; Yu, H.; Liu, Y.; Hai, Y.; Zhang, M.; Chen, P. Isolation and characterization of cellulose nanofibers from four plant cellulose fibers using a chemical-ultrasonic process. *Cellulose* **2011**, *18*, 433–442. [CrossRef]
10. Li, X.F.; Ding, E.Y.; Li, G.K. A method of preparing spherical nano-crystal cellulose with mixed cryslalline forms of cellulose I and II. *J. Polym. Sci.* **2001**, *19*, 291–296.
11. Li, W.; Yue, J.; Liu, S. Preparation of nanocrystalline cellulose via ultrasound and its reinforcement capability for poly(vinyl alcohol) composites. *Ultrason. Sonochem.* **2012**, *19*, 479–485. [CrossRef] [PubMed]
12. Frone, A.N.; Panaitescu, D.M.; Donescu, D.; Spataru, C.I.; Radovici, C.; Trusca, R.; Somoghi, R. Preparation and characterization of pva composites with celluose nanofibers obtained by ultrasonication. *Bioresources* **2011**, *6*, 487–512. [CrossRef]
13. Chen, W.; Yu, H.; Liu, Y.; Chen, P.; Zhang, M.; Hai, Y. Individualization of cellulose nanofibers from wood using high-intensity ultrasonication combined with chemical pretreatments. *Carbohydr. Polym.* **2011**, *83*, 1804–1811. [CrossRef]
14. Parveen, S.; Rana, S.; Ferreira, S.; Filho, A.; Fangueiro, R. Ultrasonic dispersion of micro crystalline cellulose for developing cementitious composites with excellent strength and stiffness. *Ind. Crops Prod.* **2018**, *122*, 156–165. [CrossRef]
15. Girard, M.; Vidal, D.; Bertrand, F.; Tavares, J.R.; Heuzey, M.C. Ultrason. Evidence-based guidelines for the ultrasonic dispersion of cellulose nanocrystals. *Ultrason. Sonochem.* **2021**, *71*, 105378. [CrossRef] [PubMed]
16. Barbosa, A.M.; Robles, E.; Ribeiro, J.S.; Lund, R.G.; Neftali, L.V.C.; Labidi, J. Cellulose nanocrystal membranes as excipients for drug delivery systems. *Materials* **2016**, *9*, 1002. [CrossRef]

17. Wong, S.; Kasapis, S.S.; Huang, D. Molecular weight and crystallinity alteration of cellulose via prolonged ultrasound fragmentation. *Food Hydrocoll.* **2012**, *26*, 365–369. [CrossRef]
18. Sun, B.; Zhang, M.; Shen, J.; He, Z.; Fatehi, P.; Ni, Y. Applications of cellulose-based materials in sustained drug delivery systems. *Curr. Med. Chem.* **2019**, *26*, 2485–2501. [CrossRef]
19. Rotaru, R.; Popescu, C.M.; Dascalu, A.; Timpu, D.; Asandulesa, M.; Fortuna, M.E.; Harabagiu, V. Influence of Ultrasonic Treatment and Heating/Cooling Under Electric Field on High-K Cellulose-Barium Titanate Composites. *Rev. Roum. Chim.* **2023**, *68*, 173–183. [CrossRef]
20. Ciolacu, D.; Chiriac, A.I.; Pastor, F.I.J.; Kokol, V. The influence of supramolecular structure of cellulose allomorphs on the interactions with cellulose-binding domain, CBD3d from *Paenibacilus barcinonensis*. *Bioresour. Technol.* **2014**, *157*, 14–21. [CrossRef] [PubMed]
21. Poletto, M.; Ornaghi Júnior, H.L.; Zattera, A.J. Native Cellulose: Structure, characterization and thermal properties. *Materials* **2014**, *7*, 6105–6119. [CrossRef] [PubMed]
22. Pimentel, G.C.; Sederholm, C.H.J. Correlation of infrared stretching frequencies and hydrogen bond distances in crystals. *Chem. Phys.* **1956**, *24*, 639–641. [CrossRef]
23. Segal, L.; Creely, J.J.; Martin, A.E., Jr.; Conrad, G.M. An empirical method for estimating the degree of crystallinity of native cellulose using the X-ray diffractometer. *CM Tex. Res. J.* **1959**, *29*, 786–794. [CrossRef]
24. Terinte, N.; Ibbett, R.; Schuster, K.C. Overviewon native cellulose and microcrystalline cellulose i structure studied by X-ray diffraction (WAXD): Comparison between measurement techniques. *Lenzinger Berichte* **2011**, *89*, 118–131.
25. Oh, S.Y.; Yoo, D.I.; Shin, Y.; Kim, H.C.; Kim, H.Y.; Chung, Y.S.; Park, W.H.; Youk, J.H. Crystalline structure analysis of cellulose treated with sodium hydroxide and carbon dioxide by means of X-ray diffraction and FTIR spectroscopy. *Carbohydr. Res.* **2005**, *340*, 2376–2391. [CrossRef] [PubMed]
26. Barzic, A.I.; Soroceanu, M.; Rotaru, R.; Doroftei, F.; Asandulesa, M.; Tugui, C.; Dascalu, I.A.; Harabagiu, V. Cellulose derivative/barium titanate composites with high refractive index, conductivity and energy density. *Cellulose* **2022**, *29*, 873–878. [CrossRef]
27. Markovic, S.; Mitric, M.; Starcevic, G.; Uskokovic, D. Ultrasonic de-agglomeration of barium titanate powder. *Ultrason. Sonochem.* **2008**, *15*, 16–20. [CrossRef] [PubMed]
28. Santos, H.M.; Lodeiro, C.; Capelo-Martinez, J.L. *Ultrasound in Chemistry: Analytical Applications, Chapter 1.3.2.3 Dead Zones*; Capelo-Martínez, J.-L., Ed.; WILEY-VCH Verlag GmbH & Co. KGaA: Weinheim, Germany, 2009; ISBN 978-3-527-31934-3.
29. SriBala, G.; Chennuru, R.; Mahapatra, S.; Vinu, R. Effect of alkaline ultrasonic pretreatment on crystalline morphology and enzymatic hydrolysis of cellulose. *Cellulose* **2016**, *23*, 1725–1740. [CrossRef]
30. Sumari, S.; Roesyadi, A.; Sumarno, S. Effects of ultrasound on the morphology, particle size, crystallinity, and crystallite size of cellulose. *Sci. Study Res. Chem. Chem. Eng.* **2013**, *14*, 229–239.

crystals

MDPI

Article

Adsorption of Ni(II) from Aqueous Media on Biodegradable Natural Polymers—Sarkanda Grass Lignin

Elena Ungureanu [1], Costel Samuil [1], Denis C. Țopa [1], Ovidiu C. Ungureanu [2], Bogdan-Marian Tofanică [3], Maria E. Fortună [4,*] and Carmen O. Brezuleanu [1,*]

[1] "Ion Ionescu de la Brad" Iasi University of Life Sciences, 3 Mihail Sadoveanu Alley, 700490 Iasi, Romania; elena.ungureanu@iuls.ro (E.U.); costel.samuil@iuls.ro (C.S.); denis.topa@iuls.ro (D.C.Ț.)
[2] "Vasile Goldis" Western University of Arad, 94 the Boulevard of the Revolution, 310025 Arad, Romania; ungureanu.ovidiu@uvvg.ro
[3] "Gheorghe Asachi" Technical University of Iasi, 73 Prof. Dr. Docent Dimitrie Mangeron Blv., 700050 Iasi, Romania; b.m.tofanica@gmail.com
[4] "Petru Poni" Institute of Macromolecular Chemistry, 41A Grigore Ghica Voda Alley, 700487 Iasi, Romania
* Correspondence: fortuna.maria@icmpp.ro (M.E.F.); olguta.brezuleanu@iuls.ro (C.O.B.)

Abstract: Heavy metals are pollutants that pose a risk to living systems due to their high toxicity and ability to accumulate and contaminate. This study proposes an alternative approach to the static adsorption of Ni(II) from aqueous media using Sarkanda grass lignin crystals, the non-cellulosic aromatic component of biomass, as an adsorbent substrate. To determine the best experimental conditions, we conducted tests on several parameters, including the initial and adsorbent solution pH, the concentration of Ni(II) in the aqueous solution, the amount of adsorbent used, and the contact time at the interface. The lignin's adsorption capacity was evaluated using the Freundlich and Langmuir models to establish equilibrium conditions. The Lagergren I and Ho–McKay II kinetic models were used to determine the adsorption mechanism based on surface analyses and biological parameters such as the number of germinated seeds, energy, and germination capacity in wheat caryopses (variety *Glosa*) incorporated in the contaminated lignin and in the filtrates resulting from phase separation. The results suggest that Sarkanda grass lignin is effective in adsorbing Ni(II) from aqueous media, particularly in terms of adsorbent/adsorbate dosage and interfacial contact time.

Keywords: adsorption; Ni(II) ions; Sarkanda grass lignin; pollution; germination

Citation: Ungureanu, E.; Samuil, C.; Țopa, D.C.; Ungureanu, O.C.; Tofanică, B.-M.; Fortună, M.E. Adsorption of Ni(II) from Aqueous Media on Biodegradable Natural Polymers—Sarkanda Grass Lignin. *Crystals* **2024**, *14*, 381. https://doi.org/10.3390/cryst14040381

Academic Editor: Pedro De Almeida

Received: 27 March 2024
Revised: 11 April 2024
Accepted: 16 April 2024
Published: 18 April 2024

1. Introduction

Although the negative impact of metal ions, such as Ni(II), Co(II), Cu(II), or Zn(II), on quality of life is well known, they are still widely used in many technological processes [1]. As a result, these ions are present in significant concentrations in aqueous effluents that are discharged into the environment, leading to long-term pollution [2]. The detection and analysis of such pollutants is crucial since heavy metals cannot be destroyed or degraded and tend to accumulate over time [3,4].

The elevated levels of nickel in nature have led to human pollution. This is evident in various sources such as glass, ceramic, and textile dyes, nickel-plated faucets, nickel–steel alloy tableware, and cigarette smoke [5]. Plants can act as biosorbers for heavy metals, including nickel, by absorbing them from the soil or through their aerial parts. While nickel is essential for plant metabolism, high concentrations can be dangerous for most plants [6–9]. Nickel has serious toxic potential in its gaseous form, nickel tetracarbonyl, which is considered responsible for the slow development of malignant formations [10]. Additionally, insoluble nickel oxide powders and soluble sulfate, nitrate, and chloride aerosols are also considered potential carcinogens [11–13]. To reduce pollution, it is necessary to not only decrease the amount of pollutants in the air, water, and soil but also

explore options for recovering waste from industrial activities. The literature suggests various alternatives, including the use of low-cost materials such as cellulosic and lignin biomass fractions for different purposes, as adsorbent materials for the retention of pollutant species [14–20], in gasification processes; as precursors in organic syntheses [21]; or as biocyde substances for the preservation of natural composite structures [22].

Lignin is a macromolecular compound with an aromatic structure and is the main component of biomass. It is produced worldwide in large quantities as a by-product/residue from pulp manufacturing or biomass hydrolysis technologies. Its potential for valorization is a real challenge at present [23], considering its origin from renewable resources, non-toxicity, and economic benefits due to its relatively low cost [24]. Lignin's porous and branched structure, high functional group content, and small, uniformly distributed active centers on its surface enable it to complex with polluting species, such as heavy metal ions, through ionic exchange. This facilitates the formation of stable donor–acceptor and ligno-complex bonds [25,26]. As a result, different types of lignins have been tested as substrates for heavy metal ion adsorption [15,18–21,27].

Adsorption processes are evaluated by obtaining adsorption isotherms, which are then interpreted using mathematical models. The most commonly used models are Freundlich and Langmuir [28,29]. These models indicate the mass of the solute retained by a given adsorbent under specific experimental conditions, such as the initial pH of the aqueous solution, sorbent dosage, initial concentration of the metal ion, and contact time between the two phases [20,30]. Studies on the kinetics of the adsorption process provide information on its mechanism [2,21]. However, the adsorption kinetics depend on both the adsorption process and the solute diffusion from the solution to the active centers on the adsorbent surface, and the level of relative humidity [31]. The two most commonly used kinetic models for approximating the mechanism of pollutant adsorption from aqueous solutions are the first-order Lagergren kinetic model and the second-order Ho–McKay kinetic model [20,32,33].

In this study, we evaluate the adsorption of Ni(II) from aqueous media under static conditions using Sarkanda grass lignin as the adsorption substrate. The evaluation is based on thermodynamic, kinetic, and biological parameters. Sarkanda grass lignin is a renewable, cheap, and non-toxic resource that shows promise as a future biosorbent, as supported by the experimental data obtained.

2. Materials and Methods

2.1. Materials

Main chemical materials: Unmodified Sarkanda grass lignin supplied by Granit Récherche Development S.A., Lausanne, Switzerland [20], and $NiSO_4 \cdot 6H_2O$ supplied by ChimReactiv S.R.L., Bucharest, Romania.

Biological material: Autumn wheat seeds *(Glosa*), a variety resistant to drought, overwintering, shattering, and current varieties of yellow rust, recommended for cultivation in southeastern Romania [34], offered by "Ion Ionescu de la Brad", Iasi University of Life Sciences, Iasi, Romania. The seeds used in the experiments were harvested in 2023. The gluten content was 23.2%, protein content was 12.8%, lipid content was 1.14%, the hectoliter mass was 76 Kg, and the mass of 1000 grains (MMB) was 41.8 g.

2.2. Experimental Procedure

2.2.1. Adsorption Experiments

To determine the optimal conditions for adsorption efficiency, we conducted preliminary experimental tests on initial Ni(II) concentrations, initial solution pH, adsorbent dosages, and contact times between the two phases. We chose to use 5 g of lignin per liter of the Ni(II) aqueous solution to ensure an adequate number of adsorption centers, considering the limited number of active centers in the lignin structure [20].

The carboxyl and hydroxyl functional groups on the lignin surface can deprotonate and associate via a Ni^{2+} donor–acceptor bond in the aqueous solution, re-emerging as ligno-complexes. Following experimental trials, a pH value of 5 was chosen, with a moderate/low acid medium proving to be suitable in other systems, such as lignin–Pb(II)/Zn(II)/As(III)/Cd(II) [18–20].

Metal ion stock solutions were prepared by dissolving $NiSO_4$-$6H_2O$ in distilled water to a concentration of 0.001 mg/L. Working solutions were then created by diluting a precisely measured volume of the stock solutions with distilled water. The concentrations of the metal ions in the resulting aqueous solutions are as follows: 5.8693, 11.738, 17.6079, 23.4772, 29.3465, 35.2158, 41.0851, 46.9544, 52.8237, and 58.693 mg/mL. A 20 mL volume of $NiSO_4$-$6H_2O$, with the concentrations mentioned above, was added to the lignin powder. The samples were then left to stand under laboratory conditions for different contact times (30, 60, and 90 min) to reach a steady state. This allowed for the optimal retention time of Ni^{2+} to be captured and for the kinetics of the process to be interpreted.

2.2.2. Germination Experiments

The effectiveness of lignin in adsorbing Ni(II) was also tested in a laboratory setting by evaluating the germination capacity of *Glosa* wheat seeds in three replicates, both on contaminated lignin and on filtrates. The biological process, expressed by germination energy and germination capacity, was monitored for 7 days. Distilled water was used as a control sample for filtrates, and an uncontaminated adsorbent was used for contaminated lignin.

2.3. Characterization Methods

2.3.1. Spectrophotometric Determination of Ni(II)

For determining the concentration of Ni(II), rubeanic acid was used, with maximum absorption at 590 nm. The rubeanic acid solution was obtained by dissolving 0.05 g of a solid reagent in 100 mL of 96% ethanol [1].

The quantitative determination of the metal ion obtained after filtration from the aqueous solutions was carried out by an analysis of an exactly measured volume (2 mL) according to the experimental procedure, and the concentration value for each sample was calculated from the regression equation of the calibration curve.

For the spectrophotometric analysis, we used a Visible Spectrophotometer for a laboratory, model VS-721N, 300–1000 nm, manufacturer JKI, Shanghai, China.

2.3.2. Isotherm Models

Adsorption isotherms characterize the interaction between the adsorbent and the adsorbate. They are interpreted using mathematical models, such as Freundlich or Langmuir, which are commonly used [35].

The adsorption capacities were determined according to the following equation [36]:

$$q = (c_i - c_e)V/m, \text{ (mg/g)} \quad (1)$$

where c_i is the initial concentration (mg/mL), c_e is the equilibrium concentration (mg/L), V is the volume of the metal ion solution (L), m is the mass of the adsorbent (g).

The Langmuir–Freundlich isotherm includes the knowledge of adsorption heterogeneous surfaces, such as the lignin surface. It describes the distribution of adsorption energy onto the heterogeneous surface of the adsorbent [37].

The Langmuir equation can be written in the following linear form [38]:

$$c_e/q_e = 1/q_m \cdot k_L + c_e/q_m \quad (2)$$

where q_e is the amount of metal ions adsorbed per unit of mass of the adsorbent (mg/g) at equilibrium, q_m is the maximum amount of metal ions retained on the absorbent after

saturation (mg/g), K_L is the Langmuir constant (L/mg), c_e is the equilibrium concentration of metal ions in the solution (mg/L).

The linear form of the Freundlich isotherm is as follows [39]:

$$\log q_e = \log k_F + 1/n \cdot \log c_e \quad (3)$$

where q_e is the amount of metal ions adsorbed per unit of mass of the adsorbent (mg/g) at equilibrium, K_F is the Freundlich constant (L/mg), n is the constant characterizing the affinity of metal ions to the adsorbent, c_e is the concentration at equilibrium of metal ions in the solution (mg/L).

The model that best reproduces the experimental isotherm data is selected based on the correlation coefficient R^2 values calculated using the method of least squares [35].

2.3.3. Kinetics Modeling

By kinetic modeling, the solute uptake rate is described, which in turn controls the residence time of sorbate uptake at the solid–solution interface [40]. For this purpose, the first-order Lagergren model and the second-order Ho–McKay model are frequently used, which can be applied to many different systems with different underlying mechanisms [41].

The Lagergren model is a mathematical representation of liquid–solid adsorption [42]:

$$\ln [q_e/(q_e - q)] = k_1 \cdot t \quad (4)$$

Most of the kinetic adsorption can be modeled well by the Ho–McKay model, thus indicating its superiority over other models [42]. Mathematically, it is expressed through the following relationship [41]:

$$t/q_t = (1/k_2 \cdot q_e^2) + t/q_e \quad (5)$$

where k_1 and k_2 are constant adsorption rates for model 1 and 2; q_e and q_t represent the adsorption capacity at equilibrium and at time t, respectively.

The experimental results were verified using the most suitable kinetic model chosen through linear regression.

2.3.4. Biological Stability

Germination tests were conducted on three batches of 20 wheat seeds (variety *Glosa*) under laboratory conditions with a temperature of 24 °C ± 1 and an illumination regime of 16 h light/8 h dark. Prior to testing, the seeds were disinfected with 5% sodium hypochlorite for 5 min and washed three times with MilliQ ultrapure water until the characteristic odor disappeared [43]. Wheat kernels were soaked in a filtrate or distilled water for one hour in 180 × 18 mm test tubes with intermittent shaking. The soaked seeds were then evenly distributed in 90 × 15 cm Petri dishes, each with two rounds of overlapping filter paper [20]. The toxicity of the filtrates and lignin contaminated with aqueous nickel solutions was analyzed at concentrations ranging from 5.8693 to 58.693 mg/mL and at three different contact times between phases. By using formulae (6) and (7), the germination energy and germination faculty can be determined within 30, 60, and 90 min [20,34]:

$$E_g = (a/n) \cdot 100 \quad (6)$$

$$F_g = (b/n) \cdot 100 \quad (7)$$

where a is the number of seeds germinated after three days, n is the total number of seeds analyzed, b is the number of seeds germinated at the end of the period (seven days).

Distilled water was used as a control sample for filtrates and uninfected lignin was used for contaminated lignin. It is worth mentioning that swollen, rotten, or moldy seeds at the end of the germination period were considered non-germinated.

2.3.5. Surface Morphology

Scanning electron microscopy (SEM) can be considered an efficient analysis method for organic and inorganic materials on the nanometer to micrometer (μm) scale. Energy dispersive radiography spectroscopy (EDS) provides fundamental qualitative and semi-quantitative results on the material and the species in its composition, which cannot be provided by common laboratory tests [44].

The SEM analysis was performed using the Quanta 200 scanning electron microscope (5 kV) equipped with an EDX elemental analysis system (Ametek, Berwyn, PA, USA). Quanta 200 SEM is a high-resolution environmental microscope (ESEM) capable of operating in high vacuum, variable pressure, and environmental modes. The specimens used were uncoated and untreated. The X-ray spectrometer was also utilized for element detection and spectral imaging.

3. Results and Discussion

3.1. Evaluation of Ni(II) Adsorption Efficiency on Sarkanda Grass Lignin through Analysis of Experimental Parameters Analyzed

3.1.1. Lignin Dose

The amount of adsorbent used affects adsorption and can provide valuable insights into the adsorption capacity of a material. This is primarily due to the availability of binding sites for removing a pollutant species at a specific concentration [16]. Preliminary tests were conducted to determine the optimal experimental conditions. The range of 4–40 g lignin/L Ni(II) aqueous solution, as proposed by study [21], was used. The results indicate that the ideal dose of lignin in Sarkanda grass should be 5 g/L Ni(II) aqueous solution, as seen in Figure 1.

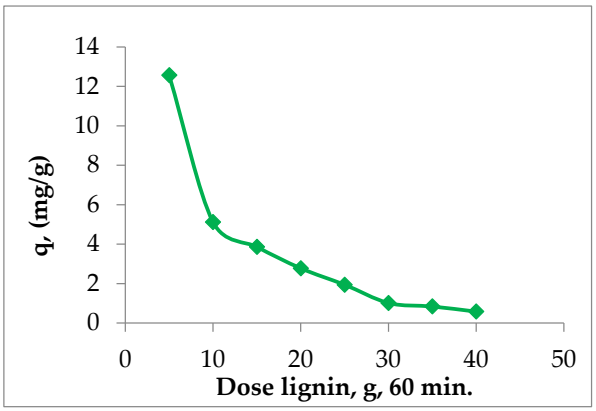

Figure 1. The influence of the Sarkanda grass lignin dose on the efficiency of the Ni(II) adsorption in a concentration of 58.693 mg/L, contact time of 60 min, pH of 5.

Figure 1 shows that increasing the lignin dose does not increase the adsorption rate, but instead decreases the amount of Ni(II) retained per unit mass of the adsorbent. This can be explained by the affinity between the functional groups on the surface of Sarkanda grass lignin and Ni(II), and possible complexation at adsorption initiation, after which the adsorbent pores become inaccessible. It is probable that saturation has been reached and that most of the functional groups in the lignin have been occupied, hindering the diffusion of Ni(II) to any unreacted (free) functional groups within the lignin.

3.1.2. Initial Concentration of Ni(II)

The concentration-dependent increase in Ni(II) resulted in a corresponding increase in the adsorption capacity of lignin. Specifically, the adsorption capacity increased from 1.2984 mg/g at a concentration of 5.86 mg/L to 12.5601 mg/g at a concentration of 58.69

mg/L after a contact time of 60 min (Figure 2). This increase can be attributed to the higher ratio between the initial number of Ni(II) moles and the number of accessible adsorption positions on the lignin fraction.

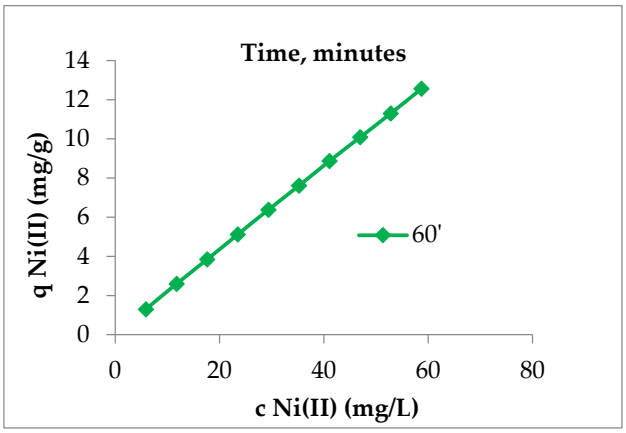

Figure 2. The adsorption capacity of the Sarkanda grass lignin, contact time of 60 min, pH of 5.

3.1.3. Contact Time

According to the literature, it is recommended that the contact time between phases be extended to capture crucial information about interfacial dynamics and the equilibrium [15]. The experimental data demonstrate that an increase in the contact time between the Sarkanda grass lignin and aqueous nickel solution results in a greater amount of the retained methyl–alkyl ion. This effect is more pronounced in the initial stage, after which the process slows down. The maximum amount is reached at 60 min, which can be considered the optimal time for achieving equilibrium (Figure 3). The 90 min contact time was excluded as there were no significant differences in adsorption capacity compared to the values recorded at 60 min.

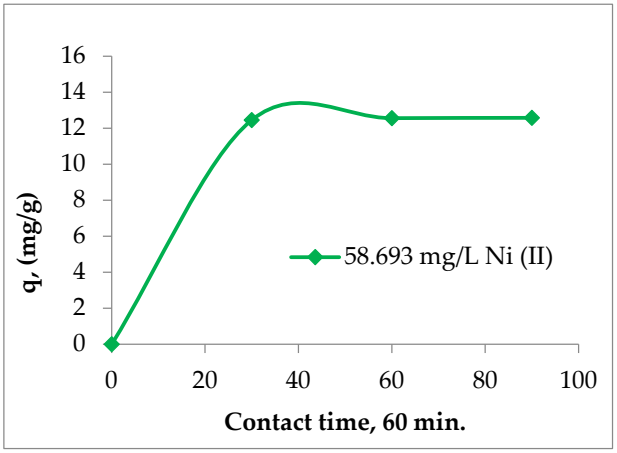

Figure 3. The influence of contact time on the adsorption of initial Ni(II) concentrations' solution on Sarkanda grass lignin.

3.1.4. pH Initial Solution

Figure 4 shows that the degree of lignin adsorption for Ni(II) increases as the initial pH of the solution increases. This is likely due to the deprotonation of functional groups on the lignin surface, which acquire a negative charge and can bind Ni(II) from the aqueous medium.

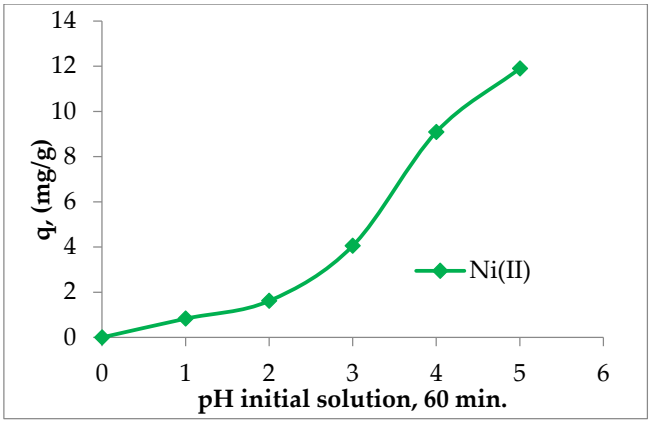

Figure 4. The influence of the pH of the initial solution on Ni(II) adsorption on Sarkanda grass lignin.

It is not recommended to use strongly acidic environments as the excess of protons can compete with nickel ions for the binding sites on lignin. Similarly, in alkaline environments, there is a possibility of the precipitation of Ni(II) in the form of an hydroxide, which reduces the efficiency of adsorption [2]. Based on the preliminary tests conducted on the adsorption of Ni(II) on Sarkanda grass lignin, it is recommended to use an optimal pH of 5. This is because the highest adsorption capacity values were obtained at this pH level.

3.2. Ni(II) Adsorption Efficiency on Sarkanda Grass Lignin Evaluated by Adsorption Isotherms

The adsorption isotherms obtained from the experiment provide valuable information about the interaction between the phases involved in adsorption [35]. These isotherms can be interpreted using mathematical models such as the Freundlich model, which can estimate adsorption on heterogeneous surfaces in a single or multiple layers, and the Langmuir model, which can describe retention in a single layer on a homogeneous surface [36].

The correlation coefficients (R^2) were calculated from the regression equations resulting from the linear representation of each individual model. Based on these coefficients, the most appropriate model can be chosen to describe the adsorption. Figure 5a,b display the linear representation of the Freundlich and Langmuir models for Ni(II) adsorption from aqueous media on Sarkanda grass lignin under optimal experimental conditions (temperature: 24 ± 0.5 °C, contact time: 60 min, pH 5). Table 1 presents the characteristic parameters of the Freundlich (R^2, 1/n, k_F) and Langmuir (R^2, q_m, K_L) models under the same working conditions.

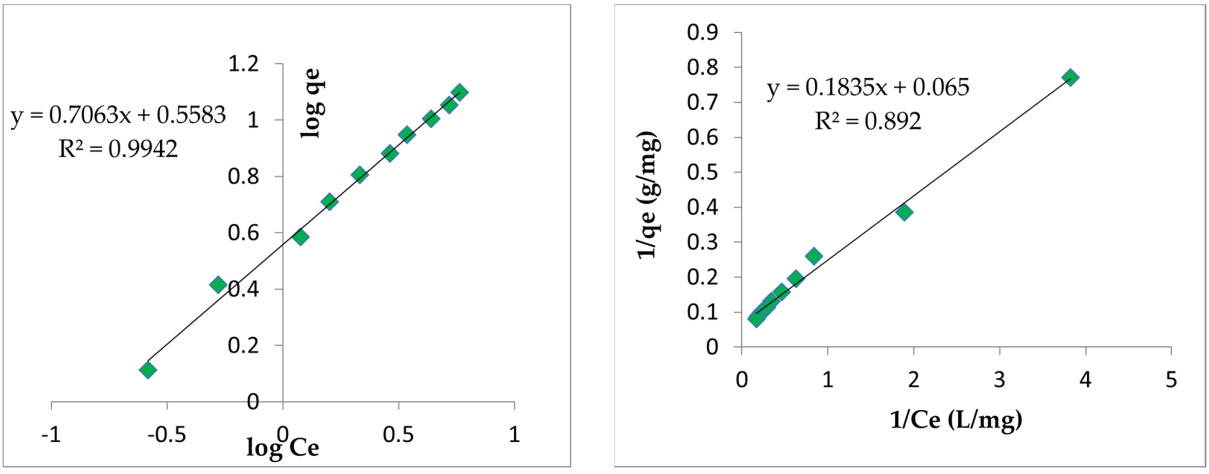

(**a**) (**b**)

Figure 5. Freundlich adsorption model (**a**) and Langmuir adsorption model (**b**) for Ni(II) adsorption onto Sarkanda grass lignin after 60 min.

Table 1. Characteristic parameters of Freundlich and Langmuir models for Ni(II) adsorption on Sarkanda grass lignin.

Pollutant	Time (min)	Freundlich Model			Langmuir Model		
		R^2	1/n	k_F	R^2	q_m (mg/g)	K_L
Ni(II)	30	0.9822	0.9028	2.1586	0.9179	12.4073	0.0801
	60	0.9942	0.9205	2.0075	0.8920	12.5206	0.0795
	90	0.9844	0.9994	1.9776	0.7766	12.5398	0.0794

The correlation coefficients (R^2) obtained for the Langmuir model range from 0.7766 to 0.9179, slightly lower than those obtained for the Freundlich model, which range from 0.9822 to 0.9942 (Table 1). This suggests that the Freundlich model better describes the Ni(II) adsorption process on Sarkanda grass lignin. It is important to note that all evaluations are objective and based solely on the experimental data.

According to the literature, the Freundlich model is recommended for adsorption on heterogeneous surfaces or those composed of functional groups with different affinities for a given metal ion [40]. The low values of K_L, 0.0794–0.0801, suggest that the surface of Sarkanda grass lignin is not perfectly homogeneous, and therefore Ni(II) retention is not in the monolayer. Furthermore, it is important to note that the intensity of interactions between Ni(II) in the aqueous medium and the functional groups of lignin increases with higher values of KF and 1/n, as stated in references [20,40].

The analysis of the data presented in Table 1 shows that the values of K_F are in the range 1.9776–2.1586, and those of 1/n are in the range of 0.9028–0.9994. This suggests the occurrence of binding energy by adsorption due to ion-exchange interactions or surface complexation. However, it is unclear whether physical or chemical adsorption predominates, requiring a kinetic approach.

3.3. Efficiency Evaluation of Ni(II) Adsorption on Sarkanda Grass Lignin through Kinetic Modeling

To interpret the kinetics of Ni(II) adsorption on Sarkanda grass lignin, two mathematical models were employed: the pseudo-I-order Lagergren model, specific to liquid–solid adsorption, and the pseudo-II-order Ho and McKay model, which indicates the adsorption capacity of the solid phase. These models are known to accurately represent the adsorption processes according to study [45].

Figure 6a,b demonstrate the linear dependence for the Lagergren model of order I and the Ho–McKay model of order II for Ni(II) adsorption from aqueous media on Sarkanda grass lignin at an initial normalized concentration of 100 mg/mL. Table 2 presents the characteristic kinetic parameters calculated from the slopes and the intercept with the ordinate of the linear dependencies obtained for each kinetic model. The correlation coefficients (R^2) were obtained by linear regression.

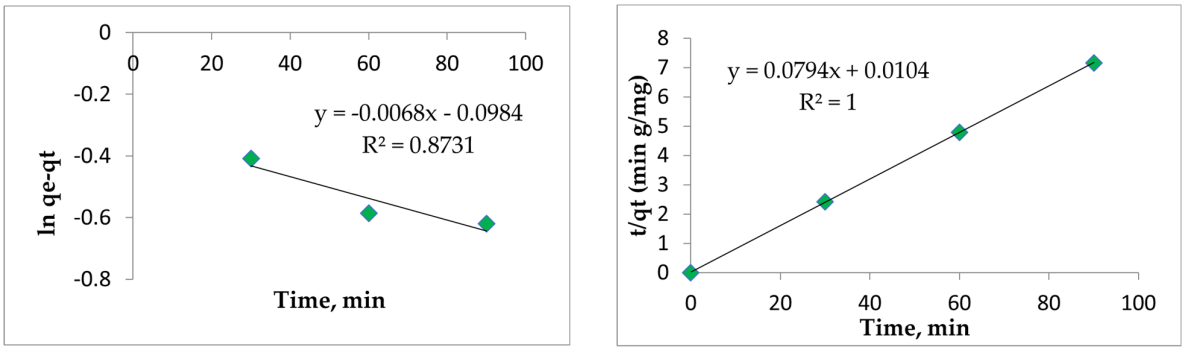

Figure 6. The linear representation of the Lagergren pseudo-I-order model (**a**) and Ho–McKay pseudo-II-order model (**b**) for the adsorption of Ni (II) onto Sarkanda grass lignin after 60 min.

Table 2. Kinetic parameters of the Lagergren and Ho–McKay models for Ni(II) adsorption on Sarkanda grass lignin.

Pollutant	c_i (mg/mL)	Lagergren Model			Ho–McKay Model		
		R^2	q_e (mg/g)	K_1 (min^{-1})	R^2	q_e (mg/g)	K_2 (g/mg·min)
Ni(II)	10	0.7903	1.1235	−0.0019	1	0.9421	1.2245
	20	0.7312	1.1643	−0.0016	1	5.5079	2.3469
	30	0.7759	4.1903	−0.0017	1	3.4399	4.1903
	40	0.6170	4.4132	−0.0021	1	6.1278	2.4210
	50	0.7052	5.4321	−0.0019	1	7.9889	2.9563
	60	0.8596	6.0234	−0.0017	1	8.8834	2.4369
	70	0.8477	7.2134	−0.0020	1	9.8973	1.8561
	80	0.7606	7.8321	−0.0020	1	10.0023	4.7597
	90	0.7697	8.0251	−0.0018	1	10.8250	2.8646
	100	0.8731	8.3267	−0.0019	1	10.6879	2.5011

The correlation coefficients (R^2) for the pseudo-I-order Lagergren kinetic model range from 0.6170 to 0.8731 (Table 2). These values are below 0.9, indicating the presence of electrostatic interactions between Ni(II) and the functional groups on the lignin surface. This suggests chemosorption rather than physical adsorption, which cannot be explained by the Lagergren model. Furthermore, the subunit values of R^2 restrict the applicability of this model for interpreting the kinetics of Ni(II) ion adsorption from aqueous media on Sarkanda grass lignin. This is consistent with previous research [18–20].

After processing the experimental data using the pseudo-second-order Ho–McKay kinetic model, the correlation coefficients (R^2) showed a value of 1 in all cases (Table 2). The other parameters, q_e and K_2, indicated a strong affinity of Ni(II) as a pollutant with Sarkanda grass lignin, which serves as a retention support. It is becoming more likely that the adsorption is active due to the presence of lignin's functional groups, which can bond covalently and coordinatively with the metal ion to form a complex.

Ni(II) adsorption on Sarkanda grass lignin follows the Ho–McKay kinetic model of the pseudo II order. The rate-determining step of the adsorption process is the chemical interaction between the nickel ion in the aqueous medium and the functional groups of the biopolymer, particularly the carboxyl and hydroxyl groups.

3.4. Efficiency of Ni(II) Adsorption on Sarkanda Grass Lignin Evaluated through Biological Parameters

3.4.1. Number of Germinated Wheat Seeds, *Glosa* Variety

The presence of Ni(II) in the contaminated samples could cause the embryo of the wheat seeds to remain in a non-active or dormant state, disrupting osmotic equilibrium or metabolic functions. This results in an indirect toxic effect on the plants. Therefore, it is necessary to monitor the germination of the wheat caryopsis for seven days, as recommended in [34].

Figure 7a–c display the average number of germinated wheat seeds after three repetitions at 3 days for samples contaminated with Ni(II). The average number of germinated seeds after three repetitions at 3 and 7 days for the filtrates resulting from the retention of Ni(II) at the three contact times between the phases is also shown.

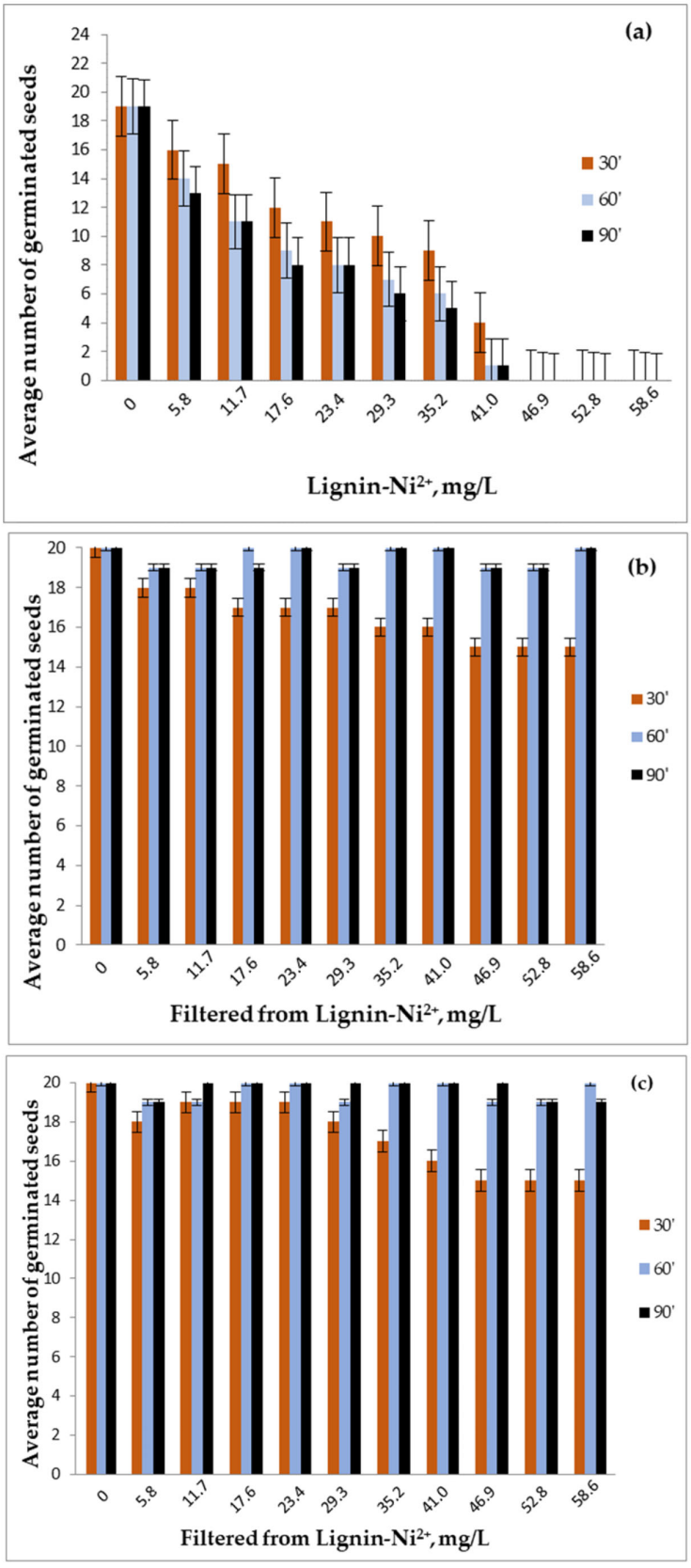

Figure 7. The average number of wheat seeds germinated at 3 days for the contaminated samples (**a**) and for the filtrates resulting from Ni(II) adsorption at 3 days (**b**) and 7 days (**c**).

From the analysis of Figure 7a–c, it is clear that Ni(II) has a negative effect on the germination of wheat caryopses, and this effect is enhanced by increasing the metal ion concentration and the duration of contact between the phases. In the control samples, 19 out of 20 seeds germinated in lignin and all 20 seeds germinated in distilled water. For the filtrates, the number of germinated seeds after 3 days and the number of seedlings after 7 days from germination are similar to those obtained in the control group at 60 and 90 min. However, at 30 min, the numbers are lower, indicating that the adsorption equilibrium is not reached within 30 min. Therefore, a longer contact time is required, which is consistent with the conclusions drawn from the interpretation of the adsorption isotherms and kinetic parameters. The optimal contact time is recommended to be 60 min.

At low Ni(II) concentrations and a contact time of 30 min, the highest number of germinated seeds appeared after 3 days when using contaminated lignin. Starting at a concentration of 35.2158 mg/L, less than half of the total 20 seeds germinated at all contact times. At a concentration of 46.9544 mg/L Ni(II), the seeds did not germinate, highlighting the toxic effect of nickel on seed germination with increasing concentration and duration of contact. Furthermore, after 7 days of germination, none of the contaminated lignin samples resulted in new germinated seeds or surviving seedlings, regardless of the contact times and Ni(II) concentration. This confirms the lignin's effective adsorption capacity for the pollutant species, as demonstrated by the obtained kinetic and chemical equilibrium results.

Figure 8 displays the germination of *Glosa* wheat seeds over seven days for four conditions: reference/uncontaminated lignin (R/UL), lignin contaminated with Ni(II) (CL), reference/distilled water (R/DW), and the filtrate (F) obtained after adsorption for 60 min at a concentration of 58.693 mg/L Ni(II).

3.4.2. Germination Energy and Capacity of Wheat Seeds, *Glosa* Variety

Table 3 shows that germination energy is correlated with the number of germinated seeds for both filtrates and samples of lignin contaminated with Ni(II). After 30 min of contact time between phases, there was no balance of adsorption. As a result, the filtrates were more concentrated, and the germination energy was lower. However, at 60 and 90 min, the germination energy was higher because the filtrates were more diluted due to the good retention capacity of lignin, eventually reaching saturation. In the concentration range of 46.9544–58.693 mg/L Ni^{2+}, an increase in nickel concentration and contact time leads to a decrease in germination energy when contaminated with lignin. At all three contact times, the germination energy has zero values.

In regards to the germinative capacity, filtrates show a proportional variation with the germinative energy, whereas contaminated lignin consistently records zero values. Furthermore, the germination energy and capacity in the filtrate samples were similar to those in the control sample, regardless of the concentration of Ni(II). However, at contact times greater than 30 min, there were negligible differences at 60 and 90 min. This confirms the efficient adsorption of Ni(II) on Sarkanda grass lignin at a contact time of 60 min, which is considered optimal in terms of chemical and kinetic equilibrium results.

The biological tests show that Sarkanda grass lignin is efficient in retaining Ni(II) from an aqueous solution due to the good affinity of the species involved. The evaluation of parameters demonstrates this efficiency.

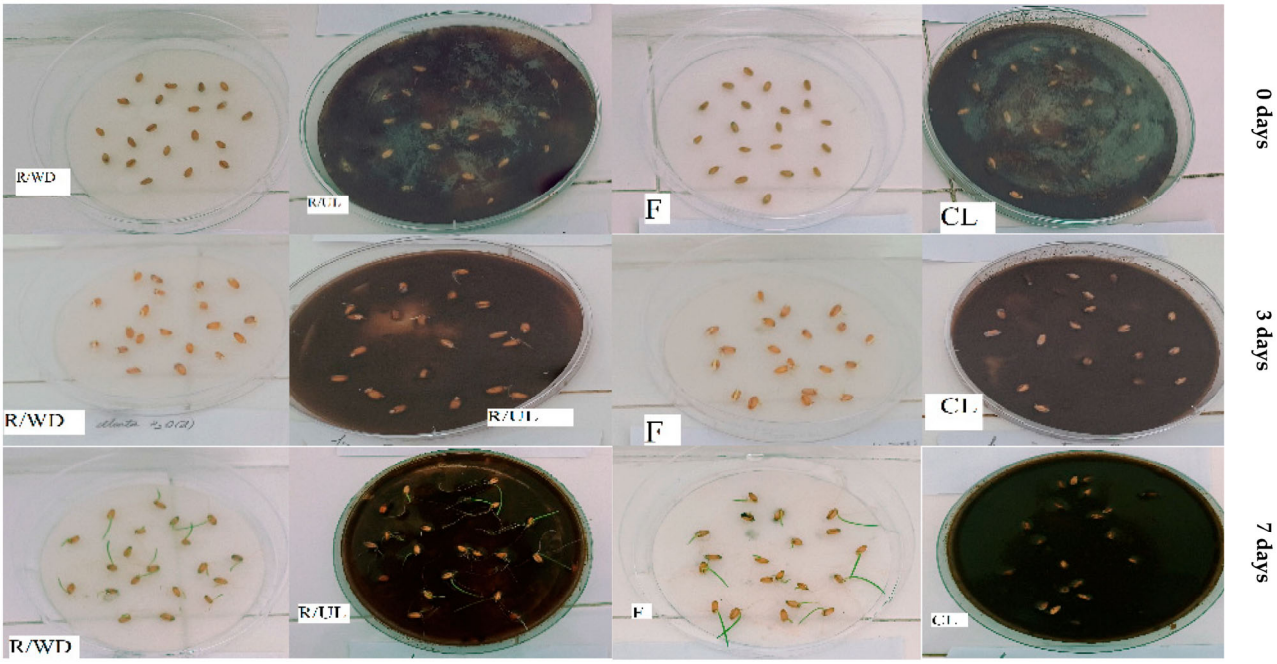

Figure 8. The germination of wheat seeds over a period of 7 days, at an adsorption time of 60 min and a concentration of 58.693 mg/L Ni (II).

Table 3. The germination energy and capacity were measured for contaminated samples and filtrates resulting from Ni (II) retention at three different contact times between the phases. This was repeated three times to obtain an average.

Lignin/Ni(II) (mg/L)	Contact Time (Min)						Lignin/Ni(II) (mg/L) Filtered	Contact Time (Min)					
	30	60	90	30	60	90		30	60	90	30	60	90
	Eg, %			Fg, %				Eg, %			Fg, %		
0	95	95	95	95	95	95	0	100	100	100	100	100	100
5.8693	80	70	65	0	0	0	5.8693	90	95	95	90	95	95
11.738	75	45	40	0	0	0	11.738	90	95	95	95	95	100
17.6079	60	40	40	0	0	0	17.6079	85	100	95	95	100	100
23.4772	55	35	30	0	0	0	23.4772	85	100	100	95	100	100
29.3465	50	30	25	0	0	0	29.3465	85	95	95	90	95	100
35.2158	45	10	10	0	0	0	35.2158	80	100	100	85	100	100
41.0851	20	0	0	0	0	0	41.0851	80	100	100	80	100	100
46.9544	0	0	0	0	0	0	46.9544	75	90	95	75	95	100
52.8237	0	0	0	0	0	0	52.8237	75	90	95	75	95	95
58.693	0	0	0	0	0	0	58.693	75	100	100	75	100	100

3.5. Efficiency of Ni(II) Adsorption on Sarkanda Grass Lignin Evaluated through Surface Analyses

In Figures 9 and 10, the morphology and composition of lignin before the adsorption and after the adsorption of Ni (II) at a concentration of 58.693 mg/L and a contact time of 60 min are presented, which were obtained by scanning electron microscopy (SEM) coupled with X-ray analysis Energy Dispersive X (EDX).

For the SEM analysis, the prepared sample has been metallized with Pt to improve the contrast, thus resulting in Pt in both samples. The SEM micrograph of the uncontaminated lignin clearly shows a well-separated particle agglomeration of approximately a 4 μm length (Figure 9a). The micrometric dimensions of these particles that form aggregates were also confirmed by the diffraction analyzer. It can be seen that the surface morphology of the unmodified lignin was different from the one observed for lignin contaminated

with Ni(II), a fact that confirms the contact between the two phases, the diffusion of the polluting species, and its adsorption in the pores of the lignin polymer (Figure 9b).

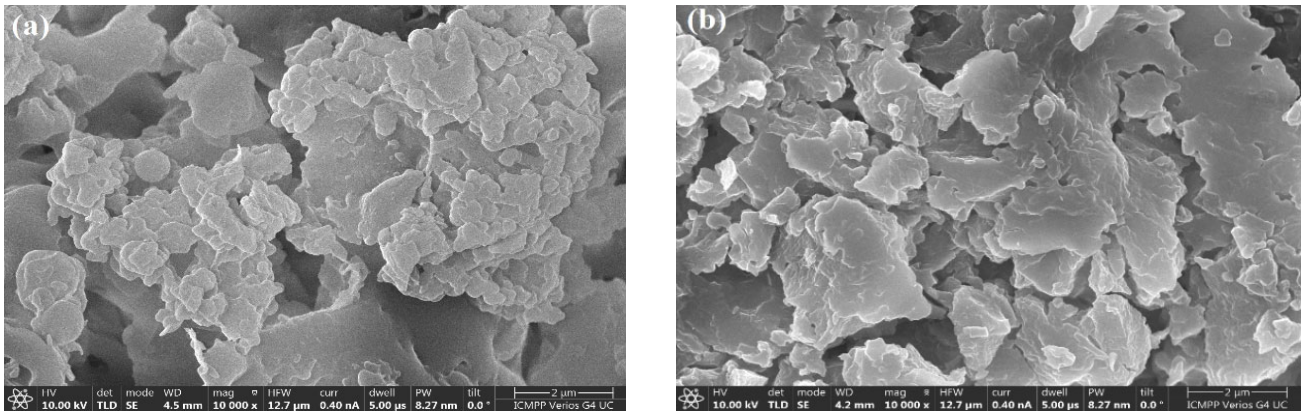

Figure 9. The SEM images for Sarkanda grass lignin before adsorption (**a**) and after Ni(II) adsorption (**b**).

Sarkanda grass lignin composition before and after $NiSO_4$ adsorption was obtained using the EDX analysis. The EDX spectra for the samples are shown in Figure 10a,b, showing the main peaks of C, O, and S elements originating from both samples, and the EDX spectrum for lignin after Ni(II) adsorption clearly shows nickel adsorption.

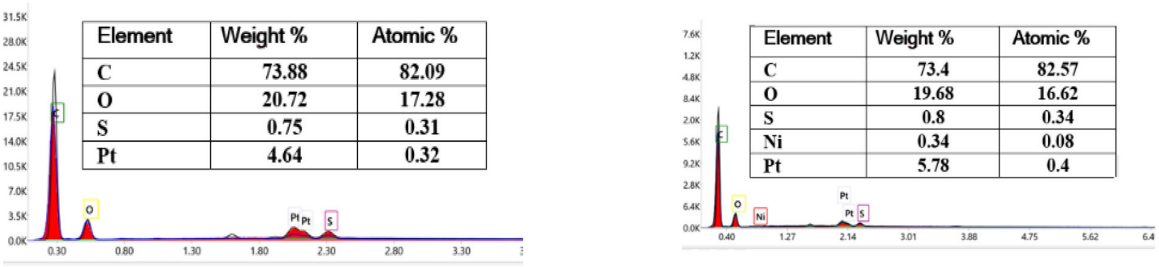

Element	Weight %	Atomic %
C	73.88	82.09
O	20.72	17.28
S	0.75	0.31
Pt	4.64	0.32

Element	Weight %	Atomic %
C	73.4	82.57
O	19.68	16.62
S	0.8	0.34
Ni	0.34	0.08
Pt	5.78	0.4

(**a**) (**b**)

Figure 10. The EDX elemental analysis for lignin before adsorption (**a**) and after Ni(II) adsorption (**b**).

In line with the trend toward sustainable development, bio-based adsorbents—which are abundant, inexpensive, and environmentally friendly—have emerged as potential sustainable alternatives to conventional synthetic adsorbents in the water purification industry. Lignocellulosic systems are highly structured and provide abundant adsorption sites for metal ion uptake thanks to various functional groups, such as hydroxyl (–OH), carboxyl (–COOH), and phenolic (–Ph) groups, that have the ability to form chemical bonds with them. For example [46,47], unmodified cellulose retains 32–40 mg/g of Cd^{2+}, Zn^{2+}, Ni^{2+}, and Pb^{2+} at a contact time of 60 min and pH of 5–7. The same and different untreated agricultural wastes had a similar adsorption capacity of 7–56 mg/g in a similar condition. In earlier research [18–20], Sarkanda grass lignin was capable of retaining an average of 9 mg/g of Zn^{2+}, up to 17 mg/g of Cd^{2+} and As^{3+}, and up to 30 mg/g of Pb^{2+}, which makes lignin a highly effective biosorbent.

Based on the reproducibility of observations in the surface analysis, kinetic data, chemical balance, and biological stability, this study recommends Sarkanda grass lignin as an effective adsorbent for polluting species, such as metal ions in aqueous environments. This recommendation is supported by the performance of the retention itself and the economic profitability resulting from the function of lignin as an easily renewable bioresource and non-polluting waste.

4. Conclusions

Under precisely established experimental conditions, including a temperature of 24 ± 0.5 °C, moderate/weak acid pH of 5 for both lignin and Ni(II) aqueous solutions, a dose of 5 g adsorbent/L pollutant solution, and a concentration range of 46.9544–58.693 mg/L Ni^{2+}, Sarkanda grass lignin has been identified as a potential adsorbent with high efficiency for retaining Ni(II) from aqueous media.

The correlation coefficients obtained from the Freundlich and Langmuir models were used to interpret the experimental adsorption isotherms and establish the efficiency of the adsorbent from a practical standpoint. However, they could not determine whether the adsorption was physical or chemical. The Freundlich model was found to be more appropriate for describing the retention of Ni(II) on the heterogeneous and porous surface of lignin, indicating a higher probability of chemosorption. This also proved the efficiency of the polymer as an adsorbent. Furthermore, SEM and EDX surface analyses clearly confirm the adsorption of Ni(II) in the pores of Sarkanda grass lignin.

Based on the interpretation of the kinetic data using the Lagergren model of the pseudo I order and Ho–McKay model of the pseudo II order, it appears that the Ho–McKay model is the most suitable for describing the adsorption of Ni(II) from aqueous media on Sarkanda grass lignin. This provides conclusive evidence regarding the electrostatic nature of the interactions between the two species involved and the triggering of an active chemical adsorption due to the good complexing capacity of lignin.

The biological analyses were conducted on *Glosa* wheat seeds incorporated in lignin contaminated with a Ni(II) aqueous solution at concentrations ranging from 46.9544 to 58.693 mg/L Ni^{2+}. The filtrates resulting from the separation of the two phases after adsorption were also analyzed at three different contact times. The biopolymer has demonstrated good retention capacity at 30, 60, and 90 min. This is likely due to the abiotic stress caused by the inhibitory effect of Ni(II) on the biological dynamics associated with the germination of wheat caryopses and subsequent seedling development.

From the perspective of the obtained experimental parameters, Sarkanda grass lignin appears to be a viable alternative for adsorbing certain pollutants, such as heavy metals, instead of Ni(II). This is due to the variety and large number of superficial functional groups present in the porous and heterogeneous structure of the polymer, which facilitates processes of ion exchange or complexation with metal ions. Additionally, it is available in large quantities globally, as it is a renewable waste resource, which can be economically profitable, and it is non-polluting.

Our future research efforts will focus on the potential of lignin as an adsorbent for heavy metal removal, exploring its effectiveness in adsorbing other heavy metals, both individually and in mixtures or combinations. This approach will allow us to assess the versatility and applicability of Sarkanda grass lignin in a wider range of environmental contexts and pollutant scenarios, contributing to the development of sustainable and environmentally friendly solutions for water purification and pollution mitigation.

Author Contributions: Conceptualization, E.U., M.E.F., and O.C.U.; methodology, C.O.B. and C.S.; investigation, E.U., M.E.F., and D.C.Ț.; resources, E.U., B.-M.T., and C.S.; writing—original draft preparation, M.E.F., E.U., and O.C.U.; writing—review and editing, E.U., B.-M.T., M.E.F., and D.C.Ț.; visualization, E.U., O.C.U., and M.E.F.; software, D.C.Ț. and B.-M.T.; supervision, C.S. and C.O.B. All authors have read and agreed to the published version of the manuscript.

Funding: This research received no external funding.

Data Availability Statement: The original contributions presented in the study are included in the article, further inquiries can be directed to the corresponding author.

Conflicts of Interest: The authors declare no conflicts of interest.

References

1. Fornea, V.; Trupină, S.; Iosub, A.V.; Bulgariu, L. Spectrophotometric determination of Cu(II), Co(II) and Ni(II) ions in mono and multi-component systems. *Bul. Inst. Polit.* **2016**, *62*, 11–20.
2. Pavel, L.V. Behavioral Studies of Heavy Metals in the Soil and of some Remedy Alternatives. Ph.D. Thesis, "Gh. Asachi" Polytechnic University of Iasi, Iasi, Romania, 2012; pp. 31–39.
3. Jaishankar, M.; Tseten, T.; Anbalagan, N.; Mathew, B.B.; Mathew, K.N. Toxicity, mechanism and health effects of some heavy metals. *Rev. Interdiscip. Toxicol*. **2014**, *7*, 60–72.
4. Duruibe, J.O.; Ogwuegbu, M.O.C.; Egwurugwu, J. N. Heavy metal pollution and human biotoxic effects. *Phys. Sci. Int. J*. **2007**, *2*, 112–118.
5. Begum, W.; Rai, S.; Banerjee, S.; Bhattacharjee, S.; Mondal, M.H.; Bhattarai, A.; Saha, B. A comprehensive review on the sources, essentiality and toxicological profile of nickel. *RSC Adv.* **2022**, *12*, 9139–9153.
6. Cavani, A. Breaking tolerance to nickel. *Toxicology* **2005**, *209*, 119–121.
7. Rothenberg, S.J.; Karchmer, S.; Schnaas, L.; Perroni, E.; Zea, F.; Fernandez, A.J. Change in serial blood lead levels during pregnancy. *Environ. Health. Perspect*. **1994**, *102*, 876–880.
8. Pokorska-Niewiada, K.; Rajkowska-Myśliwiec, M.; Protasowicki, M. Acute lethal toxicity of heavy metals to the seeds of plants of high importance to humans. *Bull. Environ. Contam.* **2018**, *101*, 222–228.
9. Khan, Z.I.; Ahmad, K.; Ahmad, T.; Zafar, A.; Alrefaei, A.F.; Ashfaq, A.; Akhtar, S.; Mahpara, S.; Mehmood, N.; Ugulu, I. Evaluation of nickel toxicity and potential health implications of agriculturally diversely irrigated wheat crop varieties. *Arab. J. Chem.* **2023**, *16*, 104934.
10. Genchi, G.; Carocci, A.; Lauria, G.; Sinicropi, M.S.; Catalano, A. Nickel: Human Health and Environmental Toxicology. *Int. J. Environ. Res. Public. Health* **2020**, *17*, 679.
11. Shen, H.M.; Zhang, Q.F. Risk assessment of nickel carcinogenicity and occupational lung cancer. *Environ. Health Perspect*. **1994**, *102*, 275–282.
12. Ellen, T.P.; Kluz, T.; Harder, M.E.; Xiong, J.; Costa, M. Heterochromatinization as a potential mechanism of nickel-induced carcinogenesis. *Biochemistry* **2009**, *48*, 4626–4632.
13. Zou, L.; Su, L.; Sun, Y.; Han, A.; Chang, X.; Zhu, A.; Liu, F.; Li, J.; Sun, Y. Nickel sulfate induced apoptosis via activating ROS-dependent mitochondria and endoplasmic reticulum stress pathways in rat Leydig cells. *Environ. Toxicol.* **2017**, *32*, 1918–1926.
14. Sciban, M.; Klasnja, M.; Skrbic, B. Modified softwood sawdust as adsorbent of heavy metal ions from water. *J. Hazard. Mater.* **2006**, *136*, 266–271.
15. Guo, X.Y.; Zhang, A.Z.; Shan, X.Q. Adsorption of metal ions on lignin. *J. Hazard. Mater.* **2008**, *151*, 134–142.
16. Zhang, Z.; Chen, Y.; Wang, D.; Yu, D.; Wu, C. Lignin-based adsorbents for heavy metals. *Ind. Crops Prod*. **2023**, *193*, 116119.
17. Hubbe, M.A.; Beck, K.R.; O'Neal, W.G.; Sharma, Y.C. Cellulosic substrates for removal of pollutants from aqueous systems: A review. 2. Dyes. *BioResources* **2012**, *7*, 2592–2687.
18. Ungureanu, E.; Trofin, A.; Trincă, L.C.; Ariton, A.M.; Ungureanu, O.C.; Fortună, M.E.; Jităreanu, C.D.; Popa, V.I. Studies on kinetics and adsorption equilibrium of lead and zinc ions from aqueous solutions on Sarkanda Grass lignin. *Cellul. Chem. Technol*. **2021**, *55*, 939–948.
19. Ungureanu, E.; Jităreanu, C.D.; Trofin, A.; Fortună, M.E.; Ungureanu, O.C.; Ariton, A.M.; Trincă, L.C.; Brezuleanu, S.; Popa, V.I. Use of Sarkanda Grass lignin as a possible adsorbent for As (III) from aqueous solutions-kinetic and equilibrium studies. *Cellul. Chem. Technol*. **2022**, *56*, 681–689.
20. Ungureanu, E.; Fortună, M.E.; Țopa, D.C.; Brezuleanu, C.O.; Ungureanu, V.I.; Chiruță, C.; Rotaru, R.; Tofanică, B.M.; Popa, V.I.; Jităreanu, D. C. Comparison adsorption of Cd (II) onto Lignin and Polysaccharide-based polymers. *Polymers* **2023**, *15*, 3794.
21. Rusu, G. Studies on the Use of Cellulosic Wastes in Reducing Environmental Pollution. Ph.D. Thesis, "Gh. Asachi" Polytechnic University of Iasi, Iasi, Romania, 2015; pp. 29–48.
22. Ungureanu, E. Aspects of Composites Biodegradation Based on Lignocelluloses Materials. Ph.D. Thesis, "Gh. Asachi" Polytechnic University of Iasi, Iasi, Romania, 2008; pp. 15–20.
23. Sethupathy, S.; Morales, G.M.; Gao, L.; Wang, H.; Yang, B.; Jiang, J.; Sun, J.; Zhu, D. Lignin valorization: Status, challenges and opportunities. *Bioresour. Technol.* **2022**, *347*, 126696.
24. Mabrouka, A.; Erdociab, X.; Alriolsb, M.G.; Labidib, J. Techno-Economic Evaluation for Feasibility of Lignin Valorisation Process for the Production of Bio-Based Chemicals. *Chem. Eng. Trans*. **2017**, *61*, 428–432.
25. Garcia-Valls, R.; Hatto, T.A. Metal ion complexation with lignin derivatives. *J. Chem. Eng*. **2003**, *94*, 99–105.
26. Todorciuc, T. Contributions to Some Complex Combinations of Natural Products with Aromatic Structure. Ph.D. Thesis, "Gh. Asachi" Polytechnic University of Iasi, Iasi, Romania, 2016; pp. 62–78.
27. Wang, X.; Li, X.; Peng, L.; Han, S.; Hao, C.; Jiang, C.; Wang, H.; Fan, X. Effective removal of heavy metals from water using porous lignin-based adsorbents. *Chemosphere* **2021**, *279*, 130504.
28. Weber, W.J.J.; McGinley, P.M.; Katz, L.E. Sorption phenomena in subsurface systems: Concepts, models and effects on contaminant fate and transport. *Water Res*. **1991**, *25*, 499–528.
29. Chong, K.H.; Volesky, B. Description of two-metal biosorption equilibria by Langmuir-type models. *Biotechnol. Bioeng.* **1995**, *47*, 451–460.
30. Rajeev, A. Adsorption of Heavy Metals—A Review. *Mater. Today Proc*. **2019**, *18*, 4745–4750.

31. Marcuello, C.; Foulon, L.; Chabbert, B.; Aguié-Béghin, V.; Molinari, M. Atomic force microscopy reveals how relative humidity impacts the Young's modulus of lignocellulosic polymers and their adhesion with cellulose nanocrystals at the nanoscale. *Int. J. Biol. Macromol.* **2020**, *147*, 1064–1075.
32. Azizian, S. Kinetic models of sorption: A theoretical analysis. *J. Colloid Interface Sci.* **2004**, *276*, 47–52.
33. Revellame, E.D.; Fortela, D.L.; Sharp, W.; Hernandez, R.; Zappi, M.E. Adsorption kinetic modeling using pseudo-first order and pseudo-second order rate laws: A review. *Clean. Eng. Technol.* **2020**, *1*, 100032.
34. Samuil, C. *General Plant Technologies*; Ion Ionescu de la Brad Iasi, Iasi, Romania, 2010; p. 280.
35. Ayawei, N.; Ebelegi, A.N.; Wankasi, D. Modelling and Interpretation of Adsorption Isotherms. *J. Chem.* **2017**, *2017*, 3039817.
36. Hanif, M.A.; Tauqeer, H.M.; Aslam, N.; Hanif, A.; Yaseen, M.; Khera, R.A. Correct Interpretation of sorption mechanism by Isothermal, Kinetic and Thermodynamic models. *Int. J. Chem. Biochem. Sci*. **2017**, *12*, 53–67.
37. Koble, R.A.; Corrigan, T. E. Adsorption isotherms for pure hydrocarbons. *J. Ind. Eng. Chem*. **1952**, *44*, 383–387.
38. Dabrowski, A. Adsorption—From theory to practice. *Adv. Colloid Interface Sci*. **2001**, *93*, 135–224.
39. Boparai, H.K; Joseph, M.; O'Carroll D.M. Kinetics and thermodynamics of cadmium ion removal by adsorption onto nano zerovalent iron particles. *J. Hazard. Mater.* **2011**, *186*, 458–465.
40. Ho, Y.S.; McKay, G. Pseudo-second order model for sorption processes. *Process Biochem*. **1999**, *34*, 451–465.
41. Major, G.H.; Chatterjee, S. Linford M.R. Resolving a mathematical inconsistency in the Ho and McKay adsorption equation. *Appl. Surf. Sci.* **2020**, *504*, 144157.
42. Tan, K.L.; Hameed, B.H. Insight into the Adsorption Kinetics Models for the Removal of Contaminants from Aqueous Solutions. *J. Taiwan Inst. Chem. Eng*. **2017**, *74*, 25–48.
43. Iyem, E.; Yildirim, M.; Kizilgeci, F. Germination, seedling growth and physio-biochemical indices of bread wheat (Triticum aestivum l.) genotypes under peg induced drought stress. *Agric. For.* **2021**, *67*, 163–180.
44. Mohammed, A.; Abdullah, A. Scanning Electron Microscopy (SEM): A Review. In Proceedings of the 2018 International Conference on Hydraulics and Pneumatics—HERVEX, Băile Govora, Romania, 7–9 November 2018; Volume 1, pp. 77–85.
45. Aziam, R.; Chibana, M.; Eddaoudi, H., Soudani, A.; Zerbet, M.; Sinan, F. Kinetic modeling, equilibrium isotherm and thermodynamic studies on a batch adsorption of anionic dye onto eco-friendly dried Carpobrotus edulis plant. *Eur. J. Phys.* **2017**, *226*, 977–992.
46. Kainth, S.; Piyush Sharma, P.; Pandey, O.P. Green sorbents from agricultural wastes: A review of sustainable adsorption materials. *Appl. Surf. Sci. Adv.* **2024**, *19*, 100562–100583.
47. Raji, Z.; Karim, A.; Karam, A.; Khalloufi, S. Adsorption of Heavy Metals: Mechanisms, Kinetics, and Applications of Various Adsorbents in Wastewater Remediation—A Review. *Waste* **2023**, *1*, 775–805.

polymers

MDPI

Article

Synthesis and Properties of Modified Biodegradable Polymers Based on Caprolactone

Maria E. Fortună [1], Elena Ungureanu [2,*], Răzvan Rotaru [1], Alexandra Bargan [1], Ovidiu C. Ungureanu [3], Carmen O. Brezuleanu [2] and Valeria Harabagiu [1]

[1] Institute of Macromolecular Chemistry "Petru Poni", 41A Grigore Ghica Voda Alley, 700487 Iasi, Romania; fortuna.maria@icmpp.ro (M.E.F.); rotaru.razvan@icmpp.ro (R.R.); anistor@icmpp.ro (A.B.); hvaleria@icmpp.ro (V.H.)
[2] "Ion Ionescu de la Brad" Iasi University of Life Sciences, 3 Mihail Sadoveanu Alley, 700490 Iasi, Romania; olgutabrez@uaiasi.ro
[3] "Vasile Goldis" Western University of Arad, 94 the Boulevard of the Revolution, 310025 Arad, Romania; ungureanu.ovidiu@uvvg.ro
* Correspondence: eungureanu@uaiasi.ro

Abstract: In this paper, the synthesis and characterization of two polycaprolactone-polydimethylsiloxane (PDMS-CL) copolymers with biodegradable properties are reported. A comparative study was carried out using an aminopropyl-terminated polydimethylsiloxane macro-initiator (APDMS) with two different molecular weights. The copolymers (PDMS-CL-1 and PDMS-CL-2) were obtained by ring-opening polymerization of ε-caprolactone using APDMS as initiators and stannous 2-ethylhexanoate as a catalyst. The copolymer's structures were confirmed by Fourier transform infrared spectroscopy (FT-IR), nuclear magnetic resonance (^{1}H-NMR) spectra, and energy dispersion spectroscopy (EDX). Surface morphology was investigated using scanning electron microscopy (SEM) and atomic force microscopy (AFM). The hydrophobic properties of the copolymers were demonstrated by the water contact angle and water vapor sorption capacity. Additionally, biological tests were conducted on San Marzano type tomato plants (*Lypercosium esculentum*) to assess the synthesized copolymers' susceptibility to the environment in terms of biological stability and metabolic activity. The biodegradation of PDMS-CL-1 and PDMS-CL-2 copolymers does not have a dangerous effect on the metabolic activity of plants, which makes it a convenient product in interaction with the environment.

Keywords: aminopropyl-terminated polydimethylsiloxane; chlorophyll; PDMS-CL copolymers; *Lypercosium esculentum*; poly-ε-caprolactone

Citation: Fortună, M.E.; Ungureanu, E.; Rotaru, R.; Bargan, A.; Ungureanu, O.C.; Brezuleanu, C.O.; Harabagiu, V. Synthesis and Properties of Modified Biodegradable Polymers Based on Caprolactone. *Polymers* **2023**, *15*, 4731. https://doi.org/10.3390/polym15244731

Academic Editors: Radu Claudiu Fierascu, Verona Iordache and Luísa Durães

Received: 30 October 2023
Revised: 15 December 2023
Accepted: 15 December 2023
Published: 17 December 2023

1. Introduction

In the last few years, interest in the preparation of biodegradable polymers has grown due to their various properties, which offer many biomedical applications [1].

Polymers such as polyesters, polycaprolactone, polylactic acid, and poly(trimethylene carbonate) are among the most widely used polymeric biomaterials because of their biocompatibility and biodegradation [2,3]. Poly-ε-caprolactone (CL) is an interesting hydrophobic polymer with a semi-crystalline structure consisting of caprolactone subunits, which were formed through ring-opening polymerization, an important technique for the preparation of copolymers [4–6]. Moreover, poly-ε-caprolactone is a biodegradable synthetic polymer used in different applications in the medical field (drug delivery, wound dressing, tissue engineering), toughening agents for epoxy resins, environmentally sustainable packaging, and many others [7,8]. CL can be degraded by many microorganisms, such as several bacteria and fungi, thus making it able to undergo biodegradation [9]. Polysiloxanes represent a unique hybrid of organic and inorganic components with a specific structure that consists of a backbone formed of alternating silicon and oxygen atoms [10,11]. Polydimethylsiloxane (PDMS) is the most well-known polysiloxane. The literature offers information on

many performance properties [5,6], including biocompatibility, low viscosity, and excellent characteristics such as hydrophobicity, flexibility, chemical inertness, stability at both high and low temperatures, and superior surface wettability. Considering the advantages of poly(dimethylsiloxane), it is used in a variety of medical applications and as a water treatment absorbent. Despite their interesting characteristics, polysiloxanes have limitations due to their increased cost and poor mechanical properties [12]. Thus, the use of PDMS in the preparation of copolymers demonstrates its many benefits, and it has been widely studied due to the many unique properties that emerge from the combinations of subunits [13,14]. Changes in the groups at the ends of the polydimethylsiloxane chain affect its properties. Polysiloxanes functionalized with aminoalkyl groups are known in textiles and cosmetics [15]. More studies reported on the synthesis of polydimethylsiloxane copolymers using reactive hydroxyl or amine functional oligomers that are mono- or difunctionally terminated as initiators [16,17].

It was shown in prior work [18] that CL allows the moderate development of two micromycetes, *Fusidium viride* and *Penicillium brevicompactum*, capable of biosynthesizing enzymes that accelerate biotic reactions and trigger the biodegradation of the copolymer. This destruction can be a potentially toxic action for the environment, and it is absolutely necessary to monitor the impact on the plant's metabolism, given the conversion of the copolymer into simple substances that can modify the metabolic activity and implicitly the structure of the plant [19]. Following the decomposition of the copolymer, the nitrogen dynamics undergo evolutionary changes, confirming the process's development with the release of organic nitrogen. In addition, the biological tests carried out (germination index, average seedling height, green and dry biomass) on *Lypercosium esculentum*, San Marzano variety tomato plants that were in direct interaction with the copolymer showed their normal growth and development, which suggests a negligible toxic effect and implicitly a compatibility of the copolymer with the environment [18]. Given the essential role of this pigment in photosynthesis and, indirectly, in the metabolism and physiological state of the plants, it is very important to quantify the total chlorophyll content of the plant leaves that came into contact with the copolymers [19]. By mixing CL with other polymers (such as polydimethylsiloxane), it is possible to synthesize copolymers or composites with modified physical, chemical, and mechanical properties [20].

The literature studies of the synthesis, characterization, and properties of PDMS-CL copolymers are limited. However, the PDMS-CL copolymer-based microspheres have unique properties and can be used to obtain biomedical devices such as scaffolds in tissue engineering and matrix resins for time-release drugs [9,19]. Polydimethylsiloxane (PDMS) has a very low glass transition temperature, which makes it a soft segment to adjust the mechanical properties of CL-based shape memory polymers (SMPs) [21]. PDMS, for instance, can be used as soft segments of varied length to tailor the mechanical properties of PCL-based polymers (acting as hard segments). By varying the segment lengths of PCL and PDMS, the mechanical properties of the obtained copolymers can be altered to achieve the desired stiffness [6].

The objective of the present study was to obtain PDMS-CL copolymers and evaluate their structure, morphology, and property behavior obtained by ring-opening polymerization. FT-IR, ^{1}HNMR, and EDX spectroscopy were used to investigate the structures of the macro-initiator and synthesized copolymers. Copolymer surface properties were examined using water vapor sorption capacity and contact angle measurements, while the morphology of copolymers was investigated using SEM and AFM. The thermal behavior of the copolymers was determined via thermogravimetric analysis (TGA) and differential scanning calorimetry (DSC).

2. Materials and Methods

2.1. Materials

Octamethylcyclotetrasiloxane (D4), tetramethylamonium hydroxide pentahydrate (Aldrich, St. Louis, MO, USA), and 1,3-Bis (3 aminopropyl)-1,1,3,3-tetramethyldisiloxane

were used for APDMS-1, which was synthesized according to the methods described by Fortuna et al., where a mass of approximately 3409 g/mol was obtained [9]. APDMS-2 (aminopropyl-terminated polydimethylsiloxane with a Mn of ca. 1000) was purchased from Aldrich; ε-caprolactone was purchased from Aldrich; and stannous octoate was obtained from Air Products. Toluene, methanol, xylene, and tetramethylammonium hydroxide were purchased from Aldrich.

Biological material: tomato plants (*Lypercosium esculentum*), San Marzano variety, vegetation period of 35 days [18].

2.2. Methods

FTIR spectra were recorded on a Bruker Vertex 70 device (Bruker Optics, Ettlingen, Germany). Registrations were performed at room temperature in the 400–4100 cm^{-1} range.

^{1}H-NMR spectrum was investigated with a Bruker NMR spectrometer (Model DRX400, Billerica, MA, USA).

The water contact angles of the copolymers were determined with an eScope Conrad USB digital microscope and ImageJ software 1.48. A quantity of 0.5 g of copolymer was dissolved in 10 mL of chloroform, and part of it was spread on a glass slide. Then the solvent evaporated. Thin polymer films were then dried under vacuum at room temperature for 48 h. The same procedure was repeated for all samples [6].

The morphology and composition of samples were examined using scanning electron microscopy and energy dispersive X-ray spectroscopy (SEM/EDX) (Ametek, Berwyn, PA, USA).

The AFM images were obtained with a NTEGRA scanning probe microscope (NT-MDT Spectrum Instruments, Moscow, Russia). For image acquisition, the Nova v.19891 Solver software was used.

Thermogravimetric (TG) measurements and differential scanning calorimetry (DSC) analyses were performed using STA 449F1 Jupiter equipment (Netzsch Company, Selb, Germany) and a DSC 200 F3 Maia device (Netzsch, Germany), respectively. The measurements were performed in the −150 to 200 °C temperature range at a heating rate of 10 °C/min in an inert atmosphere.

The water vapor sorption capacity of the PDMS-PCL copolymers was appreciated on the basis of the sorption isotherms recorded in the dynamic regime using a fully automated gravimetric device, IGAsorp, from Hidden Analytical (Warrington, UK). Registrations were completed at 25 °C in a stream of nitrogen (250 mL/min) in the humidity range 0–90% in steps of 10% with a predetermined equilibrium time between 40 and 60 min at each step.

Chlorophyll content in leaves provides pertinent information about the physiological and metabolic states of plants. Determination of total chlorophyll content: in some plant pots (having a height of 9 cm and a diameter of 6 cm), 80 g of soil-black peat was introduced and 0.3 g of samples (PCL, APDMS-1, APDMS-2, PDMS-PCL-1, and PDMS-PCL-2) together with 3 tomato seeds [21]. The experiment was synthesized according to the method described by Fortuna et al. [18].

The total chlorophyll content was read using a CCM-200 plus chlorophyll content meter from Opti-Sciences Inc., Hudson, NH, USA. The measurements were made on the tomato plant leaves after 35 days of planting, and three samples were used for replication.

2.3. Macro-Initiator Synthesis-Aminopropyl-Terminated Polydimethylsiloxane (APDMS-1)

The goal of the synthesis was to synthesize an average molecular weight aminopropyl-terminated polydime-thylsiloxane (APDMS-1), which could be used as macro-initiators in the reaction with poly(ε-caprolactone) in a subsequent step. Scheme S1 (Supplementary Materials) illustrates the reaction for the synthesis of the polymer, which has two active amino groups at the end of the chain.

An earlier experiment [9] obtained the macro-initiator (APDMS-1) by synthesizing 1,3-bis (3 ami-nopropyl)-1,1,3,3-tetramethyldisiloxane with octamethylcyclotetrasiloxane (D4) in the presence of a tetramethylammonium hydroxide catalyst. In the first stage of

the synthesis, a solution (10%) of $(CH_3)_4NOH$ (2.7 mmol) in methanol was prepared in a round-bottom flask, heated by means of an oil bath under magnetic stirring, equipped with a thermometer and with connections to argon and the vacuum pump; the D4 compound (2.7 mmol) and 15 mL of toluene were added to the prepared catalyst solution; the reaction mixture was heated to 80 ± 2 °C and kept under the protection of nitrogen for 24 h. The system was then vacuum pumped to remove the solvent. Then, D4 (40 mmol), 20 mmol of 1,3-Bis (3 aminopropyl)-1,1,3,3-tetramethyldisiloxane, and 15 mL of toluene were added and kept at 120 °C under nitrogen protection for 8 h. After the equilibration reaction was completed, unreacted cyclic oligosiloxane was separated from the linear polymer using low pressure distillation. Finally, aminopropyl-terminated polydimethylsiloxane (APDMS) was synthesized. The compounds' structures were confirmed by FT-IR and ^{1}HNMR studies.

2.4. Preparation of the Aminopropyl-Terminated Polydimethylsiloxane-Poly(ε-caprolactone) Copolymers: PDMS-PCL-1 and PDMS-PCL-2

The PDMS-PCL-1 and PDMS-PCL-2 copolymers were obtained by synthesis between the aminopropyl-terminated polydimethylsiloxane as the initiator and ε-caprolactone by ring-opening polymerization in the presence of $Sn(Oct)_2$ as the catalyst, as shown in Scheme S1 (Supplementary Materials). The final products have a yield of 92%.

3. Results and Discussion

3.1. Structural Characterization

3.1.1. Fourier Transform Infrared (FTIR) Analysis

FT-IR spectroscopy was utilized to examine the chemical composition of the copolymers and the functional groups that are responsible for the reaction between the poly-ε-caprolactone and aminopropyl-siloxane. The FT-IR spectra of the APDMS macro-initiators and the PDMS-PCL copolymers are shown in Figure 1. As observed from Figure 1, the infrared spectrum of PCL shows characteristic bands at 2936 cm^{-1} ($\nu_{as}(CH_2)$: asymmetric CH_2 stretching), 2862 cm^{-1} ($\nu_{as}(CH_2)$: symmetric CH_2 stretching), 1732 cm^{-1} (ν(C=O): carbonyl stretching), 1288 cm^{-1} (ν_{cr}: C–O and C–C stretching in the crystalline phase), 1240 cm^{-1} (ν_{as}(COC): asymmetric COC stretching), 1190 cm^{-1} (ν(OC–O): OC–O stretching), 1169 cm^{-1} (ν_{as}(COC): symmetric COC stretching), and 1157 cm^{-1} (ν_{am}: C–O and C–C stretching in the amorphous plane) [8,22].

Aminopropyl-terminated polydimethylsiloxane (APDMS-1 and APDMS-2) shows bands at 3393 and 3115 cm^{-1} (–NH_2 vibration), 2963, 2964 and 2907 cm^{-1} (–CH_3 and –CH_2 vibrations), 1413 and 1410 cm^{-1} (δ_s (C–H), CH_3), 1261 and 1259 cm^{-1} (structural vibration of Si–CH_3), 1090, 1043, 1022 and 1020 cm^{-1} (Si–O–Si asymmetric stretching vibration), 866 and 851 cm^{-1} (δ_{as} (C–H) rocking, $Si(CH_3)_2$), 702 and 698 cm^{-1} (ν_s (Si–C), $Si(CH_3)_2$) [8,23]. APDMS-2 with low molecular weights did not show NH_2 vibration, which is seen in APDMS-1 at 3115 and 3393 cm^{-1} but this is in agreement with the studies of Q. Ran [23].

PDMS-PCL-1 and PDMS-PCL-2 copolymers (Figure 2) show the presence of bands characteristic of aminopropyl-terminated polydimethylsiloxane and poly-ε-caprolactone. Thus, the asymmetric stretching vibration of the Si–O–Si bond can be seen in the wave numbers of 1097, 1036, and 1020 cm^{-1} for PDMS-PCL-1 and 1088, 1055, and 1022 cm^{-1} for PDMS-PCL-2. A high-intensity spectral band from 1732 cm^{-1} specific to caprolactone (carbonyl stretching vibration) is found in the spectrum of composites at 1724 cm^{-1} for PDMS-PCL-1 and at 1728 cm^{-1} for PDMS-PCL-2. The displacements of some wave numbers at the level of composites do not distort the fundamental structure of polysiloxane and poly-ε-caprolactone but suggest chemical interactions between the two.

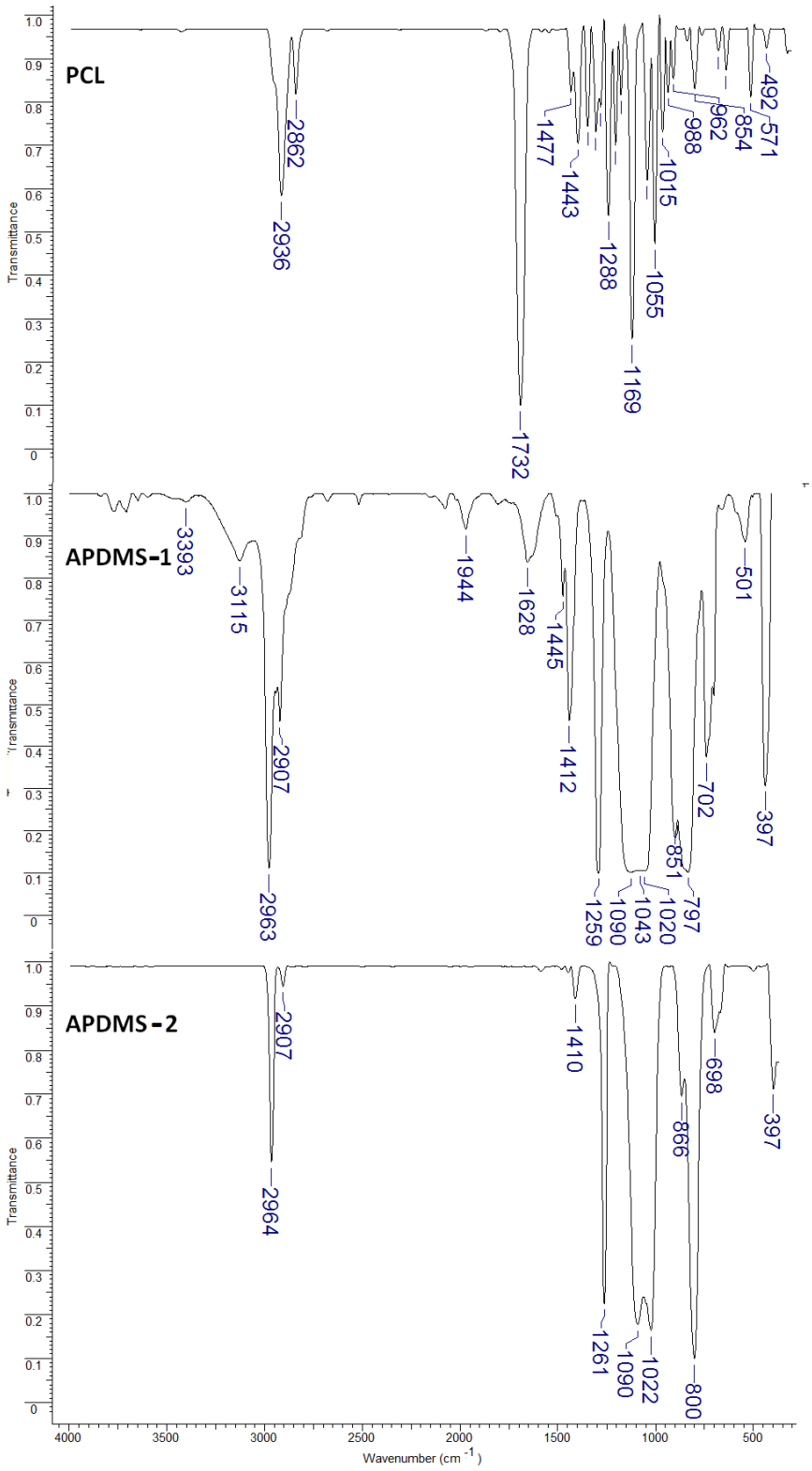

Figure 1. FTIR spectra for PCL, APDMS−1, and APDMS−2.

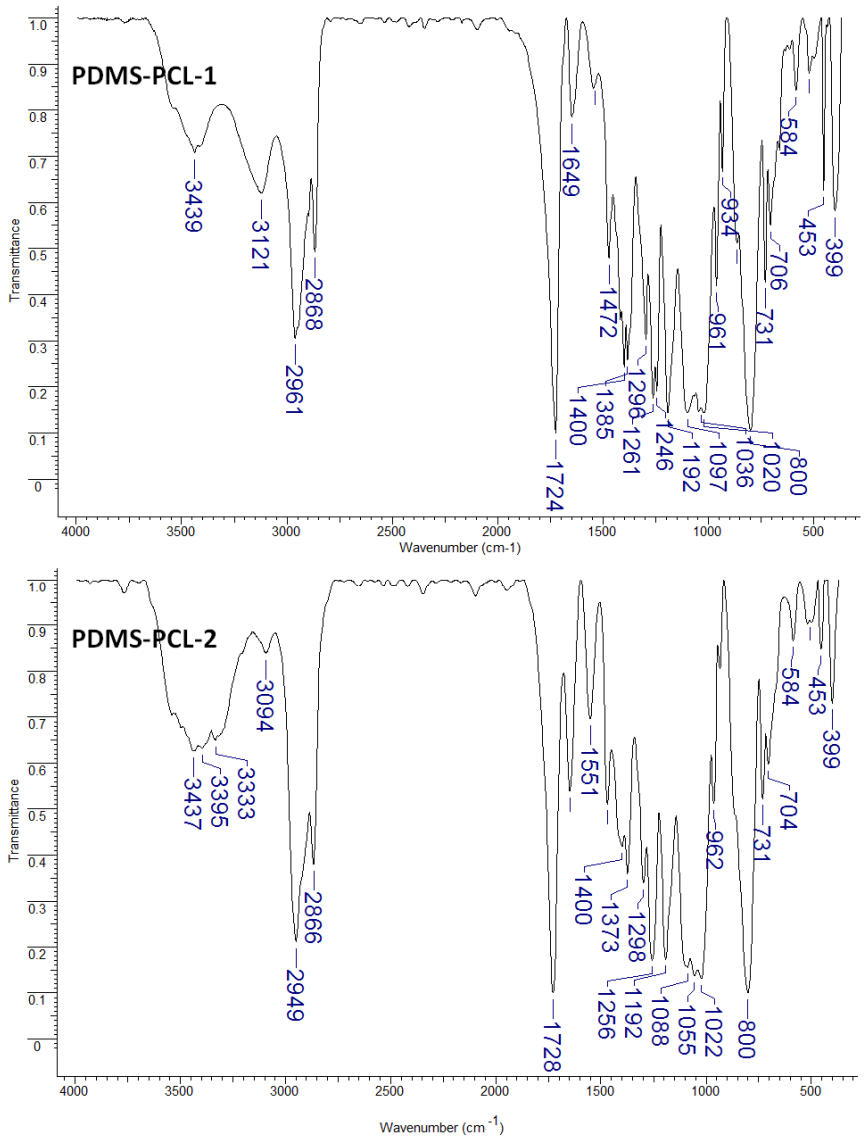

Figure 2. FTIR spectra for APDMS-PCL-1 and APDMS-PCL-2 composites.

Moreover, the structure of PDMS-PCL-1 and PDMS-PCL-2 copolymers was confirmed by ^{1}H NMR -registered spectra presented in Figure S1 (Supplementary Materials). The ^{1}H NMR spectra indicate that the obtained products combine the structural features of PCL and APDMS, which means that the PDMS-PCL-1 and PDMS-PCL-2 copolymers were successfully obtained.

3.1.2. EDX Elemental Analysis

EDX elemental analysis was used to identify and characterize the elemental composition of PDMS-PCL-1 and PDMS-PCL-2 copolymers. From Figure 3, it can be concluded that the presence of siloxane is indicated by the peak at approximately 1.75 keV, which corresponds to the silicon atom [24].

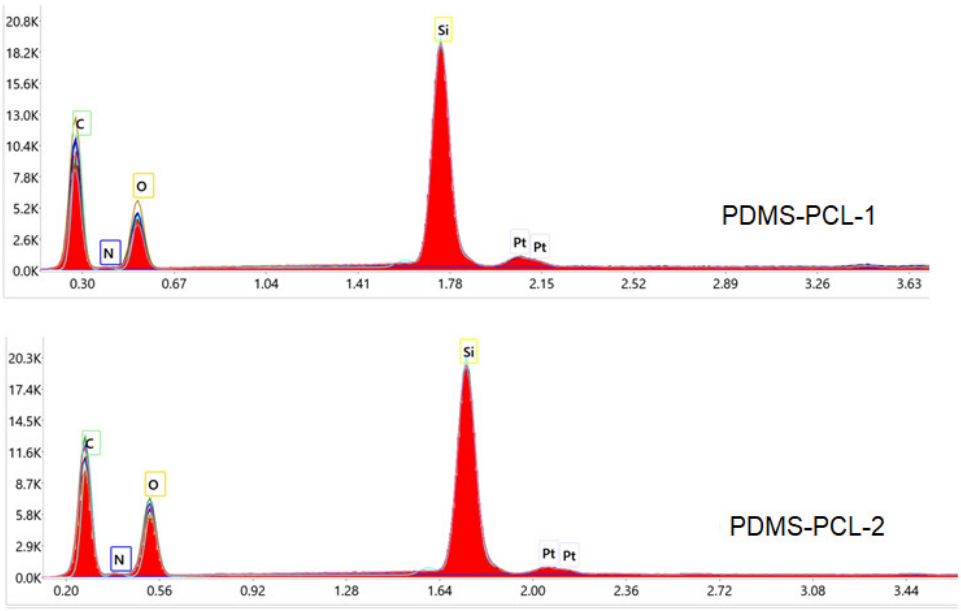

Figure 3. EDX spectra of PDMS-PCL-1 and PDMS-PCL-2 copolymers.

3.2. Surface Morphology

3.2.1. Scanning Electron Microscopy Images of PDMS-PCL-1 and PDMS-PCL-2 Copolymers

Figure 4 shows SEM images of the PDMS-PCL-1 and PDMS-PCL-2 copolymers, and different morphologies can be observed. The PDMS-PCL-1 composite is presented in the form of flat agglomerations of particles with dimensions of 20–50 microns, tightly joined together. The PDMS-PCL-2 composite is presented in the form of approximately spherical agglomerations of particles with radii of 40–50 microns. The difference in shape of the agglomerations of the two composites is probably due to the different molecular masses of the PDMS. In PDMS-PCL-2, where the PDMS has a lower molecular mass, the small lengths of the polymer chains determine windings in the form of approximately spherical balls.

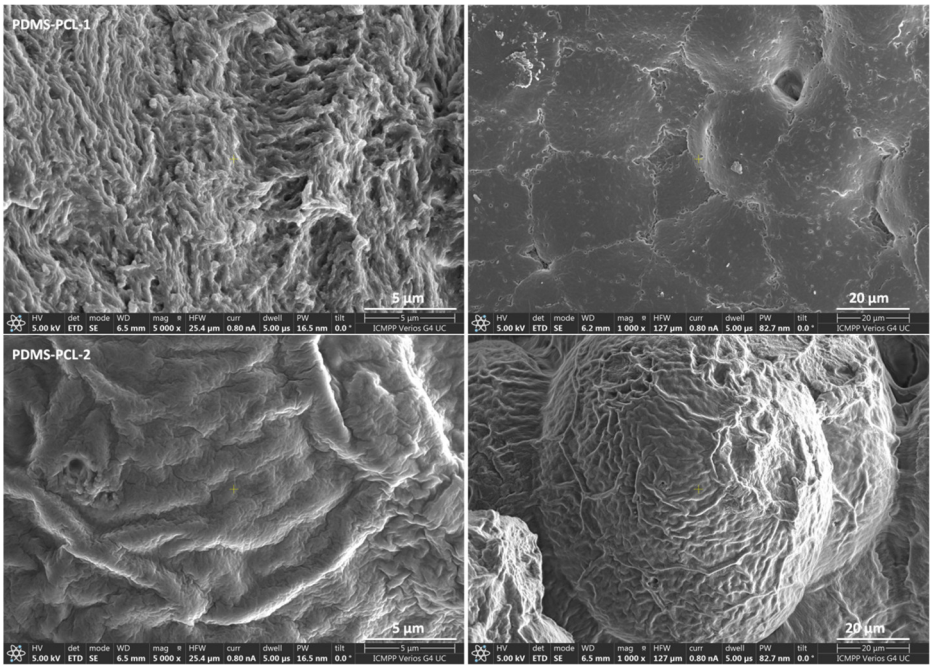

Figure 4. SEM images of PDMS-PCL-1 and PDMS-PCL-2 sample.

3.2.2. Atomic Force Microscopy (AFM) Investigations

Morphological studies were carried out via AFM investigations. AFM images (Figure 5) confirm the scanning electron microscopy (SEM). In the case of the PDMS-PCL-1 composite, the agglomerations of tightly joined particles can be clearly observed, and the surface is rough with few agglomerations on the height. In the case of the PDMS-PCL-2 composite (with a lower molecular mass), the much larger agglomerations of particles cause the appearance of large bumps in the form of hills and valleys, a phenomenon that may influence the hydrophobicity of the composite.

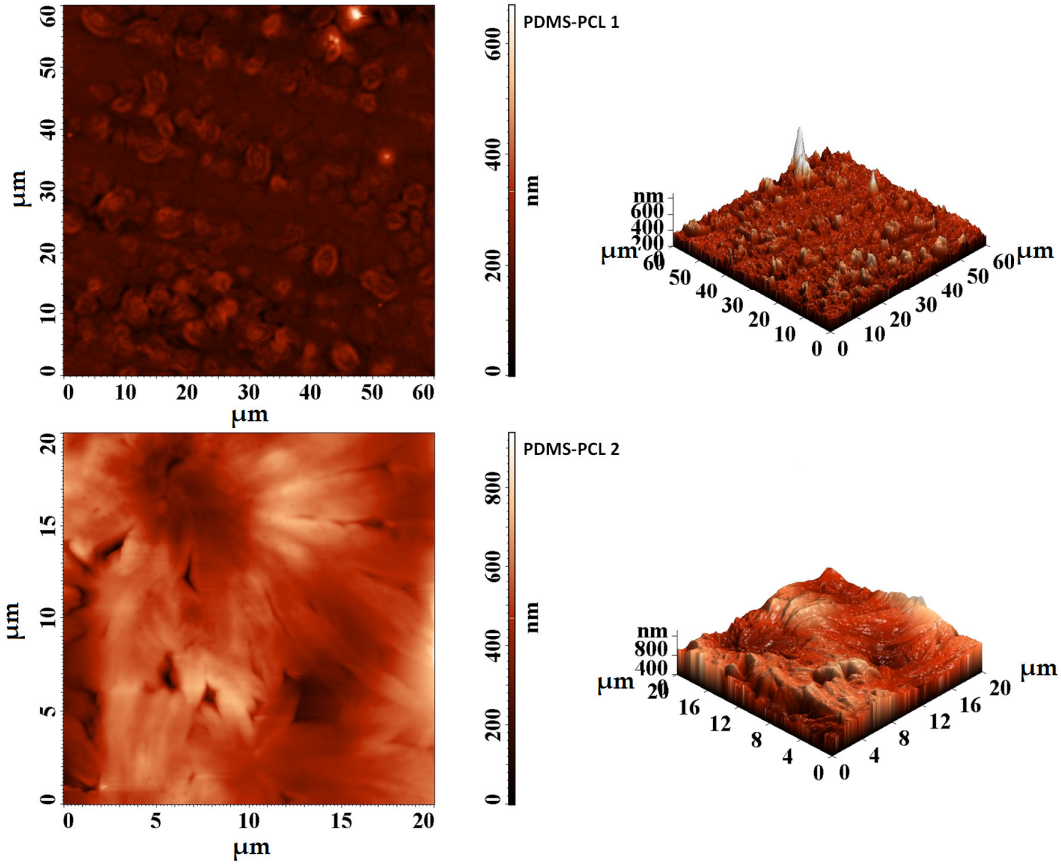

Figure 5. AFM images of PDMS-PCL−1 and PDMS-PCL−2 samples.

3.2.3. Thermal Properties of the PDMS-PCL Copolymers

Figures 6 and 7 show the registered TG and DTG curves of APDMS-1 (a) and APDMS-2 (b) macro-initiators and PDMS-PCL-1 (a) and PDMS-PCL-2 (b) copolymers under a nitrogen atmosphere. For the APDMS-1 (a) sample, weight loss can occur at 157 °C (with a weight loss of 21.54%), at 411 °C (with a weight loss of 27.48%), at 592 °C (with a weight loss of 41.67%), and at 699 °C, with a remaining residual mass of 5.57%. For the APDMS-2 (b) copolymer, it could also be observed that there are more weight loss steps situated at different temperatures: at 83 °C (with a weight loss of 3.33%), at 200 (with a weight loss of 8.54%), at 421 °C (with a weight loss of 34%), at 639 °C (with a weight loss of 47.72%), and at 699 °C, with a remaining residual mass of 5.81%.

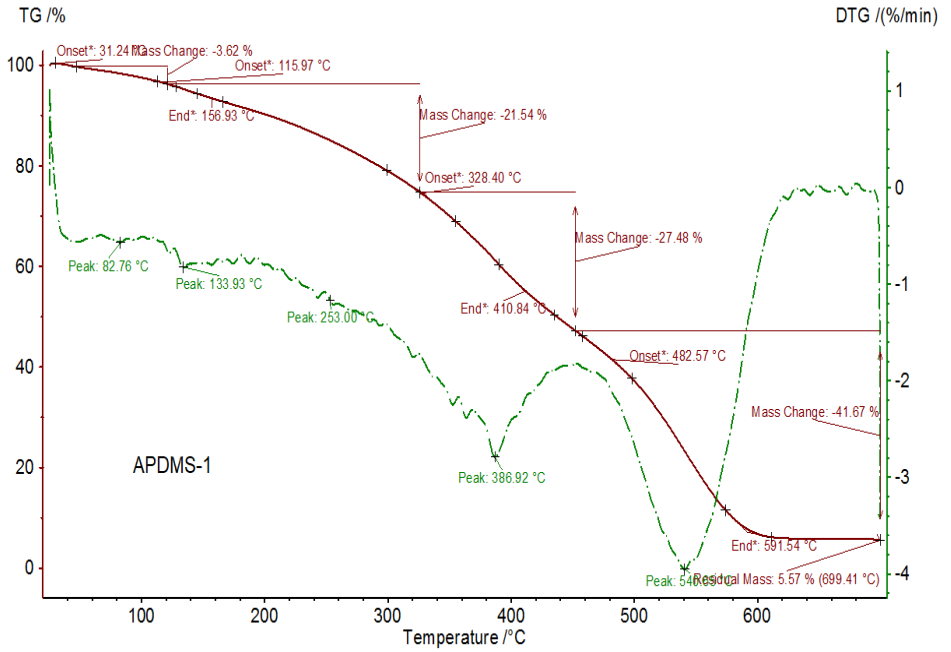

(**a**)

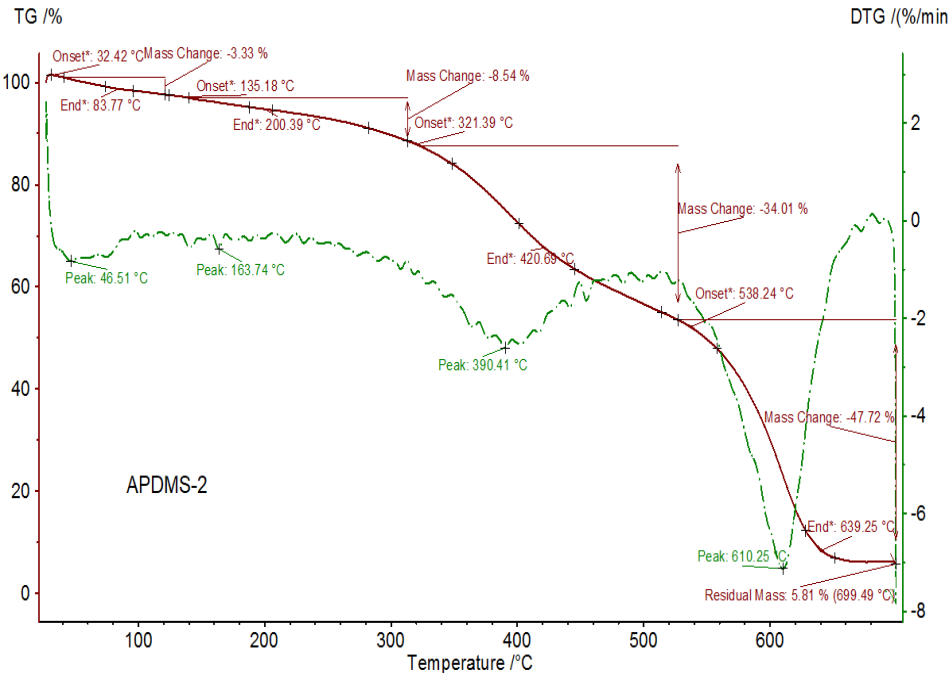

(**b**)

Figure 6. TG (red) and DTG (green) curves of APDMS−1 (**a**) and APDMS−2 (**b**) macro-initiators.

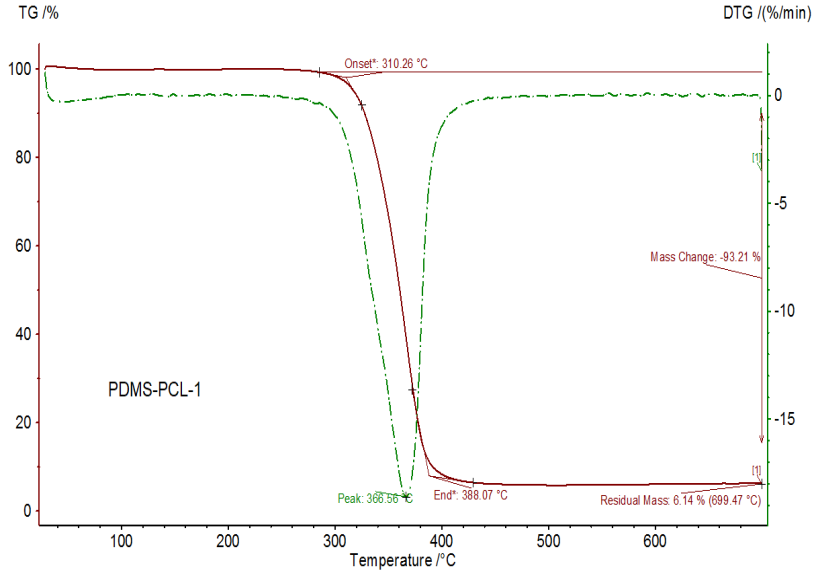

(**a**)

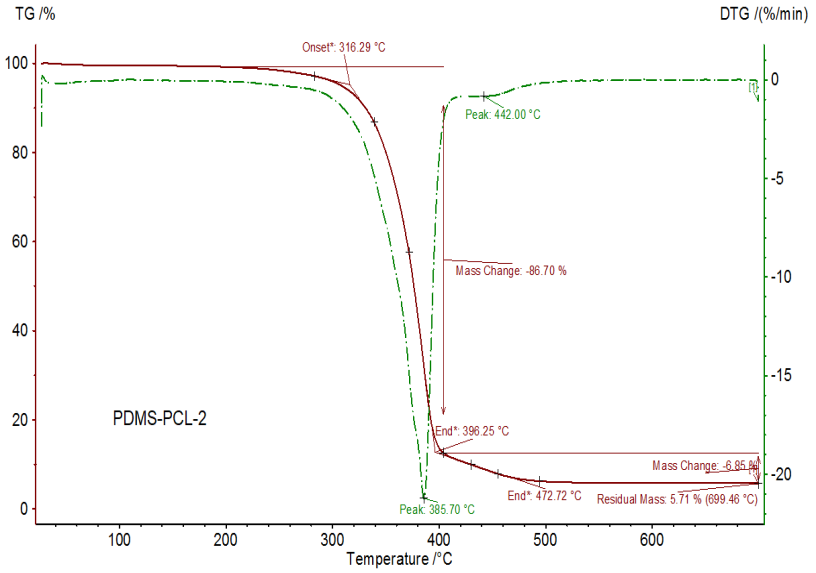

(**b**)

Figure 7. TG (red) and DTG (green) curves of PDMS−PCL-1 (**a**) and PDMS-PCL−2 (**b**) copolymers.

According to TG analysis, the macro-initiators of APDMS-1 and APDMS-2 showed thermal stability up to approximately 135 °C and 164 °C, respectively. The next steps are associated with their decomposition. The literature [25] indicates that the first process of decomposition at low temperatures is associated with water loss. The decomposition of the copolymers and the loss of structural water are the next heat processes. There were no signs of degradation at temperatures over 400–700 °C.

One weight loss step is seen for the PDMS-PCL-1 copolymer at about 367 °C with a weight loss of 93.21%, leaving at 699.45 °C a residual mass of 6.14%; for PDMS-PCL-2 copolymer, one weight loss step is observed at about 386 °C with a weight loss of 6.85%, leaving at 699.45 °C a residual mass of 5.71%. The weight loss in the residual mass range is indicative of the material's decomposition, with the mass residue remaining after it has been removed [9].

3.2.4. Differential Scanning Calorimetry (DSC) Analysis

The DSC of the copolymers is illustrated in Figures 8 and 9. The DSC measures were undertaken after the second heating scan, which was used for the elimination of residual solvents and to remove the thermal history of the polymer. The samples were heated at a rate of 10 °C per minute on a differential scanning calorimeter, ranging from −150 °C to 100 °C. DSC analyses of the copolymers confirmed the characteristic peaks associated with the melting temperatures of APDMS (low temperature) and PCL (high temperature. The first measurements (first heating) of macro-initiators demonstrate a glass transition (Tg) at −110.1 °C for PDMS-1 (Figure 8) and −121.6 °C for APDMS-2 (Figure 9). In the second heating, the glass transition was obtained at −114.2 °C and −121.9 °C.

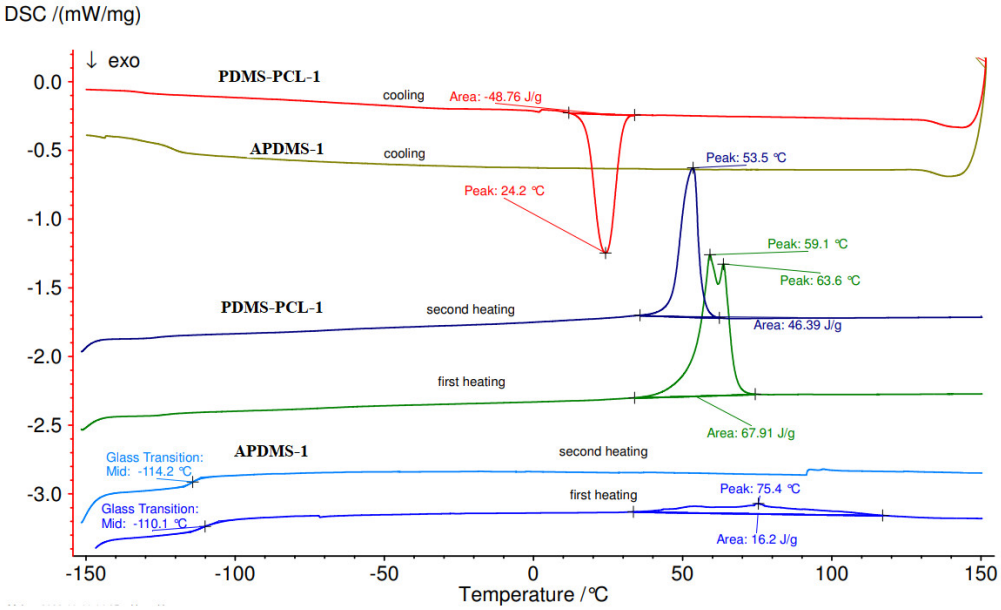

Figure 8. DSC curves of APDMS−1 and PDMS-PCL−1.

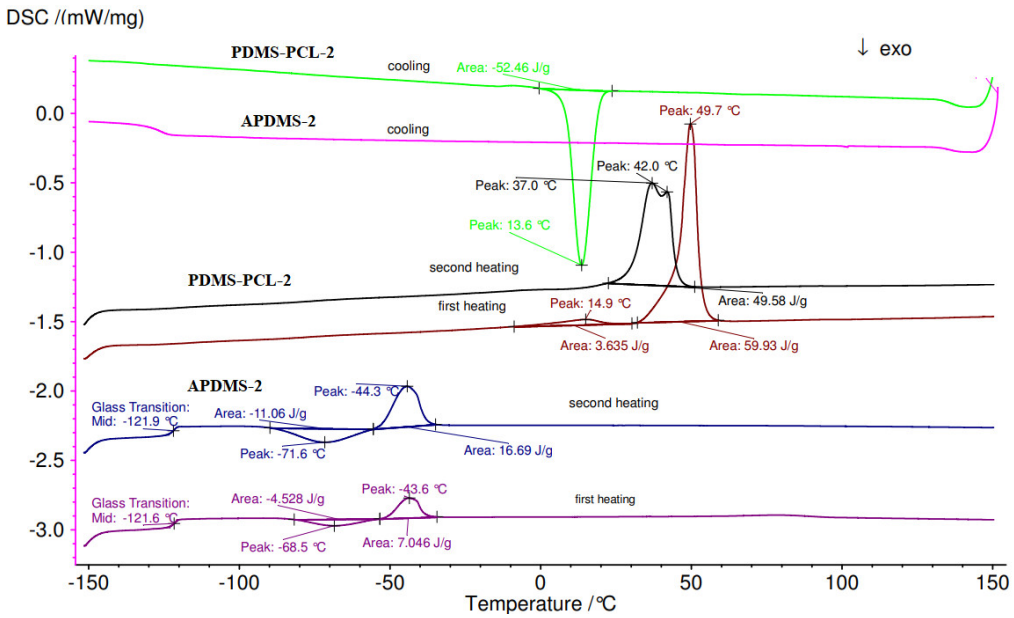

Figure 9. DSC curves of APDMS-2 and PDMS-PCL-2.

In the case of copolymers, the first measurements (first heating) showed distinct endothermic peaks at 59.1 °C and 63.6 °C for PDMS-PCL-1 (Figure 8) and 49.7 °C for PDMS-PCL-2 (Figure 9). The melting transition of the PCL is responsible for the endothermic peaks observed in the second measurement (second heating) for PDMS-PCL-1 at 53.5 °C and for PDMS-PCL-2 at 37 °C and 42 °C. When PDMS-PCL-1 and PDMS-PCL-2 were cooled, exothermic peaks were seen at 24.2 °C and 13.6 °C, respectively.

3.2.5. Contact Angle Measurement

One of the most important parameters used to measure the wettability of a material is the contact angle. By measuring the contact angle, the hydrophilicity or hydrophobicity of the copolymers was examined.

In Figure 10, the contract angle values for PDMS-PCL-1 and PDMS-PCL-2 are 107.33° and 93.46°, respectively. All the results reveal, as expected, the hydrophobic nature of the copolymers. This effect is caused by PDMS's extremely low surface energy, which causes it to migrate to the surface and cover the majority of the copolymer's surface [17]. In the case of the PDMS-PCL-2 composite, due to the agglomerations of spherical particles, at the macroscopic level, a porous surface will result in the absorption of water between the clumps of particles, so the contact angle was found to be smaller.

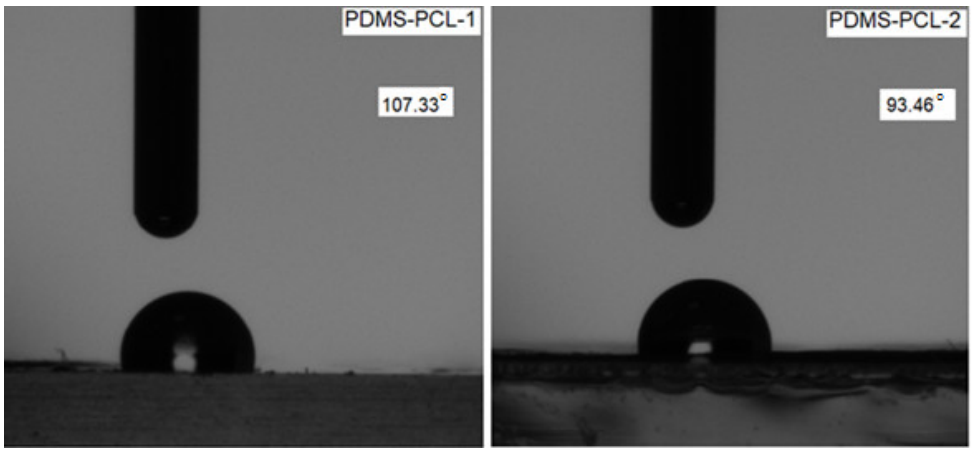

Figure 10. Water contact angle value.

Furthermore, measurements of the water contact angle were found to be reduced but above 90 when the fiber diameter was found to be larger, which indicated a hydrophobic nature. The contact angle values confirm the SEM and AFM study.

3.2.6. Dynamic Vapor Sorption Analysis/Water Vapor Behavior

The influence of the water vapor/moisture from the environment on the newly obtained PDMS-PCL copolymers was investigated using the water vapor capacity determinations in dynamic conditions employing a totally automated gravimetric instrument, the IGAsorp device (made by Hiden Analytical-Warrington, Warrington, UK). The main part of this equipment is represented by an ultrasensitive microbalance, which determines the changes in the weight of the sample as the relative humidity is varied in the sample chamber at a stable and constant temperature. The measurements are directed by user-friendly software. The PDMS-PCL copolymers were dried at 25 °C in a flux of nitrogen (250 mL/min) until their weights were in equilibrium at a relative humidity, RH, under 1%, after which the samples were deposited in a special container, i.e., a Pyrex bulb. After the drying phase, the relative humidity was continuously increased from 0 to 90%, in 10% humidity steps, with every step having a pre-established equilibrium time between 40 and 60 min, and the sorption equilibrium was reached for each step. The relative humidity was reduced, and the desorption graphs were registered [25,26].

The presence of PCL helps to maintain the structure of the copolymer and acts as a barrier for water penetration. The mass gained when the samples were placed in the dynamic vapor sorption equipment was due to the moisture penetration into the copolymer matrix/backbone. The porous structure allows for the permeability of the moisture in the copolymer samples. In agreement with the results obtained for the contact angle of the samples PDMS-PCL-1 (107.33°) and PDMS-PCL-2 (93.46°), respectively, the values of the water vapor sorption capacity are PDMS-PCL-1, 0.79%, and PDMS-PCL-2, 1.89%.

The sorption/desorption isotherms are depicted in Figure 11. Looking at the shapes of these curves, which can be associated with type V isotherms according to the IUPAC classification, this type of isotherm with hysteresis can be interpreted as being representative of the porous surfaces and characteristic for hydrophobic material or very low hydrophilic material. Important information about the surface of the PDMS-PCL copolymers can be obtained from the graphs of the sorption/desorption isotherm: reduced water vapor sorption at low values of relative humidity, RH (0 to 10%), sometimes moderate sorption at intermediate values of RH, and a high increase in water sorption at RH values close to 100% [26].

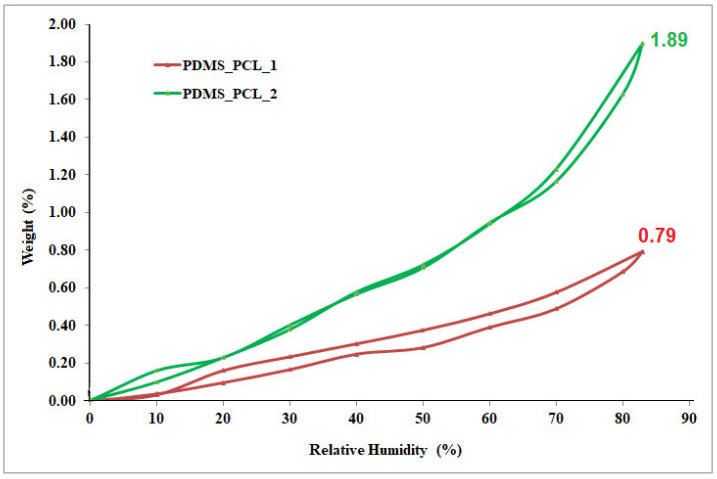

Figure 11. Sorption/desorption isotherms for the PDMS-PCL copolymers.

The Brunauer–Emmett–Teller kinetic model (BET, Equation (1)) was used to calculate the specific surface area (Table 1) by modeling the sorption isotherms measured in dynamic conditions.

$$W = \frac{W_m CRH}{(1 - RH)(1 - RH + CRH)} \quad (1)$$

Table 1. The particularities of the surface determined starting from the adsorption/desorption isotherms: moisture sorption capacity; W, final weight; r_{pm}, medium pore size and BET data for the PDMS-PCL copolymers.

Sample	W (%)	r_{pm} (nm)	BET Data *	
			Area (m^2/g)	Monolayer (g/g)
PDMS-PCL-1	0.7940	2.01	7.879	0.0022
PDMS-PCL-2	1.8993	1.26	30.007	0.0085

* Calculated based on desorption branch of the isotherm (recorded up to a relative humidity of 40%).

The parameters involved are weight of sorbed water (W), weight of water forming a monolayer (Wm), sorption constant (C), and relative humidity (RH).

The average pore sizes also influence, in a special way, the sorption capacity of the PDMS-PCL copolymers. Using the Barrett, Joyner, and Halenda model (BJF, Equations (2)

and (3)), and taking into consideration the calculation methods for cylindrical pores, the average pore size, rpm (Table 1), was calculated. This method uses the desorption branch of the isotherm. This desorbed moisture content is due either to the evaporation of the liquid core or to desorption of a multilayer. Pore size distribution is outlined as the distribution of pore volume. The association between pore volume and gas uptake can be defined if we know the density of the adsorbed phase. The first assumption of mesopore size analysis is that the phase is equivalent to the liquid phase of the adsorbate.

$$V_{liq} = \frac{n}{100\rho_a} \quad (2)$$

$$r_{pm} = \frac{2V_{liq}}{A} \quad (3)$$

where V_{liq} is the water volume, n is the absorption percentage, ρ_a is the adsorbed water density, and A is the specific surface area evaluated by the BET method.

The values of the surface parameters determined using the BET kinetic model demonstrated the hydrophobic-porous nature of the PDMS-PCL copolymers and can be used for further applications (biomedical, environmental).

3.2.7. Biological Stability: Total Chlorophyll Content

After a vegetation period of 35 days, the tomato plants (Figure 12) were analyzed from the point of view of the total chlorophyll content, considering that this chelated compound is responsible for the photochemical reactions during the photosynthesis process and for the good growth and development of the plant.

Reference APDMS-1 APDMS-2 PDMS-PCL-1 PDMS-PCL-2 PCL

Figure 12. Tomato plants after 35 days of planting.

Table S1 (Supplementary Materials) shows the total chlorophyll content, expressed in CCl units (% transmittance at 931 nm/% transmittance at 653 nm) for tomato plants in contact with five polymeric substances: PCL, APDMS-1, APDMS-2, PDMS-PCL-1, and PDMS-PCL-2, in relation to the control sample at the end of the vegetation period (35 days).

Analyzing experimental data allows observation of the chlorophyll pigments in the control plants and those developed in the presence of PCL close to and above those found in plants developed with APDMS-1 and APDMS-2, or PDMS-PCL-1 and PDMS-PCL-2, respectively. In addition, the presence of PCL in PDMS-1 and PDMS-2 contributes to a slight increase in the chlorophyll content compared to APDMS-1 and APDMS-2, respectively. It appears that PCL degradation has little effect on photosynthetic activity and the accumulation of assimilated compounds required for biological and metabolic processes during the vegetation period of the plants, indicating the copolymer's susceptibility to the environment and the minimal stress induced on the plants.

4. Conclusions

Using ε-caprolactone and aminopropyl-terminated polydimethylsiloxane as macroinitiators with two distinct molecular weights (APDMS), PDMS-PCL-1 and PDMS-PCL-2 copolymers were synthesized. The structures were experimentally confirmed using IR, ^{1}H-NMR, SEM, and EDX.

The copolymers obtained displayed two-enthalpy fusion relative to PDMS and PCL block polymers. Important facts were observed concerning the PCL crystallization evolution as a function of the PDMS content in these copolymers. The moisture sorption and desorption behavior of the copolymers was studied, and the values and the curve of the isotherms were in agreement with the results obtained for the contact angles of the samples PDMS-PCL-1 (107.33°) and PDMS-PCL-2 (93.46°) and the water vapor sorption capacities of PDMS-PCL-1 (0.79%) and PDMS-PCL-2 (1.89%), and that the isotherms have the shape and curve of the hydrophobic and porous materials. This fact can be explained by the low surface energy of PDMS, which is able to cover nearly the entire surface of the copolymers and move at the surface.

The fact that the total chlorophyll content of tomato plants grown in the presence of CL is slightly lower than, but close in value to, that obtained in the case of control plants leads to the idea that the biodegradation of the copolymers does not have a major disruptive effect on the metabolic activity of the plants, which makes it an acceptable product in interaction with the environment, thus widening its range of applications.

Supplementary Materials: The following supporting information can be downloaded at: https://www.mdpi.com/article/10.3390/polym15244731/s1, Scheme S1: PDMS-PCL copolymers synthesis; Figure S1: NMR spectra for PDMS-PCL-1 and PDMS-PCL-2 copolymers; Table S1: The total chlorophyll content in the leaves of tomato plants 35 days after planting.

Author Contributions: Conceptualization, M.E.F. and E.U.; methodology, M.E.F. and E.U.; software, R.R. and A.B.; validation, V.H., M.E.F. and E.U.; formal analysis, O.C.U. and C.O.B.; investigation, R.R., A.B. and C.O.B.; resources, C.O.B. and O.C.U.; data curation, M.E.F. and E.U.; writing—original draft preparation, M.E.F. and E.U.; writing—review and editing, M.E.F., E.U. and A.B.; visualization V.H.; supervision M.E.F. and C.O.B. All authors have read and agreed to the published version of the manuscript.

Funding: This research received no external funding.

Institutional Review Board Statement: Not applicable.

Data Availability Statement: Data are contained within the article and supplementary materials.

Acknowledgments: Co-author A.B. thanks for the support by a grant of the Romanian Ministry of Research, Innovation and Digitization, CCCDI—UEFISCDI, project number PN-III-P2-2.1-PED-2021-3900, within PNCDI III, Contract PED 698/2022 (AI-Syn-PPOSS).

Conflicts of Interest: The authors declare no conflict of interest.

References

1. Cingolani, A.; Caimi, T.S.; Casalini Klaue, A.; Sponchioni, M.; Rossi, F.; Giuseppe, P. A Methodologic Approach for the Selection of Bio-Resorbable Polymers in the Development of Medical Devices: The Case of Poly (L-lactide-co-ε-caprolactone). *Polymers* **2018**, *10*, 851. [CrossRef] [PubMed]
2. Narayanan, N.; Kuang, L.; Del Ponte, M.; Chain, C.; Deng, M. *Design and Fabrication of Nanocomposites for Musculoskeletal Tissue Regeneration, Nanocomposites for Musculoskeletal Tissue Regeneration*; Matthew Deans, Purdue University: West Lafayette, IN, USA, 2016; pp. 3–29.
3. Öztürk, T.; Kılıçlıoğlu, A.; Savaş, B.; Hazer, B. Synthesis and characterization of poly (E-caprolactone-co-ethylene glycol) star-type amphiphilic copolymers by "click" chemistry and ring-opening polymerization. *J. Macromol. Sci. A* **2018**, *55*, 588–594. [CrossRef]
4. Bezlepkina, K.A.; Sergey, A.M.; Vasilenko, N.G.; Muzafarov, A.M. Ring-Opening Polymerization (ROP) and Catalytic Rearrangement as a Way to Obtain Siloxane Mono- and Telechelics, as Well as Well-Organized Branching Centers: History and Prospects, Review. *Polymers* **2022**, *14*, 2408. [CrossRef] [PubMed]
5. Yilgor, E.; Isik, M.; Soz, C.K.; Yilgor, I. Synthesis and structure-property behavior of polycaprolactone-polydimethylsiloxane-polycaprolactone triblock copolymers. *Polymers* **2016**, *83*, 138–153. [CrossRef]
6. Song, L.; Ahmed, M.F.; Li, Y.; Bejoy, J.; Zeng, C.; Li, Y. PCL-PDMS-PCL Copolymer-Based Microspheres Mediate Cardiovascular Differentiation from Embryonic Stem Cells. *Tissue Eng.* **2017**, *23*, 627–640. [CrossRef] [PubMed]
7. Guarino, V.; Gentile, G.; Sorrentino, L.; Ambrosio, L. Polycaprolactone: Synthesis, Properties, and Applications. In *Encyclopedia of Polymer Science and Technology*; Herman, F.M., Ed.; Wiley-Interscience: Hoboken, NJ, USA, 2017; pp. 21–34.

8. Fortună, M.E.; Ignat, M.; Asandulesa, M.; Rotaru, R.; Pricop, L.; Harabagiu, V. Improved physico-chemical properties of mesoporous carbon by functionalization with aminopropyl-polydimethylsiloxane (AP-PDMS). *J. Inorg Organomet Polym Mater.* **2018**, *28*, 2275–2287. [CrossRef]
9. Böhm, P. Functional Silicones and Silicone-Containing Block Copolymers. Master's Thesis, Universitätsbibliothek Mainz, Jakob-Welder-Weg, Mainz, Germany, 2012. [CrossRef]
10. Zalewski, K.; Chyłek, Z.; Trzcinski, W.A. A Review of Polysiloxanes in Terms of Their Application in Explosives. *Polymers* **2021**, *13*, 1080. [CrossRef]
11. Sun, Y.; Liu, W. Synthesis and properties of triblock copolymers containing APDMS via AGET ATRP. *Poly. Bull.* **2021**, *68*, 1815–1829. [CrossRef]
12. Pavlovic, D.; Linhardt, J.G.; Kunzler, J.F.; Devon, A. Shipp, Synthesis and Characterization of PDMS-, PVP- and PS-Containing ABCBA PentablockCopolymers. *Macromol. Chem. Phys.* **2010**, *211*, 1482–1487.
13. Cheng, C.; Powell, K.T.; Khoshdel, E.; Wooley, K.L. Polydimethylsiloxane- (PDMS-) Grafted Fluorocopolymers by a "Grafting through" Strategy Based on Atom Transfer Radical (Co)polymerization. *Macromol* **2007**, *40*, 7195–7207. [CrossRef]
14. Reddy, S.B.M.; Ponnamma, D.; Choudhary, R.; Sadasivuni, K.K. A Comparative Review of Natural and Synthetic Biopolymer Composite Scaffolds. *Polymers* **2021**, *13*, 1105. [CrossRef]
15. Huan, K.; Bes, L.; Haddleton, D.M.; Khoshdel, E. Synthesisand Properties of Polydimethylsiloxane-Containing Block Copolymers via Living Radical Polymerization. *J. Polym. Sci. Part A Polym. Chem.* **2001**, *39*, 1833–1842. [CrossRef]
16. Pergal, M.V.; Antic, V.V.; Govedarica, M.N.; Goðevac, D.; Ostojic, S.; Djonlagic, J. Synthesis and Characterization of Novel Urethane-Siloxane Copolymers with a High Content of PCL-PDMS-PCL Segments. *J. Appl. Polym. Sci.* **2011**, *122*, 2715–2730. [CrossRef]
17. Kai, D.; Tan, M.J.; Prabhakaran, M.P.; Chan, B.Q.Y.; Liow, S.S.; Ramakrishna, S.; Loh, X.J. Biocompatible Electrically Conductive Nanofibers from Inorganic-Organic Shape Memory. *Polymers* **2016**, *16*, 30689. [CrossRef]
18. Fortună, M.E.; Ungureanu, E.; Jităreanu, D.C.; Țopa, D.C.; Harabagiu, V. Effects of Hybrid Polymeric Material Based on Polycaprolactone on the Environment. *Mater* **2022**, *15*, 4868. [CrossRef]
19. Mısır, M.; Ylmaz, S.S.; Bilgin, A. Synthesis and Characterization of ABA-Type Triblock Copolymers Using Novel Bifunctional PS, PMMA, and PCL Macroinitiators Bearing p-xylene-bis(2-mercaptoethyloxy) Core. *Polymers* **2023**, *15*, 3813. [CrossRef]
20. Işık, M. Synthesis of Aba Type Triblock Copolymers by Ring Opening Polymerization and Investigation of the Structure Property Behavior of the Copolymers. Master's Thesis, Kırşehir Ahi Evran University, Kırşehir, Turkey, August 2011.
21. Marta, A.E.; Slabu, C.; Covasa, M.; Motrescu, I.; Lungoci, C.; Jităreanu, D.C. Influence of Environmental Factors on Some Biochemical and Physiological Indicators in Grapevine from Copou Vineyard, Iasi, Romania. *Agronomy* **2023**, *13*, 886. [CrossRef]
22. Elzein, T.; Nasser-Eddine, M.; Delaite, C.; Bistac, S.; Dumas, P. FTIR study of polycaprolactone chain organization at interfaces. *J. Colloid Interface Sci.* **2004**, *273*, 381–387. [CrossRef]
23. Ran, Q.; Li, B.; Sun, D.; Yin, H.; Wan, Y.; Yang, C.; Liu, Y.; Mao, Y. Using Self-Synthesized Aminopropyl-Terminated Polydimethylsiloxane to Toughen Epoxy Resin: The Role of Molecular Weight of Polydimethylsiloxane. *J. Vinyl Addit. Technol.* **2017**, *23*, 305–311. [CrossRef]
24. Nistor, A.; Stiubianu, G.; Racles, R.; Cazacu, M. Evaluation of the Water Sorption Capacity of Some Polymeric Materials by Dynamic Vapour Sorption. *Plast. Mater.* **2011**, *48*, 33–37.
25. Iojoiu, C.; Hamaide, T.; Harabagiu, V.; Simionescu, B.C. Modified poly(e-caprolactone)s and their use for drug-encapsulating nanoparticles. *J. Polym. Sci. Part A Polym. Chem.* **2004**, *42*, 689–700. [CrossRef]
26. Gordin, C.; Delaite, C.; Bistac, S.; Schuller, A.S.; Rusu, D.; Rusu, M. PDMS migration at poly(vinyl chloride)/poly(ε-caprolactone)/poly(ε-caprolactone)-b-poly(dimethylsiloxane) blends surfaces. *Polym. Test.* **2009**, *28*, 446–451. [CrossRef]

polymers

MDPI

Article

Comparison Adsorption of Cd (II) onto Lignin and Polysaccharide-Based Polymers

Elena Ungureanu [1], Maria E. Fortună [2,*], Denis C. Țopa [1], Carmen O. Brezuleanu [1], Vlad I. Ungureanu [3], Ciprian Chiruță [1], Razvan Rotaru [2], Bogdan M. Tofanica [4,*], Valentin I. Popa [4] and Doina C. Jităreanu [1]

[1] "Ion Ionescu de la Brad" Iasi University of Life Sciences, 3 Mihail Sadoveanu Alley, 700490 Iasi, Romania; eungureanu@uaiasi.ro (E.U.); topadennis@uaiasi.ro (D.C.Ț.); olgutabrez@uaiasi.ro (C.O.B.); kyru@uaiasi.ro (C.C.); doinaj@uaiasi.ro (D.C.J.)
[2] Institute of Macromolecular Chemistry "Petru Poni", 41A Grigore Ghica Voda Alley, 700487 Iasi, Romania; rotaru.razvan@icmpp.ro
[3] Polytechnic University of Timisoara, 2 Piata Victoriei Alley, 300006 Timisoara, Romania; vlad.ungureanu@student.upt.ro
[4] "Gheorghe Asachi" Technical University of Iasi, 73 Prof. Dr. Docent Dimitrie Mangeron Blv., 700050 Iasi, Romania; vipopa@tuiasi.ro
* Correspondence: fortuna.maria@icmpp.ro (M.E.F.); b.m.tofanica@gmail.com (B.M.T.)

Abstract: Given the predominantly negative impact of heavy metals on living organisms, the present study proposed to evaluate the adsorption performances under static conditions of Cd (II) from aqueous solutions on unmodified Sarkanda grass lignin compared to the adsorption performances of polysaccharide polymers chemically functionalized, obtained by synthesis and in their native state, but which, although effective, have a cost price that does not allow for large-scale expansion. To improve the retention of Cd (II) on this aromatic component of the biomass resulting from the processing of lignocellulosic materials, different experimental conditions (pH, concentration, dose and contact time) were followed. The Freundlich and Langmuir isotherms were used to describe the equilibrium conditions. Adsorption kinetics were assessed using the Lagergren I and Ho and McKay II kinetic models, furnishing informative insights into the process mechanism. Lignin adsorption capacity was also analyzed by performing biological tests on tomato seeds (*Lypercosium esculentum*), since heavy metals are known to be a stress factor for seeds by disturbing the osmotic equilibrium. Through the prism of the investigated parameters and under precisely established experimental conditions, unmodified Sarkanda grass lignin—an aromatic biopolymer—can be recommended as a promising adsorbent for the retention of Cd (II) from aqueous solutions, successfully replacing polysaccharide, especially cellulose-based polymers.

Keywords: polysaccharide; biopolymer; lignin; adsorption; cadmium ion

Citation: Ungureanu, E.; Fortună, M.E.; Țopa, D.C.; Brezuleanu, C.O.; Ungureanu, V.I.; Chiruță, C.; Rotaru, R.; Tofanica, B.M.; Popa, V.I.; Jităreanu, D.C. Comparison Adsorption of Cd (II) onto Lignin and Polysaccharide-Based Polymers. *Polymers* **2023**, *15*, 3794. https://doi.org/10.3390/polym15183794

Academic Editors: Can Jiang, Qiang Li and Wangda Qu

Received: 16 August 2023
Revised: 12 September 2023
Accepted: 14 September 2023
Published: 17 September 2023

1. Introduction

Society has become sensible to the harmful effects of pollutants such as heavy metals, xenobiotics, and waste based on synthetic polymers, which requires the development of phytoremediation processes that are effective, inexpensive, and ecologically non-disturbing and can be applied on a large scale. From point view of their ecological significance for the existing trophic chains, where they can interfere with the functioning of vital cellular components and persist in the long term [1], heavy metals present in the environment, whether from natural sources (igneous and sedimentary rocks, erosion, and formation processes of soils) or from anthropogenic sources (industrial activities, transport, and agriculture [2,3]) are considered threats to living systems [4]. The reduction in the number of beneficial microorganisms in the soil because of the high concentration of heavy metals can influence the decrease in the decomposition process of organic matter,

leading to a reduction in soil fertility. The consequences of heavy metal stress include disturbances of metabolic processes, including seed germination disorders [5].

The mechanisms of accumulation of heavy metal have not yet been fully elucidated. Some heavy metals (Hg, Cd, Pb), have no physiological role and, moreover, have harmful effects on human health [6]. It is also possible that heavy metals effects on plants can lead to changes in proteins [7] or in the metabolism of carbohydrates and amino acids [8]. The result of changes in the processes of autoxidation of enzymes and peroxidation of lipids [9] is the consequence of an increased concentration of active oxygen [5]. By the impact of its toxicity on the ecological, evolutionary, nutritional, and environmental segments, cadmium can be considered a "main threat" to life because it is non-biodegradable, accumulates in the environment, and, subsequently, contaminates the food chain.

Due to their increased susceptibility to biodegradation, the waste of some natural polymers, such as lignin, the second most abundant organic macromolecule in plants after cellulose, is easily bio assimilated without the need for additional operations, aimed at facilitating the degradative action of environmental factors [10]. Porous or fibrous materials for the removal of saturated hydrocarbons, the heavy metals or oils work, according to two principles: adsorption (adsorbents) and absorption (absorbents) [11]. Usually porous and/or fibrous materials present both phenomena in contact with a liquid: absorption (by capillary action) and adsorption (by surface phenomena). In this case, the phenomenon is generically called sorption, and the sorbent material. Natural cellulosic materials such as lignin, moss, peat, sawdust, kapok (Java cotton), and kenafal (Deccan hemp or Java jute) are cheap, renewable, and abundant in the plant ecosystem [12,13]. There are literature data that attest to the quantitative retention of metal ions on lignin [14], but the adsorption capacity of heavy metal ions differs significantly depending on the origin of the lignin and the delignification process used.

The phenomenon of sorption of a heavy metal through the surface of a solid material occurs through physical attraction forces such as van der Waals, Debye, and Kiesom forces, components of energy dispersion of the London type [15]. Other studies show that the sorption phenomenon is closely related to the presence of hydrophobic groups on the surface of the sorbent material [16,17]. The important chemical groups that could be responsible for good sorption are the O-H, COO-H, and C=O groups [18,19]. According to some researchers [20], the adsorption of metal ions on lignin occurs through ion exchange mechanisms, but there are also literature studies [21] that assume that the adsorption of metal ions on lignin is the result of the combination of several mechanisms, such as ion exchange, adsorption, and complexation [22–24]. Sorption capacity depends not only on the nature of the sorbent but also on the type of polluting to be collected [25]. At the global level, lignin resulting in the manufacture of cellulose or from hydrolysis technologies can be harnessed as a result of its origin from renewable resources at a low price. [1]. "Low-cost" materials seem to be a lever for the future in terms of the retention of heavy metal ions, and lignin, this main aromatic component of biomass, can be considered an alternative raw material for fossil resources which can represent a plausible solution in some previous studies demonstrating the efficiency of this lignocellulosic waste in the adsorption of lead, zinc, and arsenic ions [26,27].

Also, lignin is a polyaromatic, porous and branched polymers, resistant and stable to the action of acids but sensitive to the action of oxidizing agents, consisting of thousands of phenylpropane monomer units, C3–C6 polymerized, with a high content of functional groups, which chemical bonds with metal ions, and provide to lignin cationic exchange capacity to be able the removal of polluting species, such as heavy metal ions [28,29]. Through the action of oxidants on the lignin fractions, it is possible to form fractions with properties similar to fulvinic and humic acids, which, in the presence of $Me(H_2O)^{2+}$ type aqua complexes, have the property of substituting the 2/4/6 molecules from the inner coordination sphere of water, forming complex combinations [24].

The initial pH, sorbent dose, the concentration, the contact time, and the temperature are very important factors in optimizing the adsorption process of polluting species [26,27].

To obtain information about the adsorption capacity of a given material under well-defined experimental conditions that can then be used for the design of a large-scale industrial wastewater treatment system, it is necessary to model the equilibrium data obtained experimentally [30]. Adsorption processes are evaluated with the adsorption isotherms obtained graphically, which show how much solute is retained by a certain adsorbent under well-defined experimental conditions. To interpret of experimentally obtained adsorption isotherms, a series of mathematical models are used, generically called models of adsorption isotherms (Langmuir and Freundlich models) [30–32]. From an experimental point of view, it is useful to know the adsorption kinetics and the time at which the solute is removed from the solution to be able to develop an effective experimental strategy [30,32].

In the kinetic modeling, it is considered that the driving force of adsorption is precisely the difference between the concentration of the solute in the solid phase (retained on the adsorbent) and its concentration in contact with the adsorbent. The kinetics of the adsorption process depend both on the actual retention process and on the diffusion stages that govern the transfer of the solute from the solution to the active centers on the surface of the adsorbent, providing particularly important information regarding its mechanism. Therefore, when choosing a kinetic model, the initial and final concentrations of the solute in the solution at different time intervals will be taken into account [33]. Although the adsorption process is influenced by temperature, pH of the initial solution, dosage, solute concentration, etc., the kinetic equations take into account only the influences of the noticeable parameters on the global speed [32]. The most frequently used kinetic models that try to approximate as faithfully as possible the existing mechanism in the case of the adsorption of pollutants from aqueous solutions are the Lagergren pseudo-I order and Ho and McKay pseudo-II order models [30–33].

Considering these aspects, the present study proposed to test the adsorption capacity in static conditions of unmodified Sarkanda grass lignin, used as a chemical substrate for an aqueous solution of Cd (II), considering the results obtained in other previous studies through which Sarkanda grass lignin is recommended as an effective adsorbent for Pb (II), Zn (II), and As (III) retention [26,27].

2. Materials and Methods

2.1. Materials

Chemical materials main: Unmodified Sarkanda grass lignin nanoparticles (Sarkanda Grass-100SA-140, with the properties: COOH, mmol/g: 3.3; Aromatic OH, mmol/g: 1.7; Chelating capacity (m_{echiv}/100g): 67.14; Average porosity: 74%; Particle diameter (μm): approx. 1), supplied by Granit Récherche Development S.A., Lausanne, Switzerland) and $CdSO_4 \bullet 8H_2O$ supplied by ChimReactiv S.R.L., Bucharest, Romania.

Biological material: Tomato seeds (*Lypercosium esculentum* variety) offered by "Ion Ionescu de la Brad", Iasi University of Life Sciences, Iasi, Romania.

2.2. Experimental Procedure

It was supposed that in contact with the polluting species, in the present case Cd (II), lignin, through its porous structure and the functional groups it has, will probably trigger an activated adsorption attributed to dissociation and interaction with the metal ion, forming complex combinations (Scheme 1).

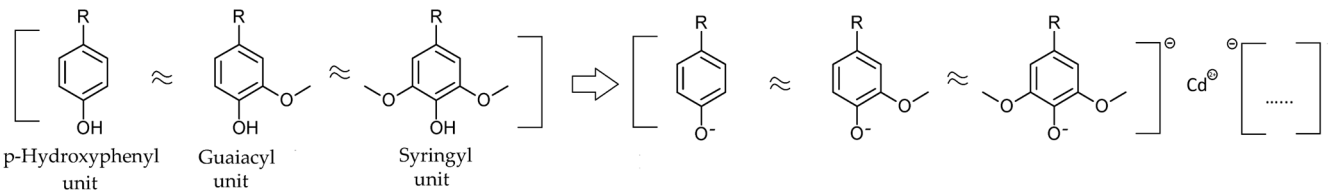

Scheme 1. Potential initial interaction between the lignin structural units and Cd (II).

The preparation of the stock solutions (0.001 mg/L) consisted of the dissolution of $CdSO_4 \cdot 8H_2O$, in distilled water. The experimental program is shown in Scheme 2.

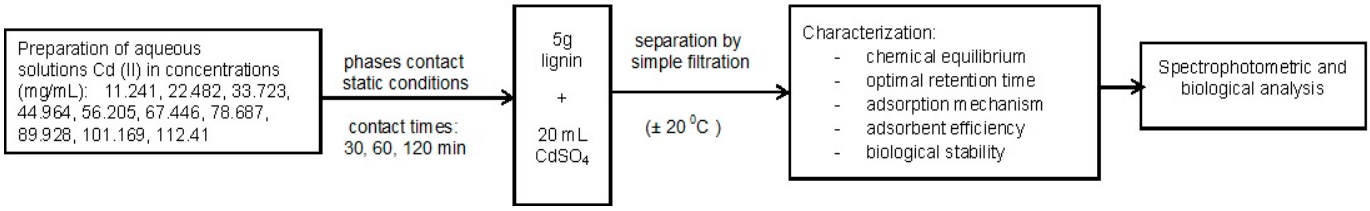

Scheme 2. Experimental program.

2.2.1. Adsorption Experiments

In order to be able to develop an effective experimental strategy, it is necessary to accurately establish the ideal experimental conditions. To this purpose, the preceding experiments targeted the different conditions of concentrations of Cd (II), the pH, the temperature, the dosages, and the contact times. Experiments were performed at ±20 °C with 5 g of lignin in 1 L of Cd (II). The significant parameters that influence the sorption processes are the pH, the species, the solubility of metal ions, and the electric charge of the surface of the solid sorbent [19]. Literature studies recommend pH 6 for the adsorption of cadmium on different lignocellulose supports [31,34]. Following the experimental tests, the initial optimum pH was established at 6.2.

2.2.2. The Germination Test

In order to have a definite conclusion on the efficiency of Cd (II) adsorption from aqueous solution on Sarkanda grass and on the toxic potential of the polluting species, biological tests were performed both on the contaminated lignin samples and on the filtrates resulting from the retention of the polluting species for tomato seeds of the variety *Lypercosium esculentum*, in laboratory conditions, in three repetitions. As control samples, distilled water was used for the filtrates and, for the contaminated lignin, uninfected adsorbent. To be able to estimate as faithfully as possible the impact of the polluting species on the evolution of the plants, the biological processes expressed by the energy and germination evolution, the height, and the mass of the seedlings were followed in order for a period of seven days.

2.3. Characterization Methods

2.3.1. Surface Morphology

Scanning electron microscopy (SEM) was used (Brno, Czech Republic) using a Quanta 200 scanning electron microscope (5 kV) equipped with an EDX elemental analysis system (Ametek, Berwyn, PA, USA). Also, to capture the images in natural and polarized light, the trinocular polarizing microscope (Inf Plan 4/10/20/40: WF10x20: 20W Hal (TL) Kern OPM 181) was needed.

The wettability of Sarkanda grass lignin nanoparticles before and after sorption of Cd (II) from an aqueous solution was investigated by measuring the contact angle of a drop of liquid (water) placed on the surface of the sample using the KSV Cam 200 device from KSV Instruments Ltd. (Helsinki, Finland). Ten measurements were performed for each liquid guide drop.

2.3.2. Spectrophotometric Determination of Cd (II)

For determining the concentration of Cd (II), Xylenol orange was used, with maximum absorption at 575 nm [31]. Quantitative determination of the metal ion obtained after filtration from the aqueous solutions was carried out by analysis of an exactly measured

volume (2 mL) according to the experimental procedure, and the concentration value for each sample was calculated from the regression equation of the calibration curve.

For the spectrophotometric analysis, we used a Visible Spectrophotometer for laboratory, model VS-721N, 300-1000 nm, manufacturer JKI, Shanghai, China.

2.3.3. Isotherm Models

Adsorption isotherms offer information about the distribution of solute particles between the two phases of the adsorption system [17,18,26,27]. The adsorption efficiency of Cd (II) was evaluated by Equation (1):

$$q = (c_i - c_e)V/m, \text{ (mg/g)} \quad (1)$$

where c_i—initial concentration (mg/mL), c_e—equilibrium concentration (mg/L), V—volume of metal ion solution (L), m—mass of adsorbent (g).

The Langmuir isotherm is expressed using Equation (2):

$$q_e = q_{max}(k_L \cdot c_e/1 + k_L \cdot c_e) \quad (2)$$

where q_e—amount of metal ions adsorbed per unit of mass of adsorbent (mg/g) at equilibrium, q_{max}—maximum amount of metal ions retained on the absorbent after complete saturation (mg/g), K_L—Langmuir constant related to the free energy of adsorption (L/mg), c_e—equilibrium concentration of metal ions in solution (mg/L).

The Freundlich isotherm uses the empirical Equation (3), where, q_e—amount of metal ions adsorbed per unit of mass of adsorbent (mg/g) at equilibrium, k_F—Freundich constant, indicating adsorption capacity, n—constant characterizing the affinity of metal ions to sorbent, c_e—concentration at equilibrium of metal ions in solution (mg/L) [26,27]:

$$q_e = k_F \cdot c_e^{1/n} \quad (3)$$

The linear regression analysis can be used to determine the most appropriate model that accurately represents the experimental data of the isotherm or the least squares method with which the correlation coefficient R^2 is calculated [34].

2.3.4. Kinetic Models

The kinetic parameters of Cd (II) adsorption on lignin are determined from the slopes and the intercept with the ordinate of the linear dependences lg ($q_e - q_t$) and t, respectively, t/q_t and t, with the two commonly used Lagergren pseudo-I order and Ho and McKay pseudo-II order kinetic models. The Lagergren model for adsorption in a liquid–solid system and the Ho and McKay model are shown in Equations (4) and (5) [26–28]:

$$\lg(q_e - q_t) = \lg q_e - (k_1/2.303)\, t \quad (4)$$

$$t/q_t = (1/k_2 \cdot q_e^2) + t/q_e \quad (5)$$

The choice of the most appropriate kinetic model for the verification of the experimental data was done with the help of linear regression.

2.3.5. Biological Stability

To evaluate the seed germination parameters, the dimensions, and the mass of the resulting seedlings, germination tests were carried out for 7 days [35,36] in three repetitions with batches of 10 seeds each. The seeds were disinfected with NaClO 5% for 5 min, after which they were washed three times with MilliQ ultrapure water until the characteristic smell disappeared [37,38]. The seeds were placed in test tubes wide enough (180 × 18 mm) to allow their mixing with the filtrates and distilled water (control). Then, they were incubated for one hour with intermittent shaking to soak the seeds with filtrate or distilled water, according to the recommendations of ISTA (Seed Science and Technology, 1993) [39], after which they were evenly distributed in Petri dishes on filter paper (90 × 15

cm). The toxicity of filtrates and lignin contaminated with aqueous cadmium solutions was tested in the studied concentration domain at the three contact times of the phases: 30, 60, and 120 min. Distilled water was used as a control sample for filtrates, and uncontaminated lignin was used as a control sample for contaminated lignin.

The following were determined: the number of germinated seeds after three days (germination energy, E_g, %) and the capacity of the seeds to germinate until the end of the germination period (germination faculty, F_g, %) and the length and weight of the plant after seven days. E_g and F_g were determined with Equations (6) and (7) [32]:

$$E_g = (a/n)100 \quad (6)$$

$$F_g = (b/n)100 \quad (7)$$

where a—number of germinated seeds in the first third of the period, n—total number of analyzed seeds, b—number of germinated seeds at the end of the period (seven days of germination

The seeds found swollen, rotten, and moldy at the end of the germination period were considered non-germinated. The experimental working parameters in the growth room (±24 °C, the alternation of 16 h light and 8 h dark) were chosen so as to match the specific living conditions of *Lypercosium esculentum*.

3. Results

3.1. Evaluation of the Efficiency Cd (II) Adsorption onto Sarkanda Grass Lignin

To evaluate the adsorptive performance of Sarkanda grass lignin, several experimental tests were carried out that had the main purpose of determining the stability of an optimum in terms of the pH, the concentration, dose, and the time of contact.

3.1.1. Dose Lignin and Initial Concentration of Cd (II)

The literature data recommend a dose of lignin fraction in the range of 4–40 g/L [33]. In this sense, experimental tests were carried out in the domain of 4–40 g lignin/L Cd (II) aqueous solution, and it was found that increasing the dose of lignin leads to a decrease in the quantity of metal ions retained per unit mass of adsorbent (Figure 1).

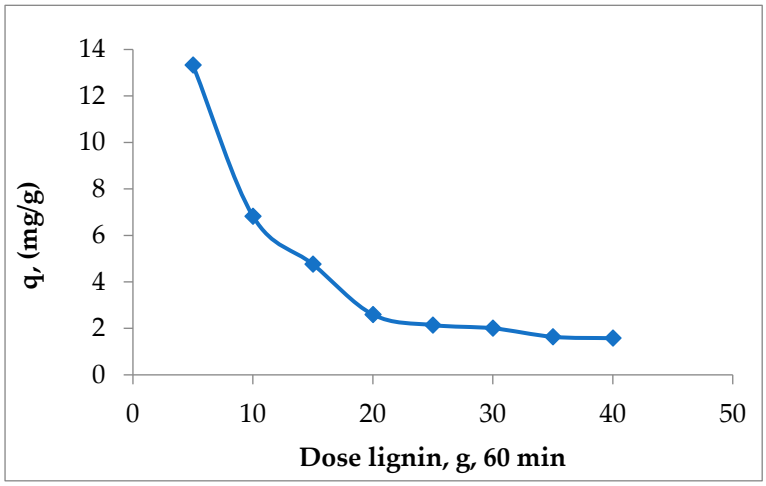

Figure 1. The influence of unmodified Sarkanda grass lignin dose on the efficiency of the Cd (II) adsorption in concentration 112.41 mg/L, contact time 60 min, pH 6.2.

This variation of the values of q with the increase in the adsorbent dose can be explained as follows: with the increase in the adsorbent dose, the number of active centers (superficial functional groups) also increased; therefore, the amount of metal ions retained from the aqueous solution increased until reaching a maximum value. Further increasing

the dose of adsorbent no longer had the same effect due to the phenomenon of agglomeration of lignin particles (a fact confirmed by microscopic analyses), which can lead to the blocking of superficial functional groups and, consequently, the values of q decreased. This is in accordance with the existing observations in the specialized literature, which show that, for a given adsorbent, the retention of metal ions from aqueous solutions occurs with high productivity when the experimental conditions are well selected [35,36]. Under these conditions and based on previous experiments [26,27], but also on the preliminary tests performed (Figure 1), it was estimated that a lignin dose of 5 g/L is optimal for the elimination of Cd (II) ions from aqueous solutions. To be able to estimate the adsorption efficiency, the quantity of Cd (II) that remains per unit mass of lignin (q, mg/g) was calculated. The increase in Cd (II) in the concentration domain studied determined a growth in the adsorption capacity of lignin from 1.3328 mg/g to the concentration of 11.241 mg/L to 13.4285 mg/g at the concentration of 112.41 mg/L, contact time 60 min (Figure 2).

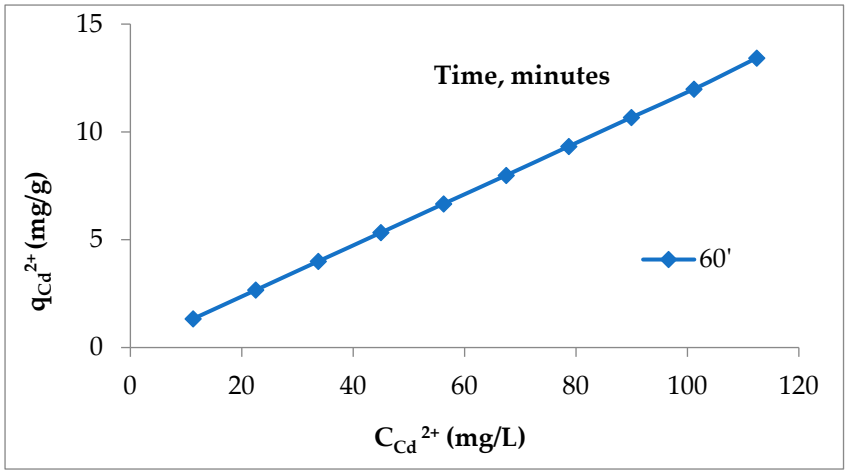

Figure 2. Quantity of Cd (II) retained per unit mass of unmodified Sarkanda grass lignin.

When the concentration of Cd (II) in the solution increased, the quantity of cadmium retained on the lignin increased, a fact explained by increasing the ratio between the initial number of moles of Cd (II) and the number of accessible positions of sorption on the lignin fraction. Also, with the lignin pores being filled with the solution of the polluting species, no matter how much the concentration of the chemical species increases, adsorption became impossible, as the saturation state had been reached.

3.1.2. Initial pH and Contact Time

From the analysis of the speciation diagram of cadmium in aqueous solutions, it emerged that up to pH 10, the dominant species was Cd (II); after pH = 8.0, the dominant species was $CdOH^-$ and $Cd(OH)_2$ species begin to form, but the fractions of these species were lower than 30% for $CdOH^-$ and 20% for $Cd(OH)_2$, respectively [30]. Therefore, it is necessary to consider the role of H^+ and OH^- ions in regulating the electric potential of the magnetic surface, which can lead to changes in the equilibrium characteristics of the adsorption process. At low pH, the excess of protons can compete with cadmium ions for the bonds with lignin, and the retained metal ions were lower. At high pH, due to the dissociation of functional groups from lignin, the level of retained metal ions on lignin was higher. On the other hand, at pH above 6.2, there was the possibility of Cd (II) precipitation in the form of hydroxide, which affects the adsorption efficiency [19]. Figure 3 shows the influence of the pH of the initial solution on Cd (II) adsorption on Sarkanda grass lignin (60 min contact time, ±20 °C).

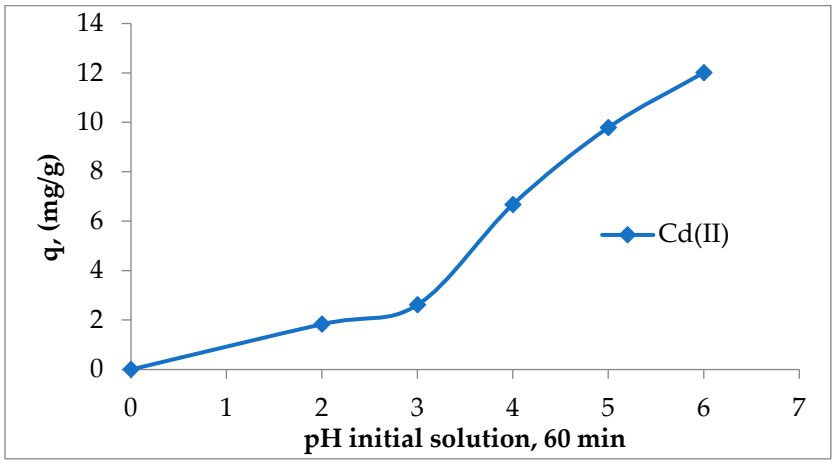

Figure 3. The influence of the pH of the initial solution on Cd (II) adsorption on unmodified Sarkanda grass lignin.

As can be seen in Figure 3, the adsorption capacity of lignin for Cd (II) increased with an increase in the initial pH of the solution. This variation was mainly determined by the fact that with the increase in the pH of the initial solution, the deprotonation of the functional groups on the lignin surface (especially the carboxyl and hydroxyl ones) took place, which became negatively charged and can bind the positively charged metal ions from the aqueous solution. Regardless of the initial concentration of Cd (II) ions, at pH higher than 6.5, quantitative precipitation took place, with the lignin particles probably becoming precipitation centers for Cd (II) ions, which find on the surface of the adsorbent sufficient hydroxyl and carboxyl groups, in particular, to allow the transformation into a difficult soluble compound. Considering these aspects and following the experimental tests carried out (Figure 3), a pH of 6.2 was chosen.

Considering the experimental data obtained (Figure 4) and the literature recommendations, which suggest a longer contact time between the phases because it can provide important clues about the interfacial dynamics and equilibrium [31,33], 60 min can be considered the optimal contact time for the absorption of Cd (II) on Sarkanda Grass lignin. Also, the contact time of 120 min was excluded because there were no variations in the adsorption capacity compared to those recorded at 60 min (Figure 4).

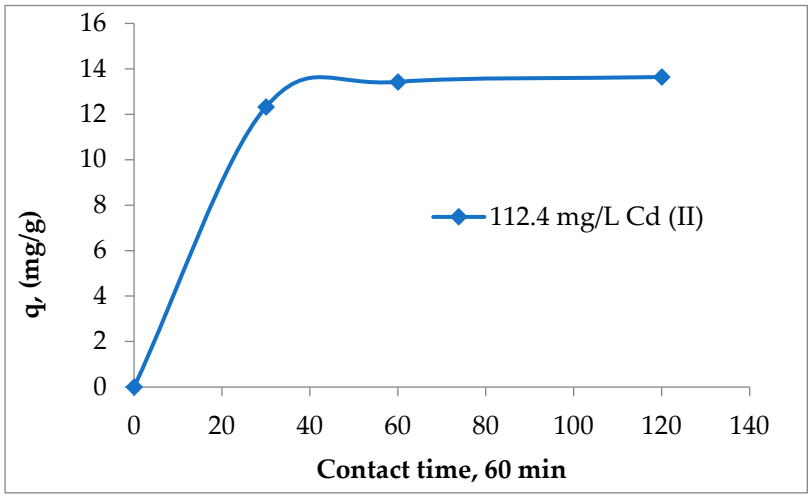

Figure 4. The influence of contact time on the adsorption of Cd (II) on unmodified Sarkanda grass lignin.

In other previous studies regarding the adsorption of Pb (II), Zn (II), and As (III) ions from aqueous solutions on lignin, the ideal contact time was also 60 min [26,27], which

ensured good reproducibility of data and recommended this duration as being optimal for the adsorption of heavy metal ions from aqueous solutions on lignin Sarkanda grass substrate.

3.2. Assessment of Cd (II) Adsorption on Sarkanda Grass Lignin Based on Observations Deduced from Surface Analysis

Microscopic studies show that lignin, through its porous structure (Figure 5), can act as a chemical substrate in which the functional groups are strongly linked to the skeleton and can retain polluting species.

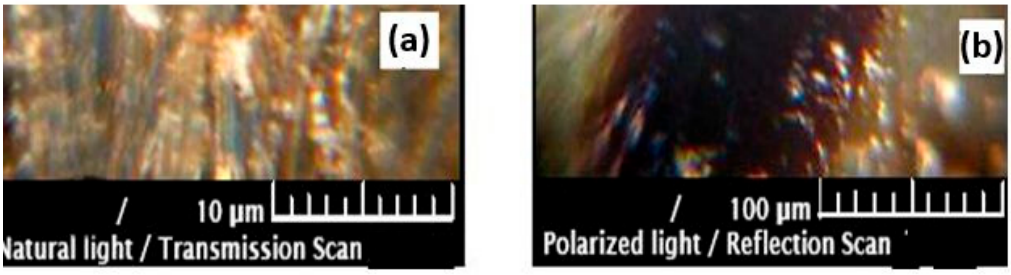

Figure 5. Microscopic images in natural (**a**) and polarized (**b**) light for unmodified Sarkanda grass lignin.

Microscopic images captured in natural (a) and polarized (b) light for the most contaminated Sarkanda grass lignin sample, at a concentration of 112.41 mg/L and contact time of 60 min (Figure 6), confirmed the diffusion of pollutant species in the pores of the adsorbent and the achievement of adsorption.

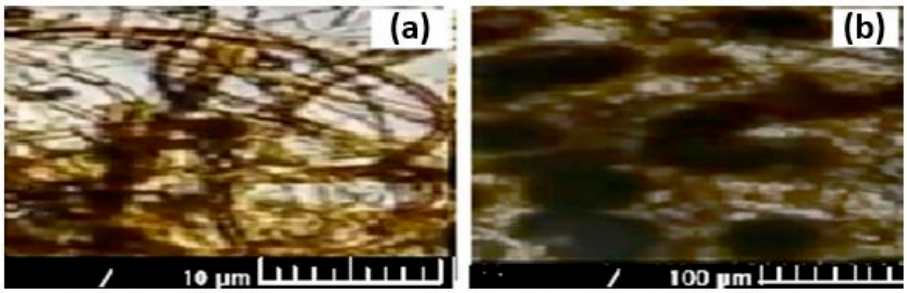

Figure 6. Microscopic images in natural (**a**) and polarized (**b**) light for Sarkanda grass lignin contaminated with Cd (II).

The morphology and composition of the lignin before adsorption and after Cd (II) adsorption at a concentration of 112.41 mg/L and contact time of 60 min were identified by scanning electron microscopy (SEM) coupled with energy dispersive X-ray analysis (EDX) (Figures 7 and 8).

The SEM micrograph of the unmodified lignin clearly showed well-separated particle agglomeration of about 4 µm lengths. The particles that form these agglomerations have micrometric dimensions, which confirm the diffraction analyzer.

The EDX spectra for the samples are given in Figure 7a,b, showing the main peaks of C, O, and S elements coming from both samples. The EDX spectrum for lignin after Cd (II) adsorption clearly shows the adsorption of cadmium. For SEM analysis, the prepared sample has been metallized with Pt to improve the contrast, thus resulting in Pt in both samples. EDX and SEM analyses of the unmodified lignin clearly show the contact, diffusion, and retention of the pollutant species in the lignin fraction in the pores of Sarkanda grass lignin particles.

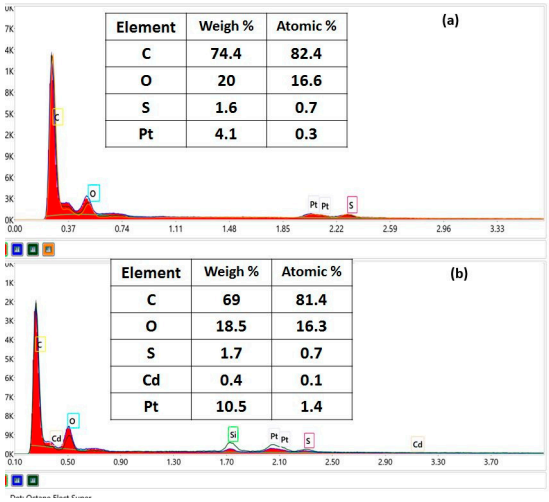

Figure 7. EDX elemental analysis for lignin before adsorption (**a**) and after Cd (II) adsorption (**b**) .

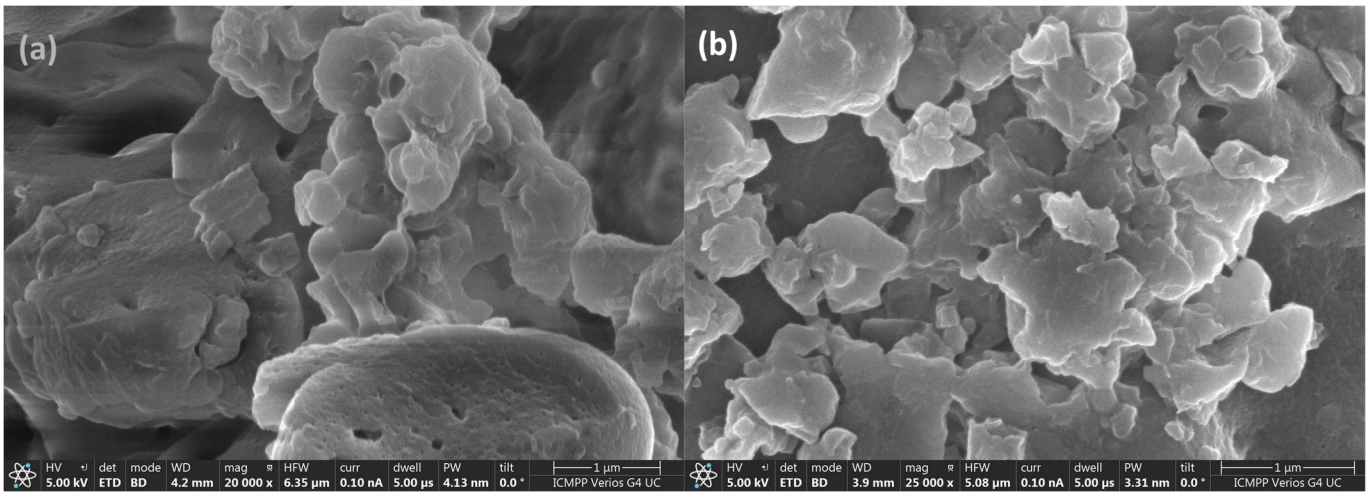

Figure 8. The SEM images for lignin before adsorption (**a**) and after Cd (II) adsorption (**b**) .

3.3. Wettability Study

It is known that lignin contains, like any organic macromolecular compound, hydrophilic and hydrophobic groups that can influence the progress of sorption processes. The measured data are given in Table 1 for unmodified Sarkanda grass lignin (not introduced into the Cd^{2+} solution) and in Table 2 for the used lignin (after the sorption of the Cd2+ solution). Time represents the duration of the contact angle measurement; CA L and CA R represent the contact angle measured on the left and right of the drop; CA M represents the calculated average of the contact angle; L, H, and V represent the width, height, and volume of the water drop; and A represents the contact surface between the water drop and the lignin.

Table 1. Measured values for unmodified Sarkanda grass lignin.

Time [s]	CA L	CA R	CA M	L [mm]	H [mm]	V [µL]	A [mm²]
0.000	83.5	85.4	84.5	1.66	0.73	1.01	3.88
0.016	81.3	82.8	82.1	1.65	0.70	0.95	3.74
0.032	81.3	82.8	82.1	1.65	0.70	0.95	3.74
0.048	81.2	82.6	82.9	1.65	0.70	0.96	3.74
0.064	80.9	82.6	81.7	1.65	0.70	0.96	3.76
0.080	83.3	85.3	81.3	1.66	0.73	1.02	3.89
0.096	81.0	82.5	81.8	1.65	0.70	0.96	3.75

0.112	81.2	82.8	82.0	1.65	0.70	0.95	3.73
0.128	81.1	82.6	81.8	1.65	0.70	0.96	3.75
0.144	81.0	82.6	81.8	1.65	0.70	0.96	3.76

Table 2. Measured values for contaminated Sarkanda grass lignin.

Time [s]	CA L	CA R	CA M	L [mm]	H [mm]	V [μL]	A [mm²]
0.000	98.9	99.5	99.2	1.53	0.86	1.15	4.23
0.016	98.4	99.0	98.7	1.53	0.85	0.13	4.19
0.032	99.9	100.2	100.0	1.52	0.87	1.17	4.27
0.048	98.5	99.3	98.9	1.53	0.86	1.14	4.21
0.064	97.8	98.3	98.0	1.53	0.70	1.10	4.11
0.080	98.8	99.4	99.1	1.52	0.84	1.12	4.16
0.096	97.8	98.7	98.3	1.53	0.85	1.13	4.17
0.112	98.0	98.5	98.2	1.53	0.85	1.12	4.16
0.128	96.5	97.2	96.9	1.53	0.83	1.08	4.05
0.144	96.5	98.3	97.9	1.53	0.84	1.10	4.11

A contact angle with a value below 90 degrees means hydrophilic character (water absorbent), and a contact angle above 90 degrees means hydrophobic character. The unmodified Sarkanda grass lignin has a hydrophilic character, it absorbs water and implicitly also the aqueous solution of Cd (II), as a consequence of its porous structure. Contaminated Sarkanda grass lignin has a hydrophobic character, it repels water in this block, meaning that the lignin has absorbed the Cd (II) solution and reached saturation (Figure 9).

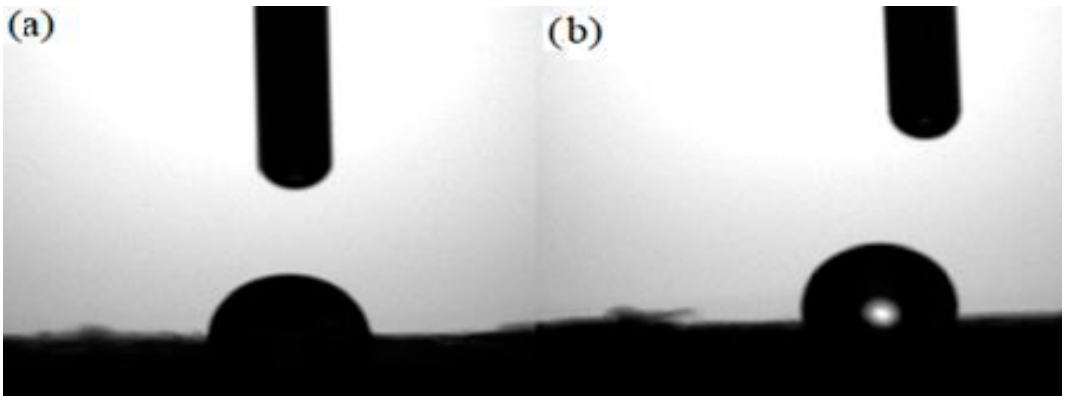

Figure 9. Contact angle images for unmodified lignin (**a**) and contaminated lignin (**b**) with Cd (II), in concentration 112.41 mg/L, contact time 60 min.

3.4. Modeling of Adsorption Equilibrium of Cd (II) onto Sarkanda Grass Lignin by Obtaining Freundlich and Langmuir Isotherms

The classic Freundlich and Langmuir isotherms show information about the type of adsorption, monolayer or multilayer, and are frequently used to model adsorption isotherms. The choice of the most appropriate model was made on the basis of the correlation coefficients (R^2), which are calculated from the linear representation of each individual model and allow the quantitative evaluation of the efficiency of the studied adsorption process.

Figure 10 shows the Freundlich (a) and Langmuir (b) models for Cd (II) adsorption from aqueous solutions on Sarkanda grass lignin.

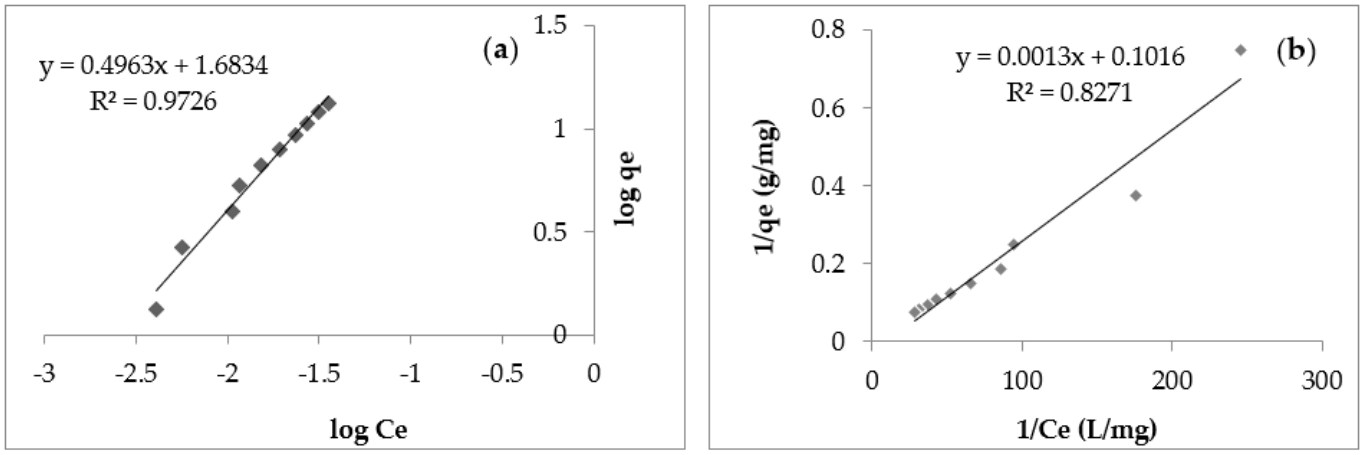

Figure 10. Freundlich adsorption model (**a**) and Langmuir adsorption model (**b**) for Cd (II) retention onto Sarkanda grass lignin after 60 min.

From Table 3, the values of the correlation coefficients (R^2) obtained in the Langmuir model fell within the domain of 0.8219–0.8863 and were lower than the values of the correlation coefficients (R^2) obtained in the case of the Freundlich model (0.9637–0.9810), showing that the experimental data better verified the Freundlich model.

Table 3. Characteristic parameters of Freundlich and Langmuir models for Cd (II) adsorption on Sarkanda grass lignin.

Pollutant	Time (Min)	Freundlich Model			Langmuir Model		
		R^2	1/n	k_F	R^2	q_{max} (mg/g)	K_L
Cd^{2+}	30	0.9810	0.9125	0.8321	0.8863	2.4224	0.2457
	60	0.9726	0.9312	1.0432	0.8276	2.5562	0.3411
	120	0.9637	0.9041	1.0359	0.8219	2.7593	0.3528

By analyzing Table 3, it can be seen that the values of K_F fell within the domain 0.8321–1.0432, and those of 1/n were included in the domain 0.9041–0.9312, which indicates the presence of a binding energy by adsorption due to interactions of ion exchange or surface complexation. The values of K_L fell within the domain of 0.2457–0.3528, being lower, as can be seen, than the values of K_F.

The value of 1/n was useful to intuit the nature and intensity of the interactions between the metal ions and the functional groups of the adsorbent. Thus, a value between 0 and 1 describes a favorable adsorption process. Moreover, the closer the value of 1/n is to 1, the stronger the interactions between the metal ions in the aqueous solution and the functional groups of the adsorbent. In the current study, the value of 1/n was in the range 0.9041–0.9312, which suggests favorable or active chemisorption with the formation of strong bonds.

Also, the contact time of 60 min seemed to be the optimal adsorption time. At 120 min, the changes were very small, a fact owed to saturation, when the concentration gradient and the adsorption speed decreased, which were otherwise normal behaviors in the case of surface processes such as adsorption.

3.5. Kinetic Modeling of the Adsorption of Cd (II) onto Sarkanda Grass Lignin

In order to interpret the kinetic data of the process, the experimental results were processed using Lagergren pseudo-I order and Ho and McKay pseudo-II order kinetic models. Through linear regression, using the Lagergren pseudo-first order and the Ho and McKay pseudo-II order kinetic models to reflect the adsorption capacity of the solid phase, the correlation coefficients (R^2) were calculated.

In Table 4, the characteristic kinetic parameters are presented and calculated. The kinetic models are represented in Figure 11a,b.

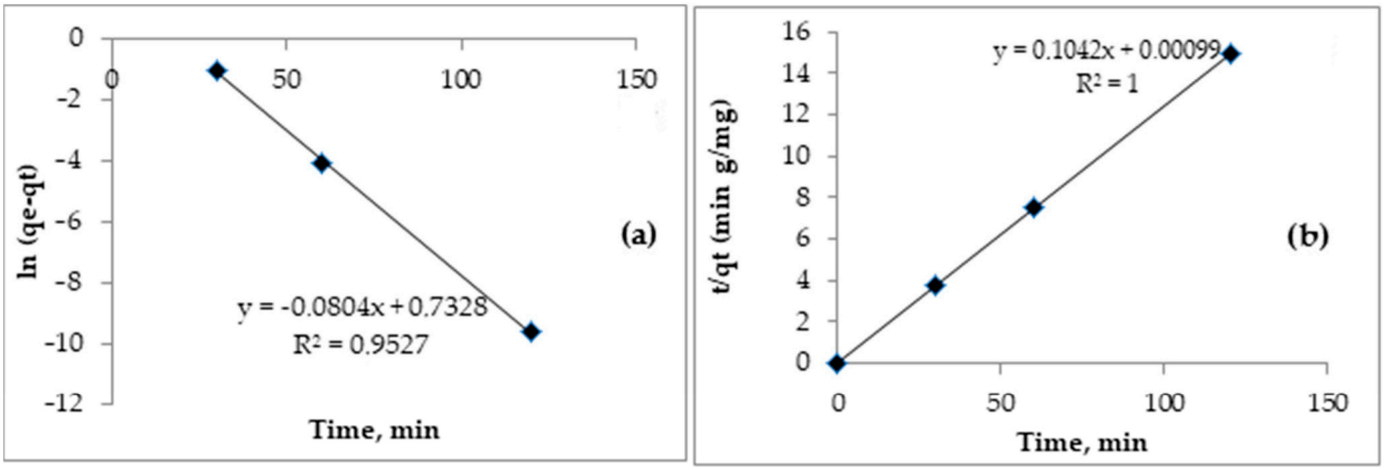

Figure 11. Lagergren pseudo-I order model (**a**) and Ho and McKay pseudo-II order model (**b**) for adsorption of Cd (II) onto Sarkanda grass lignin after 60 min.

Table 4. Kinetic parameters of the Lagergren and Ho and McKay models for Cd (II) adsorption on Sarkanda grass lignin.

Pollutant	c_i (mg/mL)	Lagergren Model			Ho and McKay Model		
		R^2	q_e (mg/g)	K_1 (min^{-1})	R^2	q_e (mg/g)	K_2 (g/mg·min)
Cd^{2+}	10	0.9423	1.1036	−0.0032	1	0.9421	16.0000
	20	0.9462	5.9245	−0.0009	1	3.0358	12.6130
	30	0.7108	7.3912	−0.0007	1	3.4399	7.1986
	40	0.9151	11.7680	−0.0006	1	4.8366	6.8051
	50	0.9084	11.5501	−0.0005	1	5.6487	5.7101
	60	0.9527	16.2793	−0.0005	1	7.3824	3.9486
	70	0.8402	16.3430	−0.0004	1	7.9946	3.2289
	80	0.9011	11.5006	−0.0003	1	8.0820	2.0197
	90	0.7186	8.2721	−0.0002	1	7.1912	0.8102
	100	0.7142	6.5019	−0.0001	1	5.9912	0.2318

For the Lagergren pseudo-I order kinetic model, the coefficients (R^2) were lower than 0.9527, falling more precisely in the range 0.7108–0.9527 (Table 4), which indicates the appearance of electrostatic interactions between Cd (II) and the functional groups. On the lignin surface, chemisorption is favored at the expense of physical adsorption, which the Lagergren model cannot explain [16–18].

The experimental data were then processed using the Ho and McKay pseudo-II order kinetic model, and the concordance obtained was much better. In this case, the correlation coefficients (R^2) showed unitary values in all situations, and the other parameters, q_e and K_2, showed the good affinity of the tested chemical agents as pollutant species (Cd II) and as substrates chemically (Sarkanda grass lignin), suggesting an active adsorption attributed to the complexation capacity of the involved species, especially the availability of the functional groups of the lignin to associate covalently. Thus, when Cd (II) arrived near the lignin surface, it interacted with the functional groups on the lignin surface ($R^2 = 1$), realizing an intense ion exchange that, thus, ensures the binding of cadmium to the lignin surface. Sarkanda grass lignin is presented as having a chelating capacity ($m_{echiv.}$/100g) of 67.14, and the Ho and McKay pseudo-II order kinetic model, through the prism of the analyzed parameters, indicates the occurrence of chemical interactions (probably donor-

acceptor) between the metal ion and the functional groups on the surface of the adsorbent and, implicitly, the complexation.

3.6. Evaluation of the Adsorptive Performances of Sarkanda Grass Lignin concerning Cd (II) Retention from Aqueous Solutions by Determining Some Biological Parameters

Testing the efficiency of Cd (II) absorption onto Sarkanda grass lignin can also be verified by evaluating some biological parameters, considering the negative impact of this chemical species on living systems.

3.6.1. Number of Germinated Tomato Seeds, *Lypercosium esculentum* Variety

Figure 12a–c shows the average number of germinated seeds at 3 days for the contaminated samples and the average number of germinated seeds for the filtrates resulting from Cd (II) adsorption at 3 days and at 7 days, for the three times of contact between phases.

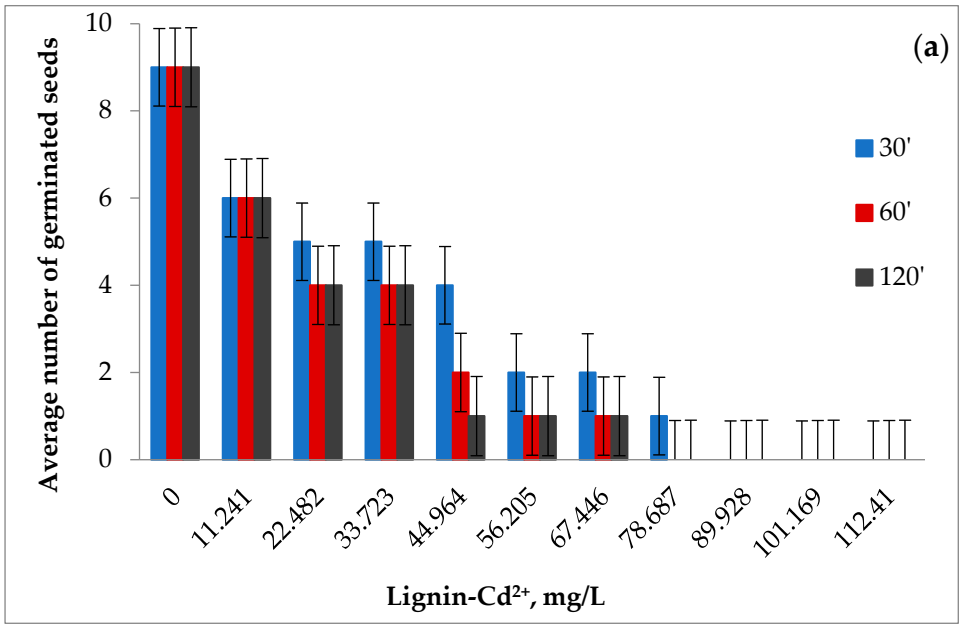

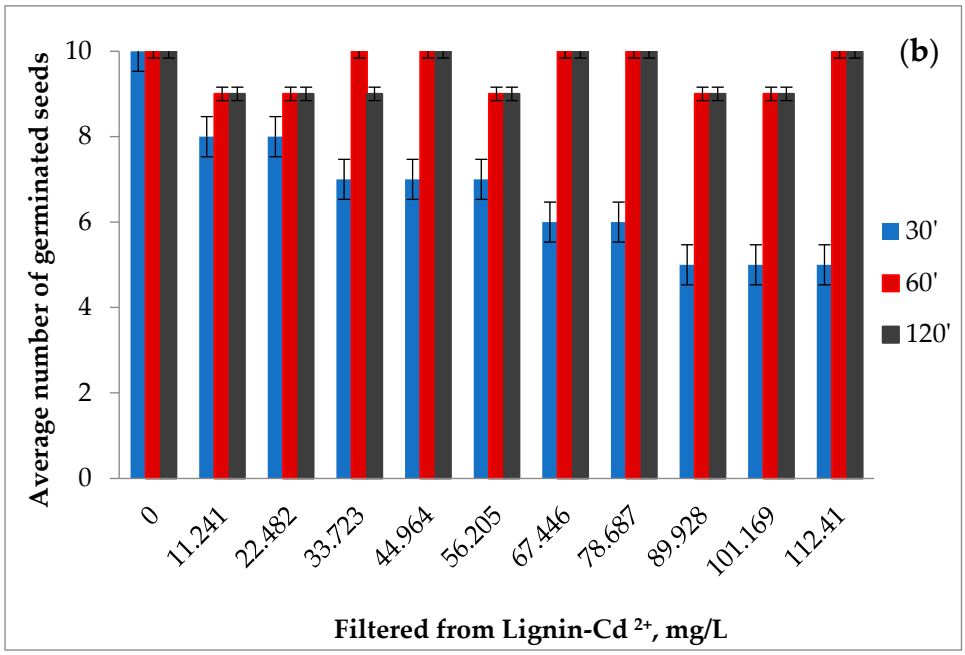

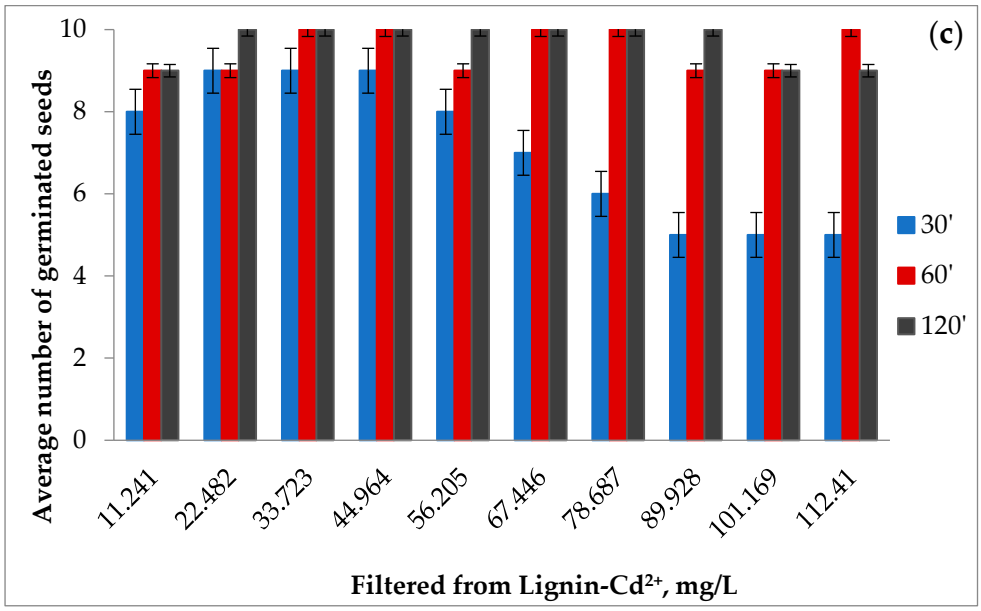

Figure 12. The average number of tomato seeds germinated at 3 days for the contaminated samples (**a**) and for the filtrates resulting from Cd (II) adsorption at 3 days (**b**) and 7 days (**c**).

The negative impact of cadmium on seed germination can be clearly observed, intensified by the growth of the concentration of metal ions and the increase in contact between the phases. In the reference samples, the number of germinated seeds was 9 for lignin and 10 for distilled water.

The germination of the seeds in the filtrate was interesting, where the number of germinated seeds after 3 days, but also the number of plants after 7 days after germination, were close to the ones obtained in the case of the control at the times of 60 and 120 min, but lower at the contact time of 30 min, which indicates the probability of a more attenuated adsorption of the polluting species in the first phase.

The data were consistent with the evolution of seed germination in the case of contaminated lignin samples. It was observed that at the contact time between phases of 30 min and at low concentrations in the polluting species, the highest number of germinated seeds appeared after 3 days, which showed a superficial retention of cadmium and confirmed the lower number of germinated seeds in the case filtrates at this contact time.

Figure 13 shows the germination of tomato seeds for 7 days with reference/uncontaminated lignin (R/UL), lignin contaminated with cadmium (CL), reference/distilled water (R/DW), and the filtrate (F) obtained after adsorption for 60 min at a concentration of 112.41 mg/L Cd (II).

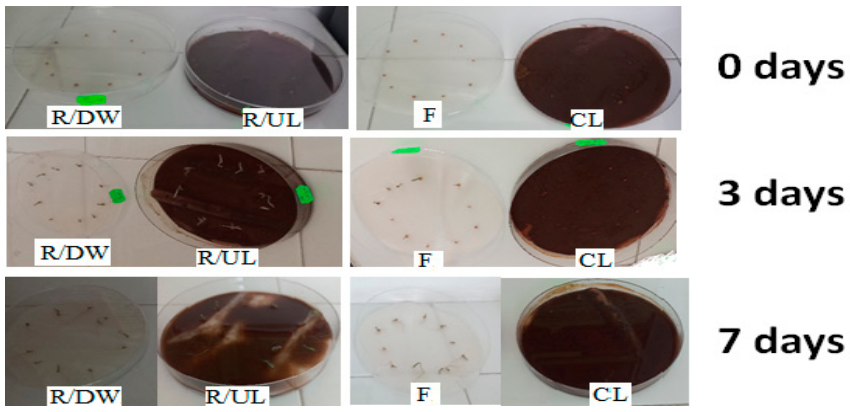

Figure 13. The germination of tomato seeds over a period of 7 days, at an adsorption time of 60 min and a concentration of 112.41 mg/L Cd (II).

3.6.2. Germination Energy and Germination Faculty for Tomato Seeds

Table 5 shows that the germination energy was correlated with the number of germinated seeds for filtrates and for contaminated lignin samples.

Table 5. Germination energy and germination faculty for the contaminated samples and for the filtrates resulting from Cd (II) retention at the three contact times between the phases and in the concentration domain studied.

Lignin/ Cd^{2+} (mg/L)	Contact Time (Min)						Lignin/ Cd^{2+} (mg/L) filtered	Contact Time (Min)					
	30	60	120	30	60	120		30	60	120	30	60	120
	Eg,%			Fg,%				Eg,%			Fg,%		
0	90	90	90	90	90	90	0	10	10	10	10	10	10
11.241	60	60	60	0	0	0	11.241	80	90	90	80	90	100
22.482	50	40	40	0	0	0	22.482	80	90	90	90	90	90
33.723	50	40	40	0	0	0	33.723	70	100	90	90	100	100
44.964	40	20	10	0	0	0	44.964	70	100	100	90	100	100
56.205	20	10	10	0	0	0	56.205	70	90	90	80	90	100
67.446	20	10	10	0	0	0	67.446	60	100	100	70	100	100
78.687	10	0	0	0	0	0	78.687	60	100	100	60	100	100
89.928	0	0	0	0	0	0	89.928	50	90	90	50	90	100
101.169	0	0	0	0	0	0	101.169	50	90	90	50	90	100
112.41	0	0	0	0	0	0	112.41	50	100	100	50	100	90

At the contact time between phases of 30 min, the retention of cadmium was more attenuated, so that the filtrates were more concentrated and the germination energy was lower, but at 60 and 120 min, the germination energy was higher because the filtrates were more diluted as a result of the good retention capacity of lignin.

In the case of filtrates, the germination power varied proportionally with the germination energy, while for contaminated lignin, zero values were recorded in all situations.

3.6.3. Mass and Average Height of Tomato Seedlings

Figure 14 shows that the mass and height of the seedlings developed in the case of the filtrates showed values close to those found in the reference, regardless of the contact times and the concentration of the retained pollutant species. In the case of contaminated lignin, these parameters could not be evaluated because, at the end of the germination, there were no seedlings, a fact attributed to the good adsorption capacity of lignin and implicitly to the toxicity of cadmium.

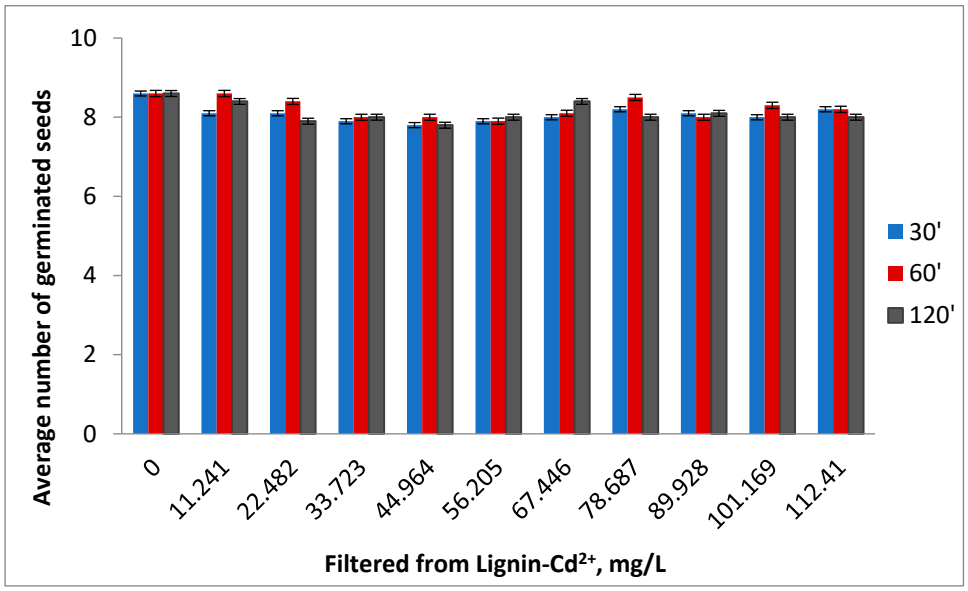

Figure 14. The mass and average height of tomato seedlings, developed in the filtrates resulting from Cd (II) adsorption on Sarkanda grass lignin.

In Figure 15, tomato seedlings of the *Lypercosium esculentum* variety are presented, developed in laboratory conditions 7 days after germination for reference/uncontaminated lignin (R/UL), reference/distilled water (R/DW), and for filtrate (F) obtained after adsorption after 60 min at a concentration of 112.41 mg/L Cd (II).

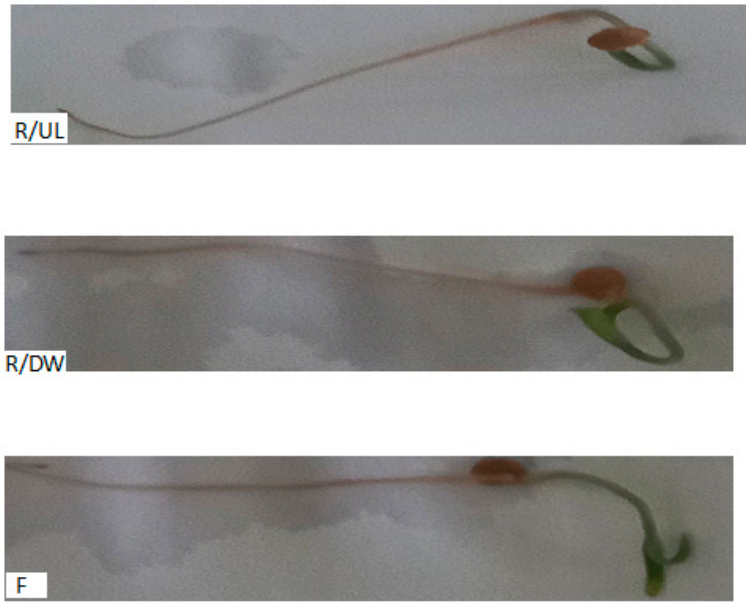

Figure 15. Tomato seedlings developed in reference and filtered samples 7 days after germination.

Biological tests, by analyzing the evaluated parameters, demonstrated the efficiency of Sarkanda grass lignin in the adsorption of Cd (II) from aqueous solution, which seemed to be due to the ion exchange capacity of the involved species.

4. Discussion

4.1. The Influence of Lignin Sarkanda Grass Dose on the Efficiency of Cd (II) Adsorption from Aqueous Solution

Considering mainly the economic segment, in order to optimize the Cd (II) adsorption, the use of the smallest possible dose of lignin was pursued. The experimental data obtained recommend that the ideal dose of lignin from Sarkanda grass is 5 g/L Cd (II) aqueous solution (Figure 1). The increase in the concentration of polluting species contributes to a more pronounced adsorption on lignin until the adsorbent pores become inaccessible, a fact that can be explained if we consider that adsorption is a surface process. It seems that at saturation, most of the functional groups of lignin are occupied, so their diffusion towards the unreacted (free) functional groups, which are found inside the lignin particles, is difficult, a fact that respects the principle of mobile equilibrium. Also, the functional groups on the surface of lignin and its structural particularities can form coordinative bonds as a result of its good affinity with Cd (II).

4.2. The Effect of pH and Contact Time on the Adsorption of Cd (II) onto Sarkanda Grass Lignin

The initial pH influences the speciation and solubility polluting (whether they are ions metallic or organic dyes), and the capacity of separation of the functional groups on the surface of the adsorbent, considered adsorption centers mainly the economic segment, in order to optimize the experimental conditions of Cd (II) adsorption, the use of the smallest possible dose of lignin was pursued [33]. When the pH of the initial solution is greater than 8.0, most of the ions and metals from the solution precipitate in the form of

hydroxides, and the adsorption process is either stopped or involves a totally different mechanism [19]. The results of the preliminary tests carried out regarding the retention of cadmium on Sarkanda Grass lignin as the adsorption substrate at pH variation recommend the value of 6.2 as being an optimal value (Figure 3). After a contact time of 120 min, the quantities of Cd (II) retained on Sarkanda grass lignin are identical, in most cases, to those recorded after a contact time of 60 min or vary negligibly (Figures 4). Although there are very small, almost imperceptible, variations in the amount of Cd (II) retained on Sarkanda grass lignin at times of 60 and 30 min, respectively, 60 min is recommended as the optimal contact time. The contact time of 60 min is also recommended from the perspective of surface and microscopic analyses and the contact angle, important parameters in the qualitative and quantitative characterization of surface processes such as adsorption, and agrees with the experimental results obtained in previous studies [26,27], where the adsorption of lead, zinc, and arsenium on Sarkanda grass lignin was tested under the same experimental conditions.

4.3. Highlighting the Adsorption of Cd (II) onto Sarkanda Grass Lignin through Surface Analysis

The presence of functional groups and the porous structure of lignin, demonstrated through microscopic studies (Figure 5), show that this material can be used as an adsorbent for the retention of polluting species from aqueous solutions and, therefore, can be utilized in environmental pollution reduction processes. Microscopic images (Figure 6) in natural (a) and polarized (b) light for Sarkanda grass lignin contaminated with Cd (II) reflect the possibility of the formation of chemical bonds (Sarkanda grass lignin-Cd (II)) and underline the cationic exchange capacity of this biomass fraction.

The composition of the lignin before and after adsorption of $CdSO_4$ was obtained using EDX analysis. As expected, the surface morphology of the unmodified lignin was different from that observed in the lignin contaminated with Cd (II), a fact that confirms the diffusion of the polluting species and its retention in the pores of the lignocellulose substrate (Figure 8). The contact angle also analyzed and confirmed the interaction of lignin and metal ions. The unmodified lignin had values of the contact angle below 90 degrees (Table 2), which denotes the existence of some hydrophilic groups willing to participate in the ion exchange. In Table 3, the contact angle values recorded for lignin contaminated with Cd (II) exceeded 90 degrees, which corresponds to a hydrophobic character. Therefore, the lignin adsorbed the Cd (II) solution, saturation and hydrophobicity were reached, and the lignin pores became inaccessible (Figure 9).

4.4. Adsorption Isotherms

Modeling equilibrium data obtained experimentally in order to evaluate the adsorption capacity of a given material under exact experimental conditions allows for the acquisition of particularly useful information that can then be used to design a large-scale industrial wastewater treatment system. Studies in the literature [36,37] highlighted the fact that the more complex the composition of a wastewater, the more adsorption systems used for its treatment must be described and selected with greater accuracy. The experimentally obtained isotherms for the adsorption of Cd (II) on lignin in the studied concentration domain are non-linear, and their slope is typical. The literature recommends the use of the Freundlich model for the interpretation of adsorption processes that take place on heterogeneous surfaces or are composed of functional groups with different affinities for a given metal ion [37] and the Langmuir model to describe adsorption in monolayers and on homogeneous surfaces [20,24,28]. The values obtained for the Lagmuir K_L constant show that the adsorption would not take place in the monolayer, and the Sarkanda grass lignin surface is not perfectly homogeneous. Using the Freundlich constants (n and K_F), the degree of adsorption can be estimated; thus, the nature of the process mechanism can be deduced. The higher the values of K_F and 1/n, the more intense the interactions between Cd (II) in the aqueous solution and the functional groups of lignin [26,27].

The experimental parameters obtained following the application of the Freundlich model have higher values than those obtained in the case of the application of the Langmuir model (Table 3), which would suggest that the Freundlich model is more appropriate to describe the retention of Cd (II) onto Sarkanda Grass. Analyzing the correlation coefficients (R^2) obtained in the case of the two models (domains: 0.82–0.88 for the Langmuir model and 0.96–0.98 for the Freundlich model), the idea emerges that Sarkanda grass lignin seems to be an alternative as an adsorbent for Cd (II), but the physical or chemical nature of the adsorption cannot be established exactly, which makes the interpretation of the data by kinetic modeling necessary.

4.5. Kinetics of Cd (II) Adsorption onto Sarkanda Grass Lignin

The kinetics of Cd (II) adsorption on Sarkanda grass lignin were analyzed using the two models frequently recommended by the literature: Lagergren pseudo-I order and Ho and McKay pseudo-II order kinetic models [18,26–28]. After applying the two kinetic models through the prism of the parameters obtained (Table 4), it can be found that the adsorption of Cd (II) on Sarkanda grass lignin is more precisely described by the Ho and McKay pseudo-II order kinetic model, which shows the compatibility of the experimental data with this kinetic model. It is noteworthy that the correlation coefficient (R^2) obtained at the Ho and McKay pseudo-II model was unitary in all case studies, which confirms the good adsorption capacity of Sarkanda grass lignin.

4.6. Verification of Cd (II) Adsorption Efficiency onto Sarkanda Grass Lignin by Biological Tests

It was based on the idea that in the case of low retention of the polluting species, the embryo of a seed would pass from the state of dormancy to the active state, and a seedling would appear—that is, the embryo would germinate. Therefore, the samples contaminated with the polluting species could clearly inhibit the germination process, given that a heavy metal, therefore also cadmium, represents a stress factor for seeds, being able to disturb the osmotic equilibrium or metabolic functions and replace essential nutrients through ion exchange [40]; hence, the indirect toxic effect on plants.

The experimental data (Figure 12) show that the presence of cadmium negatively influences the germination capacity of tomato seeds. Starting with the concentration of 33.723 mg/L, the number of germinated seeds was less than half of the total of 10, for all contact times, and for the concentration of 89.928 mg/L Cd (II), the number of germinated seeds was zero (the seeds are not germinated), which suggests both a more intense adsorption but also the negative effect of cadmium on the germination power of the seeds with the increase in concentration and duration of contact. Moreover, 7 days after germination, in the case of all samples of contaminated lignin, regardless of the contact time and concentration, no new germinated seeds appeared, and the existing seedlings died, which confirmed the toxicity of cadmium and its good capacity for lignin adsorption, as demonstrated by the kinetic and chemical equilibrium results obtained. It should be noted that seeds found swollen, rotten, or moldy at the end of the germination period were considered non-germinated.

As can be seen (Table 5), the germination energy and the germination power in the filtrates had values close to those in the control sample, regardless of the concentration of the polluting species that contaminated the lignin, which confirmed the efficient adsorption of Cd (II). Also, the values of these parameters at contact times of 60 and 120 min differed insignificantly, which agrees with the kinetic and chemical equilibrium conclusions, which give 60 min as the optimal adsorption time. The average mass and height of tomato seedlings developed in the case of the filtrates show values close to those found in the reference, regardless of the contact times or the concentration in Cd (II), a fact that confirms the good retention capacity of Sarkanda grass lignin. The mechanisms involved in the adsorption of metal ions on lignin are the subject of a continuous world debate that has several hypotheses. Therefore, further exploration of the complexation process and

the nature of the active centers on the lignin substrate is a priority and a challenge that we want to develop in a future study.

We also considered studying the thermodynamic behavior of the adsorption of Cd (II) on Sarkanda grass lignin, because the thermodynamic parameters (variation of free energy, entropy, and enthalpy) can provide valuable information on the nature of interactions between chemical species involved in a process. The reproducibility of the experimental data, resulting from the approaches of chemical equilibrium, kinetic stability, and biological stability, recommends Sarkanda grass lignin, under precisely established experimental conditions, as a possible adsorbent, both from the point of view of its properties and from the point of view of the ratio price/quantity, given that it is one of the main fractions of biomass and implicitly a reusable plant resource. The large-scale use of lignocellulosic waste in the process of reducing environmental pollution has primarily an economic justification because there are significant amounts of such waste produced annually that could be utilized in several directions at low costs.

4.7. Comparative Cd (II) Adsorption on Lignin and Polysaccaride-Based Gels

Dead biomass has higher metal uptakes and the process is nutrient independent. Biomass immobilization is an essential step for an industrial scale-up of biosorption. Natural polysaccharide gels, such as alginate, are used as a cost-effective alternative to synthetic polymers, but the cost limits their widespread use [41]. Each polysaccharide gels has its own unique characteristics and advantages, and the choice of adsorbent depends on factors such as availability, cost-effectiveness, selectivity, and the specific requirements of the application [42,43]. Hybrid materials and optimization strategies can also be employed to develop efficient and sustainable Cd removal processes in various environmental contexts. Alginate is an unbranched linear polysaccharide of alternating blocks of β-d-mannuronic and α-l-guluronic acids, and alginate gels in the presence of divalent cations have been shown to be effective biosorbents of heavy metals [44].

Cellulose-based materials and cellulosic gels, agricultural-based residual hydrogels are spatially structured systems and offer extensive adsorption sites for Cd (II) thanks to various functional groups, such as hydroxyl (-OH), carboxyl (-COOH), and phenolic (-Ph) groups, that have the ability to form chemical bonds with metal ions [45–49]. For example, Cellets cellulose hydrogel, obtained from microcrystalline cellulose and distilled water, without any additive, at a concentration of 78.46 mg/L Zn (II), retains 3.17 mg/g, contact time: 60 min, pH-6.4, [23], and Sarkanda grass lignin, at 60 min contact time: 60 min, pH-6.0, at a concentration of 65.38 mg/L Zn (II), retains 8.19 mg/g [27], which makes lignin a possible effective biosorbent.

Lignin has the advantage of being a by-product of the wood and paper industries and readily available in large quantities, making it a cost-effective option for Cd adsorption. The versatility of lignin allows for modification and optimization to enhance its adsorption capacity and selectivity. Polysaccharide-based gels have specific advantages, such as high surface area, natural abundance and availability (agricultural waste) [30], and unique functional groups (chitosan) [42]. Some materials may have a higher affinity for Cd ions over other competing metal ions, while others may show co-adsorption behavior [50–53]. The presence of co-existing ions and the composition of the aqueous solution can influence the competition for adsorption sites on different biogels. Comparing the experimental results obtained for cadmium adsorption on lignin with those existing in the literature regarding cadmium adsorption on different polysaccharide gels [45–49], this biomass fraction can be an alternative for cadmium adsorption.

5. Conclusions

Polysaccharide-based gels are effective in retaining heavy metals such as cadmium, but their use is limited due to economic considerations and Sarkanda grass lignin can be a solution for Cd (II) retention under precisely established experimental conditions (temperature, pH, dose of adsorbent/L pollutant in the studied concentration range, contact time), considering the efficiency and availability of the biopolymer.

Spectral and microscopic surface morphology analyses demonstrated the porous structure of Sarkanda grass lignin and showed that Cd (II) from aqueous solutions was effectively adsorbed into the active centers of the biopolymer.

From the analysis of the correlation coefficients obtained in the case of the Freundlich and Langmuir models, in order to establish the efficiency of the adsorbent from a practical point of view, it was not possible to clearly establish the physical or chemical nature of the adsorption, a fact elucidated with the help of kinetic models, but it was concluded that Sarkanda lignin appeared to be an alternative adsorbent C.

From a kinetic point of view, the Ho and McKay model best describes the adsorption of Cd (II) on the lignin substrate, providing conclusive details regarding the electrostatic nature of the interactions between the two partners and the triggering of an activated chemical adsorption as a result of the good complexation capacity between the involved species, with lignin benefiting from a wide variety of functional groups.

Biological analyses highlighted, on the one hand, the inhibitory effect of polluting species on the germination and growth of seeds subjected to abiotic stress and, on the other hand, the good capacity of lignin to retain polluting species and constitute a starting point for future studies, considering the complexity of the topic.

Next, it was considered necessary to carry out detailed research on Sarkanda grass lignin regeneration and metal ion recovery, which would allow the quantitative evaluation of the conditions under which the desorption processes take place and increase their practical application in wastewater treatment.

The utilization of lignin in environmental pollution reduction processes is not only economically justified but also environmentally sustainable due to its status as a renewable raw material. As a by-product of the wood-processing and paper-manufacturing industries, cellulose, cellulose-based gels, and lignin waste are readily available in substantial amounts. By harnessing this abundant lignin waste for various applications, industries can significantly reduce their environmental footprint and promote resource circularity. This renewable solution offers a viable and cost-effective approach to addressing environmental challenges while contributing to a more sustainable and eco-friendly future, by replacing some highly efficient but more expensive polysaccharide biogels.

Author Contributions: Conceptualization, E.U., M.E.F., B.M.T., and D.C.Ț.; methodology, D.C.J., C.O.B., and V.I.P.; investigation, E.U., M.E.F., V.I.U., B.M.T., C.C., and R.R.; resources, E.U., V.I.P., and D.C.Ț.; writing—original draft preparation, M.E.F., E.U., D.C.Ț., and V.I.U.; writing—review and editing, M.E.F., V.I.U., C.O.B., and E.U.; visualization, E.U., M.E.F., C.C., R.R., D.C.Ț., and V.I.U.; software, V.I.U. and C.C., supervision, D.C.J., C.O.B., B.M.T., and V.I.P. All authors have read and agreed to the published version of the manuscript.

Funding: The financial support of the "Ion Ionescu de la Brad" Iasi University of Life Sciences through Grant CNFIS-FDI-2023-0202 is gratefully acknowledged.

Institutional Review Board Statement: Not applicable.

Data Availability Statement: Not applicable.

Conflicts of Interest: The authors declare no conflict of interest.

References

1. Jaishankar, M.; Tseten, T.; Anbalagan, N.; Mathew, B.B.; Mathew, K.N. Toxicity, mechanism and health effects of some heavy metals. *Rev. Interdiscip. Toxicol.* **2014**, *7*, 60–72.
2. Micó, C.; Recatalá, L.; Peris, M.; Sánchez, J. Assessing Heavy Metal Sources in Agricultural Soils of a European Mediterranean Area by Multivariate Analysis. *Chemosphere* **2006**, *65*, 863–872.
3. Siegel, F.R. *Geochemistry in Ecosystem Analysis of Heavy Metal Pollution in Environmental Geochemistry of Potentially Toxic Metals*; Springer: Berlin/Heidelberg, Germany, 2002; pp. 1–14.
4. Modak, A.; Bhanja, P.; Selvaraj, M.; Bhaumik, A. Functionalized porous organic materials as efficient media for the adsorptive removal of Hg(II) ions. *Environ. Sci. Nano* **2020**, *7*, 2887–2923.
5. Dhankhar, R.; Hooda, A. Fungal biosorption-An alternative to meet the challenges of heavy metal pollution in aqueous solutions. *Environ. Technol.* **2011**, *32*, 46–91.
6. Wierzbicka, M.; Obidzinska, J. The Effect of Lead on Seed Imbibition and Germination in Different Plant Species. *Plant Sci.* **2011**, *137*, 155–171.
7. John, R.; Ahmad, P.; Gadgil, K.; Sharma, S. Cadmium and lead-induced changes in lipid peroxidation, antioxidative enzymes and metal accumulation in *Brassica juncea* L. At three different growth stages. *Arch. Agron. Soil Sci.* **2009**, *55*, 395–405.
8. Rahoui, S.; Chaoui, A.; El Ferjani, E. Membrane damage and solute leakage from germinating pea seed under cadmium stress. *J. Hazard. Mater.* **2010**, *178*, 1128–1131.
9. Qureshi, M.I.; Qadir, S.; Zolla, L. Proteonics—Based dissection of stress responsive pathways in plants. *J. Plant Physiol. Arch.* **2007**, *164*, 1239–1260.
10. Philip, E.; Madhavan, A.; Pugazhendhi, A.; Sindhu, R.; Sirohi, R.; Awasthi, M.K.; Pandey, A.; Binod, P. Nanocellulose as green material for remediation of hazardous heavy metal contaminants. *J. Hazard. Mater.* **2022**, *424*, 127516.
11. Rotaru, A.; Cojocaru, C.; Cretescu, I.; Pinteala, M.A.; Timpu, D.; Sacarescu, L.; Harabagiu, V. Performances of clay aerogel polymer composites for oil spill sorption: Experimental design and modeling. *Sep. Purif. Technol.* **2014**, *133*, 260–275.
12. Cojocaru, C.; Macoveanu, M.; Cretescu, I. Peat-based sorbents for the removal of oil spills from water surface: Application of artificial neural network modeling. *Colloids Surf. A Physicochem. Eng. Asp.* **2011**, *384*, 675–684.
13. Johnson, R.F.; Manjrekar, T.G. Removal of oil from water surfaces by sorption on unstructured fibers. *Environ. Sci. Technol.* **1973**, *7*, 439–443.
14. Demirbas, A. Heavy metal adsorption onto agro-based waste materials: A review. *J. Hazard. Mater* **2008**, *157*, 220–229.
15. Weber, W.J.J.; McGinley, P.M.; Katz, L.E. Sorption phenomena in subsurface systems: Concepts, models and effects on contaminant fate and transport. *Water Res.* **1991**, *25*, 499–528.
16. Abdullah, M.A.; Rahmah, A.U.; Man, Z. Physicochemical and sorption characteristics of Malaysian *Ceiba pentandra* (L.) Gaertn. as a natural oil sorbent. *J. Hazard. Mater.* **2010**, *177*, 683–691.
17. Srinivasan, A.; Viraraghavan, A. Oil removal from water using biomaterials. *Bioresour. Technol.* **2010**, *101*, 6594–6600.
18. Khan, E.; Virojnagud, W.; Ratpukdi, T. Use of biomass sorbents for oil removal from gas station runoff. *Chemosphere* **2004**, *57*, 681–689.
19. Ribeiro, T.H.; Rubio, J.; Smith, R.W. A dried hydrophobic aquaphyte as an oil filter for oil/water emulsions. *Spill Sci. Technol. Bull.* **2003**, *8*, 483–489.
20. Crist, R.H.; Martin, J.R.; Crist, D.R. Use of a novel formulation of kraft lignin for toxic metal removal from process waters. *Sep. Sci. Technol.* **2004**, *39*, 1535–1545.
21. Guo, X.Y.; Zhang, A.Z.; Shan, X.Q. Adsorption of metal ions on lignin. *J. Hazard. Mater.* **2008**, *151*, 134–142.
22. Ohan, D.; Chander, S. Removal and Recover of Metal Ions from Acid Mine Drainage Using Lignite—A Low Cost Sorbent. *J. Hazard. Mater.* **2006**, *137*, 1545–1553.
23. Mahuli, S.; Agnihotri, R.; Chauk, S.; Ghosh-Dastidar, A.; Fan, L.S. Mechanism of arsenic sorption by hydrated lime. *Environ. Sci. Technol.* **1997**, *31*, 3226–3231.
24. Todorciuc, T. Contributions to Some Complex Combinations of Natural Products with Aromatic Structure. Ph.D. Thesis, "Gh. Asachi" Polytechnic University of Iasi, Iasi, Romania, 2016; pp. 59–73.
25. Husseien, M.; Amer, A.A.; El-Maghraby, A. Experimental investigation of thermal modification influence on sorption qualities of barley straw. *J. Appl. Sci. Res.* **2008**, *4*, 652–657.
26. Ungureanu, E.; Trofin, A.; Trincă, L.C.; Ariton, A.M.; Ungureanu, O.C.; Fortună, M.E.; Jităreanu, C.D.; Popa, V.I. Studies on kinetics and adsorption equilibrium of lead and zinc ions from aqueous solutions on Sarkanda Grass lignin. *Cellul. Chem. Technol.* **2021**, *55*, 939–948.
27. Ungureanu, E.; Jităreanu, C.D.; Trofin, A.; Fortună, M.E.; Ungureanu, O.C.; Ariton, A.M.; Trincă, L.C.; Brezuleanu, S.; Popa, V.I. Use of Sarkanda Grass lignin as a possible adsorbent for As (III) from aqueous solutions-kinetic and equilibrium studies. *Cellul. Chem. Technol.* **2022**, *56*, 681–689.
28. Hanif, M.A.; Tauqeer, H.M.; Aslam, N.; Hanif, A.; Yaseen, M.; Khera, R.A. Correct Interpretation of sorption mechanism by Isothermal, Kinetic and Thermodynamic models. *Int. J. Chem. Biochem. Sci.* **2017**, *12*, 53–67.
29. Suhas, P.; Carot, J.M.; Carot, R. Lignin-from natural adsorbent to activated carbon: A review. *Bioresour. Technol.* **2007**, *98*, 2301–2312.
30. Wang, X.; Qin, Y.; Li, Z. Biosorption of zinc from aqueous solutions by rice bran: Kinetics and equilibrium studies. *Sep. Sci Technol.* **2006**, *4*, 747–756.

31. Pavel, L.V. Behavioral Studies of Heavy Metals in the Soil and of some Remedy Alternatives. Ph.D. Thesis, "Gh. Asachi" Polytechnic University of Iasi, Iasi, Romania, 2012; pp. 28–36.
32. Chong, K.H.; Volesky, B. Description of two-metal biosorption equilibria by Langmuir-type models. *Biotechnol. Bioeng.* **1995**, *47*, 451–460.
33. Rusu, G. Studies on the Use of Cellulosic Wastes in Reducing Environmental Pollution. Ph.D. Thesis, "Gh. Asachi" Polytechnic University of Iasi, Iasi, Romania, 2015; pp. 29–48.
34. Chen, W.Q.; Shi, Y.L.; Wu, S.L.; Zhu, J. Anthropogenic arsenic cycles: A research framework and features. *J. Clean. Prod.* **2016**, *139*, 328–336.
35. Seguchi, M.; Uozu, M.; Oneda, H.; Murayama, R.; Okusu, H. Effect of outer bran layers from germinated wheat grains on bread-making properties. *Cereal Chem.* **2010**, *87*, 231–236.
36. Kouam, E.B.; Ngompe-Deffo, T.; Beyegue-Djonko, H.; Mandou, M.S.; Chotangui, A.H.; Tankou, C.M. Genotypic evaluation of cowpea germplasm for salinity tolerance at germination and during seedling growth. *Agric. Trop. Et Subtrop.* **2021**, *54*, 71–88.
37. Kizilgeçi, F.; Mehmet, E.I.; Yıldırım, M. Germination, seedling growth and physio-biochemical indices of bread wheat (*Triticum aestivum* L.) genotypes under peg induced drought stress. *J. Agric. For. Environ.* **2021**, *67*, 163–180.
38. Norouzi, Y.; Mohammadi, G.; Nosratti, I. Seed germination and seedling growth of wheat (*Triticum aestivum*) as influenced by safed behman (*Centaurea behen*) water extract. *Biharean Biol.* **2017**, *11*, 98–101.
39. Brandes, R.; Belosinschi, D.; Brouillette, F.; Chabot, B. A new electrospun chitosan/phosphorylated nanocellulose biosorbent for the removal of cadmium ions from aqueous solutions. *J. Environ. Chem. Eng.* **2019**, *7*, 103477.
40. Ahmad, I.; Akhtar, M.J.; Zahir, Z.A.; Jamil, A. Effect of cadmium on seed germination and seedling growth of four wheat (*Triticum aestivum* L.) cultivars. *Pak. J. Bot.* **2012**, *44*, 1569–1574.
41. Mehta, S.K.; Gaur, J.P. Use of algae for removing heavy metal ions from wastewater. Crit. Rev. Biotechnol. **2005**, *25*, 113–152.
42. Boamah, P.O.; Huang, Y.; Hua, M.; Zhang, Q.; Liu, Y.; Onumah, J.; Wang, W.; Song, Y. Removal of cadmium from aqueous solution using low molecular weight chitosan derivative. *Carbohydr. Polym.* **2015**, *122*, 255–264.
43. Salman, M.; Athar, M.; Farooq, U. Biosorption of heavy metals from aqueous solutions using indigenous and modified lignocellulosic materials. *Rev. Environ. Sci. Biotechnol.* **2015**, *14*, 211–228.
44. Mata, Y.N.; Blázquez, M.L.; Ballester, A.; González, F.; Muñoz, J.A. Characterization of the biosorption of cadmium, lead and copper with the brown alga Fucus vesiculosus. *J. Hazard. Mater.* **2008**, *158*, 316–323.
45. Puițel, A.C.; Moisei, N.; Tofănică, B.M.; Gavrilescu, D. Turning Wheat Straw in a Sustainable Raw Material for Paper Industry. *Environ. Eng. Manag. J.* **2017**, *16*, 1027–1032.
46. Chesca, A.M.; Nicu, R.; Tofănică, B.M.; Puiţel, A.C.; Vlase, R.; Gavrilescu, D. Pulping of Corn Stalks—Assessment in Bio-Based Packaging Materials. *Cellul. Chem. Technol.* **2018**, *52*, 645–653.
47. Belosinschi, D.; Tofanica, B.-M. A New Bio-Material with 3D Lightweight Network for Energy and Advanced Applications. *Cellul. Chem. Technol.* **2018**, *25*, 897–902.
48. Tofanica, B.-M.; Belosinschi, D.; Volf, I. Gels, Aerogels and Hydrogels: A Challenge for the Cellulose-Based Product Industries. *Gels* **2022**, *8*, 497.
49. Mikhailidi, A.; Saurov, S.K.; Anderson, S.; Kotelnikova, N. Lignocellulose fibers elaborating super-swollen three-dimensional cellulose hydrogels from solution in N, N-dimethylacetamide/lithium chloride. *TAPPI J.* **2018**, *17*, 81.
50. Garg, U.; Kaur, M.P.; Jawa, G.K.; Sud, D.; Garg, V.K. Removal of cadmium (II) from aqueous solutions by adsorption on agricultural waste biomass. *J. Hazard. Mater.* **2008**, *154*, 1149–1157.
51. Ghoneim, H.M.; El-Desoky, H.S.; El-Moselhy, K.N.M.; Amer, A.; El-Naga, E.H.A.; Mohamedein, L.I.; Al-Prol, A.E. Removal of cadmium from aqueous solution using marine green algae, Ulva lactuca. *Egypt. J. Aquat. Res.* **2014**, *40*, 235–242.
52. Sciban, M.; Klasnja, M.; Skrbic, B. Modified softwood sawdust as adsorbent of heavy metal ions from water. *J. Hazard. Mater.* **2006**, *136*, 266–271.
53. Kumar, U.; Bandyopadhyay, M. Sorption of cadmium from aqueous solution using pretreated rice husk. *Bioresour. Technol.* **2006**, *97*, 104–109.

materials

MDPI

Article

Design of Functional Polymer Systems to Optimize the Filler Retention in Obtaining Cellulosic Substrates with Improved Properties

Elena Ungureanu [1], Maria E. Fortună [2,*], Denis C. Țopa [1], Andrei Lobiuc [3], Ovidiu C. Ungureanu [4] and Doina C. Jităreanu [1]

[1] Department of Plant Science, "Ion Ionescu de la Brad" University of Life Sciences Iasi, 3 Mihail Sadoveanu Alley, 700490 Iasi, Romania
[2] Inorganic Polymers Department, "Petru Poni" Institute of Macromolecular Chemistry, Grigore Ghica Voda Alley 41A, 700487 Iasi, Romania
[3] Department of Biomedical Sciences, "Stefan cel Mare" University, 13 Universitatii Str., 720229 Suceava, Romania
[4] Department of Biology and Life Sciences, "Vasile Goldis" Western University of Arad, 94 The Boulevard of the Revolution, 310025 Arad, Romania
* Correspondence: fortuna.maria@icmpp.ro

Abstract: In the present work, the possibility of increasing the calcium carbonate ($CaCO_3$) content in sheets of paper to optimize their properties was investigated. A new class of polymeric additives for papermaking is proposed as well as a method for their use in paper sheet containing the $CaCO_3$ precipitated addition. Calcium carbonate precipitated (PCC) and fibers cellulose were adjusted with a cationic polyacrylamide flocculating agent (polydiallyldimethylammonium chloride (plyDADMAC) or cationic polyacrylamide (cPAM)). PCC was obtained in the laboratory by a double-exchange reaction between calcium chloride ($CaCl_2$) and sodium carbonate (Na_2CO_3) suspension. After testing, the dosage of PCC was established at 35%. To improve the systems of additives studied, the materials obtained were characterized and their optical and mechanical properties were analysed. The PCC had a positive influence over all of the paper samples, but in the case of use of cPAM and polyDADMAC polymers the paper obtained had superior properties compared to the paper obtained without additives. Also, the samples obtained in the presence of cationic polyacrylamide exhibit superior properties to those obtained in the presence of polyDADMAC.

Keywords: calcium carbonate precipitated (PCC); cationic polyacrylamide (cPAM); cellulosic substrates; filler; mechanical and optical properties; polyDADMAC

Citation: Ungureanu, E.; Fortună, M.E.; Țopa, D.C.; Lobiuc, A.; Ungureanu, O.C.; Jităreanu, D.C. Design of Functional Polymer Systems to Optimize the Filler Retention in Obtaining Cellulosic Substrates with Improved Properties. *Materials* **2023**, *16*, 1904. https://doi.org/10.3390/ma16051904

Received: 16 January 2023
Revised: 21 February 2023
Accepted: 22 February 2023
Published: 25 February 2023

1. Introduction

The use of methods of filling cellulose fiber paper with calcium carbonate precipitate registered a continuous increase [1,2]. The initial aim was reduce the cost, to improve the printing properties of high-fill paper, decreased energy consumption, improvement in machine speed [3,4]. However, at a high content of filler material in the paper, the strength can reduced due to the interference of the inter fiber bonding [5]. The filler can be added to a cellulosic substrate by different methods. By conventional procedure the filler are incorporated directly into the fiber stock suspension and the mineral is retained in the paper either by mechanical filtration or by use of retention aid. The additives can be used in paper manufacture as agents for improving retention, paper machine operation and the strength properties of the final product [6].

For enhancing paper quality, filler loading is performed which, in its conventional setting, means dosage of filler particles and their uniform incorporation into the suspension of fibers. However, in these conventional methods, fillers aren't always well retained into the paper sheet as the filler particles start forming strands, leading to lower efficiency and

high residual levels of filler into wastewater. A method [1,7] developed to overcome these problems was to directly precipitate calcium carbonate within pulp fibers walls and lumen. Using this method [1,8], paper strength was reduced compared with conventionally loading paper with filler. Furthermore, a decrease in the environmental impact was obtained when combinations of different additives were used, by reducing the contamination of the process water due to high filler retention and also reducing energy requirements for pulp stock [1,4].

Further improvements of paper quality can be obtained when calcium carbonate ($CaCO_3$) is in a definite crystal form, and superior brightness and durability of the end product can be obtained using well defined particle size and distribution. Calcium carbonate precipitate (PCC) offers traits, such as reduced particle size, high purity, tight particle size distribution, regular crystal shape, compared to unmodified calcium carbonate [9,10]. While PCC exists in 3 basic forms, calcite, aragonite, and vaterite [11], the properties induced by calcium carbonate filler depend on the quality of water used in suspensions, on dissolved and colloidal substances and on the retention polymer added [10]. Additives can be used in paper manufacture to control the particle size and morphology of PCC [11], as well as agents for improving retention, paper machine operation and optical and strength properties of the product [12,13].

A mechanism for explaining the properties of additives is the difference of potential between the negatively charged fibers and the positively charged additive polymers which interact due to electrostatic forces [14,15]. While filler materials can improve paper properties such as opacity other properties such as strength and brightness [16] can be reduced. As such additives should be used in a way that paper properties are kept or enhanced. To accomplish such goals fillers should have a high ability to bond to fibers, a property less common in their natural forms therefore chemical modification is required. In the meantime, additives should be as environmentally friendly as possible therefore new and renewable or low-cost materials are sought after [17–19]. An example of such material is lignin, a polymer which is widely available in natural sources, or often as a byproduct in economical processes. When developing a new polymer as an paper additive, observing the synergism or way of interaction of its pigments or other molecules with fibers is the probable way to design high performance additives [20]. Polymers, such as polyDADMAC and cPAM, are currently introduced as retention additives in paper production. Optimized paper properties were shown to be obtained using both pigments and cellulosic materials [20–22]. One cationic polymer with significant flocculant properties and good performance is polyDADMAC, which is also non-toxic, while also aiding in papermaking sewage treatment reduction costs. Flocculation by polyDADMAC is due to bridging adsorption between polymer and suspended colloidal particle. One mode of action of polyDADMAC is explained by the ability to neutralize negative surface charges, thus acting as an effective additive [23,24].

Polyacrylamide is the most usually water-soluble synthetic retention polymer used in the paper industry. Polyacrylamides can be homopolymers or copolymers, nonionic, anionic or cationic polymers. In the paper manufacturing, polyacrylamide has a more of uses according to the different molecular weight (dispersant, reinforcer, retention and filtration aid, flocculants in papermaking wastewater treatment). cPAM flocculates of $CaCO_3$ even in the presence of large excess of dissolved anionic such as sulfonated kraft lignin. It representing the typical retention aid, acts by bridging mechanism [25,26].

Both polyDADMAC and cPAM cationic polymers are used to improve retention of fine particles in papermaking. They can affect the PCC fillers and can affect the interaction of these with pulp fibers in different mods [27,28].

The objective of this work was to analyze and optimize the efficiency of fillers using calcium carbonate precipitated by double exchange reactions in combination with cationic polymers which are used to improve retention of fine particles in papermaking.

A single-component system consisting of two additives (polyDADMAC and cPAM polymers) was designed, which proved to be efficiency alternative for calcium carbonate fillers deposition on fibers. The optimum percent of polymers, their behavior and the

impact over optical and mechanical paper properties were analyzed. Cationic polymers added in the paper pulp offer positive effects on retention, dehydration and cellulosic substrate properties.

2. Experimental

2.1. Materials

Kraft pulp fibers from Braila, Romania; $CaCl_2$ (96%) and Na_2CO_3 (99.8%) from Chemical Company, Iasi were used to obtained PCC. Retention additives: cationic polyacrylamide (cPAM) Ciba® Percol® Co 455 (charge density = 3% and mass ~4–10 million Daltons) were acquired from CIBA Specialty Chemicals Canada Inc; poly(diallyldimethylammonium chloride) as Alcofix® 169 (polyDADMAC), Sigma-Aldrich, Germany (0.5 g/L).

2.2. Methods

To determine refining degree was used the Schopper-Riegler instrumentation (Hangzhou, Zhejiang, China) and 30° SR was obtained for all samples studied.

Paper sheets obtained with weight of 70 g/m^2 were conditioned (24 h at 23 °C and 50% RH) and analyzed.

$CaCO_3$ was measured according to the Tappi Standard—T413 (Tappi Test Methods, 1999). The $CaCO_3$ content is calculated from the ash content in the hand sheets, taking into account the incineration loss of the precipitated calcium carbonate.

Air permeability, measured by the DL-WEB apparatus at a 1 kPa pressure, Guangdong, China.

Opacity and brightness (according to ISO 2471), were determined by the spectrophotometer L&W Elrepho 2000 apparatus, Kista, Sweden.

Strength properties: breaking length (km) measured by Instron apparatus, according to ISO 1924 and burst factor ($kPa \cdot m^2/g$) measured by the Schopper-Dale apparatus, according to ISO 2758, Bucuresti, Romania.

Scanning electron microscope (SEM) images were obtained with VEGA/TESCAN instrument, Netzsch, Germany.

X-ray diffraction was determined on a D8 ADVANCE, Bruker-AXS apparatus, (Billerica, MA, USA).

Thermogravimetric analyses (TG and DTG) were obtained using STA 449F1 Jupiter equipment (Netzsch, Selb, Germany).

2.3. Experimental Procedure

Precipitated calcium carbonate can be produced as a heterogeneous liquid-solid mixture, following the very rapid precipitation reaction of two aqueous solutions of carbonate salts by the next reaction:

$$CaCl_2 + Na_2CO_3 \rightarrow CaCO_3 + 2NaCl \quad (1)$$

For this purpose, PCC was added to pulp suspension under stirring. After more retention tests the content of calcium carbonate was at 35%. The paper pulp was treated with cationic polyacrylamide or polyDADMAC under stirring. After several tests, it was found that it is more efficient to add cationic polymers after adding the $CaCl_2$ solution and before adding the Na_2CO_3 solution.

For the polyDADMAC samples the added doses were: 0%, 0.2%, 0.4%, 0.8% and 1% *w*/*w* on pulp and it was added to the suspension of pulp with 1% consistency and was allowed to stir during 10 min.

For the cPAM samples the added doses were: 0%, 0.02%, 0.04%, 0.08% and 0.1% *w*/*w* on pulp and also as in the case of using polyDADMAC, it was added to the suspension of pulp with 1% consistency and was allowed to stirring during 10 min.

The paper sheets were obtained and for each samples, three variants were used for replication:

1. pulp fibers/35% PCC
2. pulp fibers/35% PCC/polyDADMAC (0%, 0.2%, 0.4%, 0.8% and 1%)
3. pulp fibers/35% PCC/cPAM (0%, 0.02%, 0.04%, 0.08% and 0.1%).

According to Scheme 1, the experimental design includes obtaining fibrous pulps filled with calcium carbonate precipitated and preparing paper sheets from these pulps, as well as forming paper sheets by using additives.

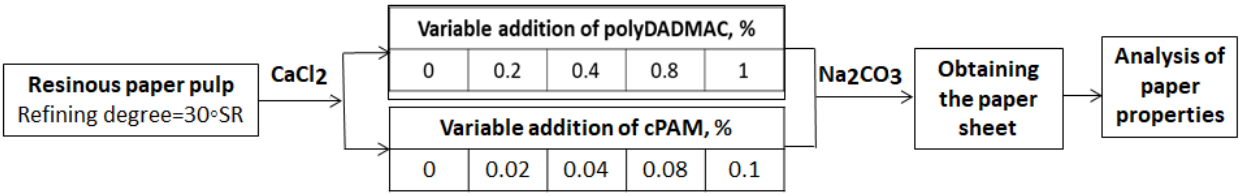

Scheme 1. Experimental program.

3. Results and Discussion

3.1. Effects of Polymers on Paper Stock Properties

The results obtained shown that it is possible to obtain pulps with 11–14% of $CaCO_3$ content, which thus can be 100% retained in paper sheet that is formed of these pulps. The content of PCC increase with the addition of cationic polymers.

The porosity of fibers loading with PPC and polymers was represented by air permeability and it was found that this was influenced by the type of fiber used, the content of filling material, as well as by the type and doses of retention additives used.

The results from Table 1 show that air permeability increases with increasing $CaCO_3$ content. Although the calcium carbonate content registers very close increases for the both additives (polyDADMAC and cPAM), the air permeability is higher for cPAM, which shows that cPAM has a stronger influence on the paper structures.

Table 1. The characteristics paper fibers obtained with 35% $CaCO_3$ for different percentages of polyDADMAC and cPAM polymers.

Properties	**% polyDADMAC**				
	0	**0.2**	**0.4**	**0.8**	**1**
Ionic charge, meq/g	−14.28	8.49	10.46	11.49	16.16
$CaCO_3$ content, %	11.4	12.36	12.52	13.00	13.38
Air permeability, µm/kPa·s	190	191	193	195	195
Properties	**% cPAM**				
	0.02	**0.04**	**0.08**	**0.1**	
$CaCO_3$ content, %	12.30	12.55	13.88	13.98	
Ionic charge, meq/g	−27.5	−25.77	−24.96	−23.26	
Air permeability, µm/kPa·s	196	198.5	202	204.5	

From Figure 1a,b result that the addition of the additives, polyDADMAC and cPAM have positive effects on the retention of the filling material, as well as on the dehydrating capacity of the pulp.

The both additives behave similarly in terms of dehydration time. Calcium carbonateretention increases with the addition of retention additives. For cPAM, PCC retention increases by 6.5 units comparatively with the system using polyDADMAC where PCC retention increases by only 4.5 units.

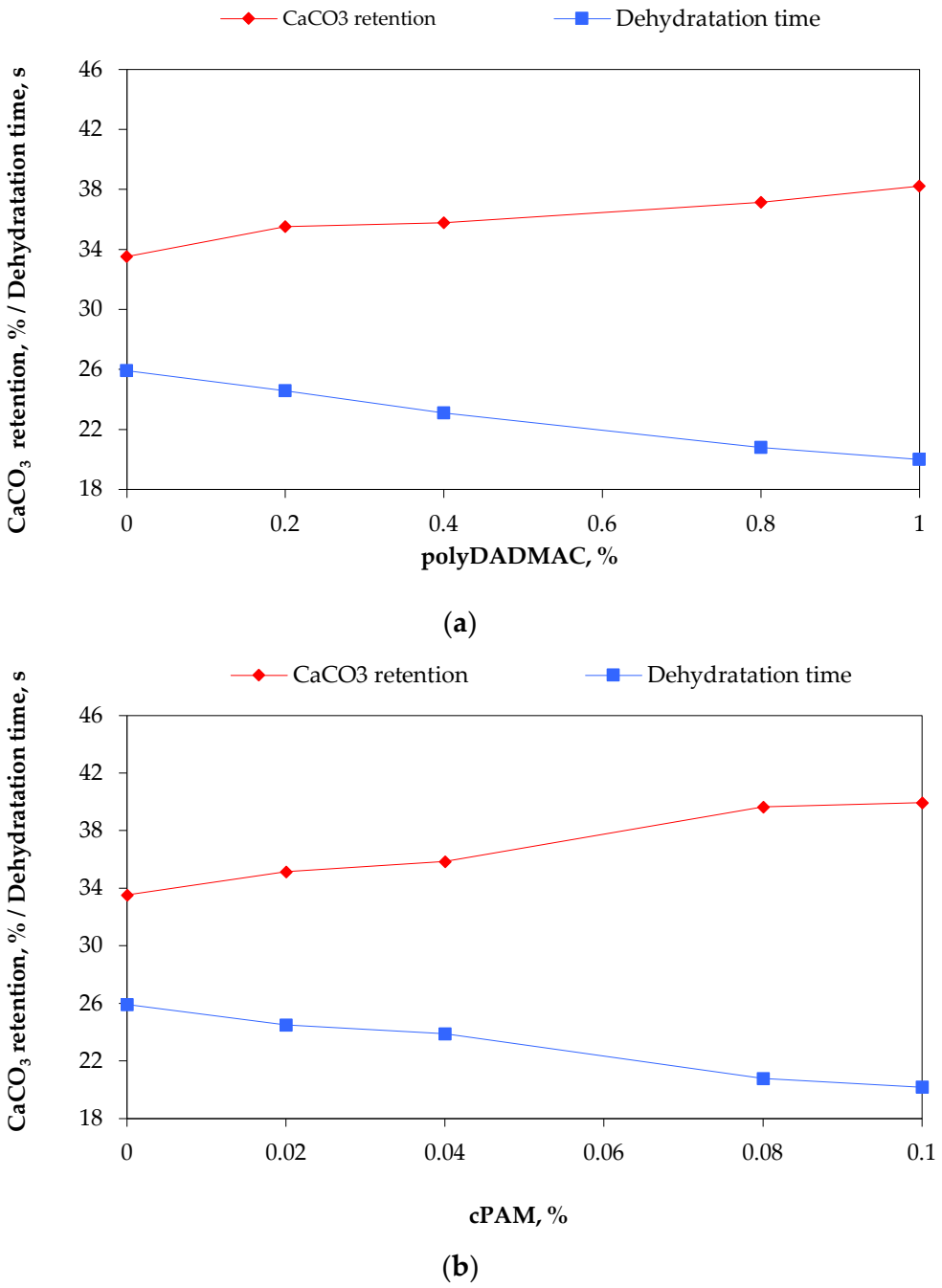

Figure 1. Influence of pDADMAC (**a**) and cPAM (**b**) polymers on PCC retention and dehydration time of PCC filled fibers.

3.2. X-Ray Diffraction

The presence of PCC in the fibers and the polymorphic form of PCC particles retained in paper pulp were determinates by X-ray diffraction analysis. Figure 2 presents the X-ray diffraction results for PCC and for paper pulp loaded with PCC. X-ray diffraction of the PCC and of the fibers analysis had shown a characteristic calcite diffraction model. In Figure 2, the peak at 29.3° (104) has shown the calcium carbonate content for calcite, and for cellulose it is show at 22.5° (002).

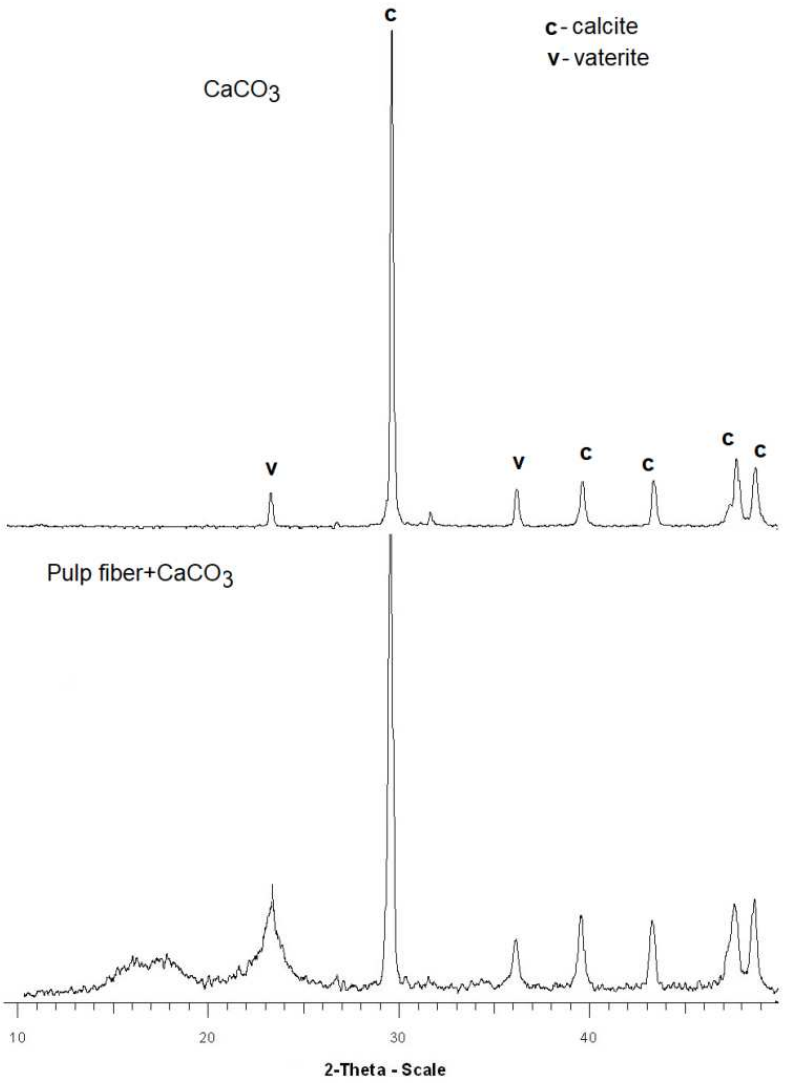

Figure 2. X-ray diffraction spectrum for PCC and paper loaded with PCC.

By adding polymers (polyDADMAC and cPAM), no significant differences are observed.

3.3. Thermogravimetric Analysis

Thermal degradation properties (DTG and TG) of PCC samples were investigated. The weight losses as a function of temperature for all samples are shown in Figure 3.

The PPC decomposition behavior at 850 °C, 20 min in pure N_2 atmosphere (Figure 3a) reveals similar processes of samples decomposition. Up to 4 phases including weight loss are recorded for samples, but there only one weight loss phase occurs during decomposition of calcium carbonate at 550–830 °C. The conversion of PCC to CaO is indicated by weight loss, usually occuring rapidly in the range 550 to 830 °C. After than 850 °C, no further significant weight loss was observed, thus, this temperature was chosen as holding temperature to investigate the effect of calcination dwelling time. All materials recorded up to 44% weight loss and a residual ~55 wt% of converted CaO, thus resulting a conversion factor of ~ 0.55 $gCaO/gCaCO_3$.

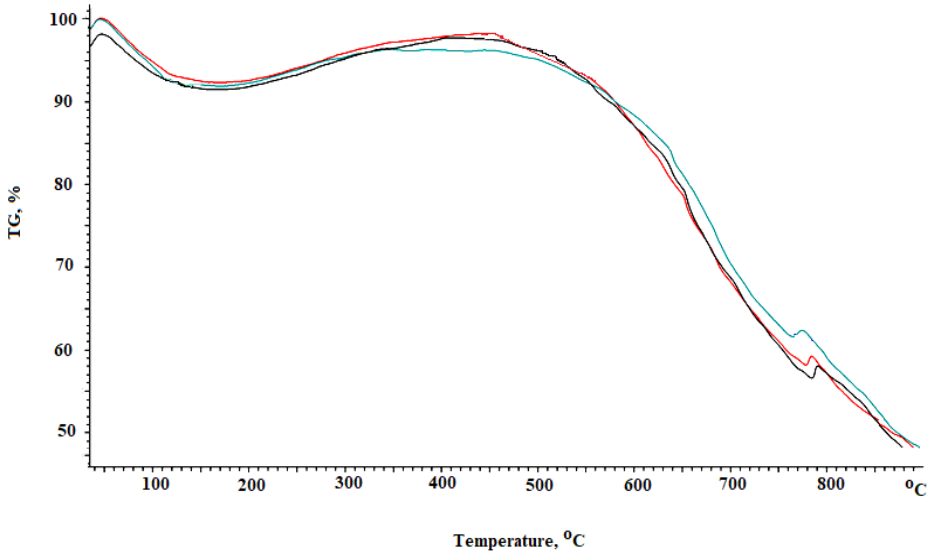

(**a**)

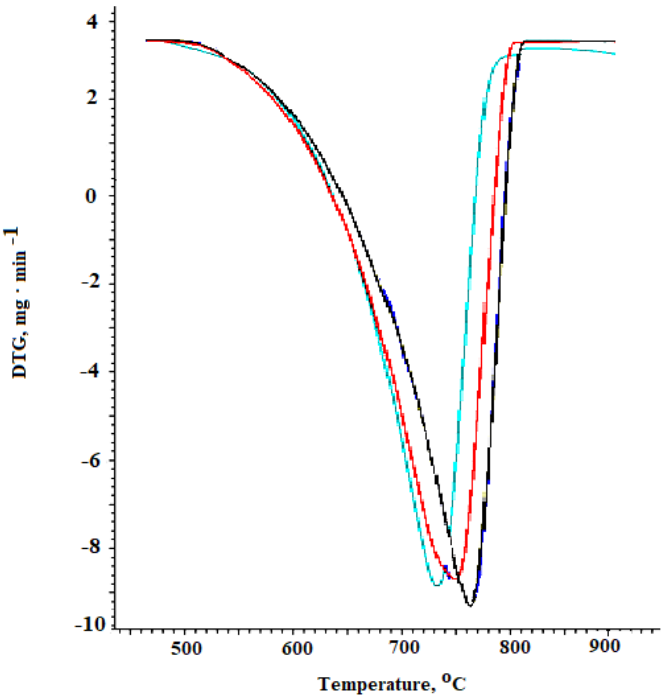

(**b**)

Figure 3. TG (**a**) and DTG (**b**) curves of PCC (black) PCC/polyDADMAC (blue) and PCC/cPAM (red).

Thermogravimetric characteristics of the samples are presented in Table 2.

Table 2. Thermogravimetric characteristics of the samples.

Samples	Stages	T_{onset}	T_{peak}	T_{endset}	PPC%	Residuum
PCC	I	676	764	778	44.12	55.28
PCC/cPAM	I	657	768	780	44.18	55.82
PCC/polyDADMAC	I	662	757	774	44.08	55.92

DTG analyses (Figure 3b) showed that PPC displays only one peak corresponding to substance decarbonation, whereas, by polymer addition, the decomposition peak was shifted to a higher temperature value.

3.4. Scanning Electron Microscopic Images (SEM)

The morphological characteristics of PCC particles deposited onto the cellulose fibers were investigated by SEM.

From SEM images (Figure 4a–c) we can observe the crystallization of PCC which take place with the formation of calcite microcrystals of specific shape.

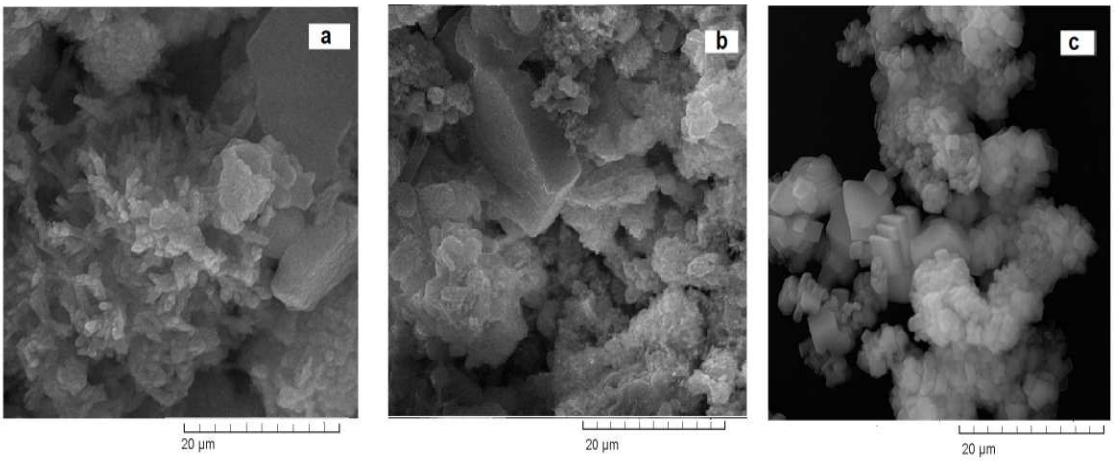

Figure 4. SEM images of PCC (**a**), PCC/1% polyDADMAC (**b**) and PCC/0.1% cPAM (**c**) saples.

The polymers are most widely used in control the size of the particles and morphology of PCC [29]. Due superior optical properties, the scalenohedral calcite has reached like most used PCC filler in papermaking.

The SEM images (Figure 5a–d) of the paper samples showed that they are obtained PCC calcite microcrystals of specific shape and also revealed that the largest number visible surface crystals of PCC show up for 35% PCC/1% polyDADMAC sample.

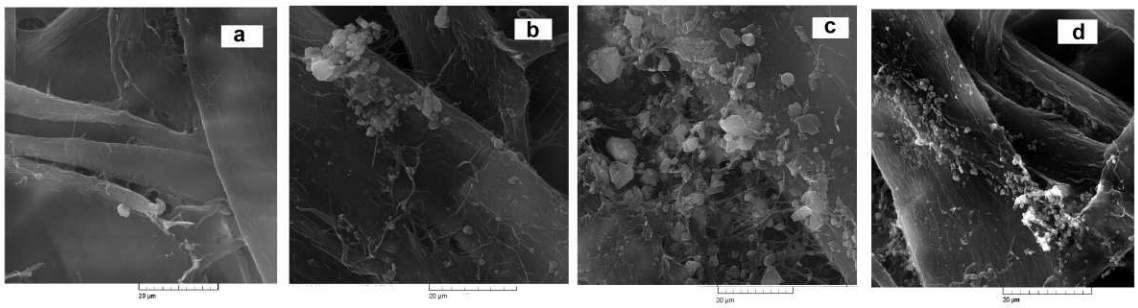

Figure 5. SEM images of paper samples: without PCC (**a**), 35% PCC (**b**), 35% PCC/1% polyDADMAC (**c**) and 35% PCC/0.1% cPAM (**d**).

3.5. Optical Properties

A series of factors as particle size, particle shape and distribution of the PCC contribute to the optical and mechanical properties of the paper. The efficiency of the production of writing/printing paper depends most of the time on the solutions used to obtain the optical properties sought. This aspect is very important because some factors that have a positive effect on the degree of whiteness and opacity can negatively influence the mechanical properties such as the strength of the product.

Both polymers used led to small variations in the filling material content, for close values of the degree of whiteness and opacity. Table 3 shows the optical properties and the

average deviation calculated for the both cases studied. The influence of polyDADMAC and cPAM cationic polymers on brightness and opacity properties of the paper loaded with PPC are presented in Figure 6a,b.

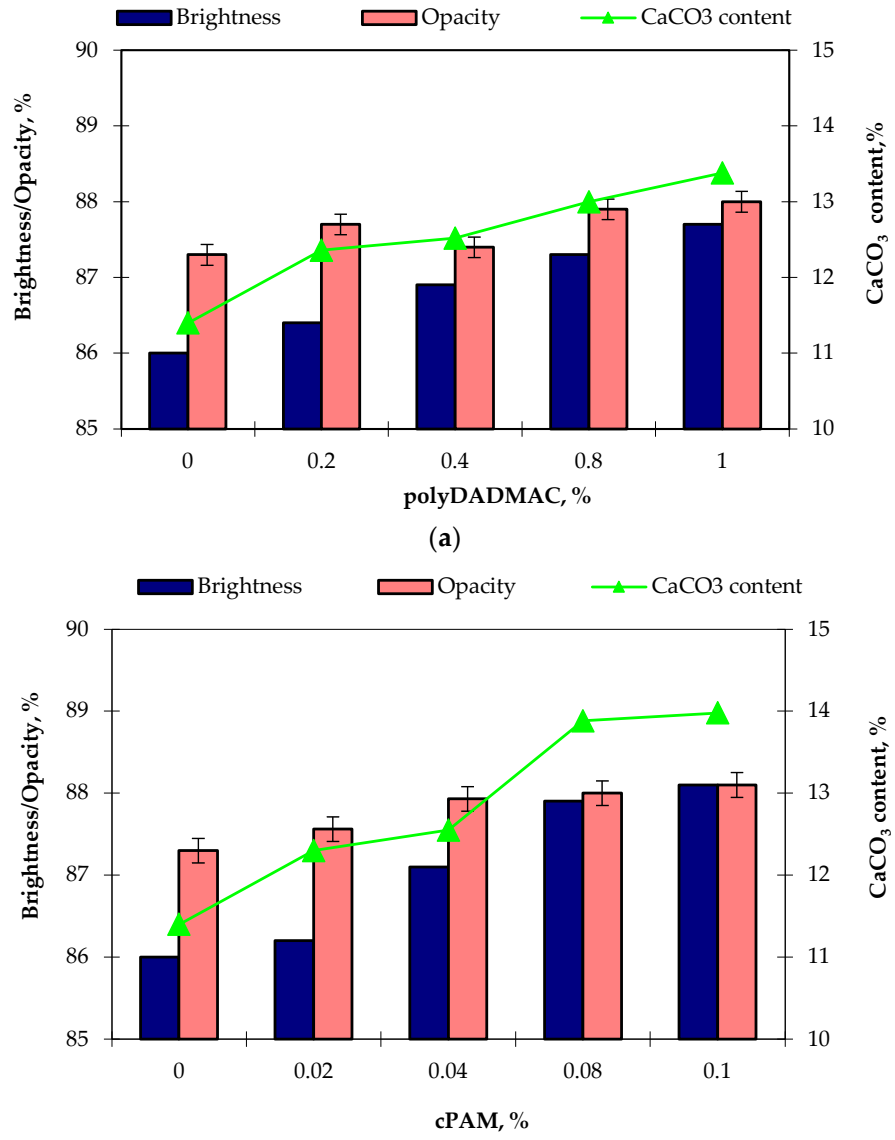

Figure 6. The influence of polyDADMAC (**a**) and cPAM (**b**) polymers on brightness and opacity properties of the paper loaded with PPC.

Table 3. Optical properties for the samples.

Optical Properties	**% p-DADMAC**				
	0	**0.2**	**0.4**	**0.8**	**1**
Brightness, %	86	86.4	86.9	87.3	87.7
Opacity, %	87.3	87.7	87.4	87.9	88
Optical Properties	**% cPAM**				
	0.02	**0.04**	**0.08**	**0.1**	
Brightness, %	86.2	87.1	87.9	88.1	
Opacity, %	87.56	87.93	88	88.1	

From Figure 6 we can see that the highest opacity is obtained in the case of loaded sample with PCC/cPAM. This can be explaining due the presence of PCC particles at the fibre surface, as well as within the fibre wall pores which are well dispersed. This is also evident from the SEM images by the smaller PCC particle size. The lower opacity of the PCC sample without the addition of polymers can be explain by non-uniformity disppersion of the PCC particles into the paper structure.

3.6. Physical-Mechanical Properties of Paper Samples

For a good evaluation of the effectiveness of cationic polymers on the strength properties, the breaking length of the paper was calculated taking into account its calcium carbonate content (35%). At variable addition of polyDADMAC and cPAM the breaking length of the paper filled with 35% $CaCO_3$ shows higher values with increasing additive addition (Figure 7). Also the PCC content in the paper registers a greater increase in the case of the cPAM sample and the breaking length is superior in this case, compared to the sample with polyDADMAC where statistically insignificant variations are observed.

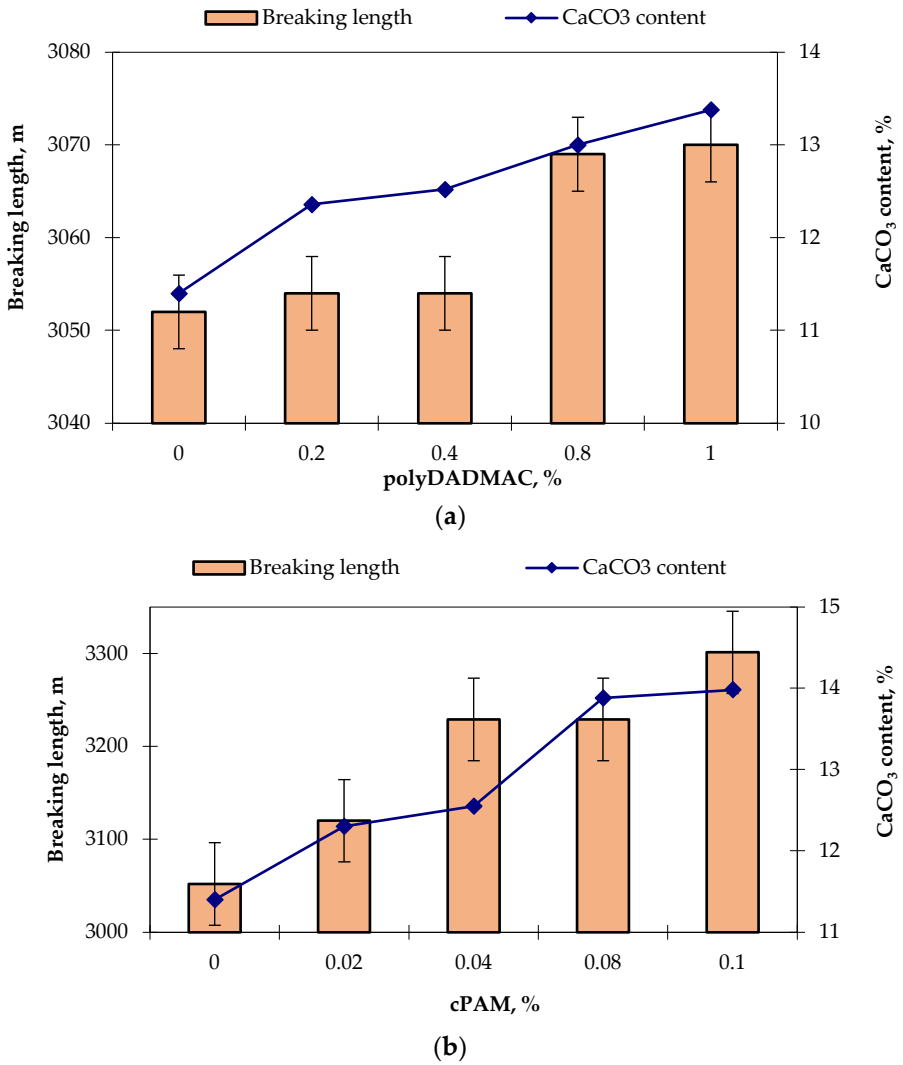

Figure 7. Influence of addition of polyDADMAC (**a**) and cPAM (**b**) on break length of the paper loaded with PPC.

The burst index does not register important changes with the addition of additives, as can be seen from Figure 8. The evolution of the burst index for the sample with polyDADMAC is comparable to cPAM sample.

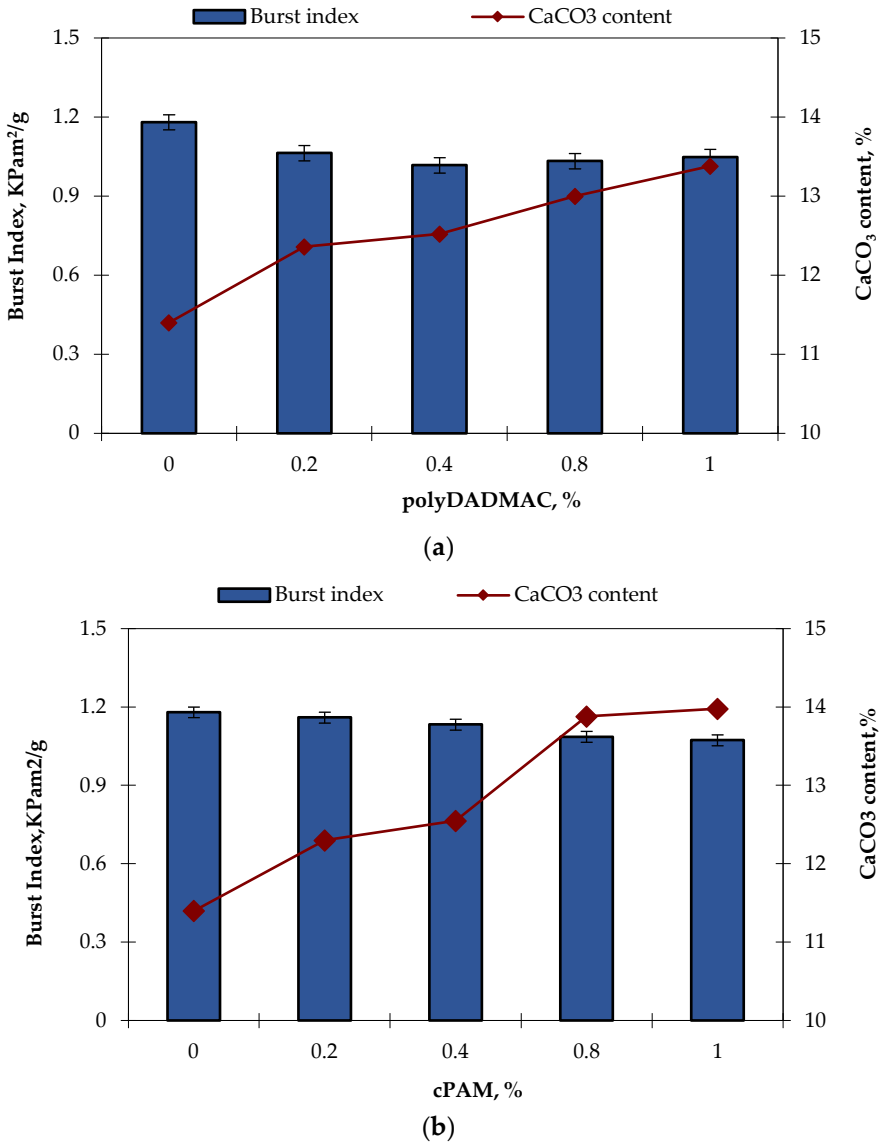

Figure 8. Influence of the addition of polyDADMAC (**a**) and cPAM (**b**) on the burst index of the paper.

4. Conclusions

The retention has been found to be a critical aspect of the manufacturing process of writing/printing papers with alkaline media, so by testing different chemical additives at different additions (polyDADMAC and cPAM), improvement of the retention of the filler material was achieved: cPAM gives the best results in terms of $CaCO_3$ retention, but the optical properties values are similar with other treatments; air permeability is better when cPAM is used as an additive compared to the polyDADMAC system. The strength properties of the paper filled with 35% $CaCO_3$ increase with the addition precipitate of the additive, for both types of additives used.

The effects of the PCC on paper properties showed a greater stabilization when a cationic polymers was added.

Author Contributions: Conceptualization, E.U., M.E.F. and A.L.; methodology, D.C.J.; investigation, M.E.F., E.U. and D.C.Ț.; resources, O.C.U.; writing—original draft preparation, O.C.U.; and D.C.J.; writing—review and editing, M.E.F. and E.U.; visualization, M.E.F. and D.C.Ț.; supervision, D.C.J. and A.L.; funding acquisition, D.C.Ț. and O.C.U. All authors have read and agreed to the published version of the manuscript.

Funding: This research received no external funding.

Institutional Review Board Statement: Not applicable.

Informed Consent Statement: Not applicable.

Data Availability Statement: Data is contained within the article.

Conflicts of Interest: The authors declare no conflict of interest.

References

1. Hubbe, M.A.; Gill, R.A. Fillers of papermaking: A review of their properties, usage practices, and their mechanistic role. *BioResources* **2016**, *11*, 2886–2963. [CrossRef]
2. Fortună, M.E. *Fibrous Pigments of Nanocomposite Type*; Pim: Iasi, Romania, 2022; pp. 21–119, ISBN 978-606-13-6707-8.
3. Chauhan, S.V.; Singh, P.S.; Pramod, K.B. Fiber loading of hardwood pulp by in-situ precipitation of aluminosilicate. *BioResources* **2007**, *2*, 560–571.
4. Fortună, M.E.; Ungureanu, E.; Jităreanu, C.D. Calcium Carbonate–Carboxymethyl Chitosan Hybrid Materials. *Materials* **2022**, *14*, 3336. [CrossRef] [PubMed]
5. Othman, R.; Zakaria, S.; Chia, C.H.; Zuriyati, A.; Isa, N. Mechanical and optical properties of $CaCO_3$ lumen-loaded paper: Effect of polyethylenimine and plum. *Sains Malays.* **2010**, *39*, 435–439.
6. Miroslav, A.; Volf, P.; Pointe-Claire, P.; Pointe-Claire, L.; Baie D'Urfe, S.; Beaconsfield, M. Papermaking Additive Cross-Reference to Related Applications. U.S. Patent 7,875,150 B2, 25 January 2011.
7. Fortuna, M.E.; Harja, M.; Bucur, D.; Cimpeanu, S.M. Obtaining and Utilizing Cellulose Fibers with in-Situ Loading as an Additive for Printing Paper. *Materials* **2013**, *6*, 4532–4544. [CrossRef]
8. Fortună, M.E.; Ignat, M.; Asandulesa, M.; Rotaru, R.; Pricop, L.; Harabagiu, V. Improved physico-chemical properties of mesoporous carbon by functionalization with aminopropyl-polydimethylsiloxane (AP-PDMS). *J. Inorg. Organomet. Polym. Mater.* **2018**, *28*, 2275–2287. [CrossRef]
9. Jimoh, O.A.; Ariffin, K.S.; Hussin, H.B.; Temitope, A.E. Synthesis of precipitated calcium carbonate: A review. *Carbonates Evaporites* **2018**, *33*, 331–346. [CrossRef]
10. Saghavaz, K.M.; Resalati, H.; Ghasemian, A. Cellulose-precipitated calcium carbonate composites and their effect on paper properties. *Chem. Pap.* **2014**, *68*, 774–781.
11. Selin, J.; Hangaslammi, A. Method of Adding Pigment to Paper. Patent WO0214603, 21 February 2002.
12. Klungness, J.H.; Sykes, M.S.; Tan, F.; Abubakr, S.; Eisenwasser, J.D. Effect of fiber loading on paper properties. *Tappi J.* **1996**, *79*, 297–301.
13. Fortună, M.E.; Lobiuc, A.; Cosovanu, L.M.; Harja, M. Effects of in-situ filler loading vs. conventional filler and the use of retention-related additives on properties of paper. *Materials* **2020**, *13*, 5066. [CrossRef]
14. Lin, L.; Yin, X.; Retulainen, E.; Nazhad, M.M. Effect of chemical pulp fines on filler retention and paper properties. *Appita J.* **2007**, *60*, 469–473.
15. Silenius, P. Preparation of Filler Containing Papermaking Materials by Precipitating Calcium Carbonate In-Situ in the Presence of Cellulosic Materials. Master's Thesis, Department of Chemical Technology, Lappeenranta University of Technology, Lappeenranta, Finland, 1996.
16. Li, L.; Collis, A.; Pelton, R. A new analysis of filler effects on paper strength. *J. Pulp Pap. Sci.* **2002**, *28*, 267–273. [CrossRef] [PubMed]
17. Ungureanu, E.; Căpraru, A.M.; Ungureanu, O.; Jităreanu, C.D.; Iacob, V.; Ulea, E.; Popa, V.I. Ecologycal biocide systems based on unmodified and epoxydation lignins, furan resin and copper. *Cell. Chem. Technol.* **2012**, *46*, 599–603.
18. Ungureanu, E.; Trofin, A.; Trincă, L.C.; Ariton, A.M.; Ungureanu, O.C.; Fortună, M.E.; Jităreanu, C.D.; Popa, V.I. Studies on kinetics and adsorption equilibrium of lead and zinc ions from aqueous solutions on Sarkanda Grass lignin. *Cell. Chem. Technol.* **2021**, *55*, 939–948. [CrossRef]
19. Ungureanu, E.; Jităreanu, C.D.; Trofin, A.; Fortună, M.E.; Ungureanu, O.C.; Ariton, A.M.; Trincă, L.C.; Brezuleanu, S.; Popa, V.I. Use Of Sarkanda Grass Lignin as a possible adsorbent for As (III) from aqueous solutions—Kinetic and equilibrium studies. *Cell. Chem. Technol.* **2022**, *56*, 681–689. [CrossRef]
20. Middleton, S.R.; Desmeules, J.; Scallan, A.M. Lumen loading with calcium carbonate fillers. *J. Pulp Pap. Sci.* **2003**, *29*, 241–246.
21. Hubbe, M.A.; Nanko, H.; McNeal, M.R. Retention aid polymer interactions with cellulosic surfaces and suspensions: A review. *BioResources* **2009**, *4*, 850–906. [CrossRef]
22. Ungureanu, E. Aspects of Composites Biodegradation Based on Lignocelluloses Materials. Ph.D. Thesis, "Gh. Asachi" Polytechnic University of Iasi, Iasi, Romania, 2008; pp. 34–62.
23. Nicke, R.; Pensold, S.; Tappe, M.; Hartmann, H.J. Poly-diallyldimethylammonium Chloride as a Flocculating Agent. *Wochenbl. Papierfabr.* **1992**, *14*, 559–564.
24. Swerin, A.; nWågberg, L. Size-Exclusion Chromatography for Characterizationof Cationic Polyelectrolytes Used in Papermaking. *Nordic Pulp Paper Res. J.* **1994**, *9*, 18–25. [CrossRef]
25. Ungureanu, E. *Lignin, Aromatic Natural Polymer with High Potential for Recovery*; Pim: Iasi, Romania, 2011; pp. 103–194, ISBN 978-606-13-0384-7.

26. Bown, R. Physical and chemical aspects of the use of fillers in paper. In *Paper Chemistry*; Roberts, J.C., Ed.; Backie Academic & Professional: Hong Kong, China, 1996; Chapter 11; pp. 202–229.
27. Anerek, A.V. *Filler Retention in Papermaking by Polymeric and Microparticulate Retention Aid Systems*; Department of Chemistry McGill University Montréal: Montreal, QC, Canada, 2004; pp. 2–245.
28. Siven, S.K.; Manner, H.J. Fibre loading using an aluminum compound. *Appita J.* **2003**, *56*, 438–441.
29. Laukala, T.; Lyytikäinen, J.; Mielonen, K.; Backfolk, K. Effect of PCC crystallization and morphology on flocculation with microfibrillated cellulose, on sheet densification and liquid absorption behavior. *Cellulose* **2020**, *27*, 10151. [CrossRef]

materials

MDPI

Article

Effects of Hybrid Polymeric Material Based on Polycaprolactone on the Environment

Maria E. Fortună [1], Elena Ungureanu [2,*], Doina C. Jităreanu [2], Denis C. Țopa [2] and Valeria Harabagiu [1]

[1] Institute of Macromolecular Chemistry "Petru Poni", 41A Grigore Ghica Voda Alley, 700487 Iasi, Romania; fortuna.maria@icmpp.ro (M.E.F.); hvaleria@icmpp.ro (V.H.)
[2] Department of Plant Science, "Ion Ionescu de la Brad" University of Life Sciences, 3 Mihail Sadoveanu Alley, 700490 Iasi, Romania; doinaj@uaiasi.ro (D.C.J.); dennistopa@uaiasi.ro (D.C.Ț.)
* Correspondence: eungureanu@uaiasi.ro

Abstract: Polymers are of great interest in areas such as agriculture, medicine and pharmacy, the food and cosmetic industries, and the chemical and construction industries. However, many polymers are nonbiodegradable and are not environmentally friendly. They are highly resistant to degradation and therefore can lead to waste disposal problems. In recent years, the interest in the microbial degradation of polymeric materials has grown due to the desire for less waste pollution in the environment. In this study, the biodegradable polymer that was obtained by the ring-opening polymerization of ε-caprolactone (CL) using an aminopropyl-polydimethylsiloxane (APDMS) oligomer and the effects of the polymer towards the growth and development of tomato plants (*Lypercosium esculentum*) were investigated. The obtained product was characterized using FTIR spectroscopy, NMR spectroscopy, and energy dispersion spectroscopy (EDX) analysis, and the effects of this compound on the evolution of tomato plants (*Lypercosium esculentum*) were studied. We also studied the biological stability of the product by identifying some of the microorganisms that developed on the surface, given its susceptibility to biodegradation.

Keywords: aminopropyl-terminated polydimethylsiloxane; environmental impact; ε-caprolactone; hybrid; tomato plants (*Lypercosium esculentum*); microorganisms

Citation: Fortună, M.E.; Ungureanu, E.; Jităreanu, D.C.; Țopa, D.C.; Harabagiu, V. Effects of Hybrid Polymeric Material Based on Polycaprolactone on the Environment. *Materials* **2022**, *15*, 4868. https://doi.org/10.3390/ma15144868

Academic Editor: Manoli Zubitur

Received: 15 June 2022
Accepted: 7 July 2022
Published: 13 July 2022

1. Introduction

Due to their mechanical and chemical properties with numerous applications, polymers play an important role in a multitude of fields [1]. In general, synthetic polymers offer excellent mechanical and thermal properties, while biobased polymers are mostly biodegradable. Therefore, by combining the advantages of natural polymers and synthetic polymers, the resulting hybrid materials have the potential for biomedical and environmental applications [2].

The polymers with potential toxicity that accumulate in nature influence the environment and the various organisms exposed to them. For this reason, the environmental impacts of polymers and their waste should be studied [3].

A series of polymers are nonbiodegradable and are not decomposed by microorganisms, and this can lead to waste disposal problems; therefore, an alternative is needed for the disintegration of this waste. The fabrication of materials containing both biodegradable and nonbiodegradable polymers can be an effective method to reduce the total amount of polymer waste, which cannot be degraded in nature [4].

Biodegradation is a very valued process that harnesses the power of the microorganisms present in an environment to remove plastic products in a safe and efficient way [5]. The microorganisms growing in the rhizosphere have a significant role in the biodegradation of the hybrid materials [6,7]. The composites suffer different changes by being decomposed into simple organic compounds that modify the metabolism of the plant,

leading to the modification of the plant structure. The quantity of nitrogen from the roots and stalks of the plant varies both according to the type of product used and its addition [8].

Contact between the microorganisms and the hybrid structure will result in an increase in the contact surface between the microorganisms and the synthetic polymer and acceleration of biotic reactions [9]. Other organisms, such as insects, snails, or beetles, can also contribute to the degradation process by digesting these products, and through biodegradation, they can form ketone groups, thus accelerating the destruction of the synthetic matrix [2]. Therefore, biodegradation is influenced by many factors: the nature and structure of the polymer and its compounds, reaction conditions, and microorganisms [10,11]. Given these aspects, natural or synthetic and degradable or non-degradable polymers have received much more attention in recent decades [12,13].

Polydimethylsiloxane (PDMS) is a synthetic polymer with many interesting properties such as chemical stability, biocompatibility, a low glass transition temperature (T_g), gas permeability, high hydrophobicity, and resistance to biodegradation [14]. Therefore, it can be used for functionalizing various surfaces and as a building block for polymers and hybrid organic–inorganic systems [15–17]. Due to its properties, PDMS has a wide range of applications, and its elimination has an impact on the environment. PDMS is nonbiodegradable and is missing in the environmental impact studies of siloxanes and the siloxanes compounds [18]. However, it is assumed that the siloxane stability in biodegradation is due to the lowered electron density in the carbon atoms and in the polydimethylsiloxanes and a steric shielding effect in the methyl groups. The insertion of functional groups into polysiloxane chains may be a promising approach to benign organosilicon compounds [19–21].

Polycaprolactone (PCL) is a semi-crystalline polymer with native biocompatibility and biodegradability, a high solubility at room temperature, and a low melting temperature and is known to be miscible with a large variety of polymers. PCL degradation is readily degraded by the lipases and esterase of the microorganism [22].

The block copolymers are obtained through a combination of excellent properties of PDMS and PCL, which makes it a synthetic biomaterial with various applications, particularly biomedical ones. In this regard, the literature has reported it as a method for the preparation of block copolymers and for the ring-opening polymerization of ε-caprolactone with mono or difunctionally terminated reactive hydroxy or amine functional oligomers as initiators [23,24].

In this study, the synthesis and characterization of the block copolymer of polycaprolactone with aminopropyl-terminated polydimethylsiloxane and the effects of this compound on the growth and development of tomato plants (*Lypercosium esculentum*) along with the isolation and characterization of microorganisms involved in environmental impact were evaluated comparatively with the starting materials.

2. Experimental Section

2.1. Materials

Black peat that was harvested in September 2020 was offered by "Ion Ionescu de la Brad" Iasi University of Life Sciences (IULS) and was used as a soil with the following properties: 58.14% relative humidity; 41.82% dry substance; 3.84% ash; 96.16% volatile substances; 76.00% porosity; 38.12% water retention capacity; pH = 7.12; C% = 52.29; N_t% = 0.94; C/N = 55.62; P(P_2O_5)% = 0.14; K(K_2O)% = 0.12. Peat is predominantly found in hill and mountain regions and consists of a set of organic matter (decomposed leaves, grass, fungi, or insects) and has a number of advantages over ordinary soil: it accelerates seed germination and plant growth; allows for higher yields, both quantitatively and qualitatively, in terms of economic efficiency; it has a neutral or slightly alkaline pH; and has a higher mineral content [2].

Biological material: Tomato seeds (*Lypercosium esculentum*), San Marzano variety, IULS. The fruits have an elongated form and the weight is 60/80 g.

Chemical materials: ε-Caprolactone and octamethylcyclotetrasiloxane (D4) were purchased from Aldrich; stannous octoate was obtained from Air Products. Toluene was purchased from Aldrich and was freshly used after distillation over sodium wires. Xylene and methanol were purchased from Sigma-Aldrich (St. Louis, MO, USA).

2.2. Synthesis of Aminopropyl-Terminated Polydimethylsiloxane

APDMS was synthesized using the chemical equilibration of 1,3-Bis(3-aminopropyl)-1,1,3,3-tetramethyldisiloxane with octamethylcyclotetrasiloxane in the presence of tetramethylammonium hydroxide catalyst, according to a previous experiment [25].

In a round-bottom flask, a solution of tetramethylammonium hydroxide (10%) in methanol was prepared under magnetic stirring. Then, 0.8 g of D4 and 10 mL of toluene were added. The reaction mixture was stirred for 12 h to 80 °C under an argon atmosphere. APDMS was obtained after the distillation of octamethylcyclotetrasiloxane at 150 °C under vacuum (1 mmHg). The solvent was also removed under vacuum.

2.3. Synthesis of Aminopropyl-Terminated Polydimethylsiloxane-Caprolactone (APDMS-CL) Copolymers

APDMS-CL copolymer was obtained using ring-opening polymerization of ε-Caprolactone in the presence of stannous octoate as the catalyst (Scheme 1) [26,27].

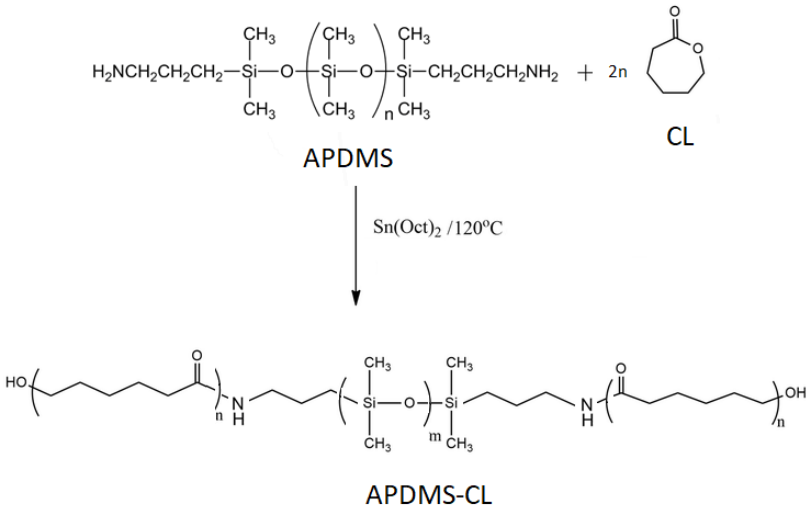

Scheme 1. Synthesis of APDMS-CL triblock copolymers.

In a reaction, 3 g CL, 1.6 g APDMS as a macroinitiator, 0.023 g of stannous octoate catalyst, and 2 g of xylene were added to a 50 mL three-neck round bottom flask. Then, the reaction mixture was heated to 120 °C and stirred under nitrogen for 24 h. Due to viscosity, 10 g of xylene was added and stirred. Purification was performed by precipitating the reaction mixture in methanol. The precipitate was dried in a vacuum oven at 40 °C for 24 h, and the product was accessed to have a yield of 91.5%.

2.4. Characterization Methods

Fourier Transform Infrared (FTIR) spectroscopy was used to investigate the surface chemistry of the synthesized materials. The absorption spectra were recorded using a Bruker Vertex 70 FTIR spectrometer (Bruker Optics, Ettlingen, Germany). Registrations were performed in transmission mode within a 400–4000 cm^{-1} range with a resolution of 2 cm^{-1} at room temperature on samples dissolved in KBr pellets. Nuclear Magnetic Resonance (^{1}H-NMR) spectra were recorded with a Bruker NMR spectrometer at 400 MHz (Bruker, Billerica, MA, USA). The standard for a chemical shift in $CDCl_3$ (deuterate chloroform) is TMS (dilute tetramethylsilane).

The surface morphologies were visualized by Scanning Electron Microscopy (SEM) (Brno, Czech Republic) and a Quanta 200 scanning electron microscope (5 kV) with an EDX

elemental analysis system (Ametek, Berwyn, PA, USA) that was used to identify the surface morphology and composition.

Thermogravimetric (TGA) and differential scanning calorimetry (DSC) analyses were performed using STA 449F1 Jupiter equipment (Netzsch, Selb, Germany) and a DSC 200 F3 Maia device (Netzsch, Selb, Germany), respectively.

The environmental impact of the siloxane matrices was carried out by evaluating parameters that provide clues on the initiation of the ecotoxicological impact, such as capacity and germination index, plant size, amount of green and dry biomass, nitrogen dynamics, and the study of biological stability was determined by identifying biological agents in the system.

The experimental laboratory conditions consisted of 23–25 °C for 35 days, during which time visual observations and biometric analyses were carried out. Vegetation vessels (height of 9 cm and diameter of 6 cm) and a culture medium consisting of black peat were used as supports [3]. The sample weights of APDMS, CL, and APDMS-CL were 0.3 g.

The mass of the soil introduced into each vessel was 80 g. Firstly, a layer of soil (3 cm) was placed into each vessel, then the fraction of the sample (APDMS, CL, and APDMS-CL) was added. A 4 cm layer of soil was added on top of that, and then 3 tomato seeds were added, which were covered with a 2 cm layer of soil. As a reference, the soil was only used with tomato seeds (Reference sample). The experimental samples are notated as follows: Reference, CL, APDMS, and APDMS-CL.

Subsequently, the non-disintegrated solid siloxane fractions were collected and transported in sterile bags for mycological testing.

In order to correctly determine any installed microorganisms, the samples were inserted into Petri plates on wet filter paper and submitted to thermostatation. After that, the samples were passed on to a culture medium containing 40 g $NaNO_3$ (sodium nitrate), 20 g K_2HPO_4 (dipotassium hydrogen phosphate), 10 g $MgSO_4$ (magnesium sulphate), 10 g KCl (potassium chloride), 0.2 g $FeSO_4$ (iron sulphate), 30 g sucrose, and 20 g agar. Finally, the samples were dissolved in 1000 mL distilled water, in which micromycetes needed to develop in order to correctly determine the genus and species concerned. The resulting medium was sterilized for 20 min at 120 °C and then distributed in Petri dishes with diameters of 10 cm, followed by another sterilization. The micromycetes that appeared after 48 h on the matrix fragments were repainted. These were cultivated until the appearance of fungal colonies. All cultures were incubated in a dark cultivation chamber for 28 days at a temperature of 25 ± 2 °C and a relative air humidity of 80 ± 2% [28]. At the end of the test period, macro- and microscopic examination was performed to detect and identify any microorganisms.

For the microscopic analysis, the classical method was used using the Kern OBN 135 microscope, RS 136-3498. For greater accuracy of the results, mass spectrometry was used—a high-performance method that precisely identifies the unique "molecular footprint" of each microorganism, which was achieved by using a Maldi TOF MS spectrophotometer [29–31].

The IG germination index was then calculated using the following Equation (1):

$$IG = \text{x } 100 \frac{\text{number of germinated seeds (\%) x root length for samples}}{\text{number of germinated seeds (\%) x root length for reference sample}} \text{ (\%)} \quad (1)$$

3. Results and Discussion

3.1. Structural Characterization

The samples were investigated by Fourier Transform Infrared spectroscopy. The results confirm the synthesis of APDMS-CL triblock copolymers (Figure 1).

The APDMS structure was confirmed by the presence of a $–CH_2–NH_2$ bend at about 1588 cm^{-1}, which was assigned to the amine group. The 1023–1093 cm^{-1} bands were assigned to Si–O–Si, and the 800 cm^{-1} band was attributed to CH_2–Si–O vibrations. The 1261 cm^{-1} band was assigned to Si–CH_3. The APDMS-CL structure was confirmed by the presence of the absorption band at 1099 cm^{-1}, which was assignable to the stretching

vibration of the Si–O bonds of the APDMS polymer, and the presence of the very strong stretching vibration of the carbonyl groups at 1728 cm^{-1} was attributed to the ester group in CL. The 1018–1099 cm^{-1} region was assigned to the Si–O–Si bands, the band at 1261 cm^{-1} was attributed to the Si–CH_3 band, and 800 cm^{-1} was attributed to the CH_2–Si–O vibrations.

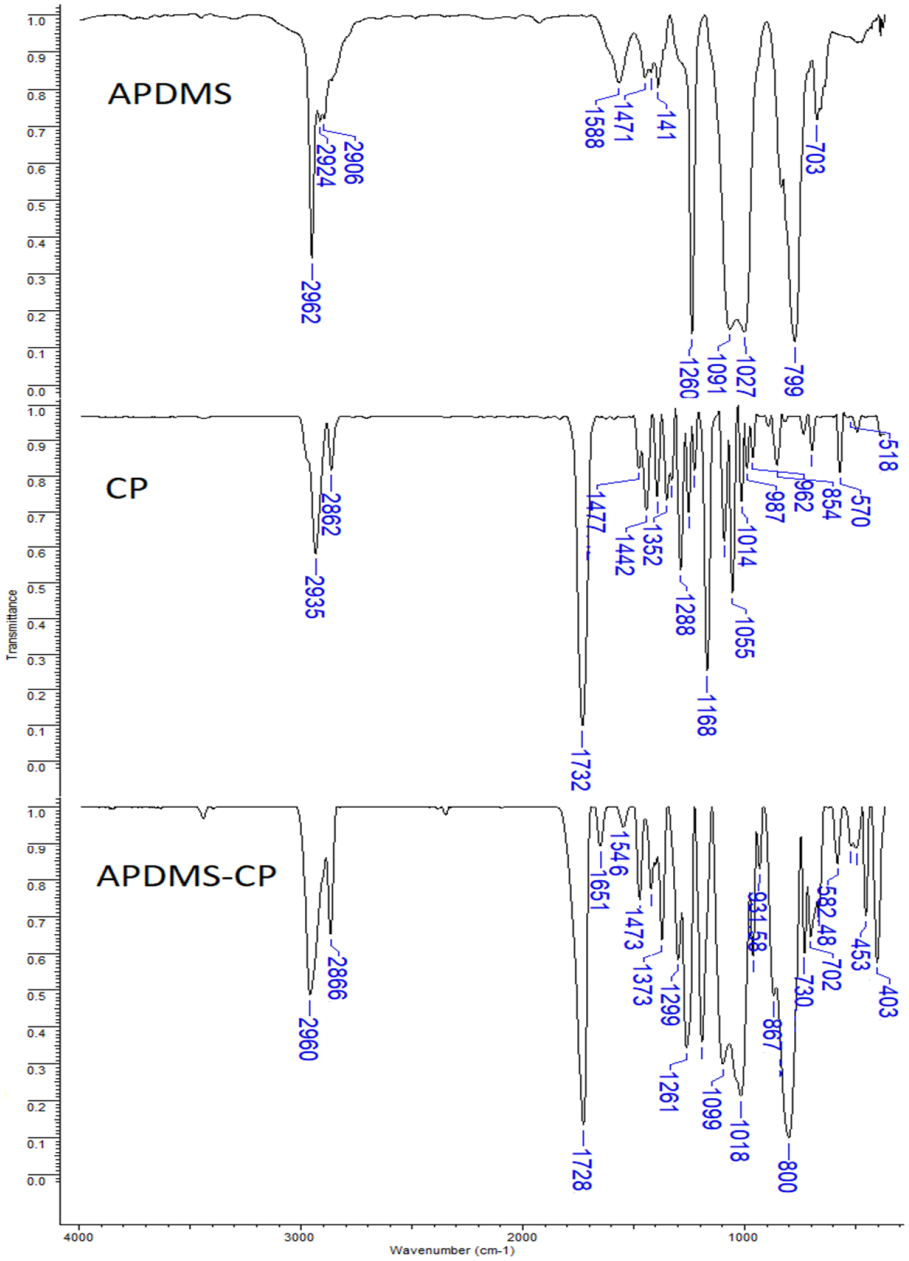

Figure 1. Infrared spectrum of APDMS, CL, and APDMS-CL.

The amide I (from the C=O stretching vibrations) and amide II (from the C–N stretching and CNH) bands correspond to 1651 and 1546 cm^{-1}, respectively [32,33].

The synthesis of the well-defined copolymer was confirmed by the NMR spectrum (Figure 2).

The attribution of the peaks of the copolymer, as seen in Figure 2, were as follows: –CH_2–H (3.61 ppm); –CH_2–NH– (4.04 ppm); –CH_2–CH_2–CH_2–NH– (1.62 ppm); –CO–CH_2–CH_2–CH_2– (1.42 ppm); –CO–CH_2–CH_2– (1.62 ppm); –CO–CH_2– (2.32 ppm); –Si(CH_3)$_2$– (0.07 ppm); –Si–CH_2–(0.5 ppm); and –CH_2–CH_2–CH_2 (1.47).

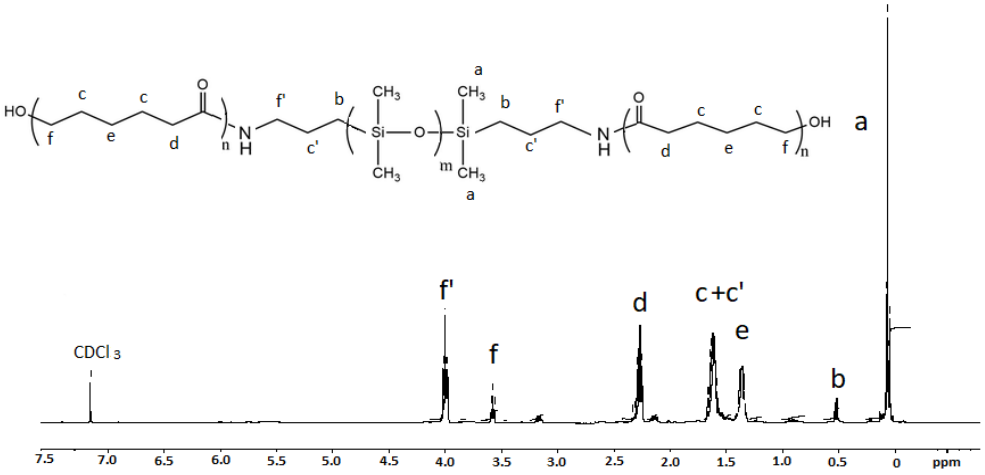

Figure 2. NMR spectrum for synthesized APDMS-CL.

3.2. Surface Morphology

An EDX elemental analysis system was used to identify the surface morphology and composition. The elemental analysis was calculated after three repeated measurements.

Figure 3 illustrates the EDX spectra for the APDMS-CL copolymer. The presence of siloxane was confirmed by the high peak at around 1.8 keV, which is characteristic of silicon atoms.

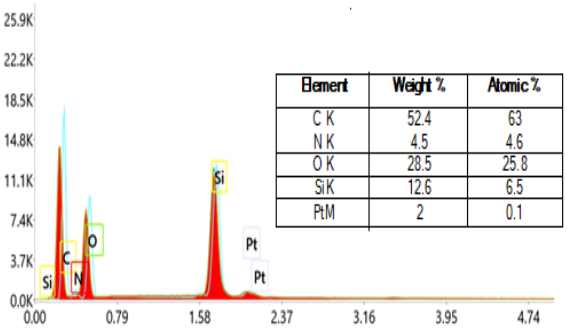

Element	Weight %	Atomic %
C K	52.4	63
N K	4.5	4.6
O K	28.5	25.8
Si K	12.6	6.5
Pt M	2	0.1

Figure 3. EDX spectra for APDMS-CL.

A scanning electron microscope was used to study the phase separation. The SEM results indicate that the APDMS-CL sample has a phase segregation morphology (Figure 4).

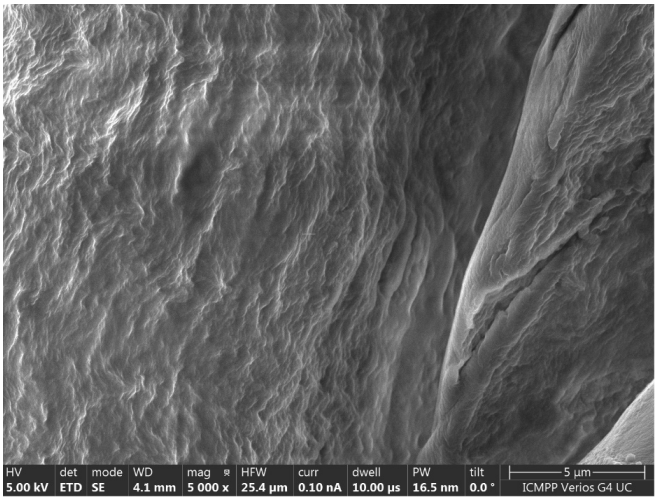

Figure 4. The SEM images of APDMS-CL.

3.3. Thermal Properties of the APDMS and APDMS-CL

Shown in Figure 5 are the registered TG and differential thermogravimetric (DTG) curves of APDMS (a) and APDMS-CL (b) under a nitrogen atmosphere. The thermal behavior of these materials was assessed in terms of percentage loss in weight from ambient temperature up to 700 °C.

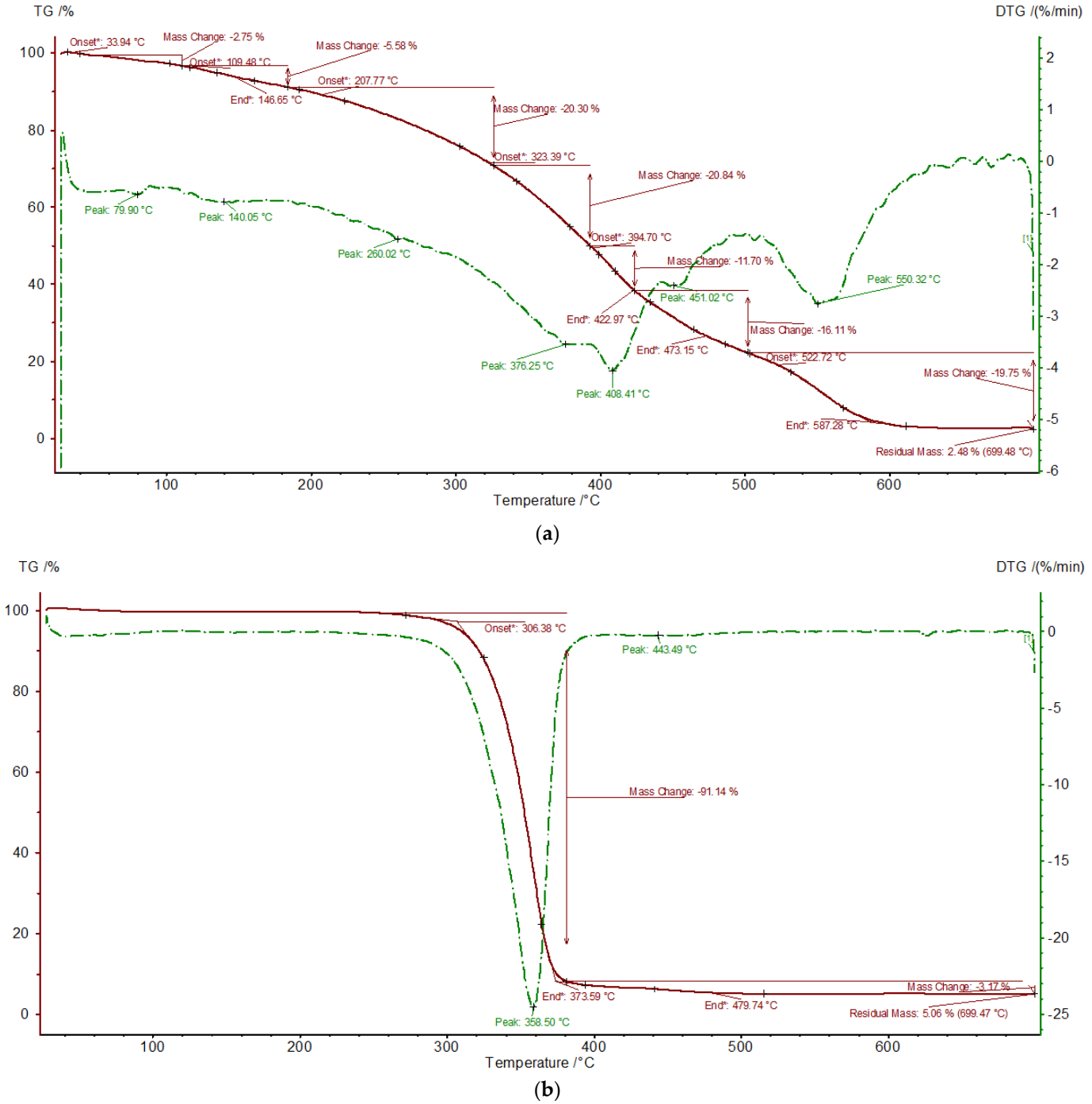

Figure 5. Thermogravimetric (red) and differential thermogravimetric (green) curves of APDMS (**a**) and APDMS-CL (**b**).

More weight loss steps could be observed for the APDMS sample, with maximum decomposition peaks situated at about: 80, 140, 260, 376, 408, 451, and 550 °C. It could be observed that APDMS has four weight loss steps that occur at 146.65 °C (with the weight loss of 5.58%), at 422.97 °C (with a weight loss of 11.70%), at 473.15 °C (with a weight loss

of 16.11%), and at 587.28 °C (with a weight loss of 19.75%), and at 699.48 °C, a residual mass of 2.48% remains. The weight loss in the range of the residual mass corresponds to material decomposition and the leftover mass residue. For the APDMS-CL composite, two maximum decomposition peaks situated at 359 and 443 °C could be observed. It could also be observed that APDMS-CL has two weight loss steps that occur at 373.59 °C (with the weight loss of 91.14%), and at 479.74 °C (with a weight loss of 3.17%), and at 699.47 °C, a residual mass of 5.06% remains.

The DSC analysis for APDMS and its APDMS-CL composite were made in reference to temperature values between −100 and 200 °C (Figure 6).

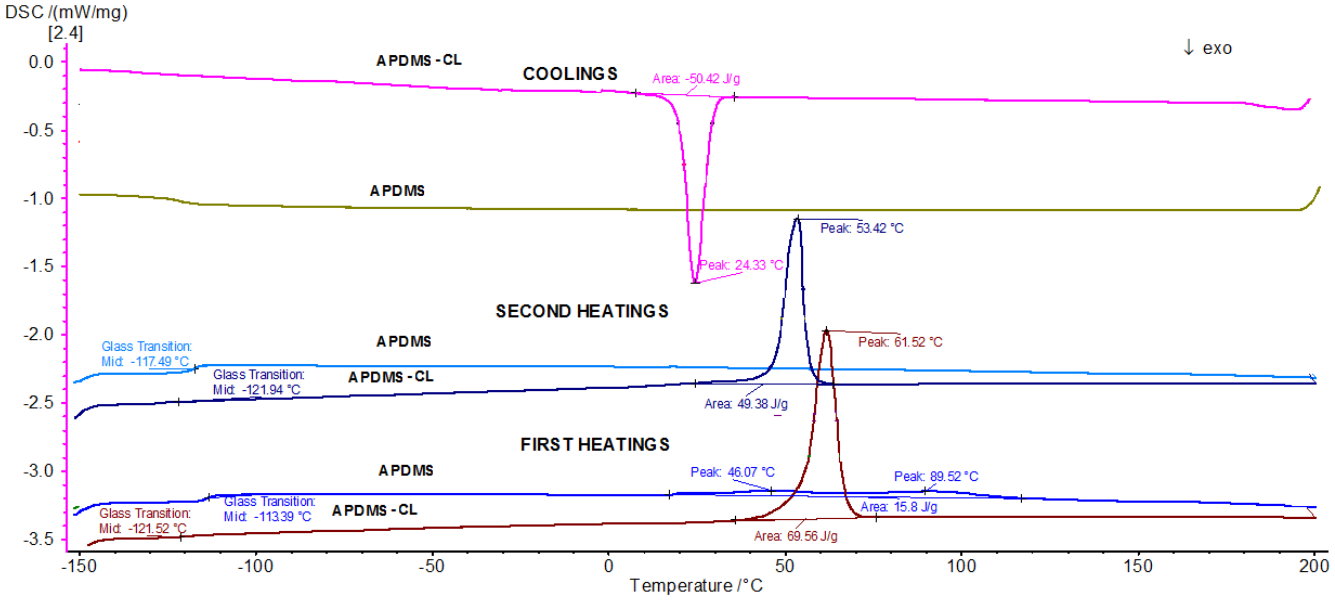

Figure 6. DSC curves of APDMS and APDMS-CL.

The first measurements (first heating) showed a glass transition (T_g) at –114 °C (two peaks centered at about 46 and 90 °C) for APDMS and at –122 °C for the APDMS-CL composite (a peak at about 62 °C). For the second measurement (second heating), the glass transition was obtained at –117 °C and –122 °C for APDMS and APDMA-CL, respectively. As heating continued, a shift was observed in the composites yielding peaks at 24 °C, potentially indicating crystallization.

In this study, biometric testing analyzes the evolution of tomato plants, and microbiological analysis assesses the biological stability of the samples.

3.4. Tomato Seed Germination Test

The germination test is the most sensitive parameter for the assessment of toxicity and a method of estimating the nutritional qualities of the soil, i.e., the substrate obtained when applied as a nutrient to plant growth. Seed germination is influenced by temperature, with each plant having a minimum threshold, an optimal threshold, and a maximum threshold of the thermal values between which this process takes place.

During the growing season, all of the experimental samples were visually monitored periodically, every 7 days, and biometric measurements were taken for the purpose of assessing the development of plant size (Figure 7).

In order to determine the germination index, it was necessary to measure the length of the plant root. Table 1 presents the average length of the plant roots 35 days after planting and the germination index.

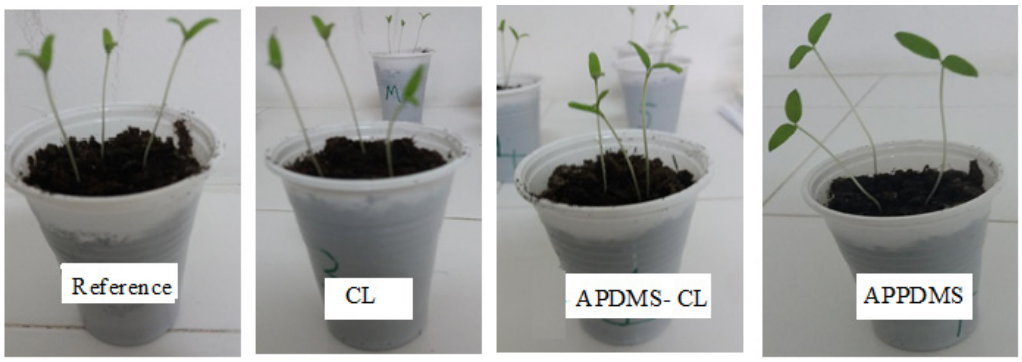

Figure 7. Tomato plants 7 days after planting.

Table 1. The average length of plant roots and germination index.

Analyzes	Samples			
	Reference	APDMS-CL	CL	APDMS
Medium root plant length 35 days after planting, cm	1.6	0.7	1.4	1.1
Germination index, %	100	50.4	87.5	68.75

From the experimental data analysis, the size of the roots varied in descending order, as follows: Reference—1.6 cm, CL—1.4 cm, APDMS—1.1 cm, and APDMS-CL—0.7 cm.

As expected, the germination index has the maximum value in the case of the reference sample, a fairly high value, approximately 90%, in the CL sample, a value of more than 50% in the APDMS sample, and a value slightly below 50% in the APDMS-CL sample.

3.5. The Average Height of the Plants

The average height of the tomato plants for every sample is presented in Figure 8.

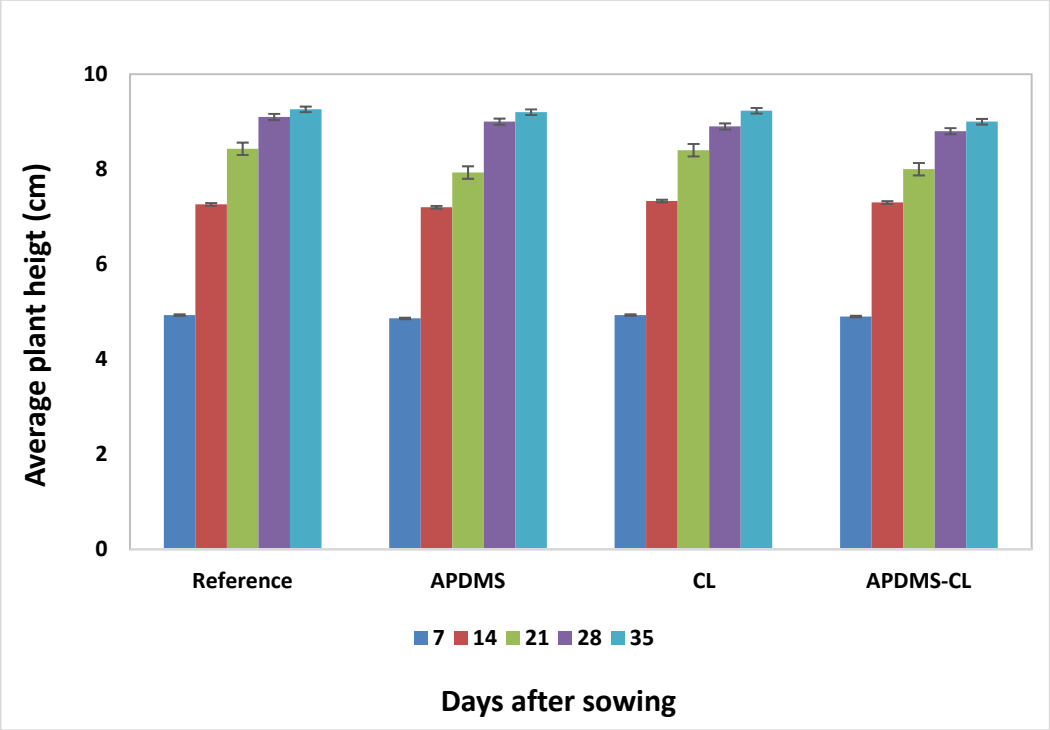

Figure 8. Average height of tomato plants during the experiment.

The plant height for APDMS had smaller development than what was recorded for the reference, CL, and APDMS-CL samples and degraded more slowly. It seems that the state of liquid aggregation allows for faster interaction with the soil, and the effect on the growth and development of the plants is a more pronounced one.

In the case of APDMS-CL, after 14 days, the size of the plant had similar development to the reference sample, which can be explained by the non-initiation of biodegradation. After 21, 28, and 35 days, the size of the plant is less evolutionary for APDMS-CL and CL than in the reference sample, which confirms the initiation of biodegradation, but is higher than in APDMS, which had faster interaction with the soil, due to its liquid state.

In the CL sample, the size of the plant evolved similar to that of the reference sample, with no major variations.

Plant growth and development are below the reference level for all of the samples studied, except for the CL sample, which behaves similarly to the reference, but there is no major decrease, which can be attributed to the susceptibility of the samples to the environment to some extent.

3.6. Dry and Green Biomass

Subsequently, in order to determine the amount of green biomass, the tomato plants were weighed on the analytical balance. Because the plants were smaller in size, the weighing was conducted in its entirety. After three days of weighing the green biomass, dry biomass weighing was also carried out (the drying of the plants was carried out under laboratory conditions) (Figure 9).

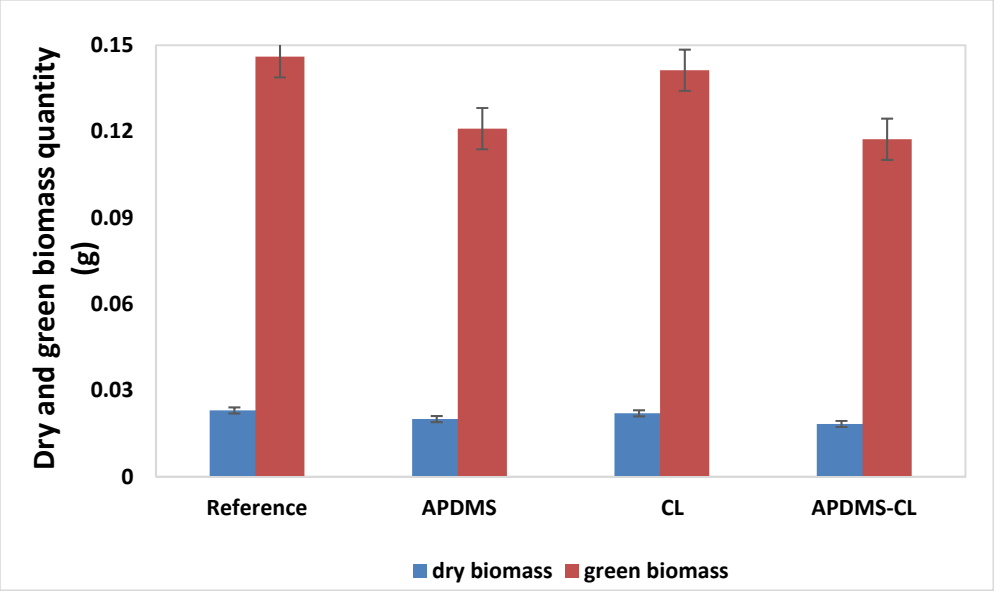

Figure 9. Dry and green biomass quantities of tomato plants.

Figure 10 represents the dry tomato plants for all of the samples three days after harvest.

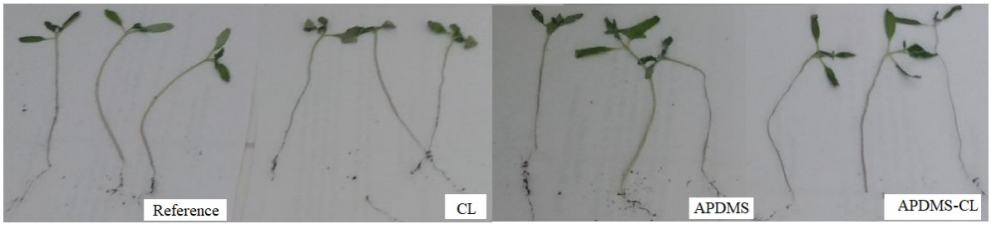

Figure 10. Dry tomato plants three days after harvest.

From the experimental data analysis, the amount of green biomass varies in descending order, as follows: Reference, CL, APDMS, and APDMS-CL. Additionally, the quantity of dry biomass varies in the same order. Compared to the reference sample, the values obtained for the samples with siloxane content show that it influences the green biomass and the dry biomass, which demonstrates the initiation of the ecotoxicological impact of these matrices and the less disturbing effect on plant evolution. In order to determine the germination index, it was necessary to measure the length of the plant root. Table 2 presents the total nitrogen determination after plant removal.

Table 2. Total nitrogen determination after plant removal.

Samples	Total Nitrogen (N_t), %			
	Reference	APDMS-CL	CL	APDMS
	0.81	1.23	0.91	1.43

After analyzing the values of this parameter, it can be concluded that the matrices incorporated in the soil are susceptible to ecotoxicological impact and influence the growth and development of plants, showing an involution compared to the reference, but not on a major scale.

3.7. Total Soil Nitrogen Dynamics

The next stage of the study consisted of the determination of the total nitrogen using the Kjeldhal method for all of the soil samples, which constituted the culture medium for the tomato seeds. Nitrogen fixation is vital for plants, although very few species (soybeans, clover, peas, beans, lentils) have the ability to fix nitrogen from the atmosphere through bacteria.

The nitrogen deficiency in tomatoes is manifested by the yellowing of the leaves from the tip to the petiole along the main rib, and in the case of seedlings, the plants are light green, which are characteristics that were not visible in our experiment. The nitrogen amount in the soil depends on two antagonistic processes: mineralization and immobilization.

The first (mineralization) consists of the decomposition of the organic substance under the action of soil microorganisms and the release of ammonium ions, and the second (immobilization) consists of the conversion of mineral nitrogen from the soil, also under the action of microorganisms, into cellular proteins and other compounds with organic nitrogen [34].

$$\text{N from the soil} \underset{\text{immobilization}}{\overset{\text{mineralization}}{\rightleftharpoons}} NH_4^+ \underset{\text{nitrifying reduction and immobilization}}{\overset{\text{nitrification}}{\rightleftharpoons}} NO_3^- \quad (2)$$

Regarding the dynamics of the total nitrogen in the soil, the differences between the samples studied are small and statistically insignificant.

It is known that most plants need nitrogen from the soil and for most crops; this means that they are dependent on nitrogen fertilizers and beneficial bacteria from the soil [35]. This is also confirmed by the experimental data obtained, as the nitrogen content of the reference sample in the final measurement is lower than that recorded in the reference sample in the initial measurement.

In comparison, it was found that the lowest nitrogen content is recorded in the reference sample, while in the other experimental samples, it is higher, which demonstrates the contribution of organic nitrogen released from the studied samples.

The visual analysis during the growing season of the experimental samples, the biometric measurements, and the amounts of green and dry biomass conclude that the plants had enough nitrogen for normal growth and development.

3.8. Biological Stability

The impact of the siloxane matrices as well as their susceptibility to the environment were also tested by a biological stability study based on the isolation and characterization of the microorganisms involved.

On the one hand, the presence of siloxane can act selectively by inhibiting the action of microorganisms that would biodegrade the matrix, while on the other hand, it allows for the selection of species that are tolerant to these polymeric structures.

At the end of the experiment, the visual analysis found that in the case of the APDMS-CL sample, there were traces of undisintegrated compounds, so the siloxane matrices were harvested and subsequently transported in sterile bags for mycological testing. In the other samples studied, mycological testing could not be performed.

Two species of fungi (Fusidium viride and Penicillium brevi-compactum) were identified from the analyses, with colony diameters varying inversely proportionally to the amount of solid siloxane matrix (the larger the diameter, the smaller the amount of siloxane) (Figure 11). The macroscopic observations [9,36] on the degree of the development of fungal mycelium on APDMS-CL are presented in Table 3.

Figure 11. Macroscopic and microscopic images of the APDMS-CL sample on the surface of which the fungus Fusidium viride developed.

Table 3. The macroscopic observations on the degree of development of fungal mycelium on APDMS-CL.

Samples	Microorganisms	Macroscopic Observations
APDMS-CL	Fusidium viride	*Poor–moderate* development of fine grey mycelium covering approximately 20–30% of the surface
	Penicillium brevi-compactum	*Moderate* mycelium development, with the maximum degree of moulding on the surfaces being maximum of 40%.

The isolated Fusidium viride fungus formed on Czapek's agar (CZA) or Czapek–Dox medium and took the form of a very fine filament from which the conidiophores could hardly be distinguished. The oval conidia that may or may not be sharp towards the ends of the filament are hyaline and measure 5–7 × 3 µm (Figure 12).

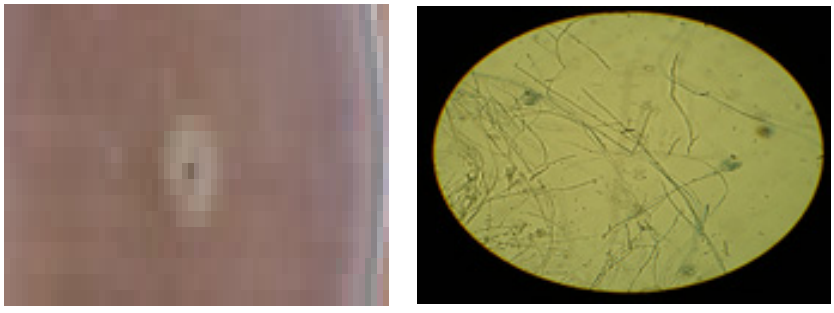

Figure 12. Macroscopic and microscopic images for penicillium brevi-compactum fungus developed on the siloxane matrix.

In *Penicillium brevicompactum*, the colonies that appeared on the medium are quite small and green–gray against the yellow-gray-colored medium under the colony. The diameter of the colony reached 2–3 cm 10–12 days after emergence. The conidiophores varied in length and were shorter than in other Penicillium species, forming areas on the surface of the colony with a higher center and slightly yellow droplets. Under the colony, the mycelium was yellow. The conidiophores were 300 × 3.5 µm, with sparse branches and smooth walls. The branches were 20 × 3 µm, the meticulous were 12 × 2.5 µm, and the fields were 10 × 2.5 µm, and there was an absence of smooth conidia, with ovate to subglobulation measurements of 2.5 × 2.5–3 µm.

The fact that the siloxane matrices function as new hosts for the two micromycetes: Fusidium viride and *Penicillium brevicompactum*, is a first, as this aspect has not been reported in the literature thus far.

Microscopic aspects are edifying for the effects of the studied matrices and for the development of microorganisms [37]. Thus, it is possible on the one hand to highlight the characteristics of fungi capable of biosynthesizing the enzymes that can degrade the siloxane material. On the other hand, these results allow the clarification of the ability to inhibit the development of microorganisms. Plant cultivation also involves the manifestation of the rhizosphere and the stimulation of the development of microorganisms that may be involved in the environmental impact.

4. Conclusions

In the light of the parameters studied, the experimental results demonstrated the environmental impact of the tested samples. The products were released into the soil, which influenced the growth and development of the plants. The analyzed parameters showed lower values compared to the reference sample (in the vessel without siloxane material, the plants developed better than if they were introduced into the soil alongside the tested matrices) but were at an acceptable level. The development of microorganisms, in particular, Fusidium viride and *Penicillium brevicompactum*, were first identified on hybrid polymeric materials based on polycaprolactone, which also confirms that these products do not have a major disturbing effect on soil composition and plant evolution and show acceptable susceptibility to the environment.

Moreover, due to the superior performance compared to the individual materials and through the possibilities of modeling the properties according to the field of use, the researched hybrid can be a solution for the future, without negatively influencing the bioremediation of the soil.

Author Contributions: Conceptualization, M.E.F., E.U. and V.H.; methodology, D.C.J.; investigation, M.E.F. and E.U.; resources, E.U.; Visualization, D.C.Ț.; writing—original draft preparation, M.E.F. and D.C.J.; writing—review and editing, M.E.F. and E.U.; visualization, D.C.J.; Software, D.C.Ț.; supervision, D.C.J. and V.H.; funding acquisition, D.C.Ț. All authors have read and agreed to the published version of the manuscript.

Funding: This research received no external funding.

Conflicts of Interest: The authors declare no conflict of interest.

References

1. Milani, P.; França, D.; Balieiro, A.G.; Faez, R. Polymers and its applications in agriculture. Review Article. *Polímeros* **2017**, *27*, 256–266. [CrossRef]
2. Hamad, K.; Kaseem, M.; Ko, Y.G.; Deri, F. Biodegradable Polymer Blends and Composites: An Overview. *Pol. Sci. Ser. A* **2014**, *56*, 812–829. [CrossRef]
3. Song, J.H.; Murphy, R.J.; Narayan, R.; Davies, G.B.H. Biodegradable and compostable alternatives to conventional plastics. *Philos. Trans. R. Soc. B Biol. Sci.* **2009**, *364*, 2127–2139. [CrossRef]
4. Ungureanu, E. Aspects of Composites Biodegradation Based on Lignocelluloses Materials. Ph.D. Thesis, "Gh. Asachi" Polytechnic University of Iasi, Iasi, Romania, 2008; pp. 15–20.
5. Kurakula, M.; Koteswara, G.S.N.; Rao, K.; Yadav, S. Fabrication and characterization of polycaprolactone-based green materials for drug delivery. In *Applications of Advanced Green Materials*; Woodhead Publishing: Sawston, UK, 2021; pp. 395–423.

6. Shukla, K.P.; Sharma, S.; Singh, N.K.; Singh, V.; Bisht, S.; Kumar, V. *Rhizoremediation: A Promising Rhizosphere Technology. Applied Bioremediation: Active and Passive Approaches*; Patil, Y., Rao, P., Eds.; InTech: London, UK, 2013; pp. 94–108.
7. Redouane, E.L.M.; Mugani, R.; Lahrouni, M.; Martins, J.C.; Zerrifi, S.E.L.A.; Oufdou, K.; Campos, A.; Vasconcelos, V.; Oudra, B. Role of Rhizospheric Microbiota as a Bioremediation Tool for the Protection of Soil-Plant Systems from Microcystins Phytotoxicity and Mitigating Toxin-Related Health Risk. *Microorganisms* **2021**, *9*, 1747. [CrossRef] [PubMed]
8. Havstad, R.M. Biodegradable plastics. In *Plastic Waste and Recycling: Environmental Impact, Societal Issues, Prevention, and Solutions*; Letcher, T., Ed.; Academic Press: Cambridge, MA, USA, 2020.
9. Moenne-Loccoz, Y.; Mavingui, P.; Combes, C.; Normand, P.; Steinberg, C. Microorganisms and Biotic Interactions. In *Environmental Microbiology: Fundamentals and Applications: Microbial Ecology*; Bertrand, J.C., Caumette, P., Lebaron, P., Matheron, R., Normand, P., Ngando, T.S., Eds.; Springer: Dordrecht, The Netherlands, 2015; pp. 395–444.
10. Iftime, M.M.; Ailiesei, G.L.; Ungureanu, E.; Marin, L. Designing chitosan based eco-friendly multifunctional soil conditioner systems with urea-controlled release and water retention. *Carbohydr. Polym.* **2019**, *223*, 115–140. [CrossRef]
11. Zambrano, M.C.; Pawlak, J.J.; Venditti, R.A. Effects of chemical and morphological structure on biodegradability of fibers, fabrics, and other polymeric materials. *BioResources* **2020**, *15*, 9786–9833. [CrossRef]
12. Vroman, I.; Tighzert, L. Biodegradable Polymers. *Materials* **2009**, *2*, 307–344. [CrossRef]
13. Ghanbarzaeh, B.; Almasi, H. Biodegradable Polymers. In *Biodegradation*; Chamy, R., Rosenkranz, F., Eds.; InTech: London, UK, 2013; pp. 10–19.
14. Reddy, M.S.B.; Ponnamma, D.; Choudhary, R.; Sadasivuni, K.K. A Comparative Review of Natural and Synthetic Biopolymer Composite Scaffolds, Review. *Polymers* **2021**, *13*, 1105. [CrossRef]
15. Bhatia, S. Natural Polymers vs. Synthetic Polymer. In *Natural Polymer Drug Delivery Systems*; Springer International Publishing: Cham, Switzerland, 2016; Volume 3, pp. 95–118.
16. Fortună, M.E.; Pricop, L.; Zaltariov, M.; Popovici, D.; Ignat, M.; Harabagiu, V.; Simionescu, B.C. Cu(II)/Guanidine Functionalized Disiloxane Complex of Supramolecular Structures for Visible Light-Driven Photocatalysis of Congo Red. *Polymers* **2022**, *14*, 817. [CrossRef]
17. Ekin, A.; Webster, D.C. Library Synthesis and Characterization of 3-Aminopropyl-Terminated Poly(dimethylsiloxane)s and Poly (ε -caprolactone)-b-Poly(dimethylsiloxane)s. *J. Polym. Sci. A Polym. Chem.* **2006**, *44*, 4880–4894. [CrossRef]
18. Ariati, R.; Sales, F.; Souza, A.; Lima, R.A.; Ribeiro, J. Polydimethylsiloxane Composites Characterization and Its Applications: A Review. *Polymers* **2021**, *13*, 4258. [CrossRef] [PubMed]
19. Lehmann, R.G.; Miller, J.R.; Kozerski, G.E. PDMS is nonbiodegradable and they are missing environmental biodegradation studies of siloxanes and the siloxanes compounds. *Chemosphere* **2002**, *41*, 743–749. [CrossRef]
20. Grabitz, E.; Reich, M.; Olsson, O.; Kümmerer, K. Using structure biodegradability relationships for environmentally benign design of organosilicons—An experimental comparison of organosilicons and their carbon analogues. *Sustain. Chem. Pharm.* **2020**, *18*, 100331. [CrossRef]
21. Zalewski, K.; Chyłek, Z.; Trzcinski, W.A. A Review of polysiloxanes in terms of their application in explosive. *Polymers* **2021**, *13*, 1080. [CrossRef] [PubMed]
22. Song, L.; Ahmed, M.F.; Li, Y.; Bejoy, J.; Zeng, C.; Li, Y. PCL-PDMS-PCL Copolymer-Based Microspheres Mediate Cardiovascular Differentiation from Embryonic Stem Cells. *Tissue Eng. Part C Methods* **2017**, *23*, 627–640. [CrossRef]
23. Malikmammadov, E.; Tanir, T.; Kiziltay, E.A.; Hasirci, V.; Hasirci, N. PCL and PCL-based materials in biomedical applications. *J. Biomater. Sci. Polym. Ed.* **2018**, *29*, 863–893. [CrossRef]
24. Zhang, D.; Giese, M.L.; Prukop, S.L.; Grunlan, M.A. PCL-based Shape Memory Polymers with Variable PDMS Soft Segment Lengths. *J. Polym. Sci. A Polym. Chem.* **2011**, *49*, 754–761. [CrossRef]
25. Fortună, M.E.; Ignat, M.; Asandulesa, M.; Rotaru, R.; Pricop, L.; Harabagiu, V. Improved Physico-chemical Properties of Mesoporous Carbon by Functionalization with Aminopropyl-polydimethylsiloxane (APPDMS). *J. Inorg. Organomet. Polym. Mater.* **2018**, *28*, 2275–2287. [CrossRef]
26. Yang, J.; Zhou, Q.; Shen, K.; Song, N.; Ni, L. Controlling nanodomain morphology of epoxy thermosets templated by poly(caprolactone)-block-poly(dimethylsiloxane)-blockpoly(caprolactone) ABA triblock copolymer, Review. *RSC Adv.* **2018**, *8*, 3705–3715. [CrossRef]
27. Gordin, C.; Rusu, M.; Delaite, C.; Salhi, S.; Elzein, T.; Brogly, M. Crystalinity Behaviour in Poly(ε-caprolactone)-b-Poly(dimethylsiloxane) Diblock and Triblock Copolymers through FTIR and DSC. *Mat. Plast.* **2009**, *46*, 37.
28. Barnet, J.A.; Barnet, L. *Medical Yeasts, 1800 to 2000, Book Chapter: Yeast Research: A Historical Overview*; American Society for Microbiology Press: Washington, DC, USA, 2011; pp. 227–253. ISBN 9781555815165.
29. Wieser, A.; Schneider, L.; Jung, J.; Schubert, S. MALDI-TOF MS in microbiological diagnostics identification of microorganisms and beyond (mini review). *Appl. Microbiol. Biotechnol.* **2012**, *93*, 965–974. [CrossRef] [PubMed]
30. Ulea, E. *Microbiology, "Ion Ionescu de la Brad"*; Publishing House: Iasi, Romania, 2011; p. 204.
31. Constantinescu, O. *Microbiology Methods and Techniques*; Ceres: Bucuresti, Romania, 1974; p. 130.
32. Pricop, L.; Fortună, M.E.; Popovici, D.; Asandulesa, M.; Racles, C.; Zaltariov, M.F. Nickel Complexes of Guanidine Functionalized Trisiloxane. *J. Inorg. Organomet. Polym. Mater.* **2019**, *29*, 2024–2034. [CrossRef]
33. Kopittke, P.M.; Menzies, N.W.; Wang, P.; McKenna, B.A.; Lombi, E. Soil and the intensification of agriculture for global food security. *Environ. Int.* **2019**, *132*, 105078. [CrossRef] [PubMed]

34. Fortună, M.E.; Ungureanu, E.; Jităreanu, C.D. Calcium carbonate-carboxymethyl chitosan hybrid materials. *Materials* **2021**, *14*, 3336. [CrossRef]
35. Inculet, C.I.; Mihalache, G.; Sellitto, V.M.; Hlihor, R.M.; Stoleru, V. The effects of a microorganisms-based commercial product on the morphological, biochemical and yield of tomato plants under two different water regimes. *Microorganisms* **2019**, *7*, 706. [CrossRef]
36. Ungureanu, E.; Căpraru, A.M.; Ungureanu, O.; Jităreanu, C.D.; Iacob, V.; Ulea, E.; Popa, V.I. Ecologycal biocide systems based on unmodified and epoxydation lignins, furan resin and copper. *Cell. Chem. Technol.* **2012**, *46*, 599–603.
37. Fortună, M.E.; Vasilache, V.; Ignat, M.; Silion, M.; Vicol, T.; Patraș, X.; Miron, I. Elemental and macromolecular modifications in Triticum aestivum L. plantlets under different cultivation conditions. *PLoS ONE* **2018**, *13*, e0202441. [CrossRef]

materials

MDPI

Article

Calcium Carbonate–Carboxymethyl Chitosan Hybrid Materials

Maria E. Fortună [1], Elena Ungureanu [2,*] and Carmen D. Jitareanu [3]

[1] Institute of Macromolecular Chemistry "Petru Poni", 41A Grigore Ghica Voda Alley, 700487 Iasi, Romania; fortuna.maria@icmpp.ro
[2] Exact Sciences Department, Faculty of Horticulture, "Ion Ionescu de la Brad" University of Life Sciences Iasi, 3 Mihail Sadoveanu Alley, 700490 Iasi, Romania
[3] Plant Science Department, Faculty of Agriculture, "Ion Ionescu de la Brad" University of Life Sciences Iasi, 3 Mihail Sadoveanu Alley, 700490 Iasi, Romania; doinaj@uaiasi.ro
* Correspondence: eungureanu@uaiasi.ro

Abstract: In the present work, precipitated calcium carbonate (PCC) and carboxymethyl chitosan (CMC) were prepared to obtain new hybrid materials used in papermaking. In the first step, occurred the precipitation of $CaCO_3$ in solution containing CMC at different levels (0.5%, 1%, and 1.5%). In the second step, PCC–CMC hybrid material (25%) was added to pulp suspension, and the sheets were made. The effect of PCC–CMC on paper properties (mechanical and optical) was systematically investigated. Breaking length, the brightness and opacity of the sheets obtained with the PCC–CMC material were better than the sheets fabricated with the unmodified PCC at similar levels of content.

Keywords: calcium carbonate precipitated (PCC); chitosan (CH); carboxymethyl chitosan (CMC); hybrid materials; paper loading

Citation: Fortună, M.E.; Ungureanu, E.; Jitareanu, C.D. Calcium Carbonate–Carboxymethyl Chitosan Hybrid Materials. *Materials* **2021**, *14*, 3336. https://doi.org/10.3390/ma14123336

Received: 26 April 2021
Accepted: 14 June 2021
Published: 16 June 2021

1. Introduction

In the last years, numerous researches have been utilized to fabricate hybrid materials consisting of organic and inorganic components with special chemical and physical properties for the development of numerous promising products in different fields [1–4].

Some research in the field of papermaking has shown the compatibility of precipitated calcium carbonate (PCC) with organic compounds [5–9]. The most modifications of precipitated calcium carbonate (PCC) regarding the improvement of its filler properties are those related to the use of bio-additives (starch, alginate, cellulose, and chitosan) which reduce the negative impact of fillers on the paper properties and on the technological process [10–13]. Modification of the calcium carbonate particles with the chitosan can show good benefits of using fillers in papermaking due to reducing the cost price by the partial replacement of fibers and also improving the properties of paper [6,14]. Chitosan and its derivatives have been considered as versatile candidates for preparing specific inorganic–organic hybrid materials. However, the modification of chitosan in its derivatives is necessary to confer solubility and amphoteric character. Thus, a biocompatible and biodegradable derivative of chitosan is carboxymethyl chitosan which is soluble in water [15]. In the last decade, carboxymethyl chitosan materials have been received increasing attention due to the fact that it is a source of renewable and biodegradable material and, on the other hand, due to functionality through application in biology, technology, biotechnology, medicine and agriculture [16,17]. However, trends in the paper industry to use a higher amount of secondary fiber and fillers can give negative consequences for both the papermaking process and the paper's properties. For example, a large amount of filler material introduced into the pulp paper (20–40%) will decrease the strength of the obtained paper, but this can be compensated by the use of retention additives. Retention is the most widely used parameter for an effective characteristic of additive or additive systems. By combining different additives, we can control some unwanted phenomena such as the decrease in the environmental impact of papermaking by lowering the process

water loading as a result of high filler retention and by reducing the energy consumption for the pulp stock preparation and wastewater treatment [18].

The chitosan has already been evaluated as a filler material for the papermaking industry [19,20]. However, the influence of chitosan on structural changes in PCC and their effect on paper properties has not yet been reported in the literature. In this sense, in this work, to control the particle size of PCC and to obtain new hybrid materials with modified PCC, carboxymethyl chitosan was utilized. The preparation of PCC–CMC hybrid particles did not involve any organic solvent and could offer good control over the morphology of particles with relatively narrow size distributions. The soluble chitosan is synthesized under alkaline conditions by reaction with mono-chloroacetic acid. This additive was tested in papermaking and proved to be effective. Based on these results, in this work, PCC was obtained by the double exchange reaction in the presence of carboxymethyl chitosan (CMC).

2. Experimental

2.1. Materials

•Chitosan was purchased from Vanson, Inc. Company. The main characteristics of chitosan are acetylation degree—20.8%, molecular weight—415.000 g/mol, cationic charge—4500 μeq/g.

Carboxymethyl chitosan, soluble in water (CMC), was obtained from chitosan according to previous methods [21,22]. In total, 2 g of chitosan was dispersed in 50 mL isopropanol and stirred using a magnetic stirrer at room temperature for 2 h. Then, 80 mL of aqueous NaOH solution (60% *w/v*) and 100 mL of aqueous monochloroacetic acid solution (60% *w/v*) were added, and the mixture was heated with stirring at 65 °C for a further 8 h. The reaction mixture was then neutralized using HCl solution (4 M). After the removal of the residue by filtration, the resulting CMC was precipitated by adding methanol. The product was extensively washed with 80% ethanol and dried at room temperature. The substitution degree was 0.98.

•$CaCl_2$ (96%) and Na_2CO_3 (99.8%) were used as chemicals for precipitated calcium carbonate—PCC.

•Softwood bleached kraft pulp refined at 30 °SR (Schopper-Riegler degree).

2.2. Experimental Procedure

In the following evaluations, calcium carbonate obtained from calcium chloride and sodium carbonate will be used to which were added variable amounts of carboxymethyl chitosan relative to PCC (0.5% CMC, 1% CMC, and 1.5% CMC).

PCC was obtained by the following reaction:

$$CaCl_2 + Na_2CO_3 \rightarrow 2NaCl + CaCO_3 \quad (1)$$

In a typical synthesis, CMC at different concentrations (0.5%, 1%, and 1.5%) was dissolved in deionized water, $CaCl_2$ solution was added, and finally, the Na_2CO_3 was added slowly and was left at 25 °C for 10 h. Finally, the precipitated calcium carbonate crystals were filtered, then washed and dried at 45 °C.

Paper stock preparation was performed by adding precipitated calcium carbonate/carboxymethyl chitosan (PCC–CMC) into slurries of cellulosic fibers under stirring before the formation of paper; the dosage of calcium carbonate was established at 25% after several retention tests to obtaining paper hand sheets. After that, the pulp was washed in several steps for the complete removal of the free calcium carbonate particles (Figure 1).

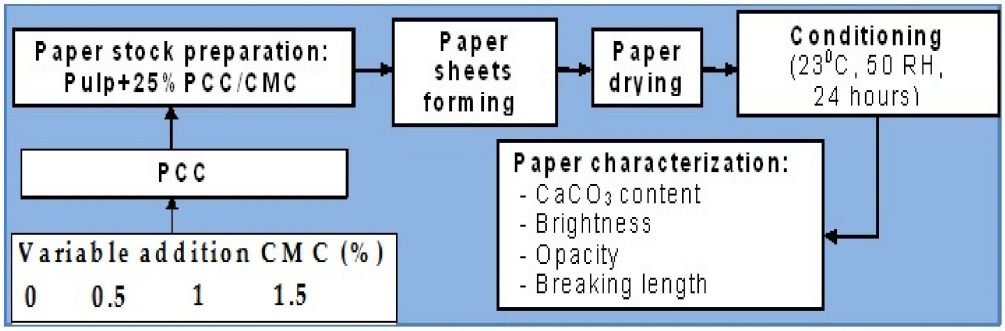

Figure 1. A schematic representation of the technological routes for the preparation of PCC–CMC and paper characterization.

2.3. Methods

The structures of unmodified chitosan (CH) and carboxymethyl chitosan (CMC) samples were studied by Fourier Transform Infra-Red (FTIR) spectroscopy, recorded using a Bruker Vertex 70 FTIR spectrometer.

The paper hand sheets were obtained on a Rapid-Köthen apparatus, at a standard basis weight of 70 g/m^2; three series of hand sheets were prepared for each type of loaded pulp. Paper sheets were conditioned under standard conditions (24 h at 23 °C and 50% RH) and analyzed regarding the calcium carbonate content, according to the Tappi Standard—T413 (Tappi Test Methods, 1999). The calcium carbonate content is calculated from the ash content in the hand sheets, taking into account the incineration loss of the precipitated calcium carbonate. Calcium carbonate retention was determined on the Dynamic Drainage Jar (DDJ)device: from the paste with a consistency of 0.5%, homogenized, 500 mL are introduced into the vessel of the DDJ apparatus with the drain valve closed, while the stirring started; the paste is stirred for about 30 s, and then PCC or PCC–CMC are added according to the experimental programs. To collect the filtrate, stirring is stopped at the same time as opening the solenoid valve, about 30 mL of the filtrate is removed, and the next 100 mL are collected in a graduated vessel. The collected greasy water is filtered on quality filter paper, recalibrated, dried, and weighed. Retention of calcium carbonate was determined by calcination of the filter paper, at approximately 600 °C.

Opacity and brightness were determined according to ISO 2471, measured by the spectrophotometer L&W Elrepho 2000.

Sstrength properties: breaking length (Km) measured by Instron apparatus, according to ISO 1924 and burst factor (KPa.m^2/g) measured by the Schopper-Dale apparatus, according to ISO 2758.

Particle size distribution of precipitated calcium carbonate was measured by a laser diffraction particle size analyzer (Sald-7001/Shimadzu Scientific Instrument).

X-ray diffraction patterns of calcium carbonate particulates were obtained on a D8 ADVANCE, Bruker-AXS apparatus, equipped with a transmission type goniometer, using nickel-filtered CuKα radiation (λ = 1.5418 Å) at 36 kV; the goniometer was scanned stepwise every 0.10° from 10 to 60° in the 2θ range.

The morphology of PCC–CMC material and of the paper surface was visualized by scanning electron microscopy ((SEM) (VEGA/Tescan)).

3. Results and Discussion

3.1. CMC Modification

Both unmodified and modified carboxymethyl chitosan samples were characterized using FTIR spectroscopy (Figure 2). The modifications observed in the FTIR spectra appear due to the changes in the chemical structure.

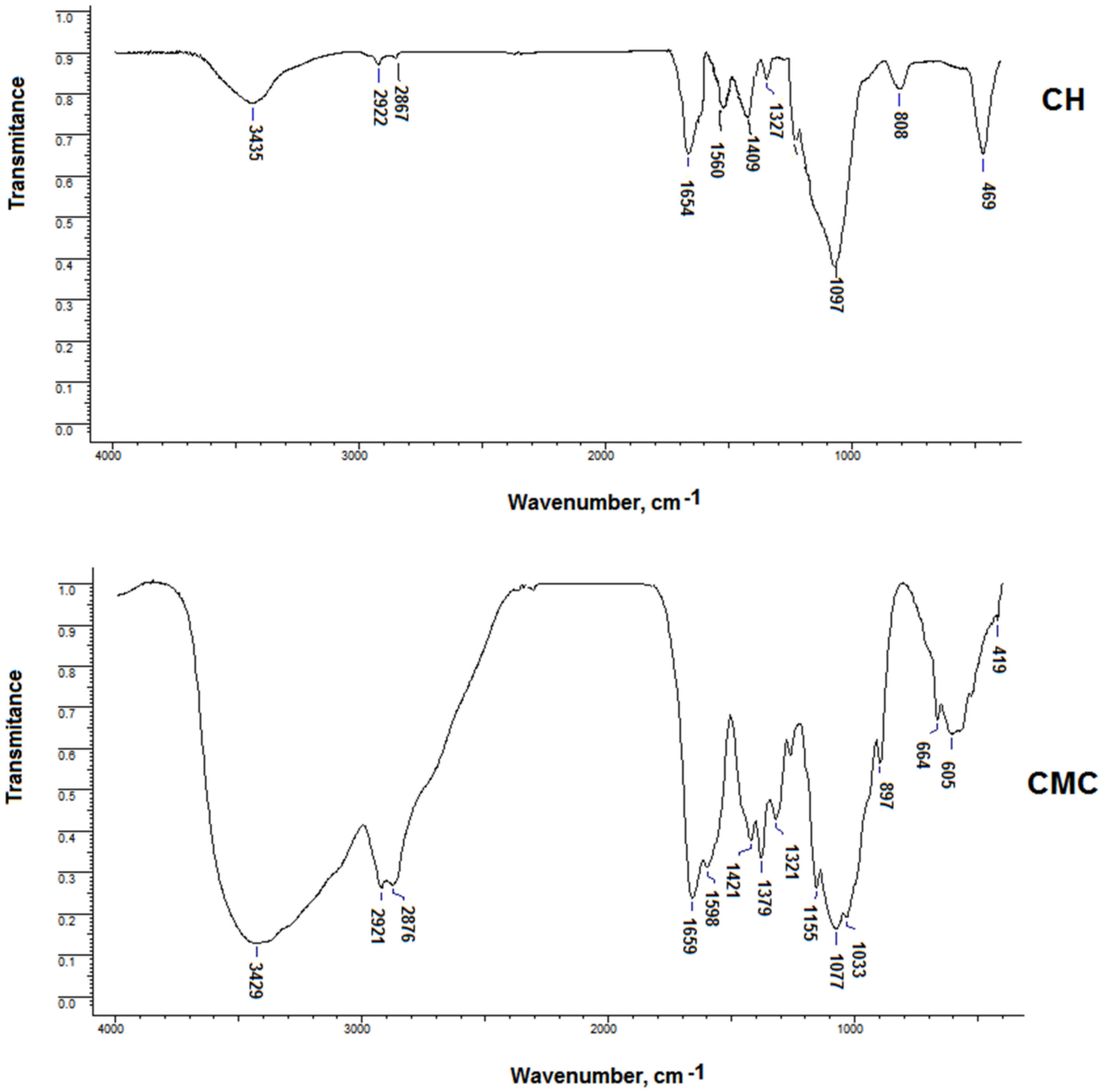

Figure 2. FTIR spectra of CH and CMC.

According to FT-IR Spectra, as shown in Figure 2, the main characteristic peaks of chitosan are at 3435 (O-H and N-H), 2867–2922 (C-H stretch), 1560 (N-H bend), 1654 cm^{-1} (C=O stretch, amide I band), 1165 (bridge O stretch) and 1097 cm^{-1}(C-O stretch).

For CMC, its spectrum is different from the spectrum of chitosan: 3429 (O-H and N-H bend); 2876 and 2921 (C-H stretch); 1598 (COO-); 1379 and 1421 (-CH_2- and -CH_3-); 1077 and 1321 (C-O). CMC presents an absorption band at 1598 cm^{-1} specific for the COO- group, indicating that the carboxymethyl group is grafted onto the molecular chain of chitosan [23].

3.2. Surface Morphology

The morphology of CH, CMC, PCC, and PCC–CMC material hybrid was observed by Scanning Electron Microscope. The shape and dimensions of PCC particles, obtained in the laboratory at various CMC additions, were analyzed and the results obtained are presented in Figure 3.

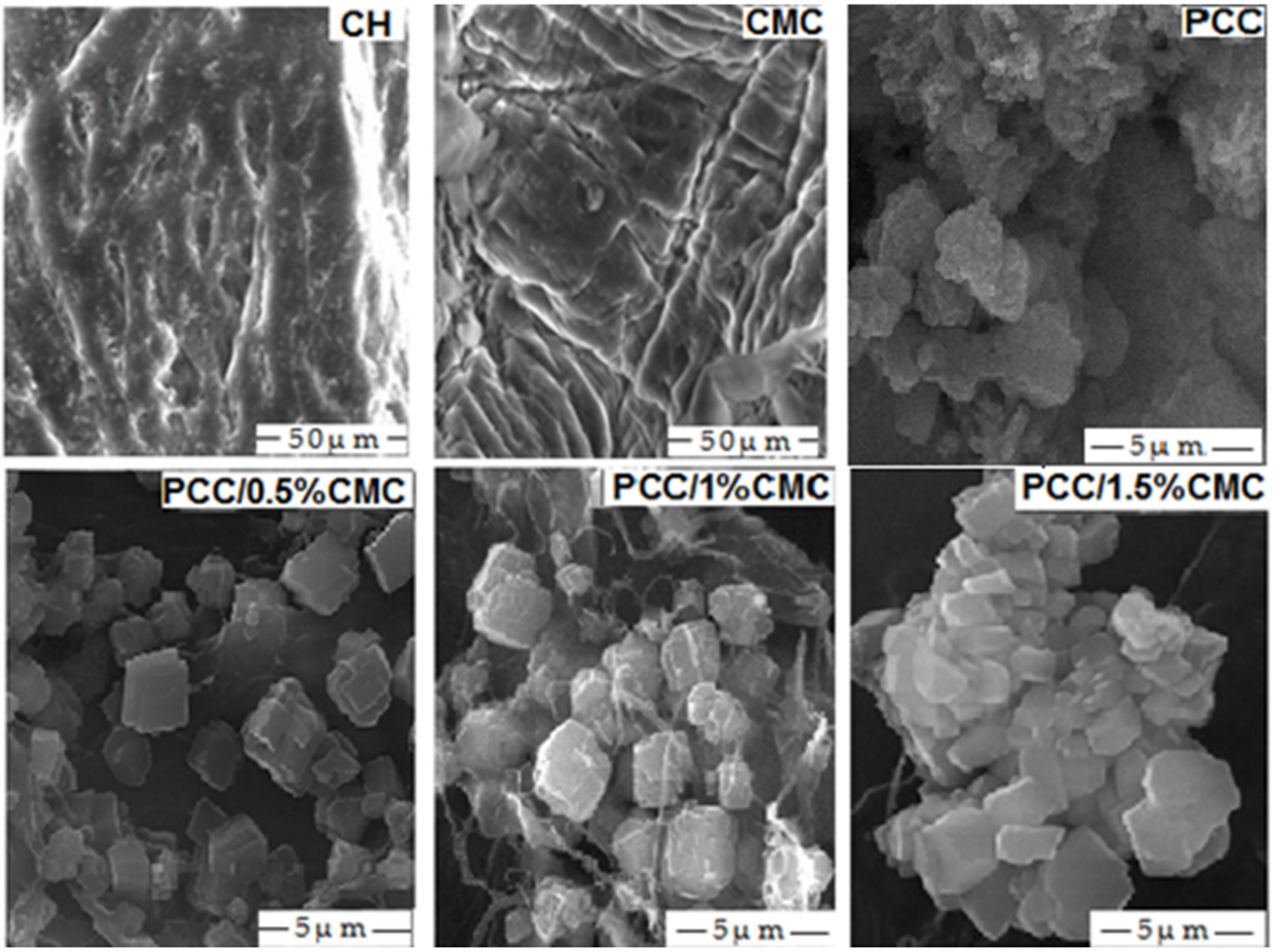

Figure 3. SEM images of CH, CMC, PCC, and PCC with addition CMC.

The three polymorphic forms of precipitated calcium carbonate are calcite (thermodynamically stable at room temperature), vaterite, and aragonite, which are easier to be transformed into calcite.

In the literature [4,24], following the reaction between $CaCl_2$ + Na_2CO_3 at different temperatures, the calcite form was obtained at 25 °C.

In our case, the examination of the SEM images (Figure 3) evidence that the forms are spindle-shaped and cubic type.

3.3. X-ray Analysis

For the synthesis of new filling materials with unique properties, it is very important to follow the particle size, polymorphism, and morphology.

X-ray diffraction remains the main method for the identification of atom arrangement in minerals. In this study, X-ray analysis was applied to determine the polymorphic form of modified and unmodified calcium carbonate particles (Figure 4).

XRD calibration graphs were constructed using the 104 reflections of calcite, the 221 reflections of aragonite, and the 110 reflections of vaterite.

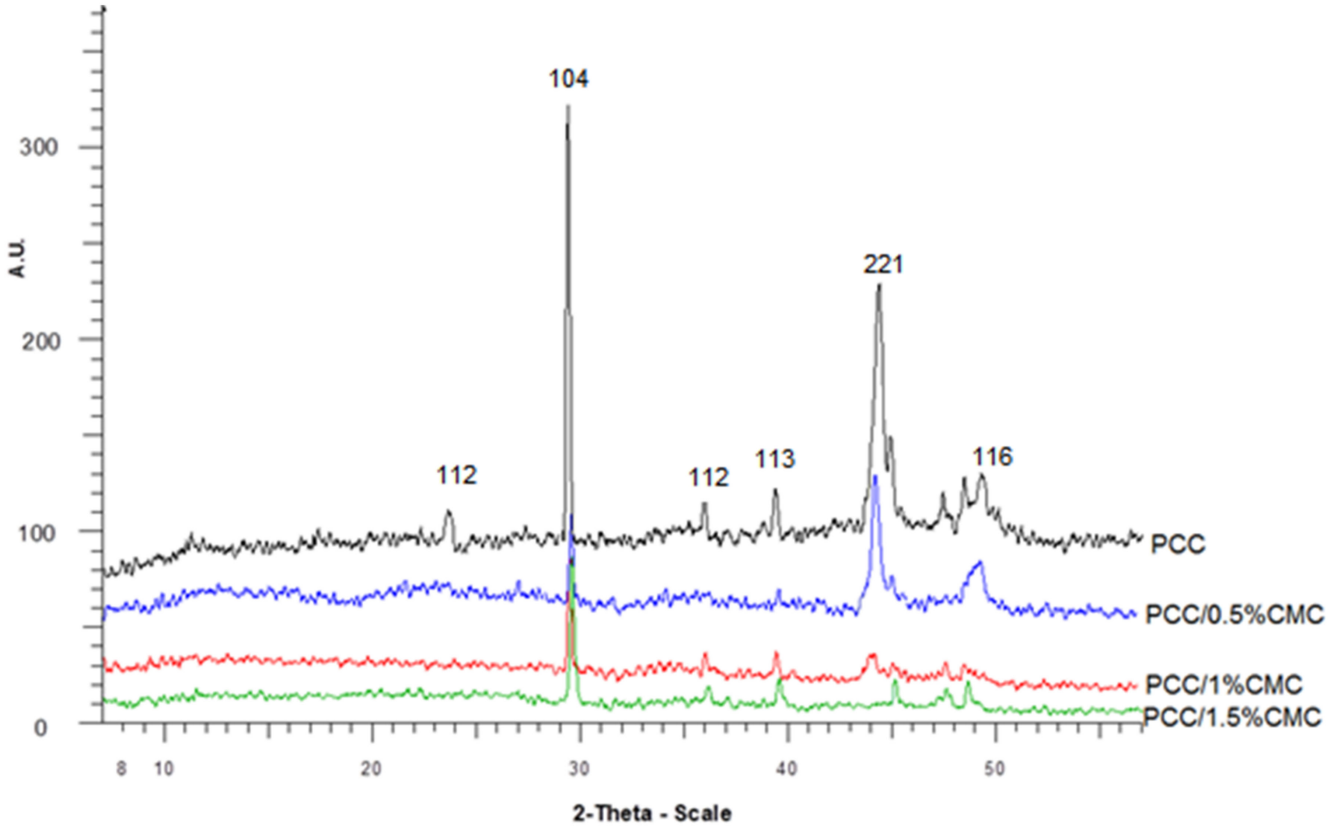

Figure 4. XRD patterns of PCC and PCC–CMC.

According to with X-ray analysis, the peaks at 2θ of 23.5° (112) and 29.4° (104) are assigned with calcite, whereas 2θ of 36.1° (112), 44.8° (221), and 49.2° (116) are associated to the aragonite phase [25,26]. After introducing CMC in PCC dispersion, the intensity of peaks at 2θ = 23.5°, corresponding to the plane (112), and 2θ = 36.1°, corresponding to the plane (112), have disappeared. Additionally, the intensity of the peak at 29.4° associated to the plane (104) of calcite and 44.8° (221) of aragonite has been reduced. At a higher concentration of CMC (PCC/1.5% CMC), the peaks at 44.8° (221) and 49.2° (116) have disappeared.

PCC modified with CMC samples appeared as a mixture of the majority of calcite with smaller amounts of aragonite.

Particle Size of Modified and Unmodified PCC

The size of unmodified PCC and CMC modified PCC were analyzed with a laser diffraction particle size analyzer (Figure 5). The PCC and PCC–CMC were submitted to ultrasound in distilled water for 10 min and analyzed.

It is found that with the increase in the carboxymethyl chitosan addition, the calcium carbonate particles obtained in the laboratory are slightly smaller than the control particles obtained without the addition of carboxymethyl chitosan, which should lead to better retention in the paper's structure.

From Figure 5, it was determined that PCC/1.5% CMC has the d_{50} of 0.058 μm, and particle distribution is into narrow diameters.

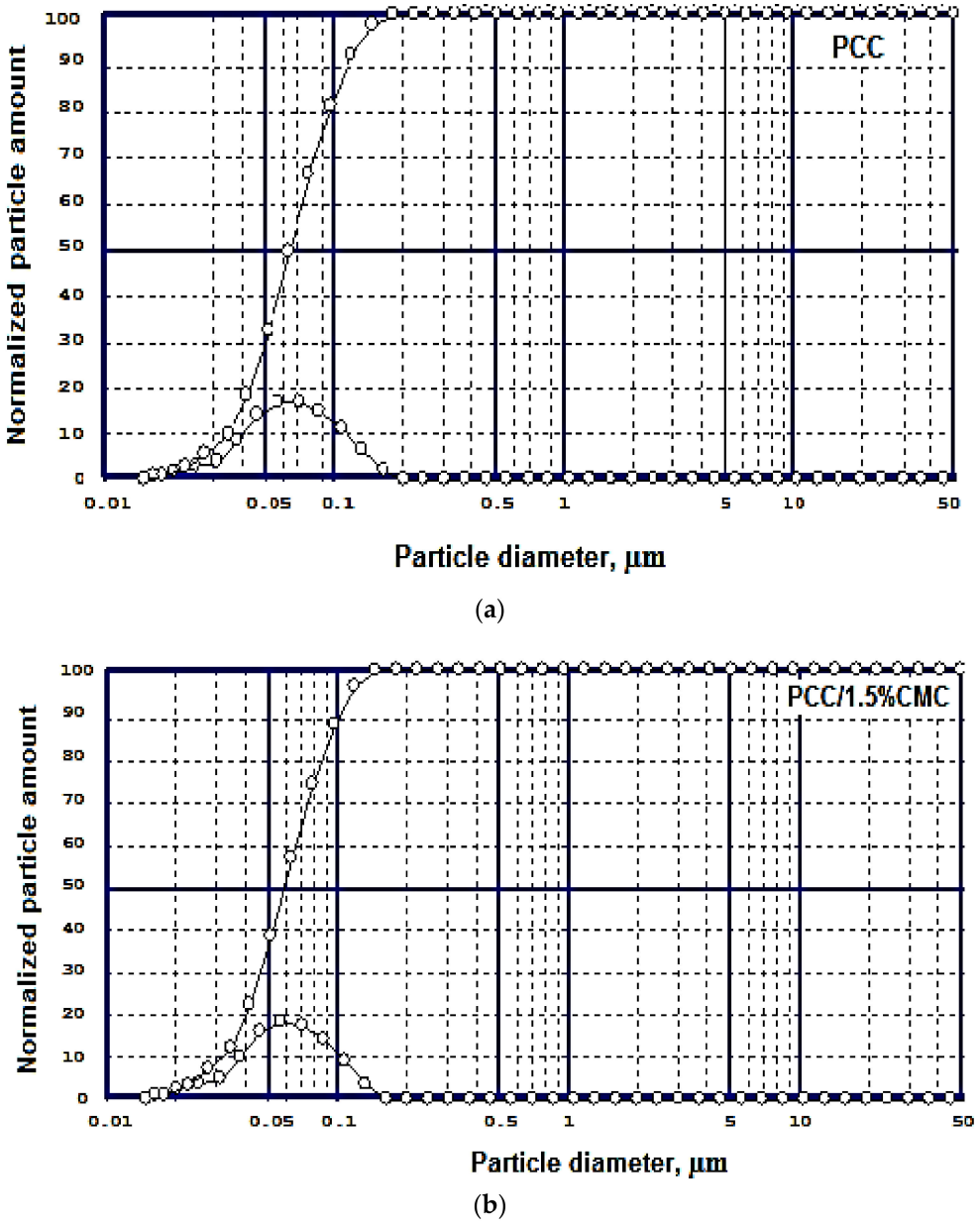

Figure 5. Particle size distribution of PCC (**a**) and PCC/1.5% CMC (**b**) (particle diameters and cumulative curve).

3.4. Properties of Filled Paper Sheets

3.4.1. Retention

Current trends in the paper industry are to use a higher amount of secondary fiber, fillers and coating pigments have negative consequences for the paper properties. Thus, a large amount of filler material introduced into the pulp paper will decrease the strength of the obtained paper, but this can be compensated by the use of retention additives. Retention is the most widely used parameter for an effective characteristic of additive or additive systems.

Carboxymethyl chitosan can be used to improve the dry strength of the paper and to replace the cationic starch in the pulp composition in the manufacture of printing paper.

Figure 6 shows the evolution of the retention yield and the $CaCO_3$ amount in the sheets as a function of the addition of carboxymethyl chitosan in the pulp. The content of precipitated calcium carbonate without CMC is 12.2%, compared to 13.3% for PCC/1.5% CMC. Retention yield increases with increasing $CaCO_3$ amount, which progressively

increases with the CMC addition (from 48.9% for PCC without CMC to 53.2% for PCC/1.5% CMC). The use of CMC as an individual component leads to an aggregation mechanism that results in the formation of a compact structure, and consequently, retention and formation are advantageous.

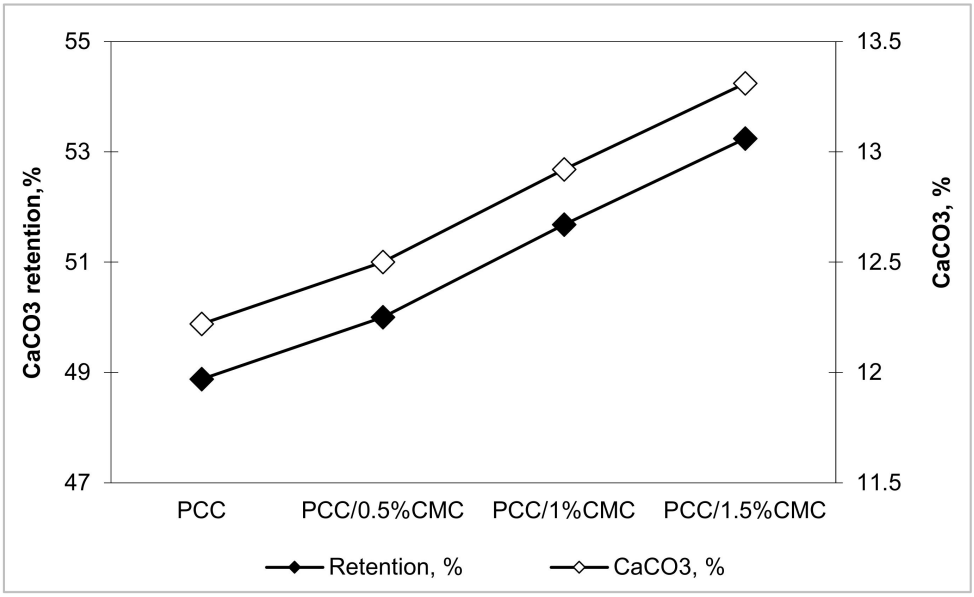

Figure 6. The influence of CMC addition on retention efficiency and calcium carbonate content in the paper.

3.4.2. SEM Images of Paper Samples

SEM images of paper samples with PCC and PCC–CMC are shown in Figure 7. As expected, the surface morphology of the samples with PCC–CMC was different from that with PCC, which confirms the importance of filler modification in structural change. Between fibers of pulp, some particles can be seen, and these are fulfilling the interfibers space, which leads to the improvement of physico-chemical properties.

SEM analyses showed differences among the precipitated calcium carbonate, modified and unmodified with regard to particle size and distribution within the fibers, as reflected by the levels of the opacity and tensile strength of paper sheets.

3.4.3. Optical Properties

Opacity is one of the properties of papers that depend on the content of the filler material and its distribution in the paper structure. The results in Figure 8 show the effects of CMC on the optical properties of the sheets. The brightness and opacity increase with the increase in the addition of CMC in the pulp. This can be attributed to the increase in the content of PCC between fibers and also due to the change in the sizes and distribution of particles.

3.4.4. Mechanical Strength Properties

The breaking length is significantly influenced by additives addition. The influence of filler in different levels of CMC on the mechanical properties of sheets is shown in Figures 9 and 10.

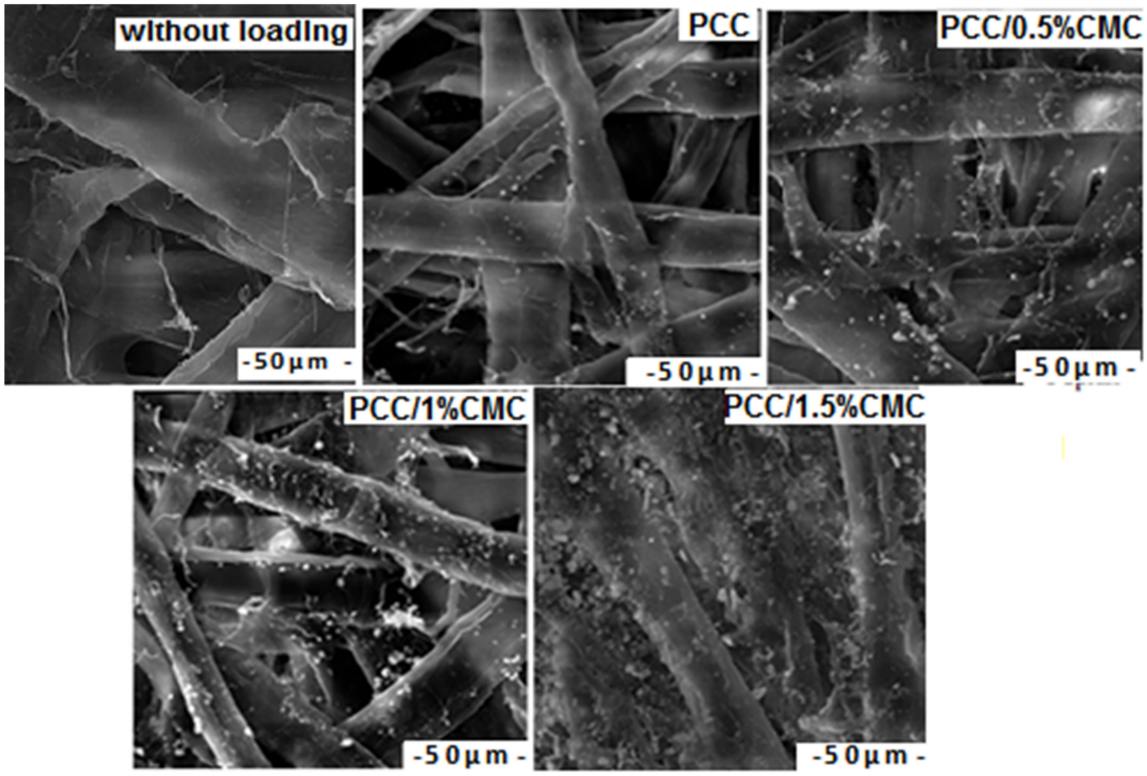

Figure 7. SEM micrographs for paper samples.

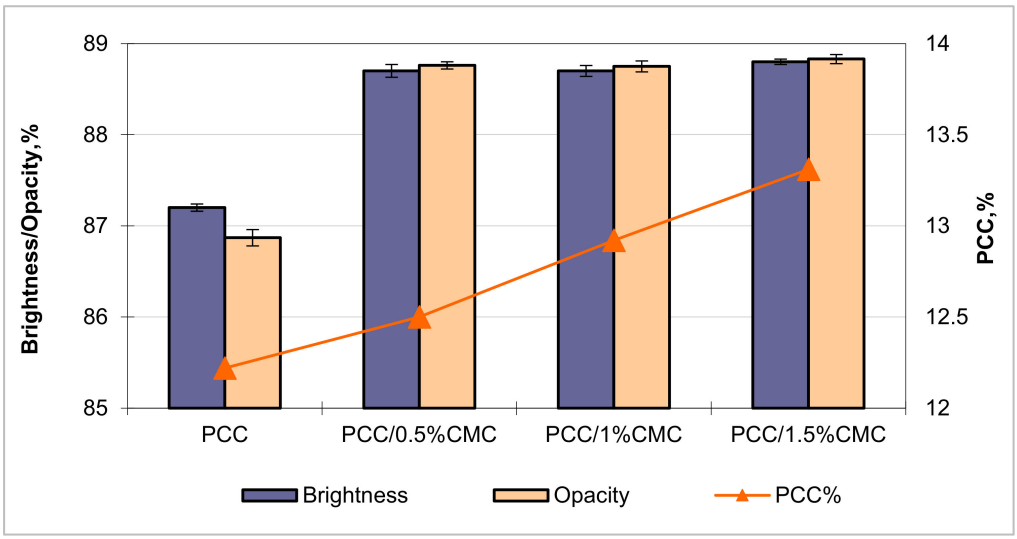

Figure 8. Brightness and opacity of paper samples.

For a correct evaluation of the efficiency of carboxymethyl chitosan on the strength of the paper, the values for the breaking length of the paper were calculated according to the calcium carbonate content. Figures 9 and 10 highlight the positive effect of carboxymethyl chitosan on the strength properties. The increase in the breaking length for samples with the addition of PCC–CMC compared to those with PCC without CMC can be attributed to the formation of composite structures such as calcium carbonate–carboxymethyl chitosan.

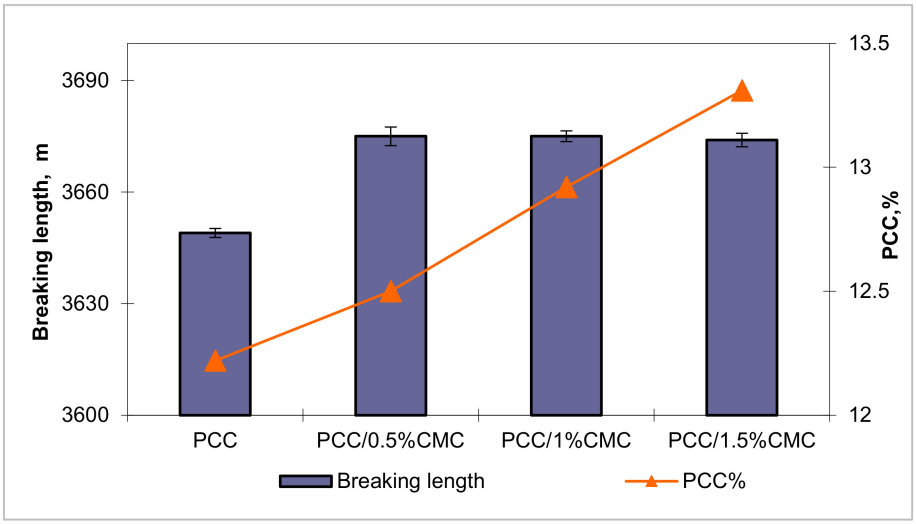

Figure 9. The effect of PCC modified with CMC of different levels on breaking length.

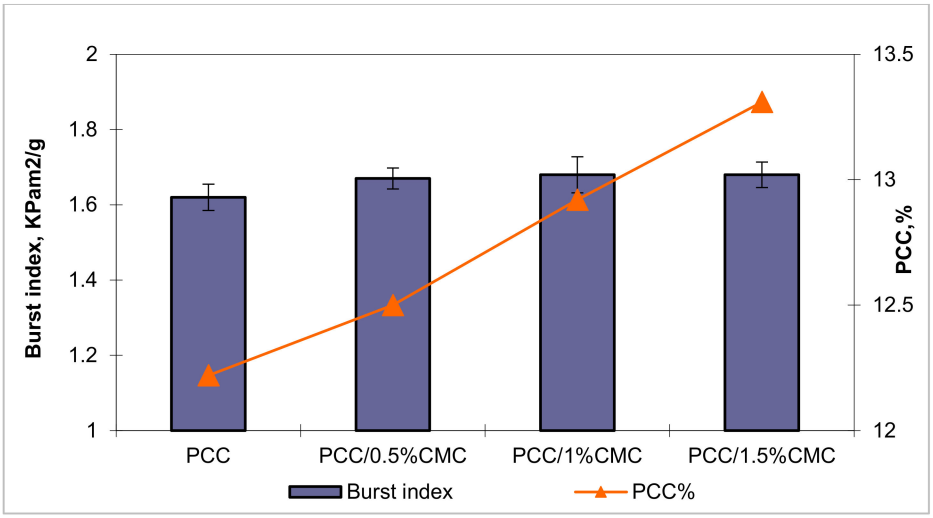

Figure 10. The effect of PCC modified with CMC of different addition levels on burst index.

This increase in paper strength for samples with the addition of PCC–CMC, compared to those with PCC obtained by the same method, in the absence of CMC, can also be explained by the fact that most fiber–pigment interfaces are made by the carboxymethyl chitosan film, which has the ability to develop hydrogen bonds.

Although the PCC content increases with the addition of CMC, the burst index is not affected, which implies that most of the calcium carbonate is precipitated in the pores of the fibers and fine material, the particles being much smaller. Under these conditions, the calcium carbonate particles being small do not contribute to the increase in interfibrillar spaces.

4. Conclusions

The particle size distribution of PCC modified with carboxymethyl chitosan was changed, but not too much, comparatively with PCC without CMC.

SEM images show that the calcium carbonate particles in the paper appear smaller by increasing the addition of CMC.

Retention of filler in dispersed form is also supported by a substantial increase in brightness and opacity.

The optical properties of sheets filled with PCC–CMC were improved in comparison to the PCC without CMC. On the other hand, sheets filled with PCC–CMC hybrid material reduced the loss of mechanical properties at the same PCC amount.

Author Contributions: Conceptualization, M.E.F.; methodology, C.D.J.; investigation, M.E.F. and E.U.; resources, E.U.; writing—original draft preparation, M.E.F. and C.D.J.; writing—review and editing, M.E.F. and E.U.; visualization, C.D.J.; supervision, M.E.F. and C.D.J.; funding acquisition, E.U. All authors have read and agreed to the published version of the manuscript.

Funding: This research received no external funding.

Institutional Review Board Statement: Not applicable.

Informed Consent Statement: Not applicable.

Data Availability Statement: Not applicable.

Conflicts of Interest: The authors declare no conflict of interest.

References

1. Song, J.; Wang, R.; Liu, Z.; Zhang, H. Preparation and characterization of calcium carbonate microspheres and their potential application as drug carriers. *Mol. Med. Rep.* **2018**, *17*, 8403–8408. [CrossRef]
2. Wang, J.; Chen, J.S.; Zong, J.Y.; Zhao, D.; Li, F.; Zhuo, R.X.; Cheng, S.X. Calcium Carbonate/Carboxymethyl Chitosan Hybrid Microspheres and Nanospheres for Drug Delivery. *J. Phys. Chem. C* **2010**, *114*, 18940–18945. [CrossRef]
3. Samyn, P.; Barhoum, A.; Öhlund, T.; Dufresne, A. Review: Nanoparticles and nanostructured materials in papermaking. *J. Mater. Sci.* **2018**, *53*, 146–184. [CrossRef]
4. Hubbe, M.A.; Gill, R.A. Fillers for Papermaking: A Review of their properties, usage practices, and their mechanistic role. *BioResources* **2016**, *11*, 2886–2963. [CrossRef]
5. Gamelas, J.A.F.; Lourenco, A.F.; Xavier, M.; Ferreira, P.J. Modification of precipitated calcium carbonate with cellulose esters and use as filler in papermaking. *Chem. Eng. Res. Des.* **2014**, *92*, 2425–2430. [CrossRef]
6. Liang, P.; Zhao, Y.; Shen, Q.; Wang, D.; Xu, D. The effect of carboxymethyl chitosan on the precipitation of calcium carbonate. *J. Cryst. Growth* **2004**, *261*, 571–576. [CrossRef]
7. Fortuna, M.E.; Lobiuc, A.; Cosovanu, M.L.; Harja, M. Effects of in-situ filler loading vs. conventional filler and the use of retention-related additives on properties of paper. *Materials* **2020**, *13*, 5066. [CrossRef] [PubMed]
8. Kalliola, S.; Repo, E.; Srivastava, V.; Heiskanen, J.P.; Sirviö, J.A.; Liimatainen, H.; Sillanpää, M. The pH sensitive properties of carboxymethyl chitosan nanoparticles cross-linked with calcium ions. *Colloid Surface B.* **2017**, *153*, 229–236. [CrossRef] [PubMed]
9. Mousavipazhouh, H.; Azadfallah, M.; Jouybari, I.R. Encapsulation of precipitated calcium carbonate fillers using carboxymethyl cellulose /polyaluminium chloride: Preparation and its influence on mechanical and optical properties of paper. *Maderas-Cienc. Tecnol.* **2018**, *20*, 703–714. [CrossRef]
10. Lourenço, A.F.; Gamelas, J.A.F.; Ferreira, P.J. Precipitated calcium carbonate modified by the layer-by-layer deposition method—Its potential as papermaking filler. *Chem. Eng. Res. Des.* **2015**, *104*, 807–813. [CrossRef]
11. Mourya, V.K.; Inamdar, N.N.; Tiwari, A. Carboxymethyl chitosan and its applications. *Adv. Mat. Lett.* **2010**, *1*, 11–33. [CrossRef]
12. Zhao, Y.; Hu, Z.; Ragauskas, A.; Deng, Y. Improvement of paper properties using starch-modified precipitated calcium carbonate filler. *Tappi J.* **2005**, *4*, 3–7.
13. Salama, A. Recent progress in preparation and applications of chitosan/calcium phosphate composite materials. *Int. J. Biol. Macromol.* **2021**, *178*, 240–252. [CrossRef] [PubMed]
14. Chen, Z.; Li, C.; Song, Z.; Qian, X. Modification of precipitated calcium carbonate filler for papermaking with adsorption of cationically derivatized chitosan and carboxymethyl chitosan. *BioResources* **2014**, *9*, 5917–5927. [CrossRef]
15. François, R.; Bertrand, S.; Pierre-Marie, B.; Crini, G. Chitosan for coagulation/flocculation processes—An eco-friendly approach. *Eur. Polym. J.* **2008**, *45*, 1337–1348.
16. Iftime, M.M.; Ailiesei, G.L.; Ungureanu, E.; Marin, L. Designing chitosan based eco-friendly multifunctional soil conditioner systems with urea controlled release and water retention. *Carbohydr. Polym.* **2019**, *223*, 115140. [CrossRef]
17. Guo, J.; Liu, J.; Qie, H.; Zhao, F.; Niu, C.H. Efficient synthesis strategy of folate-modified carboxymethyl chitosan/$CaCO_3$ hybrid nanospheres and their drug-carrying and sustained release properties. *J. Biomater. Sci. Polym. Ed.* **2021**, *32*, 799–812. [CrossRef]
18. Ali, Z.M.; Laghari, A.J.; Ansari, A.K.; Khuhawar, M.Y. Synthesis and characterization of carboxymethyl chitosan and its effect on turbidity removal of river water. *J. Appl. Chem.* **2013**, *5*, 72–79.
19. Chen, X.; Park, H. Chemical characteristics of O-carboxymethyl chitosansrelated to the preparation conditions. *Carbohydr. Polym.* **2003**, *53*, 355–359. [CrossRef]
20. El-Sherbiny, S.; El-Sheikh, S.M.; Barhoum, A. Preparation and modification of nano calcium carbonate filler from waste marble dust and commercial limestone for papermaking wet end application. *Powder Technol.* **2015**, *279*, 290–300. [CrossRef]

21. Liu, X.F.; Guan, Y.L.; Yang, D.Z.; Li, Z.; Yao, K.D.J. Antibacterial action of chitosan and carboxymethylated chitosan. *Appl. Polym. Sci.* **2001**, *79*, 1324–1335.
22. Aiping, Z.; Jianhong, L.; Wenhui, Y. Effective loading and controlled release of camptothecin by O-carboxymethylchitosan aggregates. *Carbohydr. Polym.* **2006**, *63*, 89–96. [CrossRef]
23. Nada, A.M.A.; El-Sakhawy, M.; Kamel, S.; Eid, M.A.M.; Adel, A.M. Mechanical and electrical properties of paper sheets treated with chitosan and its derivatives. *Carbohydr. Polym.* **2006**, *63*, 113–121. [CrossRef]
24. Cheng, H.; Zhang, X.; Song, H. Morphological investigation of calcium carbonate during ammonification-carbonization process of low concentration calcium solution. *J. Nanomater.* **2014**, *2014*, 503696. [CrossRef]
25. Widyastuti, S.; Kusuma, I.A. Synthesis and characterization of $CaCO_3$ (calcite) nano particles from cockle shells (Anadara granosa Linn) by precipitation method, Green Process, Material, and Energy: A Sustainable Solution for Climate Change. In Proceedings of the 3rd International Conference on Engineering, Technology, and Industrial Application, Surakarta, Indonesia, 7–8 December 2016.
26. Kontoyannis, C.G.; Vagenas, N.V. Calcium carbonate phase analysis using XRD and FT-Raman spectroscopy. *Analyst* **2000**, *125*, 251–255. [CrossRef]

Carbohydrate Polymers 223 (2019) 115040

Contents lists available at ScienceDirect

Carbohydrate Polymers

journal homepage: www.elsevier.com/locate/carbpol

Designing chitosan based eco-friendly multifunctional soil conditioner systems with urea controlled release and water retention

Manuela Maria Iftime[a,*], Gabriela Liliana Ailiesei[a], Elena Ungureanu[b], Luminita Marin[a,*]

[a] Petru Poni Institute of Macromolecular Chemistry, Grigore Ghica Voda Alley, Iasi, Romania
[b] "Ion Ionescu de la Brad", University of Agricultural Sciences and Veterinary Medicine, M. Sadoveanu Alley, Iasi, Romania

ARTICLE INFO

Keywords:
Hydrogels
Chitosan
Salicy laldehyde
Urea
Schiff base
Controlled release
Eco-design

ABSTRACT

The paper reports new soil conditioner systems obtained by *in situ* hydrogelation of chitosan with salicylaldehyde in the presence of urea fertilizer, designed to address both fertilization and water retention of the soil. The new systems were structural, supramolecular and morphological characterized by FTIR spectroscopy, XRD diffraction, POM and SEM microscopy. The rate of urea release has been investigated by NMR analysis and the release mechanism has been assessed by fitting five mathematical models. The formulations showed high water absorbency of 68 g/g, and they induced water holding capacity in soil up to 154% and an increment of the nitrogen content in soil to almost double, leading to a growth of plants with almost 70% higher compared to the reference soil. All these data revealed the new systems as new multifunctional soil conditioner ecoproducts capable to address both fertilizing and water retention issues, with high potential of application for sustainable agriculture.

1. Introduction

Soil fertilization is the most popular strategy to improve the agricultural productivity, imposed by the demographic changes (Hargreaves, Adl, & Warman, 2008). Urea is one of the most used fertilizers due to its high nitrogen content and low cost (Azeem, KuShaari, Man, Basit, & Thanh, 2014). However, due to its high volatility and high solubility in water, only a small percentage can be effectively absorbed by crops, most of it being lost by volatilization, immobilization, denitrification and leaching processes, leading to ecological and economic issues (Liu et al., 2013). A pathway for a more efficient exploitation of urea was identified in the development of systems for controlled release. An overview of the literature data evidenced different controlled release systems developed in the recent years: deposition on organic/inorganic functional materials, coating with polymers, encapsulation in matrices, copolymerization *via* immolable bonds (Naz & Sulaiman, 2016; Yang, An, Wang, Kan, & Jin, 2017; Zhao et al., 2010). A large variety of synthetic polymers were used to build these systems, and gave good results in terms of urea prolonged release, but also showed high cost and lack of biodegradability, limiting their application. To overcome these drawbacks, biopolymer based formulations were designed and investigated as an eco-friendly alternative to those based on synthetic polymers. Polysaccharides are at the forefront of these researches due to their natural origin which confer them biocompatibility, biodegradability and harmless for leaving beings (Campos, Oliveira, Fraceto, & Singh, 2015; Corradini, Moura, & Mattoso, 2010; Guilherme et al., 2015; Majeed, Ramli, Mansor, & Man, 2015; Ni, Liu, & Lü, 2009; Wu & Liu, 2008). Moreover, they are originating from renewable resources, their use contributing to the preservation of the non-renewable resources and pollution prevention. Among them, chitosan is a prototypical polysaccharide which demonstrated antiviral and antifungal activity in plants and it induces abiotic and biotic stress tolerance in various horticulture crops (Iriti & Varoni, 2015; Malerba & Cerana, 2016). In addition, it is a nitrogen source for agricultural valorization, stimulating the plant growth (Pichyangkura & Chadchawanb, 2015).

Besides nutrients, the basic requirement for plant growth is the water retention in soil, especially for arid areas. Multifunctional formulations which are capable to release nutrients in a controlled manner and also to control the moisture of the soil are desirable for an improved agricultural production. Hydrogels are proper materials for this purpose, as they can encapsulate nutrients and adsorb a large amount of water, reducing water run-off and compaction rate and improving the soil permeability and infiltration rate (Abobatta, 2018; Kato et al., 2017). Used in many systems for delivery of bioactive compounds, the chitosan based hydrogels were less used as soil conditioners (Narayanan & Dhamodharan, 2015; Perez & Francois, 2016).

In the last years, our group developed a new strategy of chitosan

* Corresponding authors.
E-mail addresses: ciobanum@icmpp.ro (M.M. Iftime), lmarin@icmpp.ro (L. Marin).

https://doi.org/10.1016/j.carbpol.2019.115040
Received 10 April 2019; Received in revised form 2 June 2019; Accepted 28 June 2019
Available online 06 July 2019
0144-8617/

hydrogelation with monoaldehydes, which allows the preparation of hydrogels with particular morphology and properties controlled by the nature of the aldehyde (Ailincai et al., 2016; Bejan, Ailincai, Simionescu, & Marin, 2018; Craciun, Mititelu-Tartau, Pinteala, & Marin, 2019; Iftime & Marin, 2018; Iftime, Morariu, & Marin, 2017; Marin, Ailincai, Morariu, & Tartau-Mititelu, 2017; Olaru et al., 2018). The use of the salicylaldehdye led to hydrogels with excellent mechanical properties, self-healing ability and outstanding swelling degree (Iftime et al., 2017). Recalling the good properties of chitosan and considering the valuable effects brought by hydrogels, we envisaged the possible profit of a design based on these hydrogels loaded with urea as multifunctional materials capable to fertilize and retain water in soil.

In line with these premises we designed and prepared soil conditioner systems by *in situ* hydrogelation of chitosan with salicylaldehyde in the presence of urea. The *in situ* hydrogelation was chosen as method of urea encapsulation, targeting its fine dispersion into hydrogels, with potential to slow down the release. The peculiarities of formation of the new formulations were investigated by FTIR spectroscopy, X-ray diffraction, SEM and POM microscopy. The urea release was investigated *in vitro* and the capability to retain water was measured by monitoring the water absorbency and largest water holding parameters. Preliminary evaluation of the fertilizing ability on tomato seedlings indicated the new formulations as promising soil conditioner eco-products.

2. Materials and methods

2.1. Materials

Low molecular weight chitosan (314 kDa, DA = 87%), salicylaldehyde (98%), urea (98%), ethanol (99.8%), and glacial acetic acid (99.8%) from Aldrich were used as received.

2.2. Preparation of the soil conditioner formulations

A series of formulations with different crosslinking degrees (NH_2/CHO ratio of glucosamine units of chitosan and salicylaldehyde from 1/1 up to 3/1) and different content of fertilizer (from 0 to 66%) were prepared by encapsulation of urea into salicyl-imine-chitosan hydrogels by *in situ* hydrogelation (Scheme 1), as follows. (1) 0.1 g chitosan (5.05×10^{-4} mmol glucosamine units) was dissolved into a mixture of

Table 1
Composition of the formulations and their codes.

Code	CS1-U0	CS1-U0.5	CS1-U1	CS1-U2
NH_2/CHO ratio (CSx)	1:1 (CS1)			
Urea content % (Ux)	0 (U0)	33 (U0.5)	50 (U1)	66 (U2)
Chitosan/mg	100			
Glucosamine/mmol	5.05×10^{-4}			
SA/mg/mmol	$62/5.05 \times 10^{-4}$			
Urea/mg	0	82.1	162	324
Bidistilled water/ mL	5			
Acetic acid/μL	35			
Ethanol/mL	6.2			
Xerogel weight/mg	161	238	322	484
Code	CS1.5-U0	CS1.5-U0.5	CS1.5-U1	CS1.5-U2
NH_2/CHO ratio (CSx)	1.5:1 (CS1.5)			
Urea content % (Ux)	0 (U0)	33 (U0.5)	50 (U1)	66 (U2)
Chitosan/mg	100			
Glucosamine/mmol	5.05×10^{-4}			
SA/mg/mmol	$41/3.36 \times 10^{-4}$			
Urea/mg	0	70.5	141	282
Ethanol/mL	4.1			
Bidistilled water/ mL	5			
Acetic acid/μL	35			
Xerogel weight/mg	140	210	280	421
Code	CS2-U0	CS2-U0.5	CS2-U1	CS2-U2
NH_2/CHO ratio (CSx)	2:1 (CS2)			
Urea content % (Ux)	0 (U0)	33 (U0.5)	50 (U1)	66 (U2)
Chitosan/mg	100			
Glucosamine/mmol	5.05×10^{-4}			
SA/mg/mmol	$31/2.52 \times 10^{-4}$			
Urea/mg	0	65	131	262
Ethanol/mL	3.1			
Bidistilled water/mL	5			
Acetic acid/μL	35			
Xerogel weight/mg	130	195	261	392
Code	CS3-U0	CS3-U0.5	CS3-U1	CS3-U2
NH_2/CHO ratio (CSx)	3:1 (CS3)			
Urea content % (Ux)	0 (U0)	33 (U0.5)	50 (U1)	66 (U2)
Chitosan/mg	100			
Glucosamine/mmol	5.05×10^{-4}			
SA/mg/mmol	$021/1.68 \times 10^{-4}$			
Urea/mg	0	60.5	121	242
Ethanol/mL	2.1			
Bidistilled water/mL	5			
Acetic acid/μL	35			
Xerogel weight/mg	120	180	241	359

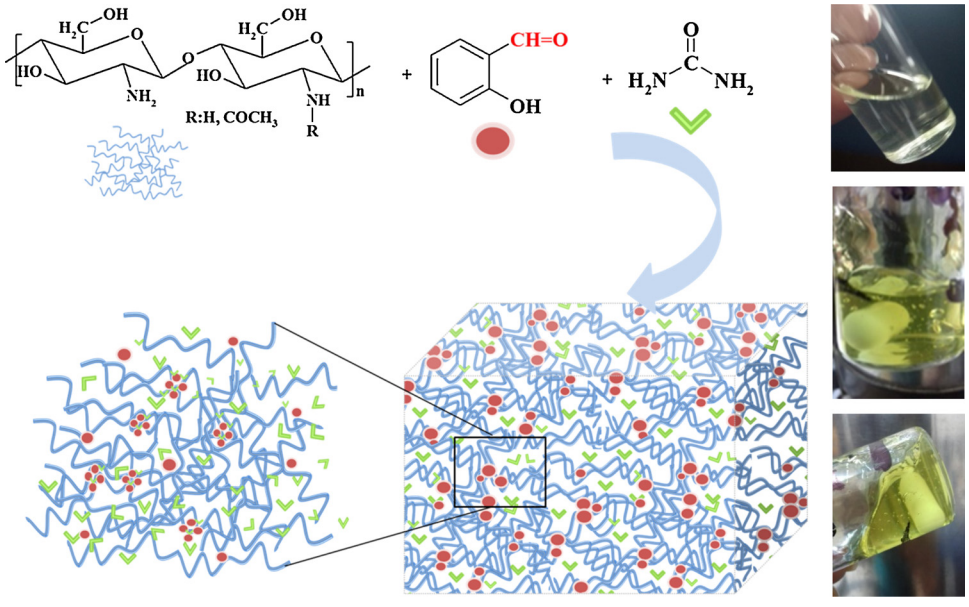

Scheme 1. Synthesis of the urea soil conditioners formulations.

4.9 mL water and 35 μL acetic acid to give a 2.02% solution, which was then heated at 50 °C. (2) Different amounts of salicylaldehyde and urea (Table 1) were dissolved into a mixture of 100 μL water with ethanol to give a 1% solution, which was (3) slowly dropped into the chitosan one, under vigorous stirring at 50 °C. The codes of the formulations with different molar ratios of the NH_2/CHO functional groups and different urea content were given in Table 1. The visual formation of hydrogels was observed after 2–3 minutes for the **CS1-Ux** and **CS1.5-Ux** formulations; 8–10 minutes for **CS2-Ux**; and 2 days for **CS3-Ux**. Reference salicyl-imine-chitosan hydrogels without urea were prepared too, when hydrogelation was observed after 3–4 minutes for **CS1-U0** and **CS1.5-U0**; 2 h for **CS2-U0**, while the **CS3-U0** transformed into a viscous liquid which still flew after two weeks. The formulations appeared as transparent yellowish semisolid materials with smooth texture, similar to the reference hydrogels (Scheme 1). Next, they were kept uncovered over 7–9 days up to the initial volume of chitosan solution was reached and after that, they were subjected to lyophilisation in order to obtain the corresponding xerogels.

The xerogels weight was almost similar with that of the initial reagents, indicating no mass loss during lyophilisation (Table 1). The sample prepared with the largest amount of salicylaldehyde (**CS1-Ux**) was brittle and had a heterogeneous appearance, while those with a lower amount (**CS1.5-Ux**, **CS2-Ux** and **CS3-Ux**) were homogeneous with a porous aspect.

2.3. Methods and equipment

The formulations and reference hydrogels were lyophilized using a Labconco FreeZone Freeze Dry System equipment, for 24 h at −54 °C and 1.512 mbar, after the prior freezing in liquid nitrogen.

Fourier-transform infrared (FTIR) spectra were recorded with a FT-IR Bruker Vertex 70 Spectrophotometer, by ATR technique, and processed using OPUS 6.5 software (see Supporting Information, Fig. S1).

Wide angle X-ray diffraction (WXRD) was performed on a Bruker D8 Avance diffractometer with Ni-filtered Cu-Ka radiation (λ = 0.1541 nm), in the range of 2 − 40° (2 theta). The dimension of the imine clusters (D) was calculated applying the Debye–Scherrer formula for the reflection peak around 6°: $D = K\lambda/\beta\cos\theta$, where D is the average diameter in nm, k is the shape factor (k¼ = 0.9); λ is the X-ray wavelength; β is the full width at half maximum of the diffraction in radians, and θ is Bragg's diffraction angle (Samoila et al., 2015). Debye–Scherrer equation was also applied to the reflections around 22 and 29°, respectively, in order to calculate the dimension of the urea crystals.

The morphology of the formulations was investigated with a field emission ***Scanning Electron Microscope*** (SEM) EDAX – Quanta 200 at accelerated electron energy of 20 KeV.

In vitro release behavior of urea from the formulations was investigated on xerogel samples containing 50 mg of urea, at room temperature, in distilled water, as follows: the samples were immersed into vials containing 10 mL of distilled water. At certain times, 1 mL of supernatant was withdrawn from the vials and replaced with 1 mL of distilled water. This procedure was applied during 35 days. The quantity of released urea was determined by ^{1}H-NMR spectroscopy, by fitting on a calibration curve previously generated for urea, as detailed into supporting information Fig. S2). The cumulative urea release was calculated with eq.: urea% = $[(10Cn + 2\Sigma Cn\text{-}1)/m_o]x100$, where Cn and Cn-1 represent the concentrations of the urea in supernatant after n and n-1 withdrawing steps, respectively, and m_o = 50 mg, corresponding to the urea in the initial samples.

In order to evaluate ***the mechanism of the urea release***, the data were fitted on the equations of the Korsmeyer-Peppas, Zero order, First order, Higuchi and Hixson-Crowell mathematical models (Craciun et al., 2019; Lin & Metters, 2006).

The ***water absorbency*** (**WA**) of the formulations was determined by gravimetric method, as follows. Samples containing the same amount of

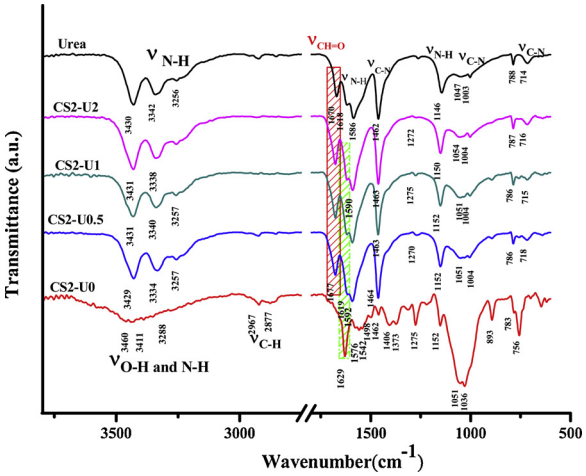

Fig. 1. FTIR spectra of a series of formulations (**CS2-Ux**), the reference xerogel (**CS2-U0**), and urea.

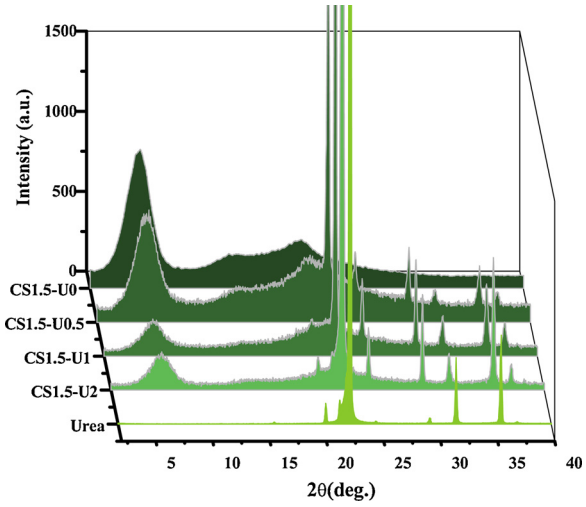

Fig. 2. X-ray diffractograms of the formulations **CS1.5-Ux** and urea.

hydrogel matrix (30×10^{-3}g **CS2-U0.5**; 40×10^{-3}g **CS2-U1** and 60×10^{-3}g **CS2-U2**) were immersed into 10 mL distilled water and allowed to soak at room temperature for 90 min. The swollen samples were weighed after removing the water on the surface with a tissue paper. The water absorbency of the formulations was calculated applying the equation: $WA = W_s - W_d/W_d$, where W_d and W_s are the weight of the samples in dried and swollen state, respectively (Ni et al., 2009).

The ***hydrolytic stability*** of the hydrogel matrix was investigated by immersing pieces of xerogels of 10 mg in buffer solutions of different pH, from 2.5 up to 10, over 15 days. The moment of their complete dissolution was noted. After 15 days, the hydrogels were taken off, lyophilized, then weighed and the loss percent was calculated.

For practical applications, the ***largest water-holding ratio***, ***dynamic of the nitrogen***, and ***growth indexes*** of tomato seeds were calculated in laboratory experiments on *black peat* soil. The detailed experimental procedure was described in Supporting Information.

Statistical analysis

The determinations were done in triplicate for all the measurements, and the average value calculated (mean ± SD; n = 3) was taken as result.

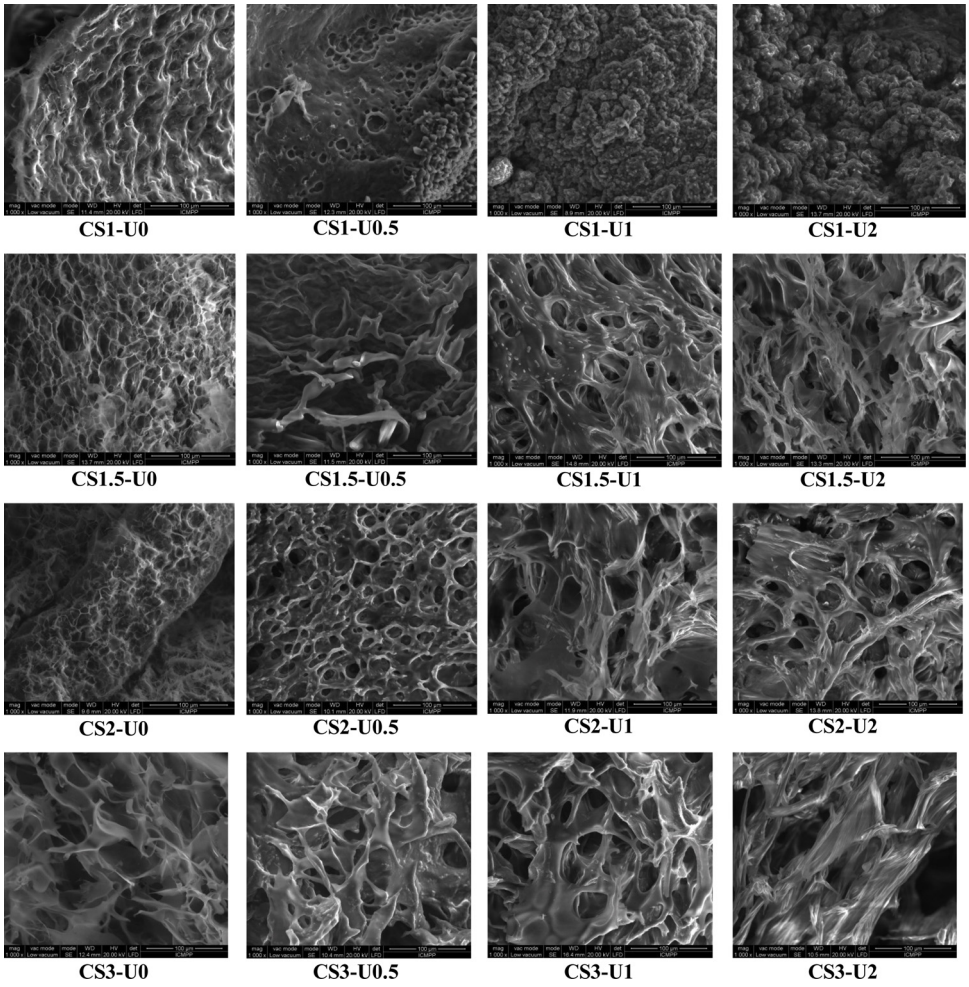

Fig. 3. Representative SEM images of the formulations and reference hydrogels (**CS1-Ux-CS3-Ux**).

3. Results and discussion

Four series of soil conditioner formulations were prepared by *in situ* hydrogelation of chitosan with salicylaldehyde in the presence of urea. It was expected that hydrogelation to take place due to the ordering of the newly formed imine units into supramolecular clusters, which play the role of crosslinking nodes, as already proved in our previous paper (Scheme 1) (Iftime et al., 2017). The four series of formulations were obtained by varying the molar ratio of the functional groups of chitosan and salicyladehyde, NH_2/CHO = 3/1; 2/1; 1.5/1; 1/1, with the aim to achieve different crosslinking degrees. Each series consists in four formulations, for which the content of urea was varied from 0 up to 66%. Thus, 16 formulations were resulted, different among them by the crosslinking degree and the content of fertilizer (Table 1).

A possible reaction of urea with chitosan *via* imine formation during the hydrogelation has been excluded by ^{1}H-NMR spectroscopy on a model reaction system (Supporting Information-Fig. S3).

The structural and supramolecular peculiarities of the formulations were investigated by FTIR spectroscopy, wide angle X-ray diffraction (WXRD) and polarized optical light microscopy (POM).

3.1. Structural investigation of the formulations by FTIR

The FTIR spectra of the formulations were recorded in order to investigate the hydrogelation mechanism of the systems and to have an insight on the pathway of urea encapsulation into them. They were assessed in comparison with the reference salicyl-imine-chitosan hydrogels and urea (Fig. 1; Supporting Information-Fig. S4). The hydrogelation of chitosan with salicylaldehyde was demonstrated by FTIR spectra by (i) the presence of the characteristic band of imine linkage as an intense, sharp band at 1628-1630 cm^{-1} and (ii) the modifications of the broad band from 3000 to 3700 cm^{-1}, attributed to the overlapped stretching bands of the O—H and N—H bonds and the intra- and inter-molecular H-bonds. These spectral peculiarities were in line with the formation of supramolecular clusters of imine units which played the role of chitosan crosslinkers (Iftime et al., 2017). The FTIR spectra of the formulations showed the bands characteristic to the reference hydrogels (**CSx-U0**) and urea, with slight modifications in position and intensity, indicating the preservation of the hydrogelation mechanism and the occurring of physical interactions between the two components.

The stretching bands of the C=O and N—H bonds into urea (1670 cm^{-1} and 1146 cm^{-1}, respectively) appeared shifted to higher wavenumbers (around 6 cm^{-1}) into the spectra of the formulations, pointing for their involvement into physical bonds with the hydrogel, extremely likely H-bonds as also evidenced for other chitosan – urea systems (Araújo, Romaoa, Doumer, & Mangrich, 2017). No obvious diminishing of intensity of the C=O band was noted, suggesting the absence of condensation reaction with amine groups of chitosan, as the model reaction indicated too. As in the fingerprint domain appeared overlapped bands from hydrogel and urea, the subtraction of the urea spectrum from that of the formulations was applied, when the imine band was clearly evidenced at 1629 cm^{-1}, similar to the reference hydrogels (Supporting Information-Fig. S1). The 3000–3500 cm^{-1} spectral domain of the formulations became dominated by the vibration bands of amine groups of urea, while the bands characteristic to hydroxyl and

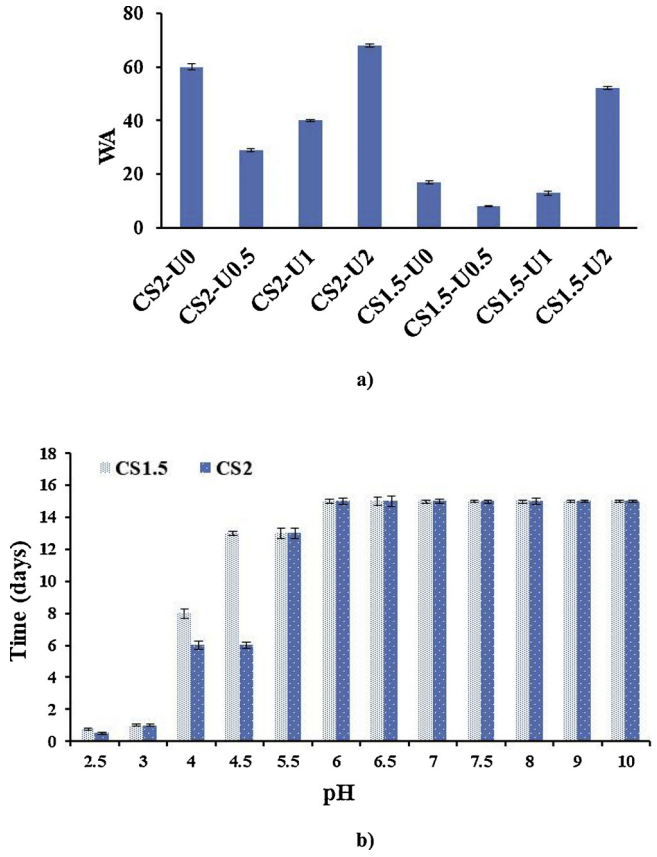

Fig. 4. a) Water absorbency of the **CS2-Ux** and **CS1.5-Ux** formulations, in distilled water; b) Time stability of **CS2** and **CS1.5** hydrogel matrix in media of different pH during 15 days.

methylene units drastically decreased in intensity, in agreement with the dominant content of urea in the detriment of chitosan.

All these FTIR data indicated the anchoring of the urea into the formulations by physical interactions, during the hydrogelation. Correlating FTIR data with the experimental observations, it appears that the occurring of the physical bonds between urea and chitosan favored the hydrogelation processes.

3.2. Supramolecular analysis of the formulations by wide angle X-ray diffraction (WXRD)

The formation of the salicyl-imine based crosslinking nodes into the reference hydrogels has been proved by WXRD mainly by the appearance of the reflection at a lower angle (6.22–6.6°), characteristic to the inter-layer distance of their layered supramolecular architecture (Iftime et al., 2017). The supramolecular architecture of the crosslinking nodes was further confirmed by the presence of broad reflections at wide angle (14 and 20°, respectively) corresponding to the inter-molecular and inter-chain distances inside them.

The formulations showed the distinct reflection peak at lower angles (6.12–6.7°), with slight variations of its maximum compared to the reference hydrogels, reflecting the environment influence, *e.g.* inter-molecular forces between the urea and chitosan, the presence of urea crystals (Fig. 2; Supporting Information-Fig. S5). The structural parameters were given in Supporting Information-Table S1. To have a quantitative insight on the formation of the crosslinking nodes, their size was calculated applying Scherer equation to the reflection band characteristic to the inter-layer distance of the ordered clusters (6.12–6.7°) (Samoila et al., 2015). The obtained results were given in Supporting Information-Table S2. For the reference hydrogels it was observed a variation of the diameter of the crosslinking nodes from 2.8 (**CS1-U0**, **CS3-U0**) to 3.5 (**CS1.5-U0**) and further to 4.2 nm (**CS2-U0**), in accordance with the balance between the density of imine units and the viscosity of the reaction system (see Supporting Information for more details). Interesting enough, except the **CS2-Ux** series, the presence of urea led to a slight increment of the size of crosslinking nodes, more pronounced in the case of the **CS1.5-Ux** series, suggesting that the physical forces developed between urea and chitosan facilitated the self-ordering of the imine units (Santos, Bacalhau, Pereira, Souza, & Faez, 2015). It can be estimated that these forces led to a stiffening of the chitosan chains and thus a decreasing of its mobility, which favored the self-assembling of the newly formed imine units, and thus a faster hydrogelation.

Besides the reflection bands characteristic to the reference hydrogels, the WXRD diffractograms of the formulations show the reflection bands characteristic to the urea (Fig. 2; Supporting Information-Fig. S5). Comparing the crystallographic profile of pure urea, attributed to a tetragonal system (Madhurambal, Mariappan, & Mojumdar, 2010) to that of the studied formulations, slight shifting of the reflection bands and changes in their intensity were noted (Fig. 2; Supporting Information-Table S1). Remarkable it was the shifting of the reflection band from 40.52° (d = 2.37 Å) to 41.58° (d = 2.32 Å), and the increase in intensity of the reflections from 24.58, 29.38 and 37.01°. Considering that urea is a hydrogen bonded molecular crystal for which the reflections correspond to the different lengths of the in-plane and out-of-plane hydrogen bonds (Gatti, Saunders, & Roetti, 1994), these changes can be speculated to occur under the influence of the chitosan–urea physical forces leading to rich-defect urea crystals (Craciun et al., 2019).

Applying Scherrer equation to the reflections around 22.4 and 29.3°, the size of the urea crystals into formulations was calculated, giving a diameter of urea crystals ranging from 28 to 39 nm (Supporting Information-Table S2). The dynamic of their size followed a similar trend to that of the imine clusters; smaller crystals were obtained for the highest and lowest crosslinking degree and bigger ones for the intermediates values, indicating similar driving forces of ordering. For each series, the size of the urea crystals increased with its content.

3.3. Formulation morphology

The formulation morphology was investigated by SEM, which also provided an insight on the urea incorporation (Fig. 3). A correlation between morphology and crosslinking degree (reflected by the content of salicylaldehyde) and the content of urea was evident.

Generally speaking, the increasing of the crosslinking degree gave a denser structure while the increasing of the content of urea led to thicker pore walls. Thus, in the case of the **CS1-Ux** series, the increasing of the urea content led to an almost compact structure with small pores; the two series with a medium crosslinking degree (**CS1.5-Ux**, **CS2-Ux**) showed a homogeneous, porous morphology, with interconnected pores and rare visible urea crystals embedded into the pore walls; the series with the lower crosslinking degree (**CS3-Ux**) showed also a porous morphology, with obvious larger urea crystals, as its content increased.

Polarized light microscopy images further supported X-ray and SEM data, confirming the presence of urea crystals for the samples with the higher and the lower crosslinking degree (Supporting Information- Fig. S6d and f) and their absence for those with medium crosslinking density (Supporting Information- Fig. S6e), when a fine birefringent texture was visualized (Marin, Popescu, Zabulica, Uji-I, & Fron, 2013).

3.4. Water absorbency and hydrolytic stability of the formulations

The potential of the formulations to absorb water was investigated in comparison with the reference hydrogels. The formulations quickly swollen when immersed in distilled water and their hydrolytic stability and water absorbency (WA) correlated with the crosslinking density and urea content; a higher crosslinking density led to a higher

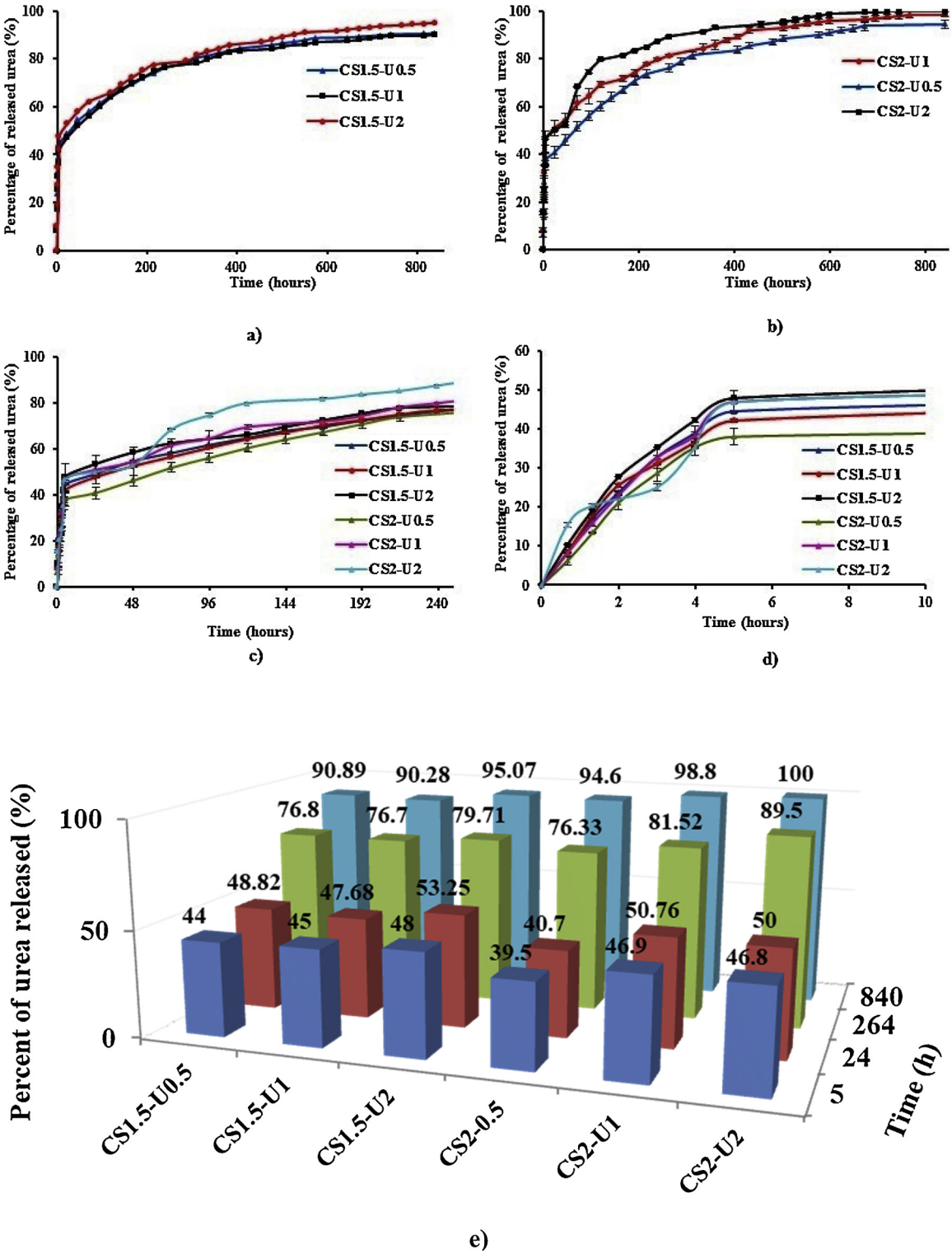

Fig. 5. Percentages of urea released during 35 days from the formulations (a,b,e) detailed for the first 10 days (c) and first 10 h (d).

hydrolytic stability but a lower absorption capacity. Thus, **CS1-Ux** samples were hydrolytic stable but presented the lowest absorption capacity, in agreement with their low porosity. Opposite, the **CS3-Ux** formulations swelled very fast, but they disintegrated simultaneously. The formulations with a medium crosslinking degree (**CS2-Ux** and **CS1.5-Ux**) proved the best balance of water absorbency/hydrolytic stability, with a **WA** from 68 to 9, while being hydrolytic stable on the entire period of investigation (35 days). **WA** increased as the content of urea increased, probably due to the increased number of pores resulted as the urea dissolved. In the case of **CS2-Ux** samples, **WA** increased progressively from 29 (**CS2-U0.5**) to 68 (**CS2-U2**), surpassing that of the reference hydrogel (Fig. 4a).

As the hydrogel matrix is based on the imine linkage known as being pH responsive (Godoy-Alcántar, Yatsimirsky, & Lehn, 2005; Tao, Liu, Zhang, Chi, & Xu, 2018), which should influence the urea release kinetics, the hydrolytic stability was further investigated in media of different pH, ranging from 2.5 to 10. As can be seen in Fig. 4b the stability over time increased as the pH increased, the hydrogels

Table 2
Water absorbency (WA) and percentage of urea released from chitosan based materials.

Formulation	Performances	Reference
Urea *in situ* encapsulated into salicylimine-chitosan hydrogels	WA = 68 g/g Burst effect≅45% in first 5h Prolonged release ≅100% after 35 days	the present study
Urea absorbed into chitosan based hydrogels (oxidized chitosan or itaconic acid grafted on chitosan)	WA = 23 g/g Prolonged release ≅ 50% in the first day	Leon et al. (2018)
Chitosan-humic material-urea-sodium tripolyphosphate microspheres	Burst effect ≅ 85% in the first 4 h Prolonged release ≅ 100% after 1 day	Araújo, Romão, Doumer, Mangrich (2017)
Urea encapsulated into chitosan microspheres crosslinked with genipin	WA = 1.64 g/g Burst effect ≅45% in first 2 days Prolonged release ≅ 90% after 7 days	Hussain, Devi, & Maji (2012)
Urea adsorbed into silk fibroin-gelatin-chitosan hydrogels	WA = 4.2 g/g Prolonged release ≅ 80% after 10 days	Rattanamanee et al. (2015)

immersed in media of pH higher than 6 still keeping their integrity after 15 days. The weighing after 15 days revealed mass loss from 14 to 56%, the hydrogels showing the best stability in media of neutral pH, superficial erosions occurring during the time (Supporting Information-Table S3).

3.5. *In vitro release behavior of urea fertilizer. Release kinetics*

The formulations with the best balance of water absorbency/hydrolytic stability, **CS2-Ux** and **CS1.5-Ux** series, were further investigated for their ability to act as matrix for controlled release of urea fertilizer, by measuring the *in vitro* release profile in distilled water, at room temperature during 35 days. The results were gathered in Fig. 5a–e. All formulations released the encapsulated urea in three stages: (i) a burst effect in the first 5 h, when up to 46% urea passed in the water medium (Fig. 5d); (ii) a slower release in the next 11 days, reaching 75% released urea (Fig. 5c); and (iii) a slower continuous release in the next 23 days when almost all the urea passed in the water medium (Fig. 5a and b; Supporting Information-Table S4).

Comparing the release rates of the six analyzed formulations, the influence of the crosslinking degree and urea content (which were reflected on the morphology and water absorbency) could be observed (Fig. 5e). As expected, the highest release rate has been recorded for the samples with the highest content of urea (**CS2-U2**, **CS1.5-U2**), according to its encapsulation as larger crystals, less anchored into the matrix and thus subjected to a faster dissolution. **CS1.5-Ux** samples showed a slightly faster release compared to **CS2-Ux**, probably due to the fact that the more viscous medium during hydrogelation influenced the growth of defect-rich urea crystals, which were more susceptible to dissolution (Craciun et al., 2019). The highest amount of released urea has been noted for **CS2-Ux**, in agreement with their lower crosslinking degree which favored a higher swelling and thus easier urea dissolution and diffusion to the release medium.

The formulations didn't show visible changes during the investigation period of 35 days, and their FTIR spectra were similar to those of the reference hydrogels (Supporting Information-Fig. S7), pointing for their stability and their further utility as soil conditioners, even after urea release.

To go in deeper details of the release mechanism of urea from the studied formulations, a mathematical analysis of the *in vitro* release profile has been performed. To proper asses the mechanism of urea release in our formulations, five different mathematical models were fitted on the *in vitro* release profile, on each of the three stages (Supporting Information-Table S5, S6, S7).

The graphical representation of the equations of the five mathematical models on the data obtained from the first stage of the *in vitro* release gave a high correlation coefficient (R^2 = 0.98–0.99) in the case of Zero Order, Higuchi and Korsmeyer-Peppas and lower correlation coefficient in the case of First order and Hixson-Crowell models, for all samples (Supporting Information-Table S5). This means that the mechanism of the first release stage can be described by these three models, as follows.

The excellent fitting of ***Zero Order*** model (R^2 = 0.98–0.99) indicates that urea release was influenced by the swelling transition of the hydrogel matrix in the first 5 h of experiment. Differences in the proportionality constant (k_o) reflect the effect of the matrix on the speed of urea dissolution, which can be correlated with the strength of its anchoring into the matrix.

The good fitting of the **Higuchi** model (R^2 = 0.996–0.999) shows that urea release was controlled by the diffusion process. At this stage, the concentration of urea into the release medium (3 mg/mL) was much under the saturation concentration (1.04 g/mL), indicating that the encapsulation of the urea into the hydrogel matrix prevented its fast dissolution and promoted its slow diffusion towards the release medium. This can be attributed to the physical forces between the urea and hydrogel matrix which on the one hand anchored the urea crystals slowing down their dissolution and on the other hand bonded the molecules of urea slowing down their sink on inner-outer direction imposed by the concentration gradient.

Further, the fitting of the Korsmeyer-Peppas model (R^2 = 0.981–0.997) confirmed the influence of the hydrogel matrix, as the two previous models suggested, and gave information related to the type of diffusion. Except **CS2-U0.5** which gave an exponent n value of 0.98 indicating a case II transport, the other samples showed the n exponent values from 0.65 to 0.89, characteristic for a non-Fickian anomalous transport when the diffusion through the matrix was occurring simultaneously with the matrix swelling. This behavior was also revealed by other polysaccharides based nutrient carriers, which showed swelling in the first stage when the water molecules penetrate the hydrogel network and dissolve the nutrient, simultaneously (Guilherme et al., 2015). In our particular formulations, it is expected that urea movements into the hydrogel walls would exercise stress on them, leading to some degree of morphological changes, *e.g.* cracks, and subsequently to a change of the diffusivity.

The lack of fitting of the First Order Kinetic model (R^2 = 0.88–0.91) indicates no control of the amount of encapsulated urea onto its release, while the absence of fitting of the Hixon-Crowell model (R^2 = 0.92–0.95) shows that urea release is mainly controlled by its diffusion through the matrix and less by its dissolution velocity. Both features can be attributed to the presence of larger crystals of urea less anchored into the matrix, susceptible to a faster dissolution in the first release stage.

In the second stage of the *in vitro* release, all the five mathematical models fitted very well on the obtained data (Supporting Information-Table S6) indicating some changes in the release mechanism. The good fitting of the First Order Kinetic model indicates that in this stage the amount of the urea remained into matrix plays an important role on its release rate. The fitting of the Hixon-Crowell model shows that the urea dissolution velocity surpasses the importance of its diffusion through the hydrogel matrix. Even if some studies recommend the use of the Korsmeyer Peppas model only for domains of up to a 60% of active compound released, it fitted very well on the second stage of urea release (60–75% released urea) and revealed a drastic decrease of the n to the range 0.14–0.33, indicating the turn of the urea diffusion to a

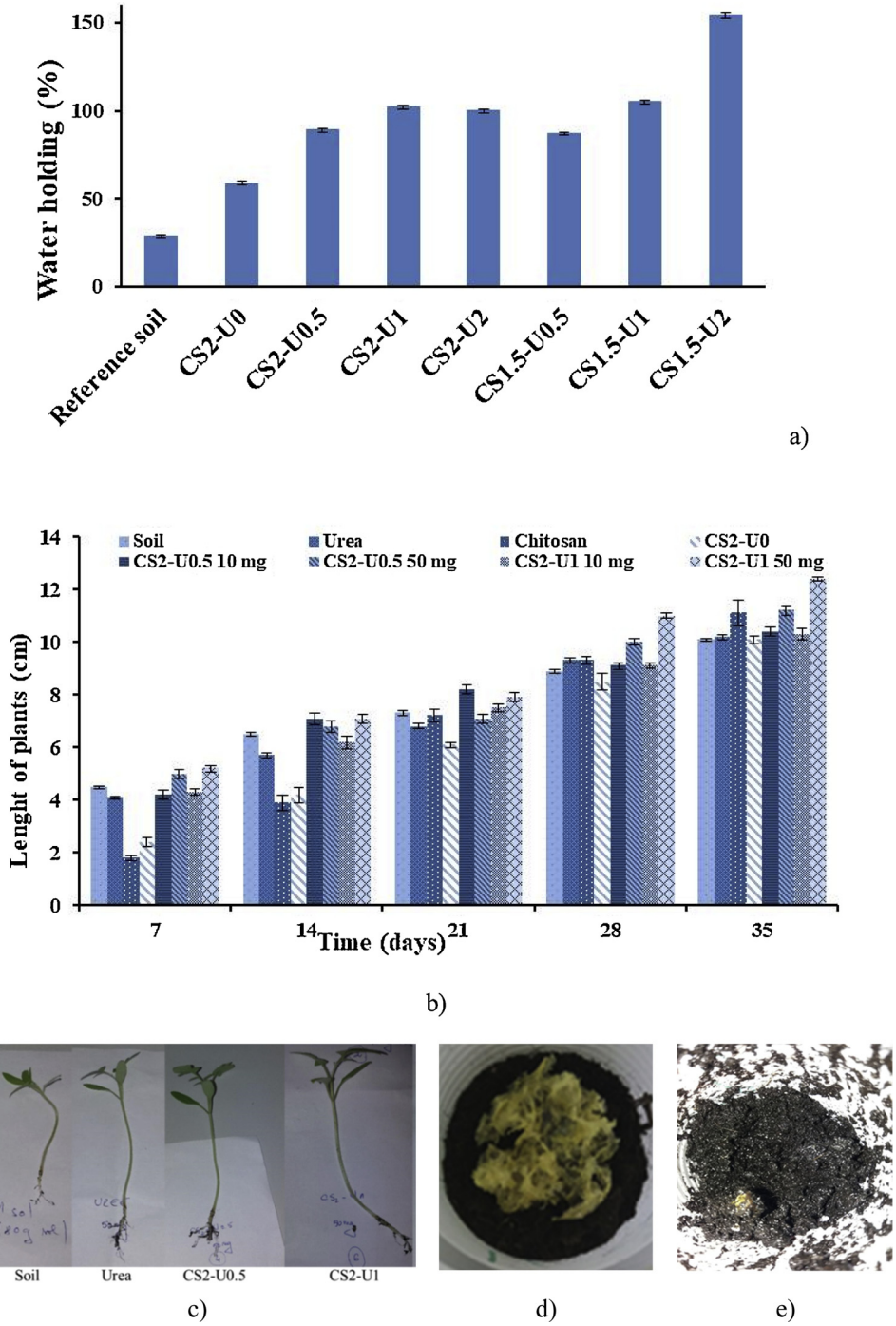

Fig. 6. Graphical representation of a) the largest water-holding ratio of the soil fertilized with **CS2-Ux** and **CS1.5-Ux** formulations; b) length of tomato seedlings function of time; c) Photographs of the tomato seedlings at the end of the experiment; Photographs of the formulation sample in soil, before (d) and after (e) seedling growth experiment.

Fickian pattern, in agreement with urea diffusion on the direction controlled by the concentration gradient. Worthy of consideration is also the drastic diminishing of the proportionality constants to close values for the second release stage, indicating an almost similar influence of the hydrogel matrix on the urea release (Supporting Information-Table S6). All these suggest that in the second stage, due to the morphological changes (*e.g.* swollen matrix, cracks into the pore walls), the diffusion of the urea molecules was facilitated, and thus the dissolution velocity became the driving force for urea sink on inner-to-outer direction. This can be related to the strong anchoring of the smaller crystals or even molecules of the remaining urea into matrix, slowing down its dissolution.

In the third second stage, except Korsmeyer Peppas, the fitting of all mathematical models failed (R^2 = 0.81–0.96) for almost all the samples (Supporting Information-Table S7), indicating that heterogeneous erosions of the matrix occurred and no control of the principal processes were longer available.

Summarizing, the urea release mechanism from salicyl-imine-chitosan hydrogels could be illustrated as follows. The soaking of the formulation samples in water allows them to swell and then transform into hydrogel. The water transferred into the crosslinked hydrogel, first through the pores and then penetrated the pore walls, dissolving the

urea. In the first stage, larger urea crystals less anchored into the hydrogels matrix were susceptible to dissolution, followed in the second and third stage by the smaller urea crystals, better anchored. The dissolved urea diffused out from the matrix and then released through the dynamic exchange with free water. Considering the mechanism of urea release, it can be estimated that the soil moisture will guide its delivery in practical applications, as also demonstrated by other authors (Agehara & Warncke, 2005).

Overall, the *in vitro* release profile of the studied formulations suggests that the salicyl-imine-chitosan hydrogels are appropriate matrixes for a sustained delivery of the urea fertilizer: an initial burst effect should help the growing of plants by a greater fertility dosage, followed by a constant release during the plant growth (Azeem et al., 2014).

Table 2 summarizes the values of water absorbency and percentage of urea released from other chitosan based formulations reported by other research groups. As can be seen, a sustained release of urea has been also achieved for other chitosan based hydrogels or microspheres, but water absorbency had significant lower values compared to the salicylimine-chitosan based formulations studied in this paper. Hence, the results obtained in this work are very encouraging and open up the possibility of using such materials as multifunctional soil conditioners at larger scale.

3.6. Practical application of the formulations

To have a preliminary insight on the ability of the designed formulations to act as soil conditioners, their ability to fertilize the soil and to hold the water were investigated on **CS2-U0.5** and **CS2-U1** samples, by measuring the largest water-holding ratio and the nitrogen dynamic in soil, and the morphological parameters of tomato seedlings in germination experiments (Fig. 6 and Table S9 in Supporting Information).

An outstanding increase of the largest water holding parameter, from 29 for the reference soil to 154 wt.% for the **CS1.5-U2** formulation has been recorded, as can be seen in Fig. 6a. Moreover, the soil sample without xerogels lost the absorbed water after 7 days while those with formulations after 12 days. These results confirmed the expectations, demonstrating that they can improve the water-holding capacity of soil and could obviously reduce the water evaporation.

The evaluation of the dynamic of the nitrogen in soil revealed highest values for the experimental variants including the studied formulations, reaching almost double values (up to 2.07% compared to 0.87% in the blank soil, see Table S9), highlighting the favorable role of the sustained urea release.

The measurements of the morphological parameters of tomato seedlings (green root weight (FW); dry root weight (DW) and length of plants (PL)) indicated the positive influence of the formulations on the plant growth, as can be seen in Table S9 and Fig. 6. These results showed that the formulations stimulated the plant growth up to almost 70% higher than the reference soil. They were supported by the increment of the total content of nitrogen in the fertilized soil with 138% compared to the blank soil. Moreover the formulations significantly reduced their dimension during experiments indicating their biodegradability, as can be seen in Fig. 6c,d, while the increment of the morphological parameters for the plants germinated in the soil conditioned with chitosan and CS2-U0 indicated the fertilizing effect of their biodegradation products (see Table S9 and Fig. 6). Considering the enriching of the soil with nitrogen and the higher growth indexes obtained when reference hydrogels samples were used, it can be estimated that the degradation products of the hydrogel matrix have no nocive effect and moreover they have a fertilizing effect, as estimated.

4. Conclusions

New systems designed as soil conditioners were prepared by *in situ* hydrogelation of chitosan with salicylaldehyde in the presence of urea. They were formulated to have different crosslinking density and urea content, in order to optimize the best compositions for the targeted application. The collected data from FTIR spectra and X-ray diffraction revealed that urea has been encapsulated mostly as submicrometric crystals anchored into the hydrogel matrix by H-bonds with chitosan. SEM images showed that the formulations were porous and urea crystals were embedded into the pore walls. *In vitro* release investigation evidenced that urea was delivered in three stages governed by the morphological changes of the hydrogel matrix and anchoring forces: (1) a burst release during first 5 h controlled by a non-Fickian diffusion through the matrix in the swelling transition; (2) a prolonged release in the next 11 days controlled by a Fickian diffusion through the swollen matrix; and (3) the release of the remanent urea up to the day 35. Preliminary investigation of the samples as soil fertilizers suggested benefits of their use, by improving the water-holding capacity and nitrogen percentage of the soil, while being biodegradable. All these findings indicate the new systems as multifunctional soil conditioners, opening up new perspectives in the design of e**co-**materials suitable for sustainable agriculture.

Acknowledgements

The research leading to these results has received funding from the Romanian National Authority for Scientific Research, MEN-UEFISCDI grant, project number PN-III-P1-1.2-PCCDI-2017-0569, Contract nr. 10PCCDI/2018.

Appendix A. Supplementary data

Supplementary material related to this article can be found, in the online version, at doi:https://doi.org/10.1016/j.carbpol.2019.115040.

References

Abobatta, W. (2018). Impact of hydrogel polymer in agricultural sector. *Advances in Agriculture and Environmental Science: Open Access, 1*(2), 59–64.
Agehara, S., & Warncke, D. D. (2005). Soil moisture and temperature effects on nitrogen release from organic nitrogen sources. *Soil Science Society of America Journal, 69*, 1844–1855.
Ailincai, D., Marin, L., Morariu, S., Mares, M., Bostanaru, A. C., Pinteala, M., et al. (2016). Dual crosslinked iminoboronate-chitosan hydrogels with strong antifungal activity against Candida planktonic yeasts and biofilms. *Carbohydrate Polymers, 152*, 306–316.
Araújo, B. R., Romão, L. P. C., Doumer, M. E., & Mangrich, A. S. (2017). Evaluation of the interactions between chitosan and humics in media for the controlled release of nitrogen fertilizer. *Journal of Environmental Management, 190*, 122–131.
Araújo, B. R., Romaoa, L. P. C., Doumer, M. E., & Mangrich, A. S. (2017). Evaluation of the interactions between chitosan and humics in media for the controlled release of nitrogen fertilizer. *Journal of Environmental Management, 190*, 122–131.
Azeem, B., KuShaari, K. Z., Man, Z. B., Basit, A., & Thanh, T. H. (2014). Review on materials & methods to produce controlled release coated urea fertilizer. *Journal of Controlled Release, 181*, 11–21.
Bejan, A., Ailincai, D., Simionescu, B. C., & Marin, L. (2018). Chitosan hydrogelation with a phenothiazine based aldehyde: A synthetic approach toward highly luminescent biomaterials. *Polymer Chemistry, 9*, 2359–2369.
Campos, E. V. R., Oliveira, J. Z., Fraceto, L. F., & Singh, B. (2015). Polysaccharides as saffer release systems for agrochemicals. *Agronomy for Sustainable Development, 35*, 47–66.
Corradini, E., Moura, M. R., & Mattoso, L. H. C. (2010). A preliminary study of the incorparation of NPK fertilizer into chitosan nanoparticles. *Express Polymer Letters, 4*, 509–515.
Craciun, A. M., Mititelu-Tartau, L., Pinteala, M., & Marin, L. (2019). Nitrosalicyl-imine-chitosan hydrogels based drug delivery systems for long term sustained release in local therapy. *Journal of Colloid and Interface Science, 536*, 196–207.
Gatti, C., Saunders, V. R., & Roetti, C. (1994). Crystal field effects on the topological properties of the electron density in molecular crystals: The case of urea. *The Journal of Chemical Physics, 101*, 10242.
Godoy-Alcántar, C., Yatsimirsky, A. K., & Lehn, J.-M. (2005). Structure-stability correlations for imine formation in aqueous solution. *Journal of Physical Organic Chemistry, 18*, 979–985.
Guilherme, M. R., Aouada, F. A., Fajardo, A. R., Martins, A. F., Paulino, A. T., Davi, M. F. T., et al. (2015). Superabsorbent hydrogels based on polysaccharides for application in agriculture as soil conditioner and nutrient carrier: A review. *European Polymer Journal, 72*, 365–385.
Hargreaves, J. C., Adl, M. S., & Warman, P. R. (2008). A review of the use of composted municipal solid waste in agriculture. *Agriculture, Ecosystems & Environment, 123*,

1–14.
Hussain, M. R., Devi, R. R., & Maji, T. K. (2012). Controlled release of urea from chitosan microspheres prepared by emulsification and cross-linking method. *Iranian Polymer Journal, 21*, 473–479.
Iftime, M. M., & Marin, L. (2018). Chiral betulin-imino-chitosan hydrogels by dynamic covalent sonochemistry. *Ultrasonics Sonochemistry, 45*, 238–247.
Iftime, M. M., Morariu, S., & Marin, L. (2017). Salicyl-imine-chitosan hydrogels: Supramolecular architecturing as a crosslinking method toward multifunctional hydrogels. *Carbohydrate Polymers, 165*, 39–50.
Iriti, M., & Varoni, E. M. (2015). Chitosan-induced antiviral activity and innate immunity in plants. *Environmental Science and Pollution Research - International, 22*, 2935–2944.
Kato, S., Kishiro, F., Yokohagi, O., Vijayanand, P. S., Satokawa, S., & Kojima, T. (2017). Synthesis of novel biodegradable superabsorbent polymer using chitosan for desert land development. *Journal of Arid Land Studies, 27*, 67–74.
Leon, O., Munoz-Bonilla, A., Soto, D., Ramirez, J., Marquez, Y., Colina, M., et al. (2018). Preparation of oxidized and grafted chitosan superabsorbents for urea delivery. *Journal of Polymers and the Environment, 26*, 728–739.
Lin, C. C., & Metters, A. T. (2006). Hydrogels in controlled release formulations: Network design and mathematical modeling. *Advanced Drug Delivery Reviews, 58*, 1379–1408.
Liu, X., Zhang, Y., Han, W., Tang, A., Shen, J., Cui, Z., et al. (2013). Enhanced nitrogen deposition over China. *Nature, 494*, 459–462.
Madhurambal, G., Mariappan, M., & Mojumdar, S. C. (2010). Thermal, UV and FTIR spectral studies of urea–thiourea zinc chloride single crystal. *Journal of Thermal Analysis and Calorimetry, 100*, 763–768.
Majeed, Z., Ramli, N. K., Mansor, N., & Man, Z. (2015). A comprehensive review on biodegradable polymers and their blends used in controlled-release fertilizer processes. *Reviews in Chemical Engineering, 31*, 69–96.
Malerba, M., & Cerana, R. (2016). Chitosan effects on plant systems. *International Journal of Molecular Sciences, 17*, E996.
Marin, L., Ailincai, D., Morariu, S., & Tartau-Mititelu, L. (2017). Development of biocompatible glycodynameric hydrogels joining two natural motifs by dynamic constitutional chemistry. *Carbohydrate Polymers, 170*, 60–71.
Marin, L., Popescu, M. C., Zabulica, A., Uji-I, H., & Fron, E. (2013). Chitosan as a matrix for biopolymer dispersed liquid crystal systems. *Carbohydrate Polymers, 95*, 16–24.
Narayanan, A., & Dhamodharan, R. (2015). Super water-absorbing new material from chitosan, EDTA and urea. *Carbohydrate Polymers, 134*, 337–343.
Naz, M. Y., & Sulaiman, S. A. (2016). Slow release coating remedy for nitrogen loss from conventional urea: A review. *Journal of Controlled Release, 225*, 109–120.
Ni, B., Liu, M., & Lü, S. (2009). Multifunctional slow-release urea fertilizer from ethylcellulose and superabsorbent coated formulations. *Chemical Engineering Journal, 155*, 892–898.
Olaru, A. M., Marin, L., Morariu, S., Pricope, G., Pinteala, M., & Tartau-Mititelu, L. (2018). Biocompatible chitosan based hydrogels for potential application in local tumour therapy. *Carbohydrate Polymers, 179*, 59–70.
Perez, J. J., & Francois, N. J. (2016). Chitosan-starch beads prepared by ionotropic gelation as potential matrices for controlled release of fertilizers. *Carbohydrate Polymers, 148*, 134–142.
Pichyangkura, R., & Chadchawanb, S. (2015). Biostimulant activity of chitosan in horticulture. *Scientia Horticulturae, 196*, 49–65.
Rattanamanee, A., Niamsup, H., Srisombat, L., Punyodom, W., Watanesk, R., & Watanesk, S. (2015). Role of chitosan on some physical properties and the urea controlled release of the silk fibroin/gelatin hydrogel. *Journal of Polymers and the Environment, 23*, 334–340.
Samoila, P., Sacarescu, L., Borhan, A. I., Timpu, D., Grigoras, M., Lupu, N., et al. (2015). Magnetic properties of nanosized Gd doped Ni–Mn–Cr ferrites prepared using the sol–gel autocombustion technique. *Journal of Magnetism and Magnetic Materials, 378*, 92–97.
Santos, B. R., Bacalhau, F. B., Pereira, T. S., Souza, C. F., & Faez, R. (2015). Chitosan-Montmorillonite microspheres: A sustainable fertilizer delivery system. *Carbohydrate Polymers, 127*, 340–346.
Tao, Y., Liu, S., Zhang, Y., Chi, Z., & Xu, J. (2018). pH-responsive polymer based on dynamic imine bonds as a drug delivery material with pseudo target release behavior. *Polymer Chemistry, 9*, 878–884.
Wu, L., & Liu, M. Z. (2008). Preparation and properties of chitosan-coated NPK compound fertilizer with controlled-release and water-retention. *Carbohydrate Polymers, 72*, 240–247.
Yang, L., An, D., Wang, T. J., Kan, C. Y., & Jin, Y. (2017). Photodegradation of polymer materials used for film coatings of controlled-release fertilizers. *Chemical Engineering & Technology, 40*, 1611–1618.
Zhao, C., Shen, Y. Z., Du, C. W., Zhou, J. M., Wang, H. Y., & Chen, X. Y. (2010). Evaluation of waterborne coating for controlled-release fertilizer using wurster fluidized bed. *Industrial & Engineering Chemistry Research, 49*, 9644–9647.